School of Civil and Mechanical Engineering

Wind Turbine Reliability Improvement by Fault Tolerant Control

Hamed Habibi

This thesis is presented for the Degree of
Doctor of Philosophy
of
Curtin University

October 2018

Declaration of Authorship

I, Hamed HABIBI, declare that this thesis titled, "Wind Turbine Reliability Improvement by Fault Tolerant Control" and the work presented in it are my own. I confirm that:

- To the best of my knowledge and belief this thesis contains no material previously published by any other person except where due acknowledgment has been made.

- This thesis contains no material which has been accepted for the award of any other degree or diploma in any university.

- Where I have consulted the published work of others, this is always clearly attributed.

- Where I have quoted from the work of others, the source is always given. With the exception of such quotations, this thesis is entirely my own work.

- I have acknowledged all main sources of help.

- Where the thesis is based on work done by myself jointly with others, I have made clear exactly what was done by others and what I have contributed myself.

Signed:

Date:

Abstract

Wind Turbine Reliability Improvement by Fault Tolerant Control

by Hamed Habibi

This thesis investigates the improvement that can be achieved to wind turbine reliability with aid of model-based fault detection and fault tolerant control designs, so that the wind turbine continues to operate satisfactorily with the same performance index in the presence of faults as in fault-free situations. In this regard, a comprehensive review is initially given to understand and appraise the directions and outcomes of the current research. Accordingly, the wind turbine bench mark model associated with the considered faults is introduced, on which the proposed controllers are designed. Also, the available industrial baseline controllers are adopted, with which the performance of the proposed controllers are compared, using the numerical criteria. Also, these baseline controllers are initially improved, with adaptive gains, using a fuzzy inference system in the low speed region, and PID-like controller with Nussbaum-type function in the high speed region. These modifications give an intuitive motivation for the rest of this research. The different operational regions of the wind turbine are considered with corresponding fault sources and, consequently, the controllers are designed to satisfy the corresponding operational objectives. Also, the considered fault information is generated, using different suitable approaches, which can be useful for maintenance purposes. The numerical simulations are conducted to investigate the performance of the proposed controllers. In this regard, firstly in the low speed region, a nonlinear FTC is proposed with adaptive laws, to keep the wind turbine operating with maximum efficiency, in the presence of pitch actuator and generator faults. Also, the unknown desired trajectory is reconstructed using a Gaussian radial basis function neural network. So, it is shown that the captured power is maximized. On the other hand, for high wind speed region, the constrained fault tolerant controller is designed to guarantee that the wind turbine speed will not violate the predefined and safe-to-operate limit, and consequently, keep the wind turbine structurally safe with less engagement of the mechanical brakes, in the presence of wind speed variation and faults. The Nussbaum-type function is utilized to tackle the unknown control direction problem. The unknown aerodynamic torque is approximated using the Gaussian radial basis function neural network. In a separate approach, the sensors fault detection is achieved via design of a novel unknown input observer with the calculated fault probability. The baseline controller is adopted in both fault-free and faulty situations, which leads to the less complicated and more industrially-acceptable scheme. Finally, conclusions of this research are summarized.

Publications list

The papers publications arising from this current research are as follows.

Published Journal Papers

- Hamed Habibi, Ian Howard, and Reza Habibi, "Bayesian Fault Probability Estimation; Application in Wind Turbine Drive train Sensor Fault Detection", Asian Journal of Control, In Press, 2020.

- Hamed Habibi, Hamed Rahimi Nohooji, and Ian Howard "Backstepping Nussbaum Gain Dynamic Surface Control for a Class of Input and State Constrained Systems with Actuator Faults", Information Sciences, Vol. 482, pp. 27-46, 2019.

- Hamed Habibi, Ian Howard, and Silvio Simani, "Reliability Improvement of Wind Turbine Power Generation using Model-based Fault Detection and Fault Tolerant Control: a review", Renewable Energy, Vol. 135, pp. 877-896, 2019.

- Hamed Habibi, Hamed Rahimi Nohooji, and Ian Howard, "Adaptive PID Control of Wind Turbines for Power Regulation with Unknown Control Direction and Actuator Faults", IEEE Access, Vol. 6, pp. 37464-37479, 2018.

- Hamed Habibi, Aghil Yousefi Koma, and Ian Howard, "Power Improvement of Non-Linear Wind Turbines during Partial Load Operation using Fuzzy Inference Control", Control Engineering and Applied Informatics, Vol. 19, No. 2, pp. 31-42, 2017.

- Hamed Habibi, Hamed Rahimi Nohooji, and Ian Howard, "Optimum efficiency control of a wind turbine with unknown desired trajectory and actuator faults", Journal of Renewable and Sustainable Energy, Vol. 9, No. 6, p. 063305, 2017.

- Hamed Habibi, Hamed Rahimi Nohooji, and Ian Howard, "Power maximization of variable-speed variable-pitch wind turbines using passive adaptive neural fault tolerant control", Frontiers of Mechanical Engineering, Vol. 12, No. 3, pp. 377-388, 2017.

- Hamed Habibi, Ian Howard, and Reza Habibi, "Bayesian Sensor Fault Detection in a Markov Jump System", Asian Journal of Control, Vol. 19, No. 4, pp. 1465-1481, 2017.

Published Conference Papers

- Hamed Habibi, Hamed Rahimi Nohooji, and Ian Howard, "Constrained control of wind turbines for power regulation in full load operation", proceedings of 11th Asian Control Conference (ASCC), pp. 2813-2818, 2017.

viii

- Hamed Habibi, Hamed Rahimi Nohooji, and Ian Howard, "A neuro-adaptive maximum power tracking control of variable speed wind turbines with actuator faults", proceedings of Australian and New Zealand Control Conference (ANZCC), pp. 63-68, 2017.

Acknowledgements

Contents

List of Figures

List of Tables

xx

List of Abbreviations

BLF	**B**arrier **L**yapunov **F**unction
CR	**C**ontroller **R**econfiguration
DSC	**D**ynamic **S**urface **C**ontrol
DT	**D**etection **T**ime
EM	**E**xpectation **M**aximization
FA	**F**ault **A**ccomodation
FD	**F**ault **D**etection
FDI	**F**ault **D**etection and **I**solation
FII	**F**ault **I**solation and **I**dentification
FIS	**F**uzzy **I**nference **S**system
FTC	**F**ault **T**olerant **C**ontrol
GRBFNN	**G**aussian **R**adial **B**asis **F**unction Neural Networks
HAC	**H**igh **A**ir **C**ontent
HAWT	**H**orizontal **A**xis **W**ind **T**urbine
HL	**H**ydraulic **L**eak
iid	**i**ndependent and **i**dentically **d**istributed
LMI	**L**inear **M**atrix **I**nequality
LPV	**L**inear **P**arameter **V**arying
MBFDI	**M**odel **B**ased **F**ault **D**etection and **I**solation
MBFTC	**M**odel **B**ased **F**ault **T**olerant **C**ontrol
PFF	**P**article **F**ilter **F**ramework
PID	**P**roportional **I**ntegral **D**erivative
PW	**P**ump **W**ear
RLS	**R**ecursive **L**east **S**quare
RMSE	**R**oot **M**ean **S**quared **E**rror
SCADA	**S**upervisory **C**ontrol **A**nd **D**ata **A**cquisition
TS	**T**akagi **S**ugeno
TSR	**T**ip **S**peed **R**atio
UUB	**U**niformly **U**ltimately **B**ounded
VAF	**V**ariance **A**ccounted **F**or
VSA	**V**irtual **S**ensor and **A**ctuator

List of Symbols

a	Unknown positive constant	$-$
a_f	Unknown non-negative constant	$-$
A	Blade swept area	m^2
A_{dt}	Drive train dynamic matrix	$-$
A_{wt}	Wind turbine dynamic matrix	$-$
B	Drive train input matrix	$-$
B_{dt}	Drive train torsional damping	$Nm/(rad/s)$
B_r	Rotor bearing viscous friction	$Nm/(rad/s)$
B_g	Generator bearing viscous friction	$Nm/(rad/s)$
B_t	Tower damping ratio	$N/(m/s)$
B_{wt}	Wind turbine input matrix	$-$
c_F	Center of fuzzy membership function	$-$
C	Drive train measurement matrix	$-$
$CC1, \ldots$ and $CC6$	Performance criteria	$-$
C_p	Power coefficient	$-$
C_q	Torque coefficient	$-$
C_t	Thrust coefficient	$-$
$C_{\dot{\rho}}$ and $C_{\dot{\Phi}}$	Upper bounds	$-$
d and d_T	Drive train sensor residuals	$-$
d_{wt}	Wind turbine disturbance vector	$-$
D	Rotor dynamic disturbance function	$-$
e_X	Tracking error of variable X	$-$
f_{T_g}	Generator bias	Nm
F	Rotor dynamic function	$-$
F_t	Aerodynamic thrust	N
G	Rotor dynamic input function	$-$
h_i	Basis functions	$-$
$H(\beta_u)$	Pitch actuator saturation	$-$
J_g	Generator shaft inertia	kgm^2
J_r	Rotor shaft inertia	kgm^2
$k_{1,\omega_g}, k_{2,\omega_g}, k_{1,\beta}$ and $k_{2,\beta}$	Positive design parameters	$-$
$k_{e_{\omega_r}}$	ω_r constraint	(rad/s)
$k_{e_{\dot{\omega}_r}}$	$\dot{\omega}_r$ constraint	(rad/s^2)
K	Drive train observer gain	$-$
K_c	Constant controller gain	$Nm/(rad/s)^2$

K_{dt}	Drive train torsional stiffness	Nm/rad
K_{FIS}	FIS controller gain	$Nm/(rad/s)^2$
K_P, K_I and K_D	PID controller gains	$-$
K_{PO}, K_{IO} and K_{DO}	PID controller gains in observer structure	$-$
K_t	Tower elasticity coefficient	N/m
K_2	Drive train friction compensation gain	$Nm/(rad/s)$
L	Lower bound of $\partial T_a/\partial \beta$	$-$
M_t	Nacelle mass	kg
N_g	Drive train ratio	$-$
$N(\xi)$	Nussbaum function of ξ	$-$
p	Density distribution	$-$
P	Fault probability	$-$
P_a	Induced wind power	W
P_g	Electrical generated electrical power	W
P_w	Available wind power	W
R	Blade length	m
s	Neurons Number	$-$
$S\left(\beta_u\right)$	Pitch saturation estimation	$-$
t_{exe}	Execution time	s
t_f	Fault time	s
$t_{g,d}$	Generator communication delay	s
$t_{p,d}$	Pitch actuator communication delay	s
T_a	Aerodynamic torque	Nm
$T_{a,NN}$	GRBFNN estimation of T_a	Nm
T_g	Generator torque	Nm
T_h	Generator driving torque	Nm
T_l	Rotor load torque	Nm
u	Drive train input vector	$-$
u_{wt}	Wind turbine controller vector	$-$
U	Upper bound of $\partial T_a/\partial \beta$	$-$
V, V_1, V_2, $V_1^{T_g}$, V_1^{β}	Positive definite Lyapunov functions	$-$
V_r	Effective wind speed	m/s
$V_{r,cut-in}$	Cut-in wind speed	m/s
$V_{r,cut-out}$	Cut-out wind speed	m/s
V_w	Free wind speed	m/s
x, x_{wt} and x_1	State vector	$-$
x_F	Range of fuzzy variable	$-$
x_t	Nacelle displacement	m
$X_{desired}$ or X_d	Desired value of variable X	$-$
X_{fa}	Faulty value of variable X	$-$
X_{ff}	Fault-free value of variable X	$-$
X_{max}	Maximum achievable value of X	$-$
X_N	Nominal value of variable X	$-$

X_{opt}	Optimum value of variable X	–
X_{ref}	Reference value of variable X	–
X_s	Measured value of variable X	–
$\hat{X}$	Estimation of variable X	–
$\tilde{X}$	Estimation error of variable X	–
$\bar{X}$	Upper bound satisfying $|X| \leq \bar{X}$	–
y	Drive train output vector	–
z_2	Virtual control	–
Z	Tracking error filter	–
α	Sensor coefficient	–
α_D	Virtual control	–
α_{f_1} and α_{f_2}	Fault indicator	–
α_X	Measurement coefficient of X	–
α_{ω_g} and α_β	Positive design parameters	–
$\hat{\alpha}_{w,t}$	Weighted RLS estimation	–
$\hat{\alpha}_{w,t,r}$	Windowed weighted RLS estimation	–
$\hat{\alpha}_{w,t,\lambda_e}$	Exponentially weighted RLS estimation	–
β	Pitch angle	°
β_{dc}	Pitch angle with dynamic change	°
β_{normal}	Normal pitch angle	°
β_u	Pitch angle effort	°
β^*	Desired pitch angle	°
γ_1 and γ_2	Positive design parameter	–
Γ	Design matrix	–
$\Delta T_a|_{\Delta C_p}$	Aerodynamic characteristic change	–
$\Delta\beta$	Pitch angle deviation	°
$\Delta\tau_g$	Internal generator fault	s
ε	Estimation error	–
η	Unknown constant	–
η_{dt}	Drive train efficiency	–
$\eta_{d_1}, \eta_{d_2}, \eta_1, \eta_2, \eta_3$ and η_4	Positive design parameters	–
η_g	Generator efficiency	–
θ_Δ	Drive train torsional twist angle	rad
θ^*	Optimal GRBFNN weights	–
$\vartheta_{i,X}$	Center of the ith input of variable X	–
λ	Tip speed ratio	–
λ_D	Adaptive controller gain	–
λ_1, λ_{D_0} and Λ	Positive design parameters	–
μ_F	Fuzzy membership function	–
ν_X	Measurement noise of variable X	–
ξ	Pitch actuator damping ratio	–
ξ_X	Damping ratio in situation X	–

ϖ	Neurons Number	$-$
ρ	Pitch actuator effectiveness loss	$-$
ρ_a	Air density	kg/m^3
ϱ	Approximation error	$-$
ϱ_1 and ϱ_2	Unknown constants	$-$
σ_F	Fuzzy shape parameter	$-$
σ, σ_0, σ_1, $\sigma_{\tilde{f}}$, $\sigma_{\tilde{f}_1}$ and $\sigma_{\tilde{f}_2}$	Positive design parameters	$-$
σ_d, σ_{d_1}, σ_{d_2}, σ_f, σ_{f_1}, σ_{f_2} and σ_c	Positive design parameters	$-$
τ_d	Generator time constant	s
τ_2	Filter time constant	$-$
Φ	Pitch actuator bias	$^\circ$
φ	Basis functions	$-$
φ_c	Width of the Gaussian function	$-$
$\varphi_f(x_1)$	Computable non-negative function of x_1	$-$
$\varphi(x_1)$	Core-function of variable x_1	$-$
ψ_1, ψ_2	Unknown constants	$-$
Ψ^*	Optimal GRBFNN weights	$-$
ω_g	Generator speed	rad/s
ω_n	Pitch actuator natural frequency	rad/s
$\omega_{n,X}$	Natural frequency in situation X	rad/s
ω_r	Rotor speed	rad/s
$\omega_{g,d}^*$	Approximated desired generator speed	rad/s
Ω_X	Considered set for variable X	$-$

To my mother and Ellie

1 Introduction

Reliability improvement of modern offshore wind turbines can provide significant impetus to turn wind power generation into one of the main power sources to respond to the world energy demands. The likelihood of failure of wind turbine components is inevitably high, especially for offshore, large and complex modern wind turbines, operating in harsh environments. Accordingly, the maintenance need increases due to unanticipated faults, which in turn, leads to higher power cost and less reliable power generation. In this regard, the Fault Detection and Isolation (FDI) and Fault Tolerant Control (FTC) designs have been extensively exploited in the last decade, as one of the most reliable solutions to have wind power generation in faulty situations, achieving the same performance index as for the fault-free case. Accordingly, in this chapter, the motivation of the current research is given. Also, the wind turbine operational control and FTC are conceptualized. Consequently, the thesis purpose and structure are summarized. Finally, the contribution of each chapter is given.

1.1 Thesis Motivation

Ever increasing energy demand is considered as one of the key factors which motivates the current energy research trends. The decrease in exploitable energy sources, significant and harmful environmental pollution, high energy price and poor availability index, are most of the commonly reported problems with fossil fuels, being the most traditional energy source. These issues have motivated researchers to seek the new energy sources. As the result, the renewable energy technologies have been considered as appropriate alternatives to the traditional energy sources, as they are abundant, and can have near zero operational greenhouse gas emissions (Hau et al., 2003; Tchakoua et al., 2014).

Among all renewable energy sources, the wind energy has demonstrated outstanding characteristics and has attracted the world's attention; from researchers to industrial points of view, and consequently has been entitled as "the world's fastest growing renewable energy source" with 30% growth annually on average throughout the last two decades (Sloth et al., 2010; Lu et al., 2009). During this time period, the planned capacity of wind farms has increased significantly on the world wide scale to provide more share of energy demand from wind energy. In Figure 1.1,

global wind power installations are illustrated, which clearly depicts the growth of captured wind power (Simani, 2015). The predicted future wind energy extraction
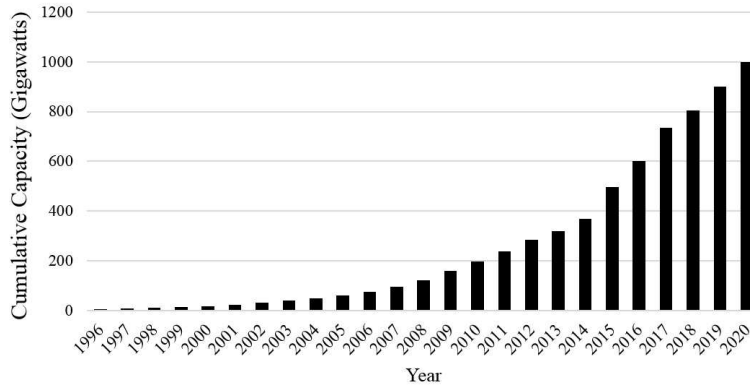
FIGURE 1.1: Global wind power installation capacity (Simani, 2015).

of some countries has been summarized in Table 1.1, in which it is evident that globally the focus will be to capture more energy from the wind. The captured energy and corresponding energy cost are two of the main considerable factors for any wind turbine farm, providing motivation for researchers to increase the captured energy while keeping the total cost at a reasonable level (Bakka et al., 2013; Sloth et al., 2011). This approach has led to two significant considerations which are the size and location of wind turbines. Indeed, implementing larger wind turbines in size, i.e. with longer blades, will cover more space, interact with more wind and, consequently, harvest more energy, and meanwhile, installing so-called offshore wind turbines in remote places, e.g. in the oceans, provides higher wind speeds and more uniform wind with more available energy to be extracted, due to lack of obstacles. Accordingly, the modern wind turbines are designed to be larger with longer blades, i.e. to increase the swept area, have higher towers and are also located in remote offshore places to encounter higher wind speeds, to increase the captured power e.g. from 75 kW to 20 MW (Amirat et al., 2009), as illustrated in Table 1.2 (Simani, 2015). Despite having the opportunity for extracting more energy, the operation of large offshore wind turbines, in harsh environments and in the presence of highly variable stochastic loads, is prone to be downgraded, due to fault occurrence, and more frequent maintenance operations will be needed (Byon et al., 2010). In fact, by operating in remote harsh environments, wind turbines are more likely to suffer from critical component faults (Sloth et al., 2011). This leads to one major challenge which is lower reliability and availability, cumulatively resulting in less sustainable power generation (Luo et al., 2014).

More maintenance has double negative effects; i.e. increased maintenance cost and also, less generated power due to increased downtime (Feng et al., 2012; Wei et al., 2011). Also, because of the difficulty in reachability and access of offshore

TABLE 1.1: The predicted wind energy extraction of some countries (Simani, 2015).

Country	Wind energy share of whole power	Expected year	Reference
United States	30% (300 GW)	2030	(Lu et al., 2009; Simani, 2015)
European Union	12% to 14% 25%	2020 2030	(Kabir et al., 2015)
China	15%	2020	(Lu et al., 2009; Kabir et al., 2015; Amirat et al., 2009)
Denmark, Portugal, Spain, France, Germany, Ireland, Sweden	9% to 21%	2015	(Zaher et al., 2009; Simani, 2015; Amirat et al., 2009)

TABLE 1.2: The wind turbines size growth (Simani, 2015).

Blade length (m)	Tower height (m)	Nominal power (kW)	Usage year	Location
8.5	30	75	1980-1990	Onshore
15	45	300	1990-1995	Onshore
25	60	750	1995-2000	Onshore
35	70	1500	2000-2005	Onshore
40	95	1800	2005-2010	Onshore
50	100	3000	2010-Present	Onshore
62.5	130	5000	2010-Present	Offshore
75	160	10000	Future	Onshore
125	220	20000	Future	Offshore

wind turbines, the maintenance cost is prone to increase significantly, which is in direct contrast to the aim of utilizing remote and larger wind turbines, which aims to keep the energy cost at reasonable levels. Accordingly, the cost of the generated power is generally increased and, consequently, the wind turbine generated power is not competitive with other traditional sources. For example, the maintenance cost of offshore wind turbines is estimated to be 20% to 25% of the total income (Simani et al., 2015a) and 10% to 15% for an onshore farm over the 20 years of operating life (Musial et al., 2006). In (Faulstich et al., 2011) wind turbine failure rates have been considered and it is indicated that electrical subsystems are more often likely to fail while mechanical component failure leads to longer downtime, as illustrated in Figure 1.2. So, it is beneficial to keep maintenance costs as low as possible, improving sustainability and decreasing downtime, ensuring that the wind turbines continue to work effectively and, consequently increase their captured power, despite the presence of faults in the wind turbine system, until the next scheduled maintenance operation can be performed (Entezami et al., 2012).

FDI and FTC are one of the best methods to improve reliability and reduce downtime and maintenance costs of wind turbines. These methods can also help the wind turbines to avoid vulnerability in dangerous wind situations. Equipping the vital components with physical or model-based identical counterparts, leads to fulfilling FDI (Ding, 2008). Indeed, the duplicated signal from redundant components can be compared to the main one to generate the so-called residual signal. Significant deviation of the residual from zero, or a predefined threshold, can be used to indicate the presence of a fault.
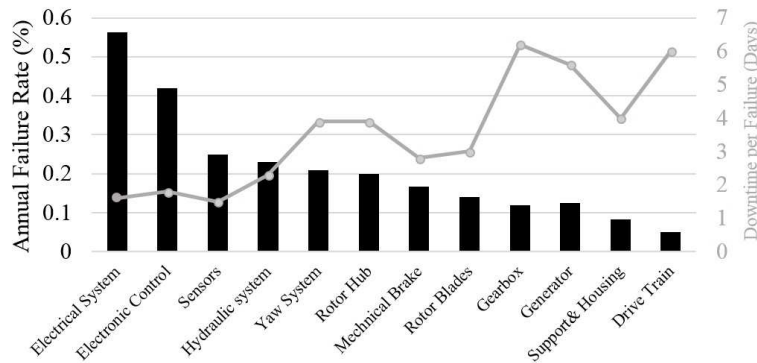
FIGURE 1.2: Wind turbine components failure rate and downtime
(Faulstich et al., 2011).

The fault information captured from FDI units, can be used to optimize the maintenance procedures via remote diagnosis. On the other hand, FTC is robust against the considered faults and, consequently, keeps the wind turbines performance at their desired level, despite the presence of faults. Also, in case of the total failure of the main component, it can be replaced with the redundant one. Consequently, the maintenance need and downtime are decreased, and the reliability will be improved.

Therefore, the final energy cost is kept as cheap as possible. As a result, premature wind turbine breakdown can be avoided (Odgaard et al., 2009a).

1.2   Wind Turbine Control System and Strategy

Wind turbines are inherently nonlinear time varying dynamic systems. Also, the modern industrial wind turbines are equipped with longer blades, higher towers and are installed in remote locations. These issues require the need for modern control strategies to be considered to increase the harvested wind energy whilst keeping the structural load at a desirable level to decrease maintenance costs (Sloth et al., 2011). The wind energy is transferred to the wind turbine by rotating the wind turbine blades which are coupled to the generator shaft. Generally, the wind turbine is highly nonlinear due to its aerodynamic characteristics which can be represented as a function of blade pitch angle, rotor rotational speed, tower oscillation and wind speed. The rotational speed of the generator is increased by utilizing a high speed ratio drive train (Bianchi et al., 2007). The effective wind speed at the rotor plane varies in space and time from the expected nominal wind speed. So, the accurate wind speed measurement, using anemometers located at the top of the turbine hub, is not possible because of the temporal and spatial distribution of the wind speed over the blade plane. Accordingly, the wind speed across the rotor plane is considered as the disturbance in control design.

In terms of control objectives, there are two distinguishable wind turbine operational regions, i.e. so-called partial load and full load regions. In partial load, it is aimed to extract as much energy as possible from the wind, while in the full load region, despite the higher available energy content in the wind, it is required to keep the generated power at its nominal value to protect the wind turbine structure from catastrophic operation that will induce more stress on the structure and consequently, may damage it (Bianchi et al., 2007). The control variable in partial load operation is the generator electrical load torque, which enables the variable speed operational mode of wind turbines. On the other hand, in the full load region, the blade pitch angle is the main control variable, which adds the variable pitch angle characteristic of wind turbines. The fixed speed and fixed pitch wind turbines are less expensive initially, but the lack of controllability leads to less economical wind turbines. So, the variable-speed variable-pitch wind turbines are dominating the wind energy industry.

In partial load operation, it is theoretically proven that the maximum wind power extraction is 59% of the wind power, which is called the Betz Limit (Bianchi et al., 2007). So, the control aim in partial load operation is to keep the efficiency as close as possible to the maximum one of the given wind turbine model. The most commonly used controller in the partial load region is known as the reference controller, in which the control law is obtained by excluding the wind speed in the

aerodynamic torque equation. This controller is designed for the nonlinear model, but it is assumed that the wind turbine is operating on the desired operation trajectory. To resolve this issue, some modern linear controllers have been applied on linearized wind turbine models (Sloth et al., 2011). Also, it has been shown that up to 5% modeling error may lead to 1% to 3% energy loss which is a significant loss (Fingersh et al., 1998). Accordingly, improvements to modern controller scheme designs has been sought over the last two decades, e.g. adaptive methods (Johnson et al., 2006), Fuzzy Inference System (FIS) (Aissaoui et al., 2013), neural networks (Shamshirband et al., 2014) and nonlinear control (Boukhezzar et al., 2011). The power regulation is crucial in full load operation to prevent the wind turbine from over speeding. Otherwise, if the rotor speed violates the predefined limit, the mechanical brakes will be activated, leading to reduction in generated structural loads (Tiwari et al., 2016). Also, this aim should not be met in a manner that reduces the generated power considerably less than the rated power. The most commonly adopted controller in full load region is the linear Proportional, Integral and Derivative (PID) controller to adjust the pitch angle (Lan et al., 2018). To improve the controller performance on the whole nonlinear model of the wind turbine, the PID controller is equipped with FIS in (Badihi et al., 2014). On the other hand, different modern controllers have been adopted for the full load operation, such as, Linear Parameter Varying (LPV) control (Sloth et al., 2011), gain scheduling (Bianchi et al., 2012), robust control (Kim, 2016), fuzzy logic system (Simani et al., 2015b), adaptive nonlinear control (Jafarnejadsani et al., 2013), optimal control (Giger et al., 2017) and evolutionary algorithms (Jaramillo-Lopez et al., 2016).

1.3   Wind Turbines FTC Design

Reliability improvement of wind turbines is the key issue that can turn the wind power into one of the main power source to respond to the world energy demands. The likelihood of fault occurrence on wind turbine components is unavoidable, especially for large rotor modern wind turbines, operating in harsh offshore environments. The fault presence on the system is defined as an "unpermitted deviation of at least one characteristic system parameter and property from the acceptable/usual/standard condition" (Gao et al., 2015). For example, blocking of an actuator, loss of a sensor and disconnection of a system component are some sources of faults. Accordingly, the faults can be categorized as actuator faults, sensor faults and system faults, which may lead to performance degradation or even system breakdown. It is obvious that if the fault is not detected and handled, the maintenance cost is prone to be increased and the safe operation may be violated, especially in the offshore wind turbine case, in which reachability is a major and costly issue. Accordingly, the maintenance need increases due to unanticipated faults, which in turn, leads to higher energy conversion cost and less reliable power generation. So, it is paramount to detect and identify potential faults as early as possible.

One of the most suitable solutions for the above mentioned problems is FTC, whose application to wind turbines has recently emerged (Odgaard et al., 2013b). In FTC schemes, a baseline controller is designed which tolerates the presence of certain faults to ensure adequate system control, so the final system will continue to operate satisfactorily, the same as for the previous fault-free situation. The first step in FTC, is Fault Detection (FD) which is to detect whether a fault has occurred and then, via Fault Isolation and Identification (FII), the component where the fault is present, and the size and type of fault, are determined, respectively. Finally, after detecting the fault and its location and size, the Fault Accommodation (FA) or Controller Reconfiguration (CR) is considered so that the effect of the fault on the overall system performance will be removed. If FA is used, the baseline controller will be the same as the previous fault-free one. However, if CR is utilised after the fault is detected, the whole or part of the baseline controller will be switched off, and a new controller inserted which is tolerant towards the detected faults.

One of the easiest methods for FTC is in using the concept of hardware redundancy in which the critical system components are equipped with multiple sets of similar structures and signals, such that these redundant components will produce duplicated signals which are similar in essence in the fault-free situation and yet will have differences or residuals between them in faulty situations. Accordingly, by installing identical counterparts for the main components and subtracting these two signals, which are expected to be similar in fault-free situations, the so-called residual signal can be constructed. So, the residual signal, i.e. the difference between the main and duplicated signals, can be used to detect and locate the faults in particular components, neglecting differences in noise contents and disturbances. Faults can then be detected and isolated in any component by considering the deviation of the corresponding residual signal from zero. Similarly, the fault size can be estimated using these two signals. On the other hand, if the fault effect cannot be identified and removed from the component by FA, the main component will be replaced by a redundant one which leads to CR.

Increasing the total cost of systems equipped with FTC, occupying too much space in the final design, and developing heavier systems with more complicated data acquisition schemes, are some of the most reported problems of FTC using hardware redundancy. Software redundancy or so-called Model-Based FTC (MBFTC) is one suitable alternative to hardware-based redundancy, where instead of using physical duplication of components, a mathematical model of the system is designed to be compared to the physical one and the need for duplicated hardware components is eliminated. So, the entire mathematical model of the system should be known precisely and be fed with the same inputs as the real system, i.e. the inputs for the system are control signals and disturbances which includes exogenous uncontrollable inputs and noises, such that in fault-free situations and when using the same input, the system and model will produce exactly the same outputs. Accordingly, the residual signal is constructed by comparing the outputs from the

system and the model that can subsequently be used for FD and FII.

In terms of FTC, the controller is designed to operate satisfactorily in the fault-free situation as well as to remove the fault effects from the overall system performance to keep it as close as possible to the fault-free one, until the next prescheduled maintenance activity can be performed (Gao et al., 2015). Also, it is advantageous to determine the fault information, including the fault time, period, size and location, either for supervisory control or to be used in the maintenance procedure. Robustness of the overall FTC scheme against system noise, model uncertainty and unmeasured exogenous disturbances, is challenging for complicated systems with different sources of noise and disturbance, such as wind turbines. Indeed, system noise and disturbance can mistakenly be seen as faults on the FCT scheme (Sloth et al., 2011).

There are two different schemes for MBFTC, including active and passive MBFTC. In active MBFTC, the first step to design the FTC is FD. Indeed, the information gathered from FD and FII will be used in FTC. On the other hand, in passive MBFTC, the baseline controller is basically designed such that this controller is robust to some given faults. So, in passive MBFTC there is no need for FD and FII, which are two challenging considerations for complicated systems. It can be concluded that the passive MBFTC is conservative compared to the active MBFTC because the anticipated faults are considered in the baseline controller design. In the active MBFTC, the residual signal is used to detect the fault and accordingly, the location and size of faults are determined. Using this information, the effect of the faults is removed from the overall system performance either by FA, i.e. correcting the generated signals from the faulty components via the Virtual Sensor and Actuator (VSA) module, and using the baseline controller the same as the previous fault-free one, or by CR, i.e. whole or part of the baseline controller will be switched off, and a new controller inserted which is tolerant towards the detected faults. On the other hand, for passive MBFTC, the baseline controller is basically designed such that this controller is robust to some given faults. The passive and active MBFTC schemes both have one step in common, which is the design of the baseline controller, prior to FTC. In other words, the baseline controller should be designed for the fault-free system to operate at its desired trajectory (Blanke et al., 2006). Also, it should be noted that the FA or CR should be considered in the design of the baseline controller such that accommodating any possible faults or reconfiguring the whole/part of the baseline controller should be seen prior to the FTC design. In terms of cost and reliability, the FA, due to lack of existence of extra components, is more desirable than CR, because in FA the baseline controller, itself, is used for removing the fault effect, while in CR, a new controller will be used, such that except for the cost of the final design, the stability and performance of the new controller should be considered. Additionally, switching from one controller to another one may cause instability. In Figure 1.3, the schematic diagram of active MBFTC including FA and CR, for wind turbine system associated with

faults, is illustrated.
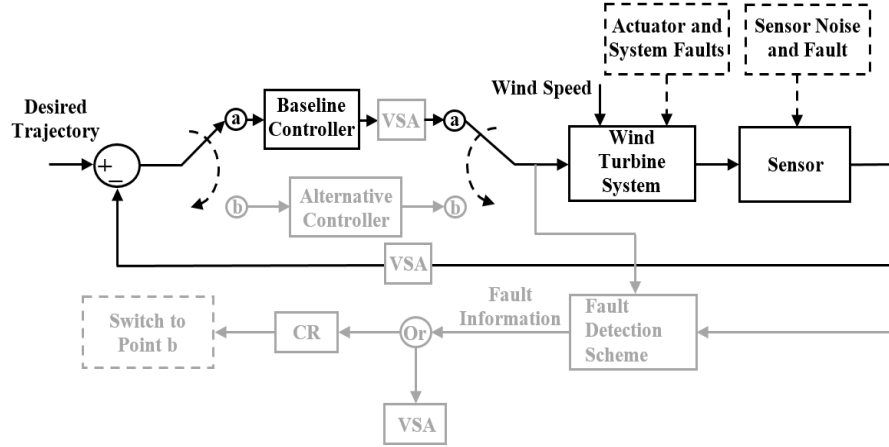
FIGURE 1.3: Wind turbine baseline control (dark line) and active
MBFTC (grey line).

As stated earlier, for active MBFTC the accurate mathematical model of the wind turbine should be known as a priori and also, the model should be fed with the same signal as the system, which is not possible for noises and disturbances. Also, using sensor measurements to construct the residual signals, which are contaminated by noise, leads to residual signals which may be different from zero in fault-free situations. In fact, because the sensor noises and exogenous disturbances, i.e. wind speed, are not measurable to be fed into the mathematical model, it can be expected that the residual deviates from zero in fault-free conditions. Consequently, it can be seen that the noise or disturbance can be translated into faults. So, a threshold can be chosen from which if the residual signals deviate then the fault is detected. Missed faults or false alarms are two of the most commonly reported problems in the case of too large or too small thresholds, which have led to the design of adaptive thresholds, which is challenging for complicated systems with different sources of noise and disturbance, such as wind turbines. Also, the CR approach may lead to the chattering control phenomenon and instability which is undesirable for wind turbines because it induces more stress on mechanical parts. The identification of fault size, using purely the noisy sensor measurements, will lead to downgraded system performance, because this inaccurately identified fault size is subsequently utilised in the FA and CR steps.

Remark 1.1. *A brief and accurate introduction to MBFTC and associated approaches for detection of faults and removing their effects from overall system performance were given in this section. However, a comprehensive literature review on the FDI and MBFTC designs for wind turbine systems, is given in Chapter 2 to enlighten the research direction and also, to signify the contributions which have been made in this thesis in the field of wind turbine MBFTC design. This literature*

review has been separated from this chapter for ease of readability of the rest of this chapter and to avoid readers' confusion.

1.4   Thesis Objectives

In this section overall objectives of this research are briefly outlined. However, goals of each chapter are appropriately introduced at the beginning of the corresponding chapter.

The first and the main objective is to comply with the industrial wind turbine operational specifications. As stated earlier, the wind turbines operation, in terms of system control, is divided into two distinguishable ones including partial load and full load regions. The operational objective in partial load region is to maximize the captured energy from the wind while in the full load region, despite the higher available energy content in the wind, the operational objective is to retain the produced power at its nominal value. Accordingly, in this thesis, it is aimed to design the controller for both operational regions, separately, satisfying the operational objectives. In fact, each designed controller is active in its corresponding operation region to achieve the operational objectives. It should be noted that, the performance of the final design is quantified considering these operational objectives.

The nonlinear dynamical behaviour of wind turbines has increased the need for more accurate and modern control designs. Otherwise, a set of linearized models should be used to take advantage of the linear controller. However, the linearized model does not ensure the accurate behavior of the wind turbine. So, in this thesis it is aimed to utilize the whole nonlinear model of the wind turbine, on which basis the controller is designed to increase the performance and practicality. On the other hand, the wind speed is highly stochastic and its accurate measurement, using anemometers located at the top of turbine hub, is not possible because of the temporal and spatial distribution of the wind speed over the blade plane. Accordingly, the wind speed can be considered as an uncontrollable exogenous disturbance acting on the wind turbine. So, in the entire thesis, the wind speed is not used in the designed controller. Instead, an appropriately-designed estimator is adopted, e.g. Gaussian Radial Basis Function Neural Networks (GRBFNN) or modified Kalman filter, to estimate the wind speed to be utilized into the designed controllers.

Considering the operational region of the wind turbine, the possible faults are considered, including sensor faults, actuator faults and system faults. Indeed, to have an accurate and effective control design, the faults on the active components of wind turbines in each operational region are studied, to improve the readability of the thesis and avoid confusion. The fault effects are removed by adoption of MBFTC design, i.e. either this feature can be integrated into the designed controller

or a separate scheme can be proposed to be implemented on the available baseline controller. On the other hand, different approaches are proposed, considering the characteristics of each given fault to be accurately accommodated. Also, the reason for consideration of the various faults are given.

Finally, it is aimed to use the available baseline industrial controllers, separately, with which to compare the performance of the proposed controllers. Indeed, it is aimed to demonstrate the deficiency of the baseline industrial controllers in the presence of the considered faults and meanwhile, to highlight the superiority of the proposed controllers.

Remark 1.2. *The theoretical materials in each chapter are presented in the order of appearance. Indeed, the structure of each chapter is self-contained. This is done to keep the main focus of this thesis on the wind turbine operation aspects and also, to let each chapter be independently effective and readable. For the same reason, the proof of the given theorems separately are given in Appendix A.*

1.5 Thesis Structure and Contribution

In this section, the current thesis structure and organization is given. Also, all contributions are outlined appropriately.

To accurately evaluate the state of the art in the FDI and FTC design of wind turbines, an extensive review is needed. So, in Chapter 2, a comprehensive review of the available FDI and MBFTC designs for wind turbines is presented, focusing on the advantages, capabilities and limitations. This chapter is captured and reorganized from the following paper.

- Hamed Habibi, Ian Howard, and Silvio Simani, "Reliability Improvement of Wind Turbine Power Generation using Model-based Fault Detection and Fault Tolerant Control: a review", Renewable Energy, Vol. 135, pp. 877-896, 2019.

To initiate the controller design, the accurate wind turbine model is needed. So, in Chapter 3, the wind turbine nonlinear model, including all possible faults, is explained. Also, the desired operational modes of available industrial wind turbines are introduced, on which basis the numerical criteria are given to evaluate the performance of wind turbines. The wind turbine model parameters are given in Appendix B.

In each chapter, to evaluate the proposed scheme, a comparison between performance of the proposed and the available industrial baseline controllers are conducted. So, it is needed to elaborate the baseline controller which is currently utilized in the industry. This is fulfilled in Chapter 4. Also, some initial modifications

are applied to the baseline controller. In partial load operation the baseline controller is modified with a proposed FIS to increase the captured energy. This section is captured and reorganized from the following paper.

- Hamed Habibi, Aghil Yousefi Koma, and Ian Howard, "Power Improvement of Non-Linear Wind Turbines during Partial Load Operation using Fuzzy Inference Control", Control Engineering and Applied Informatics, Vol. 19, No. 2, pp. 31-42, 2017.

On the other hand, in the full load region, the baseline PID controller is modified with introduction of Nussbaum adaptive control to let the wind turbine be passively, robust against pitch actuator faults. This section is captured and reorganized from the following paper.

- Hamed Habibi, Hamed Rahimi Nohooji, and Ian Howard, "Adaptive PID Control of Wind Turbines for Power Regulation with Unknown Control Direction and Actuator Faults", IEEE Access, Vol. 6, pp. 37464-37479, 2018.

In Chapter 5, the partial load region of wind turbine, FTC design is tackled to keep the power generation efficiency as close as possible to the maximum one, considering the generator torque bias, pitch actuator dynamic change and bias. Also, the wind speed is estimated using GRBFNN, as a part of the proposed controller. The considered faults are estimated adaptively, which can be used to optimize the maintenance plans. This chapter is captured and reorganized from the following papers.

- Hamed Habibi, Hamed Rahimi Nohooji, and Ian Howard, "Optimum efficiency control of a wind turbine with unknown desired trajectory and actuator faults", Journal of Renewable and Sustainable Energy, Vol. 9, No. 6, p. 063305, 2017.

- Hamed Habibi, Hamed Rahimi Nohooji, and Ian Howard, "Power maximization of variable-speed variable-pitch wind turbines using passive adaptive neural fault tolerant control", Frontiers of Mechanical Engineering, Vol. 12, No. 3, pp. 377-388, 2017.

- Hamed Habibi, Hamed Rahimi Nohooji, and Ian Howard, "A neuro-adaptive maximum power tracking control of variable speed wind turbines with actuator faults", proceedings of Australian and New Zealand Control Conference (ANZCC), pp. 63-68, 2017.

In Chapter 6, the constrained FTC design of wind turbines in the full load operation is introduced for the first time, to keep the generated power within the predefined limit and, to compensate the pitch actuator dynamic change, effectiveness loss, bias and blade debris build-up. The constrained control is introduced to lessen the mechanical brake engagement, which is inevitable for highly variable wind speed

variation. The considered faults are estimated adaptively, which can be used to optimize the maintenance plans. This chapter is captured and reorganized from the following papers.

- Hamed Habibi, Hamed Rahimi Nohooji, and Ian Howard "Backstepping Nussbaum Gain Dynamic Surface Control for a Class of Input and State Constrained Systems with Actuator Faults", Information Sciences, Vol. 482, pp. 27-46, 2019.

- Hamed Habibi, Hamed Rahimi Nohooji, and Ian Howard, "Constrained control of wind turbines for power regulation in full load operation", proceedings of 11th Asian Control Conference (ASCC), pp. 2813-2818, 2017.

In Chapter 7, using a novel unknown input observer and Kalman filter, the faults in the rotor and generator sensors are shown to be detected, isolated, identified and accommodated. Additionally, with the Bayesian setting, the fault probability is calculated which will be used for fault detection and isolation. Also, via an auxiliary signal and by checking the updated residual and fault probability, the isolation of the fault in each sensor is accomplished without the need for any redundant sensor. This chapter is captured and reorganized from the following papers.

- Hamed Habibi, Ian Howard, and Reza Habibi, "Bayesian Fault Probability Estimation; Application in Wind Turbine Drive train Sensor Fault Detection", Asian Journal of Control, In Press, 2020.

- Hamed Habibi, Ian Howard, and Reza Habibi, "Bayesian Sensor Fault Detection in a Markov Jump System", Asian Journal of Control, Vol. 19, No. 4, pp. 1465-1481, 2017.

Finally, the concluding remarks, discussions and an outlook on possible future work are all given in Chapter 8. It should be noted that the co-authors' attribution statements are clearly pointed out in Appendix C.

2 Literature Review on Wind Turbines FDI and FTC design

FDI and FTC design of wind turbines has been significantly developed over the last decade. Most of the works in this fields have been motivated from the competitions conducted by KK-electronic a/c and MathWorks (Odgaard et al., 2009a). Accordingly, the number of researches and consequent publications has been increased considerably. In Figure 2.1, SCOPUS results have been presented to signify the rapid growth by considering the published journal papers in the field of wind turbine FDI and FTC design, which implies it is currently the subject of intensive worldwide research (Badihi et al., 2015). However, there are only a few available review studies in this field (Kabir et al., 2015; Odgaard et al., 2013b; Badihi et al., 2013; Hameed et al., 2009; Márquez et al., 2012; Pourmohammad et al., 2011). So, it is beneficial to have a well-organized comprehensive overview on the status of recent developments of FDI and FTC design of wind turbines to make a framework for the next chapters of this thesis. This chapter is focused on Horizontal Axis Wind Turbines (HAWT) with upwind rotor placement, due to their dominancy on utility-scale wind turbines (Spinato et al., 2009).[1]
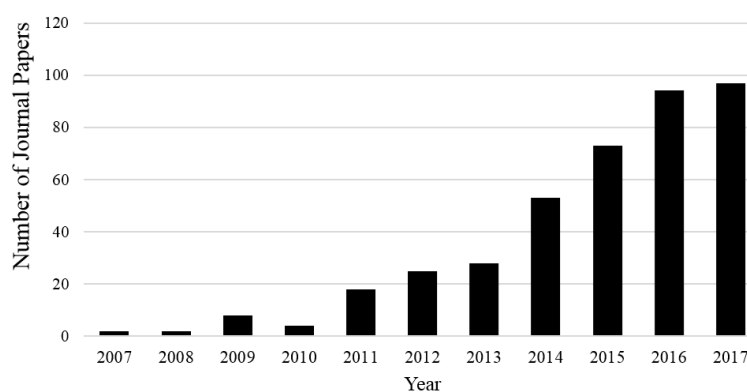
FIGURE 2.1: SCOPUS-indexed published journal papers in FDI and FTC design of wind turbines.

---

[1]This chapter is captured and reorganized from the paper "Reliability Improvement of Wind Turbine Power Generation using Model-based Fault Detection and Fault Tolerant Control: a review". The authors' attribution on this paper are given in Appendix C.

2.1   Wind Turbines FDI Design

The wind turbine FDI design can be utilized as a fully/partly automatic scheme to detect and locate the possibly occurring faults on the wind turbine to optimize the required maintenance procedures, reduce downtime, and to avoid catastrophic failure. As a result, the requisite maintenance is reduced to either of the following approaches (Tchakoua et al., 2014).

- Systematic maintenance, i.e. pre-scheduled maintenance plans.

- Proactive maintenance, i.e. current parameter-based condition maintenance.

- Corrective (reactive) maintenance, i.e. after the fault is automatically and evidently detected.

- Predictive maintenance, i.e. the maintenance is conducted to prevent the fault progressing into system failure after the potential fault is forecasted.

- Preventive maintenance (condition-based), i.e. planning annually scheduled maintenance based on previously collected fault information.

Obviously, for all maintenance approaches, except Systematic maintenance methods, fewer maintenance plans are conducted using the fault information. The modern generation of maintenance strategies aims to reduce human intervention by implementing hardware or software redundancy on the wind turbines to automatically detect the faults based on collected and analyzed data and, consequently, to reduce/remove the fault effects.

Hardware redundancy involves equipping the components such as sensors and actuators, with physically identical counterparts to generate the so-called residual which contains the possible fault information. This approach increases weight, occupied space, data acquisition complexity and, consequently, final design cost. These issues are very problematic for offshore wind turbines. In contrast, software redundancy or MBFDI techniques have been developed on wind turbines during the last decade to overcome the aforementioned problems (Chen et al., 2011b), in which instead of implementation of extra costly physical components, the model of the operational wind turbine is used to generate the duplicated signals and, accordingly, residuals. The inaccurate measurement of wind speed variation, consequent unknown aerodynamic torque, high noise contents on sensors and non-stationary operational dynamic behavior, are the main challenges of MBFDI of wind turbines (Zhang et al., 2011; Tang et al., 2014). So, in this section, the MBFDI techniques, which have already been applied on the wind turbines, are reviewed, for the faults summarized in Tables 2.1 and 2.2.

Remark 2.1. *There exist other faults in the wind turbine structure which are not mentioned in Table 2.1. For instance, degradation of drive train lubrication oil which leads to high bearing temperature and, consequently, lubrication oil aging.*

TABLE 2.1: The wind turbines fault characteristics.

Components	Symptoms	Category	Severity
Pitch sensor Rotor Sensor Generator Sensor	Biased, gained, fixed, and no output	Sensor fault	Low
Generator and converter Pitch actuator	Offset generator torque bias Pitch angle bias	Actuator fault	Medium
Generator and converter Pitch actuator Pitch actuator Pitch actuator Drive train Blade aerodynamics	Increased time delay Pump wear High air content in oil Hydraulic leakage Wear and tear Debris build up	System fault	High High Medium High Medium Medium

TABLE 2.2: The wind turbines fault consequences.

Components	Consequence	Deviation time
Pitch sensor Rotor Sensor Generator Sensor	Poor power optimization and regulation in partial load and full load regions, respectively.	Medium
Generator and converter Pitch actuator	Non-optimum power production. Poor power regulation, uneven aerodynamic torque, and excited structural load.	Fast
Generator and converter Pitch actuator Pitch actuator Pitch actuator Drive train Blade aerodynamics	Slow generator torque control and non-optimal power production. Slow pitch angle adjustment and consequently poor power regulation. Increased vibrations of drive train. Out of designed aerodynamic. relation (Non-optimal power production, poor power regulation).	Fast Medium Slow Medium Very slow Very slow

Also, due to wind gusts and consequent temporary misalignment of rotor and generator shafts, the bearings and gears are damaged. Blade cracks, bearing wear and spalls, gear teeth cracks, generator winding damage and overheating, are some other reported wind turbine faults. Condition monitoring methods based on Supervisory Control and Data Acquisition (SCADA), structural health monitoring techniques, frequency spectrum analysis and vibration signal processing are the main approaches to detect these aforementioned faults (Zaher et al., 2009). Fourier transformation analysis (Zhang et al., 2012), wavelet method (Lu et al., 2012), manifold learning (Tang et al., 2014), support vector machines (Wenyi et al., 2013), thermography, strain measurements and acoustic monitoring (Hameed et al., 2009) are some examples of condition monitoring techniques. All these methods can be categorized as signal-based FDI and there are rich reviews on applying these methods on wind turbines (Hameed et al., 2009). So these methods are not repeated here. On the other hand, yaw actuator faults, whether actuator malfunction or a stuck brake is not considered, because the yaw mechanism is mostly considered as an on/off actuator and, accordingly, inactive (Odgaard et al., 2013a).

The most challenging issue, which should be considered in wind turbines FDI schemes, is that the wind speed is poorly measured by the anemometer and, actually wind speed can be considered as the disturbance. On the other hand, the aerodynamic nonlinearities of wind turbines should be taken into consideration (Odgaard et al., 2009a). Also, FDI schemes should be robust against the considerable noise content of sensor measurements. Finally, fault severity should be taken into account to design the FDI schemes in such a manner to be more sensitive to the more severe faults. Accordingly, the predefined detection time (DT) is given. In (Odgaard et al., 2009a), for different fault sources of wind turbines DT is stated as, sensor faults DT should be less than 10 sampling times. For converter faults DT should be less than 5 sampling times. For the pitch actuator dropped pump pressure DT should be less than 8 sampling times, and for pitch actuator high air content DT should be less than 100 sampling times. No given DT is required for increased drive train friction, as it just has to be detected. Finally, the other specifications of FDI schemes include the reduction of false detection and missed (not detected) faults, which need to be kept at a reasonable level (Odgaard et al., 2013b).

There are many MBFDI methods implemented on wind turbines in the last decade to detect a variety of faults. Accordingly, to have a comprehensive and fruitful review, initially the FDI methods are categorized systematically. In this regard, the first and most important step is the mathematical description of the wind turbine which then determines appropriate FDI schemes. It is beneficial to consider the whole nonlinear model of the wind turbine, but it leads to more complicated FDI structures. On the other hand, the linearized model is not completely consistent with the nonlinear one. Accordingly, other modelling approaches are proposed to cope with the nonlinearity and take advantage of linear FDI methods, including LPV and

fuzzy Takagi-Sugeno (TS) modellings, which have shown significant characteristics. Consequently, different FDI schemes have been adopted for the modelling on which basis this section is structured, which are summarized in Figure 2.2. Accordingly, the most applicable FDI methods of wind turbines are reviewed in this section. Thereafter, to consider FDI methods from the wind turbine point of view, the reviewed methods are categorized and summarized for each of the wind turbine components.
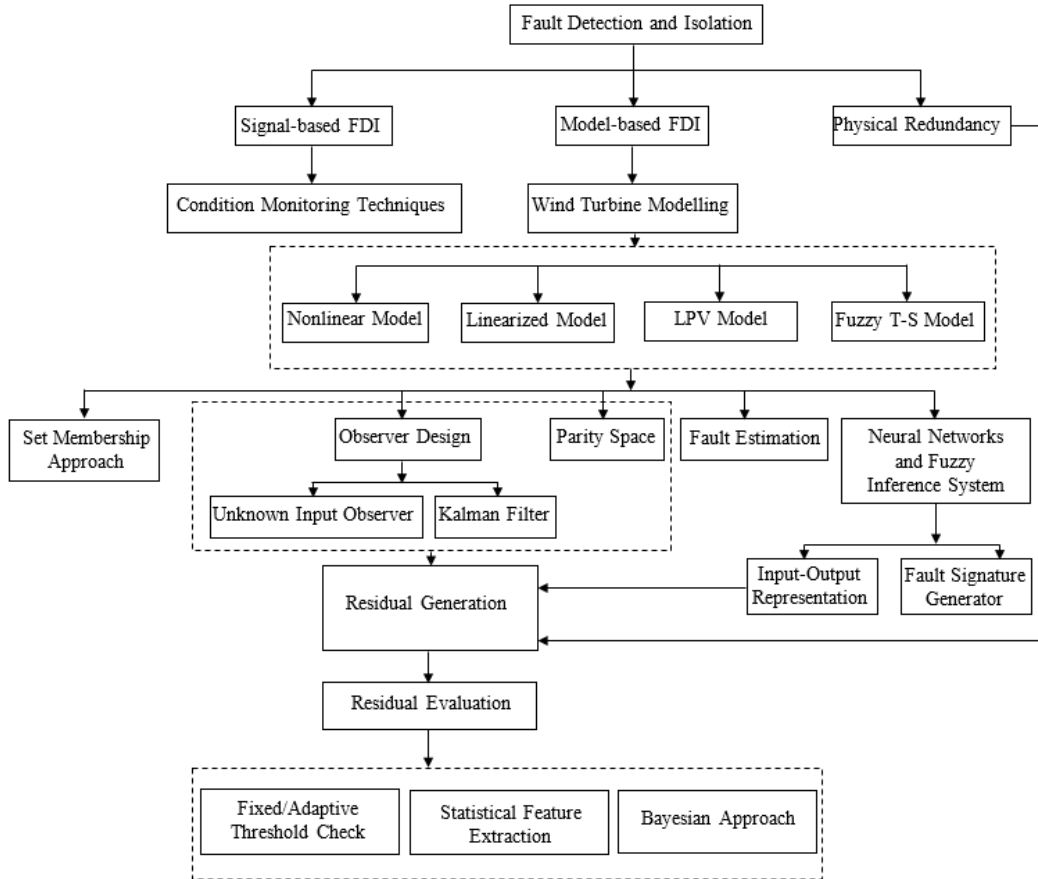
FIGURE 2.2: FDI methods applied on wind turbines.

2.1.1 Wind turbine model representation for MBFDI purposes

The modeling framework of wind turbines leads to different applied FDI methods. The whole nonlinear model of the wind turbine including faults, provides the best framework, on which basis, the FDI methods can be developed. This nonlinear model is precisely given in Chapter 3. Indeed, the nonlinear model is able to accurately represent the wind turbine behavior (Badihi et al., 2017). However, as the MBFDI methods have been mostly developed for linear models, the linearized

model of the wind turbine has dominated the recent research scope (Odgaard et al., 2013a). Nevertheless, inconsistency between behaviors of the linearized model and the highly nonlinear wind turbine, is significant, which may be seen mistakenly as the faults. So, to have more accurate model representation as well as to take advantage of already developed FDI methods, two modern wind turbine modelling frameworks have been recently proposed, which are briefly introduced here.

LPV modelling

LPV framework to model the wind turbine has emerged in the last decade (Sloth et al., 2010). In this framework, the wind turbine model is linearized around several operational points. Accordingly, throughout the operation, a set of linearized models is adopted and, according to the estimated operational point, the proper model is chosen. Indeed, as wind speed varies, aerodynamic torque is variable, which leads to variation to the state space model representation. So, for different wind speeds, different linearized models are obtained. Consequently, having all possible linearized models as the feasible dynamic descriptor set, leads to LPV wind turbine model representation. This provides proper design freedom to achieve robust FDI performance.

Fuzzy TS modelling

In this approach, to avoid the complex nonlinear mathematical description, multiple linearized models are used (Simani et al., 2015a). Then, fuzzy if-then rules are defined based on the expert's knowledge which combine all the linear models, utilizing the TS prototype to take the uncertain and time-varying operating range of the wind turbine, into consideration. The wind turbine measurements are used to estimate fuzzy TS prototypes parameters. Also, in this approach, regarding FDI design, the residual generators can be designed as fuzzy prototypes. On the other hand, different controller design or FDI methods can be sought in this framework.

Remark 2.2. *As the LPV and fuzzy TS modelings lead to linear models with computationally complicated structures, in this thesis the whole nonlinear model of wind turbine is used to have most similarity to the real industrial wind turbines and meanwhile, avoid any extra complicated procedures.*

2.1.2   Applied MBFDI methods on wind turbines

In this section wind turbines FDI methods with different fault sources are briefly introduced.

Residual-based wind turbines FDI

The most commonly adopted model-based residual generation for FDI purpose are observer design and parity relation methods (Odgaard et al., 2009b), in which the faults with different sources are detected. In these methods, despite physical redundancy techniques, the duplicated signal can be obtained via mathematical models of the wind turbine, eliminating the need for any redundant physical components. Consequently, the residual signal is constructed, by comparing the original measured signal and the extra duplicated one, which carries any probable fault information. Accordingly, by adopting an appropriate residual signal evaluation, the fault is detected (Wei et al., 2010). It should be noted that using mathematical models is also known as analytical redundancy relations which are obtained by structural analysis. The widely-exploited residual evaluation methods are simple geometric logic (e.g. threshold check), statistical scheme (e.g. statistical feature extraction), and Bayesian approaches. In the first approach, an adaptive or fixed threshold is selected, from which if violate the faults are detected. The high noise contents of wind turbine measurements, operating in harsh remote environments, may lead to false detection. Indeed, the disturbance contents on the constructed residual signal may cause the residual signal to increase above the designed threshold, while no faults have occurred (Odgaard et al., 2012c). On the other hand, selecting too large a threshold to avoid false detection, some faults with small effect of the residual are not detected, which may yet cause major operational deficiency of the wind turbine, which yields the missed detection problem. So, statistical features of the residual signal can be considered to provide more accurate fault evaluation. Generalized likelihood ratio test, cumulative variance index and the use of up and down counters, are some of the most utilized methods to extract fault information from the residuals. Bayesian inference method, as another residual evaluation scheme, will be introduced, separately.

Parity space approach

The parity residual generation approach is one of the most obvious and, accordingly, applicable methods, adopted on the whole or part of the wind turbine to fulfill FDI requirements. In this approach, the wind turbine is equipped with the identical mathematical model, implemented as a computer simulation. This model is fed with the same inputs as the wind turbine. In the fault-free case, both the wind turbine and the model, generate the same outputs. Accordingly, comparing these two outputs, the residual signal is constructed, which deviates considerably from zero in the case of fault occurrence. This approach is illustrated schematically in Figure 2.3. In (Pisu et al., 2011) the parity equations are utilized to detect and isolate faults in the blade pitch actuator and drive train. Considering the highly nonlinear wind turbine dynamic behavior and variable operation points, it is very difficult to accurately implement the whole wind turbine mathematical model. Also, the design
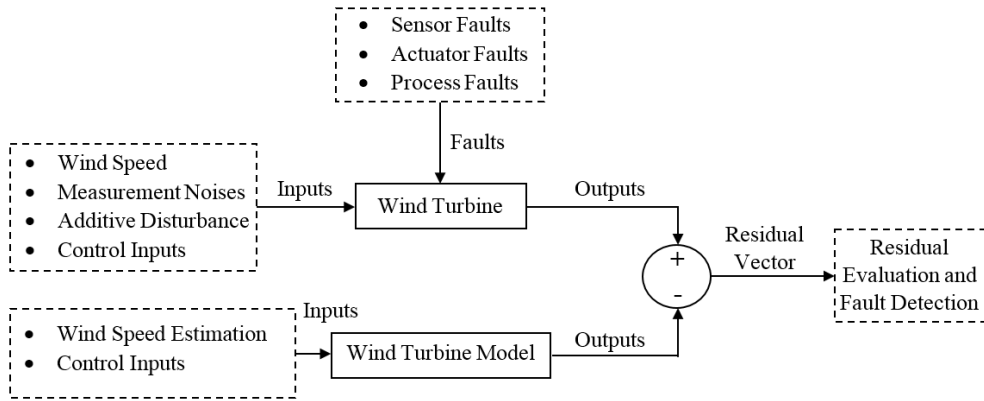
FIGURE 2.3: Parity based residual generation approach.

of different models for each well-known subsystem may increase the complexity of the final scheme. The wind speed is not accurately measurable. In Figure 2.3, it is obvious that the wind speed is one input to the wind turbine, which should be identically fed into the wind turbine model to have an accurate residual vector, which is only sensitive to the faults. So, the wind speed should be either accurately measured or estimated. Different measurement or estimation of wind speed approaches have been reviewed in (Jena et al., 2015) and are not presented here. On the other hand, in the case of offshore wind turbines, the unmeasurable sensor noise and environmental disturbances are considerable and inevitable. So, in (Pisu et al., 2011) an appropriate filter was designed to make the residual robust against noise and disturbances, while yet being sensitive to the considered faults. Also, in (Agarwal et al., 2014) an adaptive threshold was designed to accurately evaluate the constructed residual signal of the wind turbine to eliminate false detection due to noise content on the residual.

Observer design approach

The accurate residual construction can be done by design of an appropriate observer to be just sensitive to the considered faults. Indeed, in this approach the residual signal is decoupled from the unknown inputs, whether wind speed or noises (Wei et al., 2008). So far, reviewing the literature, the applied observer design of the wind turbine includes various types of Kalman filter design (Dey et al., 2015) and unknown input observer (UIO) design (Odgaard et al., 2009b). The observer design of the wind turbine, similar to any other dynamic system, comprises a parallel dynamic system alongside of the wind turbine to estimate the whole/part of the wind turbine states. In contrast to the parity approach, in the observer design, the observation error is fed back into the dynamic system to reduce the error, adopting a proper observation gain. For example, using the Kalman filter, as the optimal observer, the

reduction of wind turbine sensor noise on the observed states, is guaranteed, optimally (Dey et al., 2015). Consequently, using the observed states, the residual signal is constructed. This approach is depicted in Figure 2.4, in which it is still needed to have an estimation of wind speed. It should be noted that the Kalman filter approach is used in Chapter 7 for the drive train sensors FDI. The main disadvantage of the observer-based FDI methods is that the whole linearized model of the wind turbine should be used to take advantage of well-developed linear observer design theories (Shi et al., 2015). Recently the sliding mode observer has shown some promising results to be implemented on the whole nonlinear model of the wind turbine (Pöschke et al., 2014). In (Chen et al., 2013) the observer design is conducted on
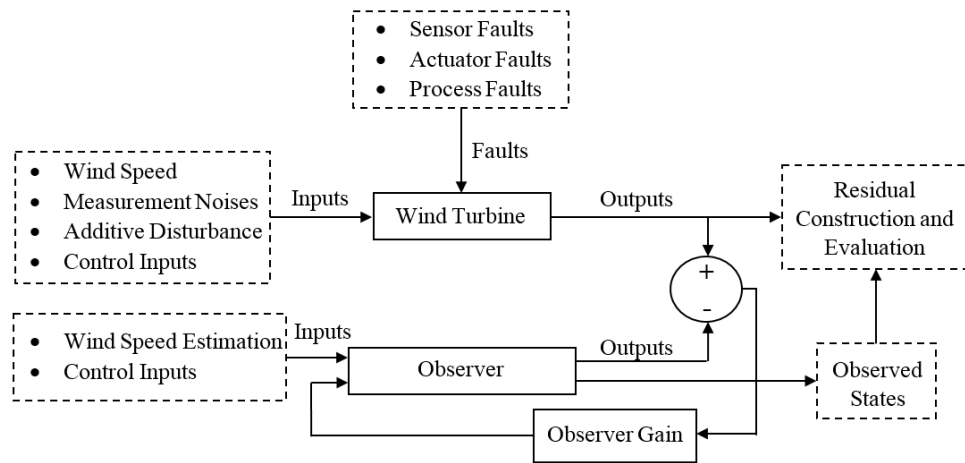
FIGURE 2.4: Observer-based residual generation approach.

the LPV model of the wind turbine to have more similarity to the nonlinear model, which shows acceptable FDI performance for different fault scenarios. In (Shi et al., 2015), an extended observer on LPV model of wind turbine was designed to estimate system states and fault signals simultaneously. Also, via H_∞ optimization the robustness of the observer was improved against additive disturbance. Similarly, in (Chen et al., 2011b), for disturbance decoupling and, meanwhile, to generate the optimal residual signal with respect to sensor noise, the Kalman filter was augmented as the observers. A bank of several observers was proposed in (Odgaard et al., 2012b), each of them being sensitive to only one fault and robust against the other faults. So, for the fault signature analysis on the observers, the FD as well as isolation are fulfilled at the same time. In (Dey et al., 2015) the performance of Kalman filter, bank of observers and parity based residual generation, are compared. It should be noted in (Sanchez et al., 2015; Casau et al., 2015) that a new observer design scheme is proposed for wind turbine FD, known as interval observer design, for a set of valid models using the so-called set-membership approach.

UIO is an improvement of the ordinary observer scheme to eliminate the need for wind speed estimation. In UIO, the observer dynamic system is totally decoupled from external unknown disturbances, i.e. wind speed, by adopting proper adaptive

observer gain, as shown in Figure 2.4. In this scheme, the wind turbine states are observed optimally, and accordingly, the disturbance effect on the residual signal is minimized. In (Odgaard et al., 2009b), the wind turbine sensor faults are detected with the UIO based approach.

Fault estimation

In this approach, a designated estimator of faults is used to detect and identify fault occurrence. Also, an estimator bank can be designed to isolate the faults with different sources. Each isolation estimator is designed for a specific fault. Despite the observer approach, in the estimation techniques, the fault information is directly extracted. The main step in the estimator design is the selection of design parameters. Indeed, in the case of proper design parameter selection, the need for the threshold is eliminated (Zhang et al., 2011). In Figure 2.5, the fault estimation is illustrated schematically. The estimator structure is designed as a dynamic system or static estimator such as the least squares filter (Shi et al., 2015). It should be noted that considering the nonlinear dynamics of wind turbines and different disturbance sources, the adaptive dynamic type estimators are dominating most recent studies (Georg et al., 2014). So, this approach is used in this thesis to estimate the faults in Chapters 5 and 6. The advantage of the adaptive estimator is that the robustness of FDI against the noises and disturbance is theoretically guaranteed, which is a promising characteristic to reduce the false detection rate (Simani et al., 2014). The most recent fault estimator design is the fuzzy sliding mode estimator, whose application of the wind turbines FDI is studied in (Schulte et al., 2015).
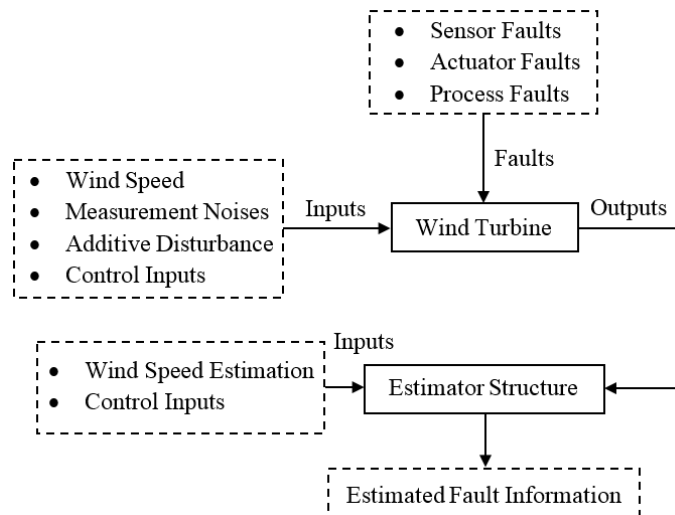
FIGURE 2.5: Fault estimation diagram.

Evolutionary algorithms and artificial intelligence

Evolutionary algorithms and artificial intelligence for wind turbines FDI design, are mainly categorized in two different approaches, including, input-output representation, and fault feature generator (classifiers), which are briefly introduced here.

Input-output representation:

Neural networks provide one of the best frameworks to represent the nonlinear and disturbed behaviour of wind turbines (Simani et al., 2012b). This approach is illustrated in Figure 2.6, in which the designed neural network is fed with actual/estimated inputs, the same as the wind turbine, to generate the duplicated outputs. It should be noted that the wind speed can be estimated in the neural network as well as the duplicated outputs. The neural network can be either designed for a whole wind turbine or dedicated to only one subsystem. The multi-layer perceptron networks and GFRFNN are the most commonly adopted ones for FDI purpose. The main step in this approach is the off-line training of the neural network to tune the neuron weights to the optimal ones. Also, an online fast learning adaptive training approach can be conducted, which is called ANFIS that takes advantage of the neural network's robustness, learning and training, and FIS interpretability. In both offline and online schemes, a properly large enough fault-free dataset should be available as a priori knowledge to train the network for the fault-free case. Accordingly, in some researches, this approach is called the data-driven learning algorithm. Finally, any significant incompatibility between wind turbine output and the corresponding one from the neural network, is interpreted as a fault. The application of this approach on wind turbines FDI has recently emerged (Qiu et al., 2012) and applied on different wind turbine components e.g. gearbox and generator faults (Garcia et al., 2006) and pitch faults (Chen et al., 2011a).

Fault signature generator:

In contrast to the previous approach, the fault information is directly extracted or inferred in this approach, with the design of an accurate priori knowledge-based network, e.g. ANFIS or FIS, as illustrated in Figure 2.7. Accordingly, the expert's knowledge is needed to be implemented in the design, whether as the numerical rules or fuzzy if-then linguistic rules. For example, the rule "If generated power is high at low wind speed region, it may imply possible sensor fault" can be used. These rules are also called the classifiers (Simani et al., 2011b). One of the best advantages of fuzzy rules is that due to the fuzzy membership representation, the rough measurement of wind speed, made by the anemometer, can be used in the design. In (Giebhardt, 2006), classification methods and evolutionary algorithms are utilized for rotor imbalance/aerodynamic asymmetry classification detection.
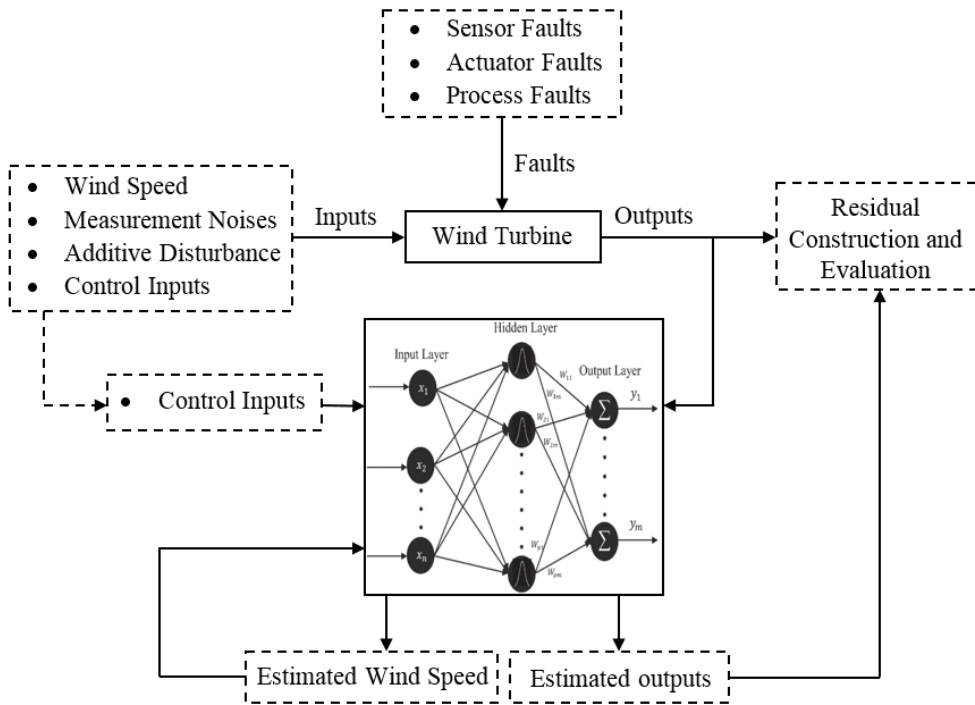
FIGURE 2.6: Neural network input-output based FDI.

Set-membership approach

In this approach, a set of mathematical models of a wind turbine is utilized to check the system consistency. The benefit of this approach compared to residual-based FDI approaches, is that a set of valid models of the wind turbine is being utilized. In this approach, model uncertainties and noises are assumed to be unknowns, with an upper bound, known as a priori. Due to unmolded dynamics, noise and uncertainty on the wind turbine, it is possible that the input/output data is consistent with more than one model (Tabatabaeipour et al., 2012). So, an active model diagnosis is adopted in which, at each time step taking the model falsification concept into consideration, an auxiliary input signal is fed into both the wind turbine and models set, to find the correct model out of the predefined set. This concept of auxiliary signal is used in Chapter 5. Then, the consistency of the current input/output data and the model is checked to detect the possible faults (Blesa et al., 2011). This approach guarantees that the valid model of the wind turbine is never falsified. Additionally, instead of the whole wind turbine, the set-membership approach can be used only for one subsystem to check only one parameter, i.e. the feasible parameter set is defined instead of the valid model set (Rotondo et al., 2012). An advantage of the set-membership approach is that the need for the threshold is eliminated while the false alarm and missed alarm are avoided (Casau et al., 2015). The conservatism of this approach, because of uncertainty propagation and over-approximations required in the set computations, is the main drawback. This approach is illustrated
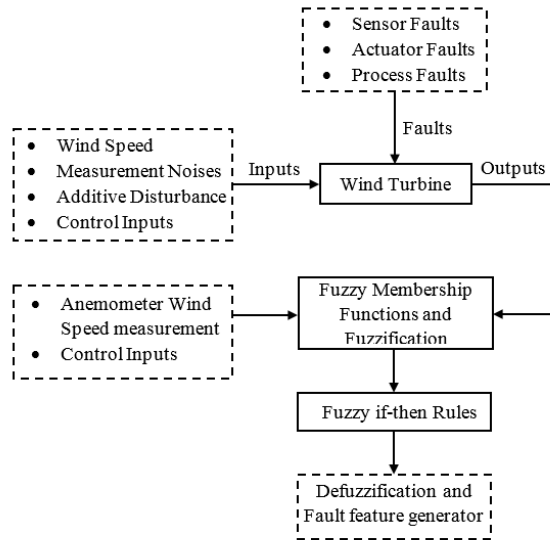
FIGURE 2.7: Fuzzy fault feature generation diagram.

in Figure 2.8. The combination of set-membership approach and observer design emerges as a new and promising approach for wind turbine FDI (Sanchez et al., 2015).

Bayesian approach

This approach is recently formulated as a model-based wind turbine FDI design (Chen et al., 2012), in contrast to its traditional application in signal-based condition monitoring. In this regard, in the Bayesian framework, the residual signal is evaluated to detect the faults. By taking advantage of Bayesian reasoning, the expert knowledge about the wind turbine structure can be directly augmented into the FD scheme (Fernández-Cantí et al., 2013). Indeed, the evaluation of the generated residual signal is done as the fault probability extraction in the Bayesian framework. The fault probability is adopted to detect the sensor faults in Chapter 7. Accordingly, the need for threshold evaluation of the residual signal is eliminated. Also, using the valid measurement, the fault can be predicted considering Bayesian fault probability, e.g. wind turbine bearing fault prediction (Herp et al., 2018). As a recent and promising approach for the highly stochastic system, in (Fernández-Cantí et al., 2013), the wind turbine set-membership FDI is reformulated in a Bayesian framework, for feasible parameter set determination.
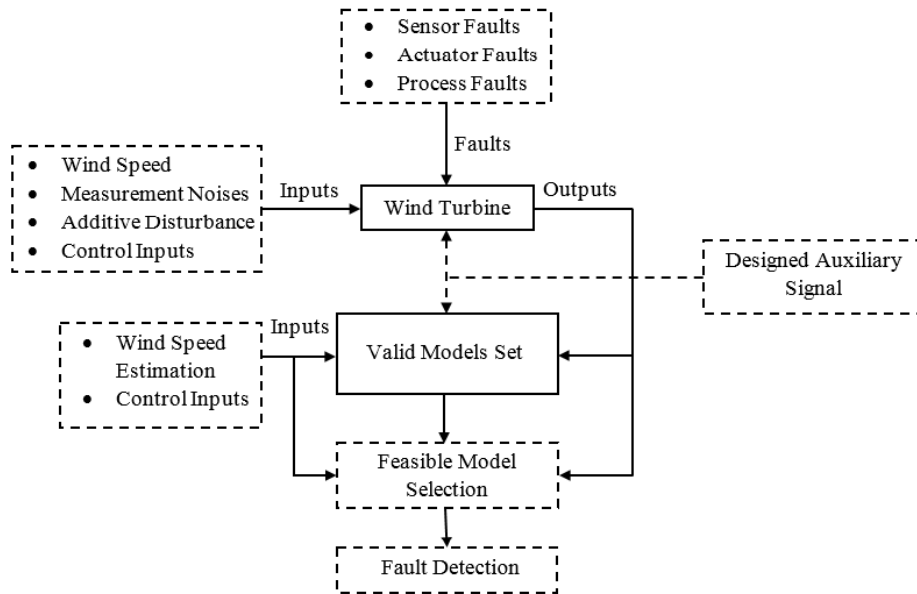
FIGURE 2.8: Set-membership FDI approach.

2.1.3   Wind turbine components FDI design review

In this section, the methods which have been introduced in section 2.1.2, are categorized based on their application on different components of the wind turbine. The aim is to critically review the methods to enable the readers to choose appropriate methods for further study.

Wind turbine sensor FDI

The most commonly applied FDI methods are focused on the wind turbine sensors. Especially, in the case of the offshore wind turbines operating in harsh environment, it is more likely that the sensor measurements are corrupted with faults (Wei et al., 2010). On the other hand, as the sensor outputs are mostly utilized in the feedback controller scheme, the whole wind turbine performance may be downgraded from the desired one, if there is a fault on the corresponding sensor (Wei et al., 2008). So, in this section the FDI methods of wind turbine sensors are reviewed.

The pitch sensor FDI is studied in (Wei et al., 2008), as the pitch angle control is a vital scheme for power regulation of wind turbines. The residual signal is generated using the physical redundant sensors and evaluated by considering mean and variance changes. In the parallel loop, the model-based pitch sensor is utilized to enable parity relation construction to isolate the detected sensor fault. Indeed, it is

aimed to identify which pitch sensor is faulty. Although, the combination of available physically redundant sensors and MBFDI approaches have shown promising results, but to remove the need of any extra sensor, the observer-based FDI design is one of the best alternatives (Rothenhagen et al., 2009). It should be noted that the major problem in observer design for wind turbines is the considerable noise content of sensors and the poor measurement of wind speed. The former one reduces the observer accuracy (Shi et al., 2015), while the latter one is needed for drive train observer design(Odgaard et al., 2009b). To increase the observation performance, in (Liu et al., 2008; Wei et al., 2008) H_-/H_∞ optimization is addressed to minimize the noise effect. On the other hand, the application of the Kalman filter, as the optimal observer, has been considered on wind turbine sensors, in which it is guaranteed that the noise effect is minimized. In (Wei et al., 2010), the Kalman filter is designed to detect and isolate pitch sensor faults. Similarly, (Chen et al., 2011b), the Kalman filter is used for the residual generation which is evaluated with the generalized likelihood ratio test and used for pitch and drive train sensors, while the redundant sensor is needed for fault isolation. Also, the applied aerodynamic torque is considered as a disturbance and the designed Kalman filter has proven to be robust against wind speed variation. The observer design has been sought in different modelling frameworks. For example in (Negre et al., 2011), the power sensor and generator speed sensors are considered and the observer is designed for the LPV wind turbine model, but the sensor noise is not considered. In (Shi et al., 2015), the extended observer for the whole wind turbine model is designed in the LPV framework to estimate the states as well as faults at the same time for pitch and drive train sensor faults using Linear Matrix Inequality (LMI). So, this approach can be considered as an estimation method. Also, the wind speed is considered as an unknown disturbance and the proposed observer is insensitive to it. The fuzzy TS framework has been considered in several papers to design the sensor FD methods. In (Kamal et al., 2013) for low wind speed regions and in (Simani et al., 2014) for high-speed wind regions, the generator current sensor fault is detected via an observer design in the fuzzy TS framework. Similarly, in (Kamal et al., 2014a; Badihi et al., 2014; Kamal et al., 2014b), the generator voltage sensor, pitch sensor and generator speed/power sensors, respectively, are considered and fuzzy TS fault observers are designed.

Regarding the unknown wind speed variation, UIO design is an appropriate choice to remove the need for wind speed estimation, especially considering drive train sensor FD (Odgaard et al., 2012b). In this approach, the wind speed variation is decoupled from the designed observer. For example, in (Odgaard et al., 2010; Odgaard et al., 2009a; Odgaard et al., 2009b) UIO is designed for drive train sensor FDI including rotor speed and generator speed sensors. Observer bank design is a suitable approach to detect and isolate the sensor faults at the same time. Each observer is designed so as to be sensitive only to one given fault and robust to other faults. In (Odgaard et al., 2012b), the UIO bank is designed for a set of sensor faults

including rotor speed, generator speed and wind speed sensors. Finally, more accurate evaluation of the residual signal to detect sensor faults can be conducted with set-membership check or Bayesian inference. In (Tabatabaeipour et al., 2012), the pitch and rotor sensor faults are considered and, utilizing the set-membership approach, the need for threshold checking is removed and also, no positive false alarm is produced. In (Chen et al., 2012) the relationship between wind turbine failure root causes and symptoms are used with a Bayesian Network for pitch sensor faults using SCADA data to reduce false alarms and missed fault rates.

Pitch actuator FDI

The power regulation of wind turbines is essential for high wind speed situations, i.e. to retain the generated power at nominal power, by adjusting the blade pitch angle to control the applied aerodynamic torque and consequently, rotor speed (Vidal et al., 2015). Also, it is aimed to feather the wind turbine by pitching the blades into the desired orientation to bring the wind turbine to a stop, in dangerous wind speed situations. So, the pitch actuator plays a vital role to accurately tune the blade pitch angle. Accordingly, the presence of faults on the pitch actuator leads to deviation of pitch angle. Pitch bias, effectiveness loss and dynamic change are considered as the most common pitch actuator faults. In this section the considered FDI methods of the pitch actuator are reviewed.

As the pitch actuator fault-free dynamic behavior is a linear and known equation, the parity relation can be used to generate the residual. As the measured pitch angle, to be used in the parity equation, is contaminated with measurement noise, in (Wu et al., 2016) the least square residual evaluation with sliding data window is used to evaluate the residual signal and detect dynamic change while minimizing noise effects. On the other hand, dynamic change can be considered as the model uncertainty and accordingly, in (Pisu et al., 2011) the robust residual filtering and parity equations, are combined to accurately detect the pitch actuator dynamic change for each blade. Also, the pitch sensor fault effect is distinguished from dynamic change, by considering the fault-end-effect, i.e. fault signature.

The pitch sensor noise, dynamic change and bias are challenging to be separated at the same time, which directs the recent pitch actuator FDI studies. In this regard, observer design is a potentially suitable approach. In (Donders et al., 2002) the Kalman filter observer is designed to detect the pitch actuator bias. Also, in (Qiao et al., 2008), the H_-/H_∞ optimization method is augmented in the observer design to generate the optimal residual. Regarding the noise effects, in (Chen et al., 2013) the observer is designed with adaptive gains to detect dynamic change with sensor noise and fault. It is shown that the adaptive observer is only sensitive to dynamic change by attenuating noise and removing the sensor fault effect. In a similar manner, in (Lan et al., 2018), the sliding mode observer is designed to detect dynamic

change with an adaptive hierarchical method to facilitate the real-time implementation. Also, in (Georg et al., 2014) the sliding mode observer is designed for the wind turbine fuzzy TS model to detect any increased time delay in the electrical pitch actuator.

The application of artificial intelligence and soft computing using SCADA data to detect pitch actuator faults have shown promising results to avoid the overly complicated FDI method. In (Chen et al., 2011a) using neural networks, a pattern recognition structure is proposed to detect pitch actuator faults. On the other hand, in (Qiu et al., 2012) the Bayesian fault probability is obtained to evaluate the SCADA alarm data and detect potential pitch actuator dynamic change.

Generator and converter FDI

The maximum power point tracking of variable speed wind turbines is achieved by regulating the electrical generator torque using converter current control. The generator torque control leads to adjusting the generator and rotor speeds to the desired values such that consequently, the power coefficient is maintained at the maximum possible one. Accordingly, the generator faults including bias and dynamic change cause the deviation of operation from the intended one. So, it is vital to detect and isolate the generator faults. The large variety of wind turbine manufacturers inevitably result in different manufacturer-specific wind turbine generator technology (Abuaisha, 2014). Accordingly, it is fruitful to consider the generator FDI methods in the system control level, for the various different electrical generator topologies, as outlined in this section. It should be noted that, in most of the literature the generator fault is modelled as an additive bias.

In (Negre et al., 2011), a wind turbine LPV model including uncertainty, uses an LPV observer to generate the residual and adopting the adaptive threshold method, the generator torque bias is detected. In (Dey et al., 2015) three different generator FDI schemes are stated. In the first scheme a cascade of two Kalman filters is utilized for alleviation of the nonlinear aerodynamic torque effect. In the second scheme, a bank of dedicated observers is used. The third scheme is designed using a H_∞ filter, with parity equations by considering the nonlinearity as a bounded disturbance. Also, in (Blesa et al., 2014), by adopting interval observers and considering the noise and modelling errors as bounded unknowns, the generator fault is detected using online analysis of observed fault signatures and comparing them with the theoretical ones obtained using structural analysis. The fault size is estimated based on the batch least squares approach. The parity relation, using analytical redundancy relations and interval observers, for unknown and bounded uncertain wind turbine model, is developed in (Sanchez et al., 2015). On this basis, using the set-membership approach, the generator bias is accurately detected. Similarly, in (Tabatabaeipour et al., 2012), a consistent set with measurements is generate using the set-membership approach. Model uncertainties, noise, and uncertainties on the

torque coefficient and generator fault are included in the wind turbine model. An effective wind speed estimator is proposed. For representing the consistent set of models with measurements, a matrix zonotope is used, which results in a computationally efficient scheme. The results confirm the effectiveness of the proposed method compared to other methods for the same fault scenario. The approach does not need to use threshold design, which is an outstanding advantage of the proposed method. In (Simani et al., 2015a), the approximation of uncertain models and management of noisy data are accomplished using fuzzy theory. The residual signal, which is only sensitive to generator faults, are generated using fuzzy TS prototypes. The data-driven diagnosis strategy, based on fuzzy TS prototypes is proposed in (Simani et al., 2011a) for converter FDI with actuator and sensor faults. The generator torque reliable regulation, including both generator uncertainties and faults is studied in (Badihi et al., 2015), and two different schemes are presented for this aim. Firstly, a FIS is proposed for parameter adaptation, without any prior knowledge of the generator faults. In the second approach fuzzy TS identification is exploited, to develop an integrated FDI scheme to detect potential generator faults in online diagnostic information. The adaptive fault estimation is exploited in (Zhang et al., 2011) for generator and converter FDI. Also, in (Simani et al., 2014) a two-dimensional polynomial is suggested to estimate the power coefficient in an analytical form. Consequently, the adaptive filter is obtained via the nonlinear geometrical approach to detect the generator faults.

Drive train FDI

The drive train dynamic change may happen very slowly but it leads to undesirable oscillation which may advance into total breakdown which causes long and costly downtime (Odgaard et al., 2009a). So, it is very beneficial to detect this fault in time. It should be noted that the most of the developed FDI methods applied to the drive train are categorized as the signal-based ones (Chen et al., 2011a), where several significant literature reviews can be found in (Kabir et al., 2015; Odgaard et al., 2013b; Badihi et al., 2013; Hameed et al., 2010; Márquez et al., 2012; Pourmohammad et al., 2011). Accordingly, in this section only the model-based FDI methods are considered.

In (Pisu et al., 2011) the parity relation is designed on the drive train to generate the residual signal and, via robust filtering the residual signal is evaluated to detect drive train dynamic change. Also, the wind speed is used in the structure of parity relation assuming that the wind speed estimation is separately available, and it is not affected by the fault occurrence which is generally not true. On the other hand, the measurement noise is not considered. Accordingly, in (Cao et al., 2016) the Kalman filter is utilized to minimize the noise effect and detect the drive train efficiency loss due to wear and increased gear friction. The dynamic change may be considered as the change in the resonance frequency and damping ratio of the drive train. In this

regard, in (Odgaard et al., 2014), this change is detected by designing a filter and using only the generator speed measurement. The uncertainties on the drive train dynamic response, i.e. unknown aerodynamic torque, and high sensor noise, have led to the development of more advanced FDI methods on the drive train. In (Garcia et al., 2006), an artificial neural network was designed for drive train FDI by training the network with a large amount of fault-free data to attenuate uncertainty and noise effects. Also, in (Schulte et al., 2015; Kamal et al., 2012) utilizing fuzzy TS prototype modelling, the drive train fault was detected by designing a sliding mode observer with adaptive gain. Also, the fault size was identified using an equivalent output injection method.

Aerodynamic characteristic change

Debris build-up and blade erosion reduce the blade aerodynamic efficiency. As a result, the captured aerodynamic torque and power are decreased. Also, the uneven oscillation of blades is a reported issue of this change (Johnson et al., 2006). On the other hand, the power regulation by pitch adjustment of the blades is not satisfactorily conducted due to the changed aerodynamic profile of the blades. So, it is very important to foresee the aerodynamic characteristic change in the controller design and to detect this potential change, which is considered in Chapter 6. It should be noted that this change is difficult to detect because it is challenging to determine if the blade's debris/erosion is the reason for the reduced power generation or simply the wind speed is lower than the measured/estimated one (Borcehrsen et al., 2014). On the other hand, as debris build-up happens slowly on the blades, it is mostly assumed that this change lies within the annual maintenance/inspection of wind turbines and the blades can be simply cleaned/replaced. So, the literature focusing on this change is still limited. In (Tabatabaeipour et al., 2012), the blade's aerodynamic change is modelled as the uncertainty on the torque coefficient. Accordingly, a consistent set of models is generated using measurements and the available wind turbine model, which includes uncertainties and noise, and by means of the set-membership approach. This set represents all possible states in which the system can exist if it is not faulty. If the current measurement is not consistent with this set, a fault is detected. Also, it is stated that when the torque coefficient change is introduced, some faults are not detectable. Consequently, in (Badihi et al., 2017) instead of the individual wind turbine FDI, the blade debris build-up and erosion are detected at the wind turbine farm level and it is shown that this change is easier to be detected and accommodated at this scale. This is achieved by comparing the output powers of the wind turbine operating under almost the same wind conditions. The nonlinear wind turbine model is obtained by fuzzy TS modelling. Also, the FDI scheme comprises a rule-based threshold test technique for residual evaluation.

2.2   Wind Turbines FTC design

FTC schemes are designed to maintain acceptable performance and stability of the wind turbines as close as possible to the fault-free conditions when faults occur, and to avoid the need for extra costly maintenance and unwanted shut downs. In fact, FTC aims to remove the fault effects and keep the performance objectives at their desirable intended levels, despite the presence of either a fault, wind speed variation or uncertainty. It should be noted that the fault tolerant capability can be either designed as an additive feature to the baseline controller or integrated into the baseline controller design. The former approach is adopted in Chapter 7 and latter one is adopted in Chapters 5 and 6. FTC techniques are normally divided into two different schemes, i.e. active and passive. The main difference between these two schemes is that active FTC needs the timely and accurate FDI information to be fed into the controller structure, i.e. to adjust the available baseline controller to the current state of faults to compensate fault effects completely and maintain system stability and keep the performance objectives level as for the fault-free case. Also, FDI information can be used in subsequent prescheduled maintenance plans. However, it may introduce some delayed detection time and the risk of false/missed detected faults. In contrast, in passive FTC the baseline controller is predetermined and designed for both fault-free and faulty conditions. Indeed, the baseline controller is designed to be optimally robust against a class of presumed faults, considered as the system uncertainties. The benefit of passive schemes is that the baseline controller is fixed and neither FD nor CR are needed, which increases the final system robustness. Even though, it introduces some performance degradation in faulty conditions and it has limited fault tolerant capability. Stability is not necessarily guaranteed for the faults other than the considered class of presumed faults (Vidal et al., 2015). The design of the baseline controller needs to be determined, on which basis the fault tolerant capability is augmented. Also, the operational objectives are defined to evaluate the designed FTC performance.

2.2.1   Wind turbines passive FTC

In passive wind turbine FTC design, the risk of false/missed detection is removed. Nevertheless, this method is not an optimal one and a conservatism is introduced into the design of the baseline controller. Also, the closed-loop system is not necessarily stable for faults outside of the presumed ones. Indeed, the baseline controller is optimized for the fault-free case and some degraded performance is guaranteed when some presumed faults occur.

In (Sloth et al., 2010; Sloth et al., 2011), a wind turbine LPV model is used in the full load region and utilizing LMI, the baseline controller is proposed to be robust against model parameter variations, caused by nonlinear aerodynamics and,

against pitch actuator faults. Also, it is shown that the designed passive FTC has better performance than an industrial PID controller. The fuzzy TS multimodel is an appropriate framework, representing the nonlinear behaviour of the wind turbine, to design the baseline controller which is robust against faults. In (Simani et al., 2012b) a fuzzy-based framework including if-then rules, is presented to regulate both pitch angle and generator torque while adding fault tolerance features to the wind turbine in a passive way, considering pitch and generator sensor faults, pitch dynamic change and generator torque bias. Also, the proposed controller is easily implementable, compared to different available strategies. It should be noted that passive FTC approach is adopted in section 4.4 to improve baseline industrial PID control in full load region.

2.2.2 Wind turbines active FTC

Active FTC, applied to the wind turbines, can be grouped as the VSA approach and the CR approach. In VSA the fault information, identified from the FDI scheme, is fed into a virtual (software) sensor/actuator module, which is placed between the actual sensor/actuator and the baseline controller, for fault effects compensation in the sensor/actuator. This can be seen as signal correction in the VSA such that the effect of the fault is mitigated. This approach is interesting industrially because the existing the baseline controller needs no modification and thus, can be used in both fault-free and faulty situations (Rotondo et al., 2012). It should be noted that this approach is adopted in Chapter 7. For some faults, e.g. system faults in Table 2.1, the fault effects cannot be accommodated via VSA. Accordingly, in the CR approach the whole/part of the baseline controller is reconfigured to an alternative controller to guarantee stability and a satisfactory performance. This alternative controller is obtained by either modification of the current baseline controller parameters, switching a new controller into the system, or using the available hardware/software redundant components (Simani et al., 2012a; Sami et al., 2012a). It should be noted that this approach is adopted in Chapters 5 and 6. Accordingly, in this approach, all available components should be considered in the baseline controller design. This approach shows promising performance for the severe faults. The VSA for FA and CR on the wind turbine are illustrated schematically in Figure 1.3.

Wind turbines VSA FA

In this section, the VSA FA techniques of wind turbines, are reviewed. It should be noted that this technique is also known as the signal correction method, as the signal from the corresponding sensor/actuator fault source is corrected before feeding into the closed-loop wind turbine system. On the other hand, this FTC technique is

mostly applied to the sensors of a wind turbine, because the actuator signal correction may lead to instability, due to inaccurate fault size identification (Blesa et al., 2014). Also, it is easier to implement the virtual sensor module in practice.

In (Odgaard et al., 2012a) this technique is used to remove the sensor bias faults, originated in drive train sensors, using UIO to detect the faults. It is illustrated that these fault effects on the wind turbine operation are severe, as the drive train sensors are fed back into the controller. Also, it is shown that the fault effects can be completely removed, if the fault size is identified accurately. Similarly, in (Rotondo et al., 2012), VSA is used for pitch and drive train sensor faults, including both biased and gained sensor outputs, in which the set-membership approach is used to detect faults. Also, the generator torque bias as an actuator fault, is accommodated. In (Casau et al., 2012) using a similar approach, in addition to the mentioned faults, the drive train decreased efficiency due to dynamic change, is detected and accommodated. The fuzzy TS framework can be used to have more accurate fault size identification which is used in the implemented VSA module. In (Badihi et al., 2014) the gained generator speed and biased pitch angle sensors are detected using the residual signal generated via fuzzy TS modelling and residual evaluation by adaptive threshold checking. The pitch angle and generator speed are corrected before the corresponding controllers using the VSA module. Also, in (McMillan et al., 2007), for wider fault categories, including fixed pitch and gained pitch angle sensor, drive train sensors, generator torque offset, drive train changed dynamic and pitch actuator dynamic change, the VSA FA is conducted by correction of the pitch angle sensor, generator sensor, pitch actuator angle and generator torque signals. The FD is achieved using a fixed threshold residual evaluation. In (Schulte et al., 2015), a fuzzy TS sliding mode observer is designed to estimate and consequently compensate for the actuator faults by modifying the controller output via the virtual actuator. In (Shi et al., 2015) the pitch sensor fault and pitch actuator dynamic change are estimated through the design of an adaptive extended state observer for an LPV wind turbine model using LMI. The PID industrial controller is used as the baseline controller and its output is corrected with the estimated fault information. Also, the robustness against wind speed variation and model uncertainty, is guaranteed by H_∞ optimization. In (Sami et al., 2012b), the fuzzy TS wind turbine model is used and through the design of an extended state observer, the drive train sensor bias is detected and accommodated by correction of the baseline controller. The corrected signal is fed into a TS fuzzy dynamic output feedback controller to keep the performance at the desirable one. In (Simani et al., 2014) the proposed scheme exploits a robust actuator fault estimation approach based on adaptive filters. The considered faults are pitch actuator dynamic change, bias and generator torque bias. Accordingly, the output of the PID controller, adopted as the baseline controller, is corrected based on the estimated fault information. Finally, in (Badihi et al., 2017), a very interesting idea is proposed to detect the debris build-up on blades at the wind farm level. Indeed, through the use of expert-generated fuzzy if-then rules, the generated power of each wind turbine in the farm is evaluated to detect the possible

debris build-up. Accordingly, the generated torque is corrected in the VSA module to compensate for the debris build-up effect and to keep the generated power at the desirable value. It is worth noting that in the VSA the sensor faults are reasonably accommodated better than the system and actuator faults (Odgaard et al., 2015). Also, this scheme has industrial acceptability because of ease of implementation.

Wind turbines CR FTC design

In this section, the CR techniques for wind turbine are reviewed, considering research methods which state that the process and actuator faults are better accommodated. Different approaches are categorized as CR, in which, it is aimed to reconfigure whole/part of the baseline controller to compensate for the fault effects. This reconfiguration is obtained either by adaption of controller parameters, switching a new controller into the controller structure, or the other available redundant hardware/software components are used.

In (Yang et al., 2012) a group of model predictive controllers are designed to accommodate the pitch actuator dynamic change. A Kalman filter is used to identify the faults and based on the detected fault, an alternative predefined controller is used to compensate for the fault effect. In (Simani et al., 2012a), modified Ziegler- Nichols rules are applied to the online adaptive controller, relying on the least square method with adaptive directional forgetting factor, to adjust the PID controller parameters of the baseline controller to remove both generator and pitch actuator faults. In (Fan et al., 2012), a FTC scheme is proposed as a combination of model reference adaptive control with neural network compensation. Although, the fault is considered as a bounded additive actuation signal, however, no physically meaningful fault is considered. In (Sami et al., 2012a), an observer is designed in the fuzzy TS framework to estimate the generator sensor faults. Also, a robust estimation of effective wind speed is given. These estimations are used to compensate for the fault effects using a fuzzy TS dynamic output feedback controller. In (Kamal et al., 2014b; Kamal et al., 2012), by deploying a robust fuzzy scheduler and multi fuzzy observers, a nonlinear wind turbine controller is design to attenuate the sensor faults, actuator faults and parameter uncertainties on the overall performance. It is desirable to reconstruct and compensate several actuator faults with one observer. The sliding mode controller design technique is advantageous in this regard. An adaptive sliding mode observer is designed in (Lan et al., 2018) to estimate the pitch actuator dynamic change and to modify the traditional PID baseline controller for fault effect compensation. In (Vidal et al., 2015) by combining a disturbance compensator with a controller in the discrete-time domain, pitch actuator FTC is developed. Fault estimation and discrete-time controller designs are simultaneously fulfilled using the disturbance compensator. In (Sloth et al., 2009), the additional redundant pitch, rotor and generator sensors are considered in the proposed controller, to be deployed when fixed/no corresponding sensor outputs are

detected. It should be noted that generally the CR techniques are more efficient in actuator faults than VSA (Odgaard et al., 2015). Recently, the adaptive control is used to deal with the faults, as a category of the active/passive combination method. Although, it may be dangerous practically, since this method may mistakenly accommodate faults, for example in critical fault situations, which requires a safety stop of the wind turbine. Accordingly, if the adaption laws are designed accurately using expert's knowledge, the need for CR is removed to have a simple practical controller similar to passive FTC, and meanwhile, the FDI information is obtained which can be used to improve the maintenance schedules. On the other hand, no presumed fixed fault sets are needed, similar to active FTC. In (Habibi et al., 2017c) adaptive laws are defined as a part of the proposed controller to be used in the controller structure and compensate actuator fault effects, including pitch actuator dynamic change, pitch bias and generator torque bias are considered. The adaptive laws for fault estimation are utilized in Chapters 5 and 6.

In this chapter, the motivation for the available and applied FDI and FTC techniques on the wind turbines were considered and consequently reviewed, focusing on the need for more reliable wind power generation and lower operational cost. Indeed, these techniques can assist the wind turbine operation to have desirable performance in both fault-free and faulty situations. The different FDI methods, which have been already applied to wind turbines, were introduced conceptually. On this basis, the application of the introduced FDI methods on the FD of different wind turbine components, was investigated. Consequently, FTC methods were reviewed, as the second step to fulfil the fault tolerance feature. Accordingly, the techniques which are used in the rest of this thesis are motivated.

3 Wind Turbine Operational Modelling

In this chapter, the theoretical model of the horizontal axis wind turbine is described, and all subsystems are explained, separately. The possible faults are introduced which may have different sources, including the sensor, actuator and system faults. Also, the general operational strategy of the wind turbine is stated, which is to be achieved using the system controller. Finally, the numerical operation criteria are introduced to quantify the wind turbine performance. It should be noted that a wind turbine benchmark model has been proposed in (Odgaard et al., 2009a) including both faults for which the wind turbine should be reconfigured to continue operation, as well as for very severe faults which should result in a safe and fast shut down. This benchmark model has initiated several recent FTC designs, which is used in this thesis and the model parameters are given in Appendix B, Section B.1.

3.1   Wind Turbine Components

In this section the physical components of a generic HAWT with three-blade model is introduced, on which basis the system model and operation are described. Accordingly, in terms of control system level, the HAWT is broken down into subsystems. In Figure 3.1 the typical HAWT components are illustrated and furthermore the detail of how the components are interconnected (Odgaard et al., 2015) is also shown.

The nacelle which is located at the top of tower, contains the rotor blade shafts, i.e. low speed shaft, gear box, high speed shaft, generator and the brake which acts on the low speed shaft. The blades encounter the wind and rotate the low speed shaft. Rotor speed is normally increased via a gear box and fed into the generator, which produces the electrical energy. It should be noted that the hub also incorporates the pitch actuators. The yaw mechanism, which is located below the nacelle, consists of an electrical motor to rotate the nacelle and, consequently, to keep the rotor plane perpendicular to the wind direction, determined by the wind vane. Also, the anemometer which is located on the nacelle behind the rotor blades, measures the wind speed roughly (Odgaard et al., 2013b).
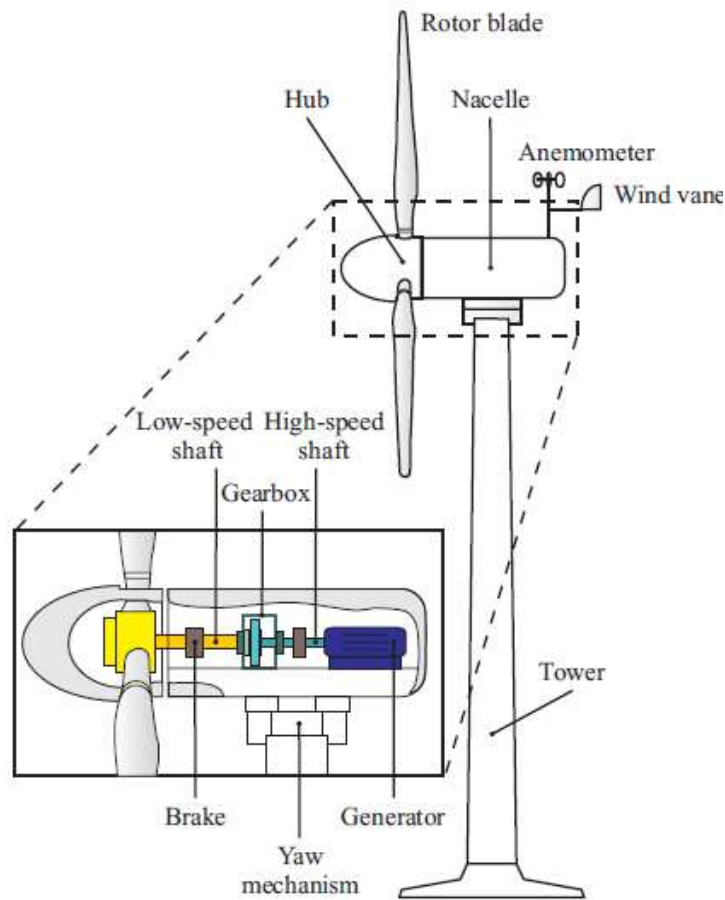
FIGURE 3.1: Wind turbine components (Sloth et al., 2009).

From the control system view point, the HAWT can readily be modelled as a number of interconnected subsystems. The incoming wind speed encounters the hub rotor blades, which are responsible for transferring the kinetic energy available in the wind into the mechanical energy of the rotor shaft. Indeed, the aerodynamic profile of the rotor blades is the main characteristic of the blades generating energy from the wind speed. This allows the hub and rotor blades to be combined as the aerodynamic model, in which the aerodynamic torque and thrust are developed and applied on the rotor. On the other hand, the drive train model, which connects the low speed shaft to the high speed shaft and includes the gearbox and bearings, is used to increase the angular shaft speed, allowing connection to the generator.

In the generator model, incorporating the power system, electrical controllers and convertor, the mechanical energy is converted into electrical energy which is then transferred into the grid. Also, it is assumed that the electrical load on the generator, which is translated as an electrical load torque, is controllable, deploying an appropriate generator, such as a doubly fed induction machine. The tower model

is considered as an elastic structure, which is swaying back and forth, i.e. having bending-wise oscillation, due to the applied aerodynamic thrust on the rotor. In fact, the tower oscillation changes the relative wind speed, acting on the rotor plane. Finally, the pitch actuator model is considered to control the pitch angle of the blades to regulate the applied aerodynamic torque.

In this section, the wind turbine model structure has been illustrated and introduced briefly. Also, the control system subsystems of the HAWT have been described, which are formulated in the following sections. In the next section the wind model is introduced.

3.2   Wind Model

In this section the characteristics of wind speed, as the main driving force of HAWT, are stated. The wind motion is created because of temperature gradients of the air, due to uneven heating of the atmosphere by the sun. The wind speed is known to be a highly stochastic process which has a mean term and a turbulence component. The mean value of wind speed is reported for different wind turbine farms, averaged over monthly or daily scales. So, there can be a rough estimation of mean wind speed, considering wind turbine location as well as yearly date of operation (Bianchi et al., 2007).

The turbulence component includes all higher frequency fluctuations of the wind speed around mean values and has a significant impact on aerodynamic loads on the wind turbine. Although, there have been considerable studies to propose statistical models for the turbulence components of the wind speed, it is apparent that some assumptions are still necessary which are not correct in general at each point in time.

The obstacles in front of each wind turbine, including building, mountains or even the other wind turbines, reduce the effective wind speed. Also, the ground friction has a major reduction on wind speed, which has led to increase the modern wind turbine heights to attenuate this so-called wind shear effect. The result is that through each rotation of the blades, the effective wind speed varies with the height of each blade element. There is an accurate mathematical model of wind shear to embed this effect into the wind speed model. Also, when each blade passes in front of the tower, the aerodynamic torque is reduced, because the tower can be seen as an obstacle behind the blade which changes the air flow and consequently, the torque. This phenomenon is called tower shadow (Odgaard et al., 2015).

The anemometer, located behind the rotor blades at the top of the nacelle, is measuring the wind speed at that location. It can be concluded then that the rough wind speed measurement, made by the anemometer, is not an accurate estimation of wind speed at the rotor plane, acting on each blade. This is because of the above

mentioned issues and also the temporal and spatial distribution of the wind speed on the rotor plane. So, in this thesis, the wind speed is considered as an external and unmeasurable disturbance acting on the wind turbine. This is incorporated into the design of the controller which does not use the wind speed measurement in the proposed controller structure.

In this section, the wind speed characteristics have been briefly outlined for the development of the aerodynamic torque and thrust on the wind turbine. The aerodynamic behavior of the wind turbine is modelled in the next section.

3.3 Aerodynamic Model

The aerodynamic profile is the main feature of the blades, which leads to the aerodynamic torque and thrust acting on the wind turbine and is formulated in this section. The available kinetic energy in the wind is transferred in to the blades and the low speed shaft, which are rotating at angular speed ω_r. Then the aerodynamic torque, T_a, applied on the low speed shaft is as,

$$T_a = 0.5\rho_a A R V_r^2 C_q, \tag{3.1}$$

where, ρ_a, A, R, V_r and C_q are air density, blade swept area, blade length, effective wind speed at rotor plane and torque coefficient, respectively. Also, $A = \pi R^2$. The aerodynamic thrust on the wind turbine, F_t, which causes the tower to sway back and forth, is given as,

$$F_t = 0.5\rho_a A V_r^2 C_t, \tag{3.2}$$

where, C_t is the thrust coefficient. Torque and thrust coefficients can be formulated as functions of blade pitch angle, i.e. β, and tip speed ratio (TSR), i.e. λ, as, $C_q(\beta, \lambda)$ and $C_t(\beta, \lambda)$, respectively (Odgaard et al., 2015). Also, λ is defined as,

$$\lambda = \frac{R\omega_r}{V_r}. \tag{3.3}$$

The wind power induced to the wind turbine, P_a, is stated as,

$$P_a = P_w C_p(\beta, \lambda), \tag{3.4}$$

where, P_w is the available power in the wind and C_p is the power coefficient, which is a function of pitch angle and TSP. Also, P_w is as,

$$P_w = 0.5\rho_a A V_r^3. \tag{3.5}$$

The torque coefficient, can be stated in terms of the power coefficient, as,

$$C_q = \frac{C_p}{\lambda}. \tag{3.6}$$

Considering (3.1) and (3.6), the aerodynamic torque can be rewritten as,

$$T_a = \frac{0.5\rho_a A V_r^3 C_p}{\omega_r}. \tag{3.7}$$

In (Habibi et al., 2017c), the power coefficient, C_p, is proposed as an empirical equation as a function of β and λ. This equation is used in this thesis to model the aerodynamic behavior of the wind turbine, which can be written as,

$$\begin{aligned}
C_p(\beta, \lambda) &= C_1(\frac{C_2}{\lambda_i} - C_3\beta - C_4)e^{\frac{-C_5}{\lambda_i}} + C_6\lambda, \\
\frac{1}{\lambda_i} &= \frac{1}{\lambda + 0.08\beta} - \frac{0.035}{\beta^3 + 1},
\end{aligned} \tag{3.8}$$

where, $C_1 = 0.5176$, $C_2 = 116$, $C_3 = 0.4$, $C_4 = 5$, $C_5 = 21$ and $C_6 = 0.0068$. Also, an equation to approximate the thrust coefficient, C_t, is adopted from (Georg et al., 2012), which is given as,

$$\begin{aligned}
C_t(\beta, \lambda) &= 0.5\tilde{C}_t(1 + sign(\tilde{C}_t)), \\
\tilde{C}_t &= a_1 + a_2(\lambda - a_3\beta)e^{-a_4\beta} + a_5\lambda^2 e^{-a_6\beta} + a_7\lambda^3 e^{-a_8\beta},
\end{aligned} \tag{3.9}$$

where, $a_1 = 0.006$, $a_2 = 0.095$, $a_3 = -4.15$, $a_4 = 2.75$, $a_5 = 0.001$, $a_6 = 7.8$, $a_7 = -0.00016$ and $a_8 = -8.88$. The thrust and power coefficients, (3.8) and (3.9), are illustrated in Figures 3.2 and 3.3.

In this section, the aerodynamic torque, thrust and power, transferred from the wind into the wind turbine, have been introduced, which causes the angular speed of the low speed shaft. In the next section the drive train, which transfers the mechanical energy from the low speed shaft to the high speed one, is modelled.

3.4 Drive Train Model

The rotor shaft speed is increased via the gearbox and transferred into the generator shaft with higher speed. The drive train model is derived in this section which includes the gearbox, gears, low speed shaft, i.e. rotor, high speed shaft, i.e. generator, and shaft bearings.

The drive train dynamic behavior is most simply modelled as a two degree of freedom rotational system as illustrated in Figure 3.4, in which ω_r and ω_g represent the angular velocities of the rotor shaft and generator shaft, whose inertia are J_r
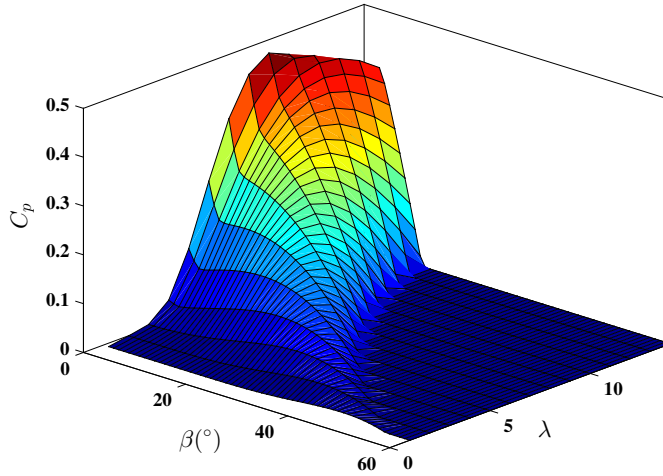
FIGURE 3.2: Power coefficient surface.

and J_g, respectively. The rotor and generator shaft bearings are modelled as angular viscous friction components with coefficients of B_r and B_g, respectively. The gearbox speed ratio is N_g. Also the torsional stiffness, K_{dt}, and damping, B_{dt}, are combined into the gearbox, to have a realistic model, which leads to a torsional angle of twist on the gears, i.e. θ_Δ. The gearbox efficiency, in terms of torque transfer is considered as η_{dt}. It should be noted that the aerodynamic torque on the rotor, T_a, is considered as the driving torque and, on the other hand, the generator torque, T_g, is considered as the load torque. Also, T_l and T_h are rotor and generator shaft loads and driving torques, respectively. The rotor shaft dynamic equation of motion, considering Figure 3.4, is given as,

$$J_r \dot{\omega}_r(t) = T_a(t) - B_r \omega_r(t) - T_l(t). \tag{3.10}$$

Also, the generator shaft dynamic equation of motion can be written as,

$$J_g \dot{\omega}_g(t) = T_h(t) - B_g \omega_g(t) - T_g(t). \tag{3.11}$$

Considering the gearbox ratio and efficiency leads to,

$$T_h(t) = \frac{\eta_{dt} T_l(t)}{N_g}. \tag{3.12}$$

On the other hand, taking the stiffness and damping of the gearbox into account leads to,

$$T_l(t) = K_{dt}\theta_\Delta(t) + B_{dt}\dot{\theta}_\Delta(t), \tag{3.13}$$
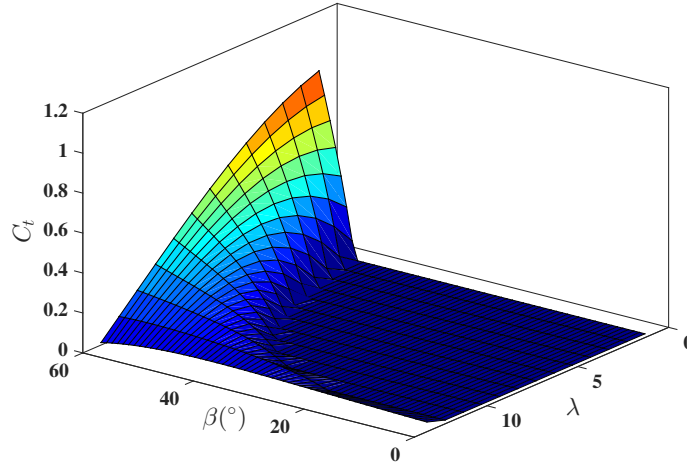
FIGURE 3.3: Thrust coefficient surface.
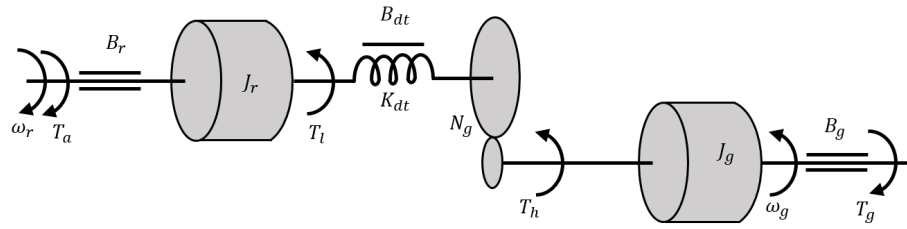
FIGURE 3.4: Drive train model.

where, θ_Δ is the torsional angle of twist, defined as,

$$\theta_\Delta(t) = \theta_r(t) - \frac{\theta_g(t)}{N_g}, \tag{3.14}$$

where, θ_r and θ_g are rotation angles of the rotor and generator shafts, respectively.

Now, combining (3.10)-(3.14), the resulting drive train model can be stated as,

$$J_r\dot{\omega}_r(t) = T_a(t) - K_{dt}\theta_\Delta(t) - (B_r + B_{dt})\omega_r(t) + \frac{B_{dt}\omega_g(t)}{N_g},$$

$$J_g\dot{\omega}_g(t) = \frac{\eta_{dt}K_{dt}\theta_\Delta(t)}{N_g} + \frac{\eta_{dt}B_{dt}\omega_r(t)}{N_g} - (\frac{\eta_{dt}B_{dt}}{N_g{}^2} + B_g)\omega_g(t) - T_g(t), \tag{3.15}$$

$$\dot{\theta}_\Delta(t) = \omega_r(t) - \frac{\omega_g(t)}{N_g}.$$

In this section the drive train model has been developed as a two degree of freedom rotational system and its combined dynamic equations of motion were derived.

In the next section the elastic tower behavior is considered.

3.5   Tower Model

In this section the bending oscillation of the wind turbine tower due to the wind thrust forces (3.2), is modelled.

The tower is considered as an elastic structure, such that the applied aerodynamic thrust causes a fore aft motion of the nacelle. The tower can then be seen as a spring-damper mechanism on which the nacelle, as the inertia, is oscillating. This model is illustrated in Figure 3.5. It should be noted that the nacelle displacement from its vertical equilibrium point, i.e. x_t, is exaggerated. In Figure 3.5, B_t and K_t represent the damping ratio and elasticity coefficient of the tower, respectively. Also, V_w is the free wind speed, before encountering the wind turbine blades. Accordingly, the dynamic behavior of the tower fore aft motion is modelled as,

$$M_t \ddot{x}_t(t) = F_t - B_t \dot{x}_t(t) - K_t x_t(t), \tag{3.16}$$

where, M_t is the mass of the nacelle. As it is obvious in Figure 3.5, the fore aft
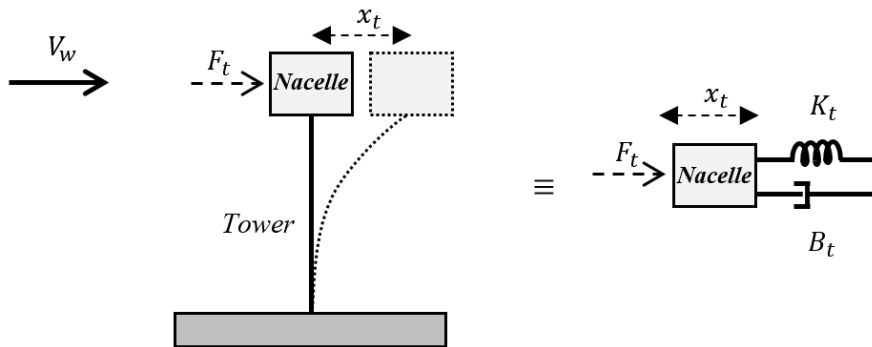
FIGURE 3.5: Elastic Tower model and its equivalent spring-damper model.

displacement of the nacelle, which holds the wind turbine blades, creates a relative speed between the free wind speed, V_w and the effective wind speed at the rotor plane, V_r, which is repeatedly used in Section 3.3. The effective wind speed at the rotor can then be expressed as a function of the free wind speed and nacelle displacement as,

$$V_r = V_w - \dot{x}_t(t). \tag{3.17}$$

In this section, the tower model and nacelle displacement have been modelled and, consequently the effective wind speed at the rotor plane was derived from the

free wind speed. In the next section the generator model, in which the mechanical energy is converted to electrical energy, is described.

3.6 Generator and Converter Model

In this section the generator and converter, which together can be considered as the power system, are modelled.

The generator shaft kinetic energy is converted into electrical energy in the generator. On the other hand, because the grid frequency is fixed, it can be induced that the generator shaft should have a given rotational speed to generate electricity with frequency the same as the grid. So, to let the wind turbine operate with different rotational speed, which is mostly the case in practice to increase wind turbine efficiency, a converter is located between the generator and grid to adjust the generated power frequency. Indeed, the current in the generator is controlled utilizing an internal electronic power controller in the converter. Control of demand current in the generator leads to regulation of the torque load on the generator. It should be noted that generator torque and power are of interest in this research. In fact, it is assumed that the generator current control is seen as the generator torque control.

In this thesis, the converter is modelled as a first order system with time delay as,

$$\dot{T}_g(t) = -a_g T_g(t) + a_g T_{g,ref}(t - t_{g,d}), \tag{3.18}$$

where, $T_{g,ref}$ is the reference generator torque load, which is requested from the generator by controlling its current, and $t_{g,d}$ is the communication delay. Also, $a_g = 1/\tau_g$, where τ_g is the system time constant.

The response of the internal electronic power controller of the wind turbine is much faster than the slow mechanical dynamic behavior. Accordingly, the generated electrical power in the generator, P_g, can then be approximated as a static relation considering the generator efficiency, i.e. η_g, as,

$$P_g(t) = \eta_g \omega_g(t) T_g(t). \tag{3.19}$$

In the generator system, to have a practical wind turbine model, maximum and minimum achievable torques with bounded possible slew rate are considered, as,

$$\begin{aligned} T_{g,min} &\leq T_g \leq T_{g,max}, \\ \dot{T}_{g,min} &\leq \dot{T}_g \leq \dot{T}_{g,max}, \end{aligned} \tag{3.20}$$

where, X_{min} and X_{max} denote the minimum and maximum value of variable *X*, respectively.

In this section, the generator and converter systems have been modelled, in which the electrical power is produced and also, the generator torque is controlled to enable variable speed operation of wind turbine. In the next section, the pitch mechanism which changes the pitch angle of the blades, is modelled.

3.7 Pitch Mechanism Model

The pitch mechanism, which changes the pitch angle of blades, is described in this section. The blade pitch angles form an important aerodynamic characteristic of the wind turbine, as is obvious in (3.8). Indeed, changes to the blade's angle of attack leads to different aerodynamic torque to the wind turbine rotor. The pitch mechanism is a hydraulic mechanism, implemented on each blade at the rotor hub, to change the pitch angle of blades, either individually or collectively, to follow the reference value of the pitch angle, β_{ref}, which is commanded from the controller. In fact, in each individual blade pitch control, there is a separate hydraulic actuator on each blade including the controller, while in the collective one, there is only one set of actuator and controller for all blades (Odgaard et al., 2015). An individual hydraulic pitch mechanism is illustrated in Figure 3.6. The hydraulic pitch mechanism
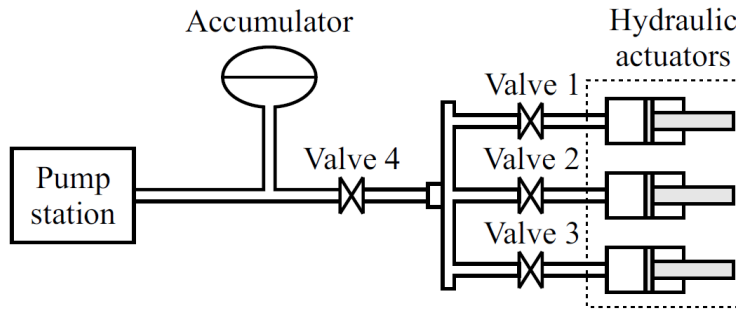
FIGURE 3.6: Hydraulic pitch mechanism (Sloth et al., 2009).

can be modelled as a second order system with communication delay as,

$$\ddot{\beta} = -\omega_n{}^2\beta - 2\omega_n\xi\dot{\beta} + \omega_n{}^2\beta_{ref}(t - t_{p,d}), \tag{3.21}$$

where, ω_n, ξ and $t_{p,d}$ are natural frequency, damping ratio and communication delay, respectively. Also, β_{ref} is the reference pitch angle, generated by the pitch controller and it is desirable to be followed by the pitch angle, β. However, the pitch actuator can be modelled including a limited slew rate and limited operational range, as

$$\begin{aligned} \beta_{min} &\leq \beta \leq \beta_{max}, \\ \dot{\beta}_{min} &\leq \dot{\beta} \leq \dot{\beta}_{max}. \end{aligned} \tag{3.22}$$

In this section the pitch mechanism has been considered, which along with the generator model forms the wind turbine actuators. In the next section the components of the wind turbine dynamics which have been ignored throughout the modelling so far, are summarized.

3.8 Neglected Dynamics and Modelling Assumptions

The assumptions which have been made in the modelling of the wind turbine, are outlined in this section. In fact, these assumptions have been taken to limit the extent of the modelling effort.

Generally, the dominant dynamic behaviour of the wind turbine is considered, and the higher frequency modes are ignored. Also, it is correctly assumed that the mechanical dynamic response of the wind turbine, due to the large rotor inertia, is considerably slower that the electrical counterparts, so the generated power is modelled as a static relation as (3.19). The yaw mechanism, which is used to change orientation of the hub, is ignored. Indeed, it is assumed that wind speed direction is always perpendicular to the plane of the blades. In practice, to avoid huge gyroscopic forces, the allowable yaw angle change rate is very small. So, the yaw mechanism can be ignored. Also, the hub gravitational force is left out. The blades are considered as stiff elements and blade bending modes are ignored, i.e. the edge-wise and flap-wise oscillations of blades are not considered. Also, it is assumed that all three blades are pitched identically and have the same pitch actuator dynamic behaviour.

In real wind turbines, the blade and rotor symmetry, i.e. non-homogeneous characteristics, is hard to be perfectly achieved. So, under wind speed actuation, the blade imperfection leads to periodic actuations in mechanical loads, with frequency of one per rotor period, i.e. 1P. On the other hand, the wind shear and tower shadow effects, mentioned in Section 3.2, are periodic with 3P frequency, as there are three blades. In this regard, the 1P and 3P frequency periodic effects are ignored. In fact, the wind speed is totally considered as an uncontrollable and unmeasurable disturbance and it is not going to be utilized in the control structure. This eliminates the modelling of the wind speed periodic effects, (Odgaard et al., 2015).

In this section some assumptions have been made which are going to be taken into accounts when studying the wind turbine behaviours. Using each subsystem models and the above-mentioned assumptions, the integrated nonlinear model of the wind turbine is constituted in the next section. It should be noted that in this thesis no model linearization is made.

3.9   Combined Wind Turbine Model

In this section the whole of the wind turbine subsystems, which have been described in previous sections, are combined to form the overall model of the wind turbine.

The free wind speed, V_w, encounters the wind turbine blades, which have transverse linear speed $\dot{x}_t$ and angular speed ω_r. The resultant relative wind speed, V_r, applies an aerodynamic torque, T_a, and thrust, F_t, on the wind turbine. From one control input, the reference pitch angle, β_{ref}, is adjusted using the pitch controller, which leads to the new pitch angle of the blades, β, through the pitch actuator. On the other hand, the reference generator torque load, $T_{g,ref}$, is tuned using the generator torque controller which causes the generator torque, T_g, to be produced via the converter current control. ω_r is fed into the drive train to have the shaft speed increased. In this regard, the mechanical dynamic response of the wind turbine is dominated by the drive train dynamic response. Consequently, the generator shaft angular speed, ω_g, is changed (Bianchi et al., 2012).

State space representation of the wind turbine dynamic model can be written as,

$$\dot{x}_{wt} = A_{wt}x_{wt} + B_{wt}u_{wt} + d_{wt}, \tag{3.23}$$

where, $x_{wt} = \begin{bmatrix} \omega_r & \omega_g & \theta_\Delta & \beta & \dot{\beta} & T_g & x_t & \dot{x}_t \end{bmatrix}^T$, $B_{wt} = \begin{bmatrix} 0 & 0 & 0 & 0 & \omega_n{}^2 & 0 & 0 & 0 \\ 0 & 0 & 0 & 0 & 0 & a_g & 0 & 0 \end{bmatrix}^T$,

$u_{wt} = \begin{bmatrix} \beta_{ref}(t - t_{p,d}) & T_{g,ref}(t - t_{g,d}) \end{bmatrix}^T$, $d_{wt} = \begin{bmatrix} T_a/J_r & 0 & 0 & 0 & 0 & 0 & 0 & F_t/M_t \end{bmatrix}^T$
and also,

$$A_{wt} = \begin{bmatrix} -\frac{(B_r+B_{dt})}{J_r} & \frac{B_{dt}}{N_g J_r} & -\frac{K_{dt}}{J_r} & 0 & 0 & 0 & 0 & 0 \\ \frac{\eta_{dt}B_{dt}}{N_g J_g} & -\left(\frac{B_g}{J_g} + \frac{\eta_{dt}B_{dt}}{N_g{}^2 J_g}\right) & \frac{\eta_{dt}K_{dt}}{N_g J_g} & 0 & 0 & -\frac{1}{J_g} & 0 & 0 \\ 1 & \frac{1}{N_g} & 0 & 0 & 0 & 0 & 0 & 0 \\ 0 & 0 & 0 & 0 & 1 & 0 & 0 & 0 \\ 0 & 0 & 0 & -\omega_n{}^2 & -2\omega_n\xi & 0 & 0 & 0 \\ 0 & 0 & 0 & 0 & 0 & -a_g & 0 & 0 \\ 0 & 0 & 0 & 0 & 0 & 0 & 0 & 1 \\ 0 & 0 & 0 & 0 & 0 & 0 & -\frac{K_t}{M_t} & -\frac{B_t}{M_t} \end{bmatrix}.$$

Signal flow of the resulting wind turbine model is illustrated in Figure 3.7, where it should be noted that the reference signals for the pitch angle and generator load torque, are generated from the controllers.

In this section, the wind turbine combined model, including all subsystems, has been introduced and the state space model has been derived. Also, the schematic wind turbine model diagram was illustrated. In the next section, the available measurements of the wind turbine are considered.
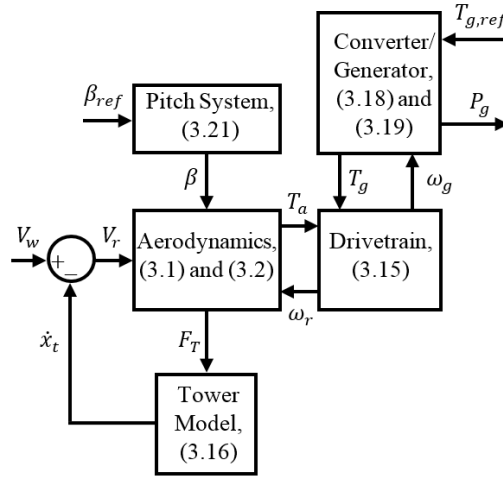
FIGURE 3.7: Wind turbine signal flow.

3.10 Measurements

In this section the available sensor measurements of the wind turbine are explained.

Generally, the sensors are modelled as static components, because they respond considerably faster than the wind turbine dynamic behaviour. However, the wind speed anemometer can be modelled as a first order low pass filter with time constant 0.5 second. The anemometer is located on the top of the nacelle behind the blades, where it gives a single point measurement, disturbed by the turbulence from the rotor blades. It is known that the anemometer does not provide an accurate wind speed indication at the rotor plane, however it does give a rough measurement which can be used for turning the wind turbine on/off. Consequently, it is not profitable for anemometer measurement to be used for control purposes. In this regard, it is aimed not to consider the anemometer measurement in the structure of the proposed controller and the wind speed is considered as an uncontrollable measurement disturbance.

In numerical simulation studies, the sensors are assumed equal to the corresponding state, which is going to be measured. On the other hand, to have a practical model, sensor noise is inevitable. So, the noises are added to the sensor measurements in the simulation. The noises are modelled as Gaussian white noise with zero mean and given standard deviation. The standard deviations are captured from practical studies which can be found in (Sloth et al., 2009; Sloth et al., 2011; Sanchez et al., 2015). Due to the different locations of each sensor, some sensors are much noisier than others. For example, rotor shaft speed, because of the huge aerodynamic torque applied to the rotor shaft, has considerable oscillation which induces significant noise on the rotor speed sensor.

The pitch angle sensors are located on the pitch actuator cylinders. Also, modern industrial wind turbines are equipped with two different pitch sensors for FDI purposes. The generator torque can be estimated from magnetic flux and current and on the other hand, the electrical power can be estimated from voltage and current. So, it is true to assume that electrical torque and power are correlated and that a sensor fault in each of them leads to a fault on the other one. In this regard, the generated power is calculated as (3.19) and there is no sensor used for generated power in this thesis. It should be noted that in industrial feedback control schemes of wind turbines using sensor measurements, notch or band-pass filters can be used to smoothen the measurement noises (Bossanyi, 2003).

The wind turbine measurements, used in this thesis, are as,

$$
\begin{aligned}
\beta_s &= \beta + \nu_\beta, & \dot{\beta}_s &= \dot{\beta} + \nu_{\dot{\beta}}, \\
\ddot{\beta}_s &= \ddot{\beta} + \ddot{\nu}_\beta, & T_{g,s} &= T_g + \nu_{T_g}, \\
\omega_{r,s} &= \omega_r + \nu_{\omega_r}, & \dot{\omega}_{r,s} &= \dot{\omega}_r + \nu_{\dot{\omega}_r}, \\
\omega_{g,s} &= \omega_g + \nu_{\omega_g}, & \dot{\omega}_{g,s} &= \dot{\omega}_g + \nu_{\dot{\omega}_g},
\end{aligned}
\tag{3.24}
$$

where, X_s denotes the measured state variable of X and ν_X represents measurement noise, modelled as white noise with Gaussian probability distribution function, as,

$$
\nu_X \sim N(0, \sigma_X^2),
\tag{3.25}
$$

where, $N(0, \sigma^2)$ is a normal distribution random number with zero mean, standard deviation σ and variance σ^2.

The measurement sensors of the wind turbine have been described in this section. The common possible faults, which are going to be considered in this thesis, are modelled in the next section.

3.11   Considered Fault Types

This section introduces the possible realistic wind turbine faults which are going to be considered and accommodated via controller design in this research. All considered faults of the wind turbine are categorized into either system, actuator or sensor faults and, accordingly, are introduced here.

As discussed earlier in Sections 3.6 and 3.7, the generator/converter and pitch mechanism are the actuators of the wind turbine. Long term operation of wind turbines in harsh remote offshore locations, i.e. with limited and difficult maintenance procedures, may lead to actuator faults. The pitch actuator in this situation is prone to suffer from bias and effectiveness loss. Regarding the system faults on the pitch mechanism which has been modelled as a hydraulic system in Section 3.7, wear

TABLE 3.1: Pitch actuator parameters in dynamic change situations.

Situation	Natural Frequency (rad/s)	Damping Ratio	Fault Indicator
Normal	$\omega_{n,N} = 11.11$	$\xi_N = 0.6$	$\alpha_{f_1} = \alpha_{f_2} = 0$
Pump Wear	$\omega_{n,PW} = 7.27$	$\xi_{PW} = 0.75$	$\alpha_{f_1} = 0.63, \alpha_{f_2} = 0.30$
Hydraulic Leak	$\omega_{n,HL} = 3.42$	$\xi_{HL} = 0.9$	$\alpha_{f_1} = 1, \alpha_{f_2} = 0.88$
High Air Content	$\omega_{n,HAC} = 5.73$	$\xi_{HAC} = 0.45$	$\alpha_{f_1} = 0.81, \alpha_{f_2} = 1$

of pump gears, hydraulic leak from oil tank, valves or pipes, and high air content in the hydraulic oil, are the most reported system faults. These faults are considered as changes to the pitch actuator dynamic behaviour, resulting changes to the natural frequency and damping ratio of the pitch mechanism from the corresponding undamaged systems. The mentioned dynamic changes leads to slower response speeds of the pitch actuator and, consequently, poor power regulation of the wind turbine. The natural frequency and damping ratio of each pitch actuator dynamic change for the benchmark model are summarized in Table 3.1 (Sloth et al., 2011).

It should be noted that in Table 3.1, N, PW, HL and HAC stand for normal, pump wear, hydraulic leaks and high air content situations, respectively. $\omega_{n,X}$ and ξ_X are natural frequency and damping ratio, respectively, in the situation X. Also, α_{f_1} and α_{f_2} are fault indicators. Also, in Figure 3.8 the effect of pump wear, hydraulic leak and high air content are illustrated, in which the initial pitch angle is set to $5°$ and the reference pitch angle is commanded as $0°$, considering (3.21). It is obvious that the settling time for all dynamic change situations are slower than the normal one.

The pitch actuator faults are considered as effectiveness loss, which can be considered as a multiplicative and bias fault on the regulated pitch angle of the blades. The effectiveness loss and bias of the pitch actuator can be modelled as,

$$\beta_u(t) = \rho(t)\beta_{ref}(t) + \Phi(t), \tag{3.26}$$

where, $\Phi(t)$ represents the uncontrollable pitch actuator bias that causes an unbalanced rotor rotation which increases the drive train fatigue probability (Badihi et al., 2014). Also, $\rho(t)$ is the unknown effectiveness of the actuator which is in the range of $0 < \rho(t) \leq 1$, where $\rho(t) = 1$ indicates a healthy pitch actuator and $\rho(t) = 0$ indicates a total loss of pitch actuation .

The pitch mechanism faults, i.e. effectiveness loss, bias and dynamic change, should be considered in the pitch actuator model. The dynamic change is modelled
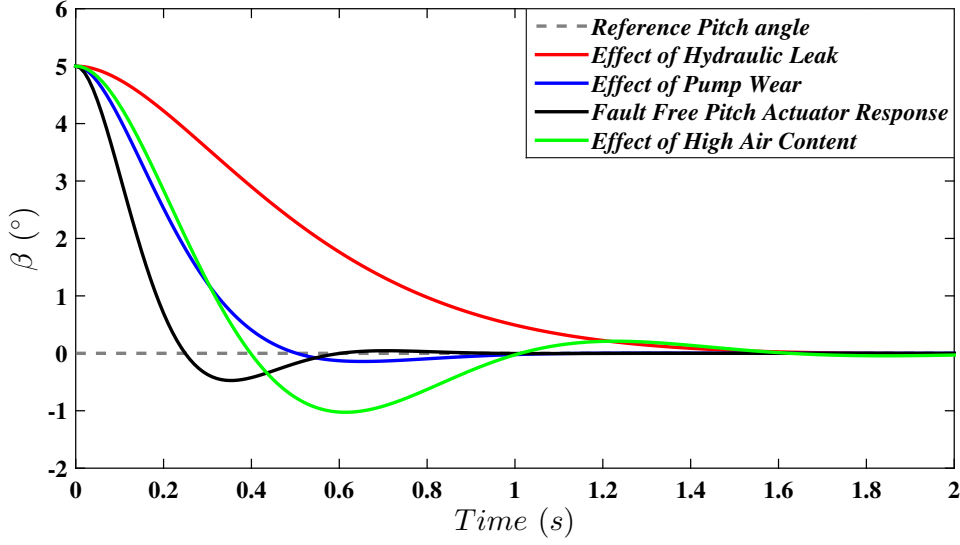
FIGURE 3.8: Effect of pitch actuator dynamic change on the response speed.

as a convex function of fault-free value of natural frequency and damping ratio (Lan et al., 2018). Also, the reference pitch angle in (3.21) is replaced with $\beta_u(t)$ to augment the possible effectiveness loss. So, the pitch mechanism (3.21) is rewritten as,

$$\ddot{\beta} = -\omega_{n,N}{}^2\beta - 2\omega_{n,N}\xi_N\dot{\beta} + \omega_{n,N}{}^2(\rho(t)\beta_{ref} + \Phi(t)) + \Delta\tilde{f}_{PAD}, \qquad (3.27)$$

where, $\Delta\tilde{f}_{PAD} = -\alpha_{f_1}\Delta(\tilde{\omega}_n{}^2)\beta - 2\alpha_{f_2}\Delta\left(\tilde{\omega}_n\tilde{\xi}\right)\dot{\beta} + \alpha_{f_1}\Delta(\tilde{\omega}_n{}^2)\beta_{ref}$, $\tilde{\omega}_n^2 = \omega_{n,N}{}^2 + \alpha_{f_1}\Delta(\tilde{\omega}_n{}^2)$, $\Delta(\tilde{\omega}_n{}^2) = \omega_{n,HL}{}^2 - \omega_{n,N}{}^2$, $\tilde{\omega}_n\tilde{\xi} = \omega_{n,N}\xi_N + \alpha_{f_2}\Delta\left(\tilde{\omega}_n\tilde{\xi}\right)$ and $\Delta\left(\tilde{\omega}_n\tilde{\xi}\right) = \omega_{n,HAC}\xi_{HAC} - \omega_{n,N}\xi_N$.

The converter system faults can be considered as the increase in the time constant τ_g in (3.18), as $\tau_g + \Delta\tau_g$. Also, due to the converter electrical malfunction, the reference generator torque is biased as (Sanchez et al., 2015),

$$T_{g,u} = T_{g,ref} + f_{T_g}, \qquad (3.28)$$

where, f_{T_g} is the generator torque bias, considered as an actuator fault, which is effective in power optimization as well as power regulation of the wind turbine. So, combining the converter dynamic response with the mentioned fault, (3.18) can be rewritten as,

$$\dot{T}_g = -a_gT_g + a_gT_{g,ref} + \Delta f_{GC}, \qquad (3.29)$$

where, it is assumed that a_g is changed to $a_g + \Delta a_g$ due to the internal generator fault, i.e. $\Delta\tau_g$ (Sanchez et al., 2015), as $\Delta a_g = -\Delta\tau_g/\left(\tau_g\left(\tau_g + \Delta\tau_g\right)\right)$ and also

$\Delta f_{GC} = \Delta a_g(-T_g + T_{g,ref}) + a_g f_{T_g}$ (Tabatabaeipour et al., 2012). It should also be noted again that because of the fast response of the converter compared to the mechanical subsystems, the change in the time constant of the converter, $\Delta \tau_g$, is not too disturbing on the overall wind turbine behavior. On the other hand, the internal electrical converter controller is reported to be able to remove the effect of $\Delta \tau_g$ much faster than the slow mechanical response of the wind turbine (Dalei et al., 2016).

Considering $C_q = C_p/\lambda$, the torque coefficient can be stated in terms of power coefficient, which is represented as a function of pitch angle and TSR, as (3.8). It has been pointed out that due to rain, icing, dust and debris on the wind turbine blades, the power coefficient is reduced both in magnitude as well as the considered relation with respect to pitch angle and TSR. Indeed, the location of the optimum power point tracking on the power coefficient surface, Figure 3.2, happens on a different pair of (β, λ) after several years of use, compared to the corresponding pair for new and clean blades. Also, the magnitude of the power coefficient may be reduced. So, this type of system fault is considered in this thesis so as to have a practical controller for long term use on wind turbines.

In this thesis sensor faults are modelled as measurement coefficient changes. Considering the sensor measurement of variable *X*, this can be modelled as,

$$X_s(t) = \alpha_X(t)X(t) + \nu_X, \tag{3.30}$$

where, ν_X is measurement noise and α_X is the measurement coefficient, modelled as,

$$\alpha_X(t) = \begin{cases} 1, & t < t_f, \\ \alpha_f, & t \geq t_f, \end{cases} \tag{3.31}$$

where, t_f is the unknown fault time and α_f is the unknown measurement coefficient after the fault occurs. Indeed, this type of sensor fault can be considered as the multiplicative fault. Also, the other types of sensor faults, including sensor bias and sensor fixed output, are considered via (3.30), as well. The considered sensor faults of the wind turbine model, which are going to be detected and identified, are rotor speed, generator speed, pitch angle and generator torque sensors. As a summary, the faults which are going to be considered in this thesis, are stated in Table 3.2.

In this section all fault types, sources and reasons of wind turbine faults which are going to be accommodated via proposed controller, have been described. In the next section, the wind turbine desired operational mode is described, on which basis numerical control criteria are stated.

TABLE 3.2: Considered wind turbine faults.

Fault	Reason	Fault type	Considered in
Pitch actuator bias and effectiveness loss	Pitch actuator fault	Actuator fault	Chapters 4, 5 and 6
Hydraulic leak Pump wear High air content	Pitch actuator dynamic change	System fault	Chapters 4, 5 and 6
Generator torque bias	Generator fault	Actuator fault	Chapter 5
Power coefficient change	Blades debris build-up	System fault	Chapter 6
Generator and rotor sensor faults	Sensor bias, coefficient change and fixed output	Sensor fault	Chapter 7

3.12 Wind Turbine Desired Operation Mode

In this section the operation mode and also the desirable performance of the wind turbine are introduced.

The wind turbine operation can be distinguished based on available actuators of the model. As described earlier, pitch actuator and generator electrical load torque are the main control inputs to control the operation of wind turbines. The generator torque control enables operation with variable speed to keep the wind turbine operating optimally at different wind speeds. Otherwise, the so-called fixed speed wind turbines achieves its optimal power extraction only at a given wind speed. On the other hand, pitch angle control leads to adjustment of the induced aerodynamic torque on the wind turbine. Consequently, the captured power can be attained at a given pitch setting. This leads to the variable pitch wind turbine type.

Generally, the wind turbine operation can be stated as power generation with respect to wind speed that should be as close as possible to the so-called ideal power curve, as illustrated in Figure 3.9. It is obvious that the wind turbine is only in operation between cut in wind speed, i.e. $V_{r,cut-in}$, and cut out wind speed, i.e. $V_{r,cut-out}$. For wind speeds below $V_{r,cut-in}$, the potential wind energy is not enough to cover the operation cost and accordingly power generation is not economically satisfying. Also, for wind speeds greater than $V_{r,cut-out}$, despite higher available wind energy, the operation causes too much structural load on the wind turbine and may lead to catastrophic damage. So, it is not safe to allow the wind turbine to operate above $V_{r,cut-out}$ and accordingly, the wind turbine is pitched-to-feather or

braked to protect it structurally and avoid catastrophic operation, despite the high available wind energy.

In Figure 3.9, V_r is the effective wind speed at the rotor plane. Also, the wind turbine produces its nominal power $P_{a,N}$ at the nominal wind speed $V_{r,N}$. The operation is divided in two different regions; namely partial load and full load. In partial
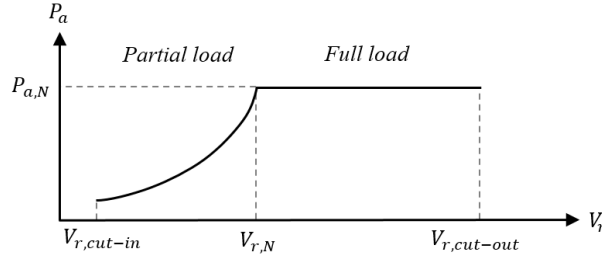
FIGURE 3.9: Ideal power curve.

load operation, which is considered from $V_{r,cut-in}$ to $V_{r,N}$, it is aimed to maximize the generated power. In fact, as mentioned earlier, the available wind energy is not that much to drive the wind turbine to hazardous operation. So, it is desirable to capture as much wind power as possible in partial load operation. Considering (3.4), it can be concluded that to maximize the produced power, $C_p(\beta, \lambda)$ should be kept at its maximum value. Also, according to (3.8), the maximum value of the power coefficient is $C_{p,max} = 0.48$ which occurs at $\beta_{opt} = 0°$ and $\lambda_{opt} = 8.1$ (Habibi et al., 2017c). So, the pitch angle of the blades should be simply kept at $0°$ via the setting $\beta_{ref} = 0°$. On the other hand, TSR should be kept at 8.1, despite wind speed variation, as considering (3.3), it is obvious that wind speed affects TSR. So, rotor speed ω_r should be controlled such that it satisfies the mentioned requirement. In this regard, by controlling the generator reference torque $T_{g,ref}$, the generator torque T_g and generator speed ω_g are tuned, and consequently, considering (3.15), ω_r is desirably adjusted. So, the main control loop in partial load operation is to control $T_{g,ref}$ and keep the power coefficient at its maximum value.

In full load operation, which is considered from $V_{r,N}$ to $V_{r,cut-out}$, it is aimed to keep the generated power at its nominal value, $P_{a,N}$. Considering (3.19), it can be seen that to have nominal power produced, T_g and ω_g should be kept at their nominal values, i.e. $T_{g,N}$ and $\omega_{g,N}$, respectively. The former requirement is easily met via setting $T_{g,ref} = T_{g,N}$. On the other hand, to keep ω_g at $\omega_{g,N}$, the aerodynamic torque is to be tuned via pitch angle control. In fact, by adjusting β_{ref}, the blade pitch angle is varied and consequently, considering (3.1), T_a and ω_a are tuned which directly vary ω_g via the drive train model (3.15), to maintain its value at $\omega_{g,N}$ (Sanchez et al., 2015).

The drive train torsion angle variation $\dot{\theta}_\Delta$ induces stress on the drive train. For both partial load and full load operation regions, it is desirable to keep $\dot{\theta}_\Delta$ as small as

possible, which, consequently, leads to lower stress on the drive train. Considering (3.15), it is obvious that $N_g \omega_r = \omega_g$ results in $\dot{\theta}_\Delta = 0$. Accordingly, in this thesis the controller is designed on the desirable operational mode of the wind turbine in which both ω_r and ω_g are being kept proportional to the gear box ratio to lessen the drive train stress (Boukhezzar et al., 2011).

The wind turbine desired operation mode is summarized as,

1. The wind turbine is shut down for wind speeds less than $V_{r,cut-in}$ and higher than $V_{r,cut-out}$.

2. In partial load operation the reference pitch angle is set as $\beta_{ref} = 0°$ and generator reference torque $T_{g,ref}$ is controlled to keep the power coefficient at $C_{p,max} = 0.48$.

3. In full load region the generator reference torque is set as $T_{g,ref} = T_{g,N}$ and reference pitch angle β_{ref} is controlled to keep generator rotor speed at $\omega_{g,N}$.

4. In all active operational regions of the wind turbine, it is aimed to satisfy $\dot{\theta}_\Delta = 0$ to reduce drive train torsional stress.

Remark 3.1. *In addition to the above mentioned operation objectives, a scheme is needed for bumpless switching between the controllers in the partial load and full load regions, due to probable inconsistency between controllers signal magnitude at the switching time. Otherwise, a bump in the control signal may cause oscillations between the two controllers and consequently, make the wind turbine unstable. It should be noted that, due to large rotor inertia, consequent slow response of variation of power generation, and inaccurate wind speed measurement, the generator speed is usually used as the switching condition to design the bumpless switching scheme. It should be noted that, as the controller design is separately fulfilled for each operational region, the switching scheme is not considered in this thesis. The reason for the approach of this thesis of considering the operational regions, is that there are still some fixed-pitch or fixed-speed industrial wind turbines in operation. So, to let the proposed controller be applicable for those wind turbines, this approach is adopted in this thesis. However, the proposed controllers can be integrated for whole operational regions, by using a simple bumpless switching scheme. On the other hand, in the design of the controller, it is very useful to implement a drive train/tower stress damper module to dampen drive train/tower oscillations and reduce structural stress. For example, the filtered generator speed and power can be added to the generator torque and the pitch angle, respectively, to filter out the resonant frequency of the drive train/tower (Badihi et al., 2015). As the main purpose of this thesis is FTC design of wind turbines, the reduced structural load does not lie within research objectives. However, once the FTC controller is designed, the corresponding induced drive train torsional stress is compared to the baseline controller, to consider its applicability.*

In this section variable speed and variable pitch operation mode of wind turbine and the reasons for this type of operation have been described. In the next section some numerical operation criteria are introduced to quantify the performance of the wind turbine and enable a comparison context for all designed controllers.

3.13   Wind Turbine Numerical Performance Criteria

In this section the operation control criteria are stated which are used to quantify the performance of the wind turbine and enable the numeric comparison under different situations. The criteria for partial load and full load operation regions are summarized in Table 3.3. The criterion $CC1$ in partial load represents the total extracted energy that is aimed to be maximized in order to increase captured energy. Also, this criterion in the full load region is aimed to be as close as possible to guarantee that the produced power is kept at the nominal value. t_{exe} represents the execution time. Also, in partial load region, the efficiency is calculated as, $Efficiency = \int_0^{t_{exe}} P_a(\tau)d\tau / \int_0^{t_{exe}} P_{maximum}(\tau)d\tau$, where $P_{maximum} = 0.5C_{p,max}\rho_a\pi R^2 V_r^3$. The second criterion is the applied stress on the drive train, defined as the total twist angle of the drive train, which is desirable to be kept as small as possible (Habibi et al., 2017c). The third and fourth criteria are only used in the full load region, which considers the deviation of the generator speed from the nominal value and the maximum deviation of the generated power from the nominal value, respectively. The fifth criterion is considered to keep the control variation into consideration, which may lead to actuator rate saturation and failure. It is expected to keep $CC5$ criterion at a reasonable level compared to the practical value. For the same reasons, the maximum and standard deviation of actuators are stated as criterion $CC6$, $CC7$ and $CC8$ (Boukhezzar et al., 2011). Throughout this thesis the defined criteria are used wherever they apply appropriately. The practical values of these criteria are obtained by using the baseline industrial controllers, and compared to the proposed controller ones, appropriately, throughout this thesis.

In this chapter, the HAWT model has been described considering all subsystems and also, the whole nonlinear model has been stated. On the other hand, the fault types, which are going to be considered throughout this thesis have been modelled. The wind turbine desired operation trajectory was defined, which is to be tracked using an appropriate controller. Finally, the numerical operation criteria have been introduced to quantify wind turbine performance. It should be noted that the numerical values of the considered benchmark wind turbine model are given in Appendix B.

TABLE 3.3: Performance criteria.

	Partial load region	**Full load region**
$CC1$	$\int_0^{t_{exe}} P_a(\tau)d\tau$	$\int_0^{t_{exe}} \left(P_g(\tau) - P_{a,N}\right)^2 d\tau$
$CC2$	$\int_0^{t_{exe}} \dot{\theta}_\Delta^2(\tau)d\tau$	$\int_0^{t_{exe}} \dot{\theta}_\Delta^2(\tau)d\tau$
$CC3$	-	$\int_0^{t_{exe}} \left(w_g(\tau) - w_{g,N}\right)^2 d\tau$
$CC4$	-	$max(P_g(t) - P_{a,N})$
$CC5$	$\int_0^{t_{exe}} \left|\dot{T}_g(\tau)\right| d\tau$	$\int_0^{t_{exe}} \left|\dot{\beta}(\tau)\right| d\tau$
$CC6$	$max\ (T_g(t))$	$max\ (\beta(t))$
$CC7$	$STD\ (T_g(t))$	$STD\ (\beta(t))$
$CC8$	$max\ \left(\dot{T}_g(t)\right)$	$max\ \left(\dot{\beta}(t)\right)$

4 Improvements of Baseline Industrial Wind Turbines Controllers

In this chapter, the baseline wind turbine controllers that are commonly used in both partial load and full load regions are introduced and their performance on the wind turbine are investigated. Also, the shortcomings of these controllers are discussed, on which basis an initial improvement on the baseline controllers is proposed. Accordingly, in the partial load region a FIS is designed to tune the controller gain. On the other hand, in the full load region, a PID-like controller is designed with adaptive gains, to take advantage of structural simplicity, while providing a better performance, compared to the baseline one, with actuator faults. It should be noted that the values of controller parameters are given in Section B.2.

4.1 Partial Load Baseline Controller

In this section, the operation of the wind turbine in the partial load region is considered and the baseline industrial controller is explained. This controller has been widely used in installed wind turbines, due to its ease of implementation as well as its simple structure. Accordingly, the performance of the modified controller on the wind turbine is compared to the baseline one.

As stated in Section 3.2, measuring accurate wind speed at the blade plane is not possible, so the wind speed cannot be considered in the controller structure to design the desired trajectory to make the wind turbine track the ideal power curve, Figure 3.9. One of the most commonly used controllers for partial load operation is a nonlinear controller designed by excluding the wind speed from aerodynamic torque. This controller is also known as the constant gain controller (Johnson et al., 2006). Also, satisfying the operation of wind turbines using this controller leads to verifying the wind turbine model, which is used in this thesis, as well as to make the baseline controller to be compared to the proposed controller results. Moreover, the control objectives in this operational region can be translated as keeping the extracted power as close as possible to the ideal case. Indeed, the maximum point on the power coefficient curve should always be reached. The maximum value of the power coefficient is $C_{p,max} = 0.48$ which occurs at $\beta_{opt} = 0°$ and $\lambda_{opt} = 8.1$, as it is obvious in Figure 3.2. The variation in wind speed only affects TSR, λ,

accordingly, the pitch angle is fixed at the optimal value as $\beta_{opt} = 0°$. On the other hand, TSR is to be kept at 8.1 which depends on wind speed as well as rotor speed. The wind speed is not controllable and is considered as a disturbance so that the rotor speed is to be controlled. This aim can be achieved by controlling the generator torque to modify the generator speed and, consequently, rotor speed. In partial load operation, to track the optimum point of the $C_p(\beta, \lambda)$, the speed of the generator is controlled by regulating the electrical torque demand on the generator through the generator torque controller. The control law determines the appropriate generator torque by excluding the wind speed from aerodynamic torque (Sloth et al., 2009).

Consider the aerodynamic torque (3.1) and TSR (3.3). Accordingly, replacing V_r in (3.1) by $V_r = \omega_r R/\lambda$, leads to,

$$
\begin{aligned}
T_a &= 0.5\rho_a A(\frac{\omega_r R}{\lambda})^3\frac{C_p}{\omega_r} \Rightarrow \\
T_a &= 0.5\rho_a A(\frac{R}{\lambda})^3 C_p \omega_r^2.
\end{aligned}
\tag{4.1}
$$

Considering the drive train dynamic behavior operating on the desired mode, causes the aerodynamic and generator torques to be related as,

$$
T_g = \frac{\eta_{dt} T_a}{N_g}.
\tag{4.2}
$$

Also, the rotor and generator speeds are proportional as,

$$
\omega_r = \frac{\omega_g}{N_g}.
\tag{4.3}
$$

Consequently, using (4.1) and (4.2), the generator torque is stated as,

$$
T_g = 0.5\eta_{dt}\rho_a AR^3 C_p \frac{\omega_g^2}{(N_g\lambda)^3}.
\tag{4.4}
$$

On the other hand, for operation on the desired trajectory, assuming maximum power generation leads to,

$$
\begin{aligned}
\lambda &= \lambda_{opt} = 8.1, \\
C_p &= C_{p,max} = 0.48.
\end{aligned}
\tag{4.5}
$$

Replacing (4.5) into (4.4), yields,

$$T_{g,desired} = 0.5\eta_{dt}\rho_a A R^3 C_{p,max} \frac{\omega_g^2}{(N_g\lambda_{opt})^3}. \tag{4.6}$$

So, it is desired to keep T_g at $T_{g,desired}$, which is only a function of ω_g. It should be noted that ω_g is measurable. Also, considering the fast dynamic response of the generator/converter model (3.18), the reference generator torque $T_{g,ref}$ is set to $T_{g,desired}$ to satisfy the aim of maximum power generation. Accordingly, the constant gain control of the wind turbine in partial load operation is summarized as (Boukhezzar et al., 2011),

$$T_{g,ref} = K_c\omega_{g,s}^2, \beta_{ref} = 0°, \tag{4.7}$$

where, $K_c = 0.5\eta_{dt}\rho_a A R^3 C_{p,max}/(N_g\lambda_{opt})^3$ and $K_c \left(Nm/(rad/s)^2\right)$ represents the constant gain of the partial load baseline controller (Sloth et al., 2011). It should be noted that the stability of the baseline controller 4.7 has already been guaranteed (Johnson et al., 2006), which is not repeated here. Also, a low pass filter can be utilized to prevent amplifying the noise content of $\omega_{g,s}$ in (4.7) (Badihi et al., 2014). The baseline controller of the wind turbine in the partial load region is illustrated in Figure 4.1.
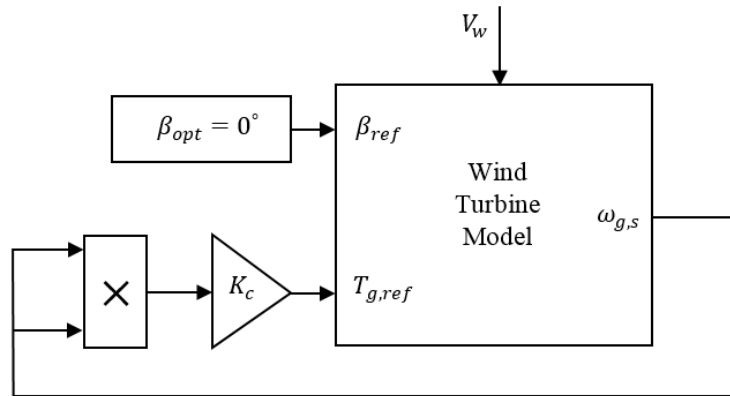
FIGURE 4.1: Partial load baseline controller diagram.

The performance of the baseline controller in the partial load region, (4.7), can be evaluated. The wind speed profile for the current analysis is shown in Figure 4.2 and the results of the controller are illustrated in Figures 4.3-4.5. The TSR is illustrated in Figure 4.3. It is obvious that TSR is tracking the optimum one, consequently, the power coefficient, depicted in Figure 4.4, is kept at the maximum one, despite the wind speed variation, after the initial transient response period. It should be noted as shown in Figure 4.5, that sometimes, the generated power is more than the theoretical maximum one available at that wind speed. Considering Figure 4.2, it is obvious that whenever the wind speed decreases significantly after a higher value,
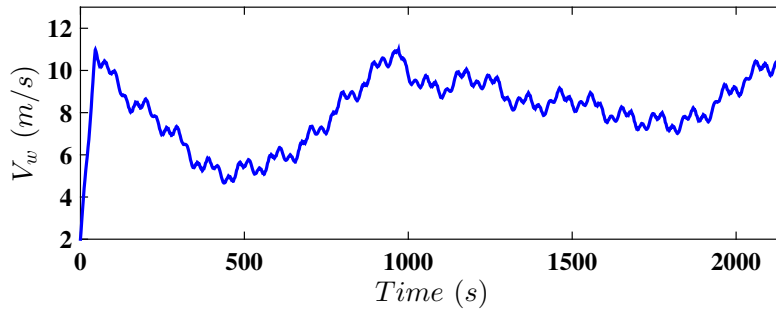
FIGURE 4.2: Wind speed profile in partial load region (Habibi et al., 2017d).
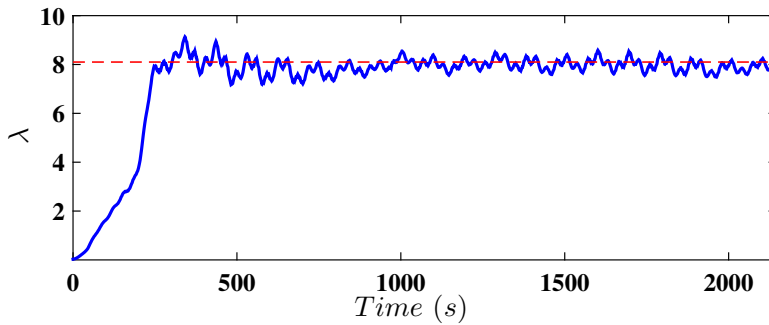
FIGURE 4.3: Actual TSR (blue solid line) and optimal one (red dashed line).

this contradiction happens. Indeed, due to the large inertia of the rotor and blades, at high wind speed values, the rotor speeds up and after the wind speed decreases, the rotor still has considerable kinetic energy which leads the rotor to rotate at a high speed and generate power more than the maximum available at that wind speed. In other words, the extracted kinetic energy of the rotor will be converted to electrical power after the wind speed drops. This phenomenon will be used to modify the baseline controller (4.7) to increase the extracted power. The performance criteria including the extracted power and drive train induced torsion angle, are shown in Table 4.1. Finally, it should be noted that when considering the results in Figures 4.3-4.5 and the expected results, the wind turbine model can be verified and, thus, this model can be utilized to evaluate the proposed controllers and FTC schemes in next chapters.

In this section, the baseline controller in partial load operation of the wind turbine has been described and evaluated. In the next section the full load region is considered, and the baseline control of this region is introduced.
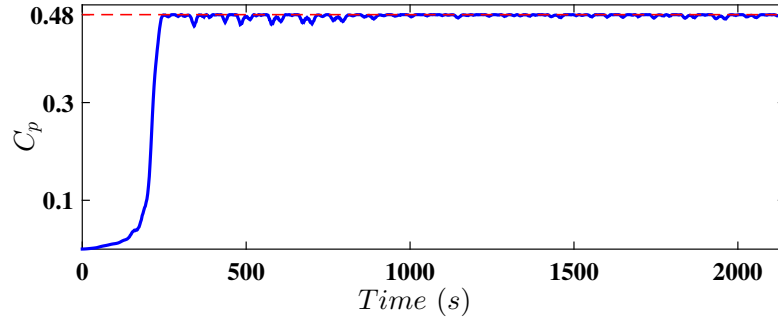
FIGURE 4.4: Actual power coefficient (blue solid line) and maximum one (red dashed line).
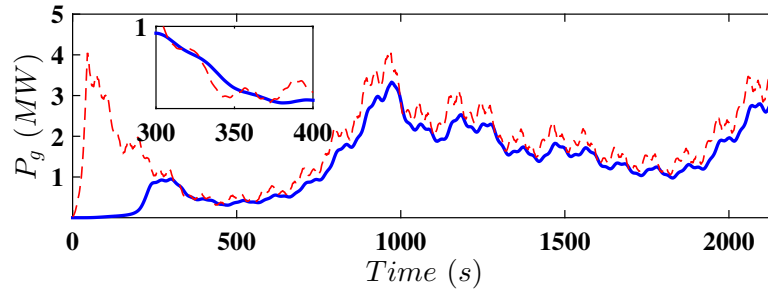
FIGURE 4.5: Generated power (blue line) and maximum extractable wind power (red dashed line).

4.2 Full Load Baseline Controller

In this section the industrial baseline controller in the full load region of operation of the wind turbine is explained, on which basis the proposed controller is evaluated.

As described in the Section 3.12, the control objective in the full load region is to keep the generated power at the nominal one $P_{a,N}$. In fact, the available wind energy, in this region, is higher than the wind turbine nominal one, but to prevent the wind turbine from over speeding and consequent breakdown, $P_{a,N}$ is just demanded. In this regard, considering (3.19), *(i)* T_g is to be fixed at the rated value $T_{g,N}$, and *(ii)* ω_g is to be maintained at the nominal value $\omega_{g,N}$ to ensure nominal power generation

TABLE 4.1: Performance criteria values of partial load baseline controller.

Performance criteria	Value
$CC1$	2.888 (GJ)
$CC2$	12.09 $(nrad^2/s)$

as (Sloth et al., 2011),

$$P_g = \eta_g T_g \omega_g = \eta_g T_{g,N} \omega_{g,N} = P_{a,N}. \tag{4.8}$$

The objective *(i)* is simply achieved via setting the generator reference torque, i.e. $T_{g,ref}$, at $T_{g,N}$ and due to the fast dynamic response of the generator, this leads T_g to follow $T_{g,ref}$, rapidly.

The objective *(ii)* is attained via regulating the blade pitch angle via the pitch actuator to vary the applied aerodynamic torque, and consequently, rotor speed. Accordingly, this leads to regulating the generator speed via the drive train model. In fact, considering variations of the applied aerodynamic torque with respect to pitch angle as function of the wind speed, as shown in Figure 4.6, it is obvious that with appropriate regulation of the pitch angle, the aerodynamic torque and consequently the rotor speed, are decreased, as wind speed increases. In this regard, it is
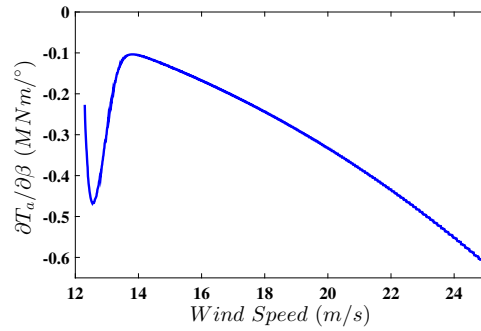
FIGURE 4.6: $\partial T_a / \partial \beta$ diagram in full load operation.

assumed that in the vicinity of any triple pair $(V_r,\ \omega_r,\ \beta)$ in the operational range of the wind turbine, T_a is not a singular function. Also, there is a given β^* for any pair of $(V_r,\ \omega_r)$, such that it steers the wind turbine to the rated power generation, via adjusting the pitch angle as $\beta = \beta^*$ (Jafarnejadsani et al., 2013). Accordingly, as the wind speed varies, β^* will take the corresponding value to satisfy the control objective. A diagram of β^* for the considered wind turbine benchmark model in the full load region is illustrated in Figure 4.7 (Sloth et al., 2011). It should be noted that, as wind speed is considered as an unmeasurable and uncontrollable disturbance, accordingly, β^* is an unknown parameter. For this reason, the wind speed variation is not considered in the controller structure. The most commonly adopted industrial controller for power regulation of wind turbines in full load operation is the PID controller, due to its simplified implementation and effectiveness (Lan et al., 2018). In this thesis, this controller is also used for performance comparison of the proposed controller. The PID controller regulates the pitch angle based on the generator speed tracking error, which is defined as,

$$e_{\omega_g}(t) = \omega_{g,s}(t) - \omega_{g,N}. \tag{4.9}$$
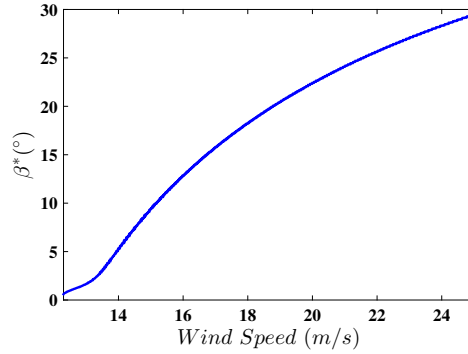
FIGURE 4.7: Profile of β^*.

Accordingly, the PID controller to adjust the reference pitch angle is fulfilled as,

$$\beta_{ref}(t) = K_P e_{\omega_g}(t) + K_I \int_0^t e_{\omega_g}(\tau)\, d\tau + K_D \dot{e}_{\omega_g}(t), \qquad (4.10)$$

where, K_P, K_I and K_D are proportional and integral and derivative gains of the controller, respectively, to be set using traditional methods, to ensure system stability as well as satisfying performance. K_P, K_I and K_D are mostly chosen as constant gains for the whole operational region, although in some research, different gains have been selected for narrower operational regions (Sloth et al., 2011). The wind turbine baseline controller in the full load region is illustrated in Figure 4.8.
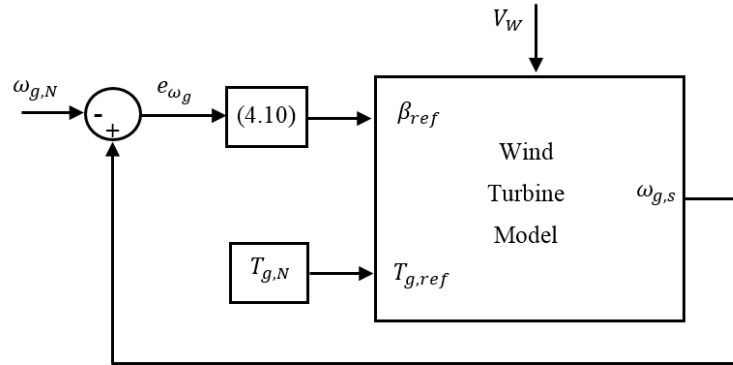
FIGURE 4.8: Full load baseline controller diagram.

The performance of the baseline controller in the full load region, (4.10), can be further evaluated. The wind speed profile for the current analysis is shown in Figure 4.9 and the results of the controller are illustrated in Figures 4.10 and 4.11, including generator speed and generated power, respectively. It is obvious that the baseline controller kept the generator speed and generated power close to their
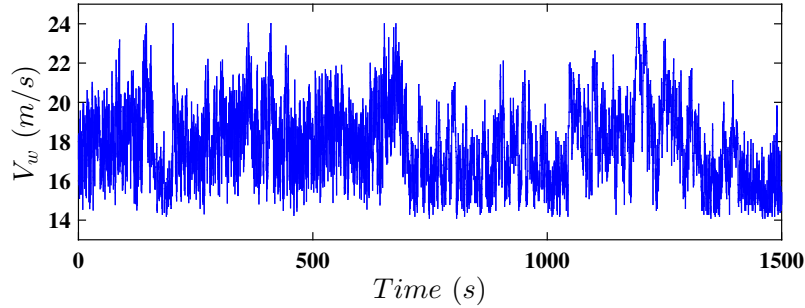
FIGURE 4.9: Wind speed profile in full load region (Habibi et al., 2017b).
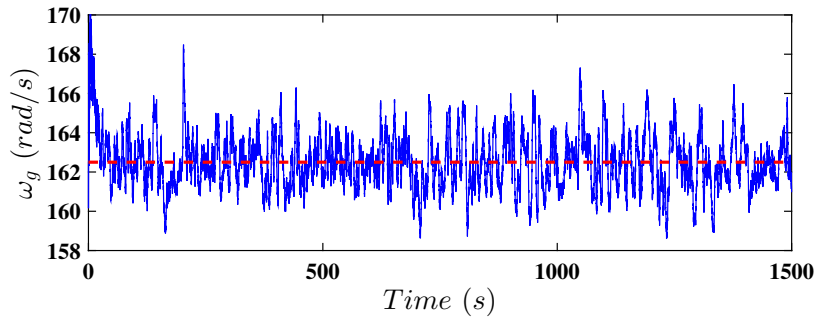
FIGURE 4.10: Generator speed using industrial baseline full load controller (blue line) and nominal generator speed (dashed red line).

nominal values. The performance criteria of the full load baseline controller are summarized in Table 4.2.

In this section the baseline controller of wind turbine in full load region has been described and evaluated via simulation. In the next section the improvement of the partial load baseline controller is introduced, and the results are compared with the baseline ones.

TABLE 4.2: Performance criteria values of the full load baseline controller.

Performance criteria	Value
$CC1$	2819 $(GW^2 s)$
$CC2$	2.103 $(mrad^2/s)$
$CC3$	2967 (rad^2/s)
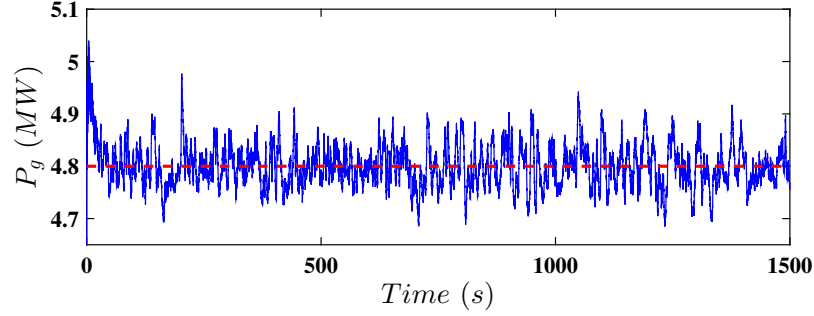
FIGURE 4.11: Generated power using industrial baseline full load controller (blue line) and nominal power (dashed red line).

4.3 Improvement of Partial Load Baseline Controller

In this section the wind turbine baseline industrial control for partial load operation (4.7) is improved taking the drive train friction into consideration and using a FIS, implemented into the controller structure to tune the constant gain K_c.[1] Firstly, the wind speed is considered as a disturbance, although it will be estimated as part of proposed the FDI schemes. However, after a fault has occurred, this estimation will not be accurate anymore, so if the controller is designed based on wind speed to design the desired trajectory, i.e. $\omega_{r,desired} = \lambda_{opt} V_r / R$, it will not be working satisfactorily after fault occurrence. For this reason, the wind speed is not used for improvement of the baseline controller. One improvement of the controller compared to the baseline one, is the consideration of drive train friction and the speed ratio in determining the generator torque (Sloth et al., 2009). Assuming that the wind turbine is operating at its desired steady-state trajectory, i.e. where the pitch angle and TSR are held at their optimal values, the time derivative of these variables will be zero. Accordingly, considering the drive train model (3.15), leads to,

$$
\begin{aligned}
0 &= T_a - K_{dt}\theta_\Delta - (B_r + B_{dt})\,\omega_r + \frac{B_{dt}}{N_g}\omega_g, \\
0 &= \frac{\eta_{dt}K_{dt}}{N_g}\theta_\Delta + \frac{\eta_{dt}B_{dt}}{N_g}\omega_r - \left(B_g + \frac{\eta_{dt}B_{dt}}{N_g{}^2}\right)\omega_g - T_g, \\
0 &= \omega_r - \frac{1}{N_g}\omega_g \Rightarrow T_a = \frac{N_g T_g}{\eta_{dt}} + \left(\frac{B_g N_g}{\eta_{dt}} + \frac{B_r}{N_g}\right)\omega_g \\
&\Rightarrow 0.5\rho_a A \left(\frac{R}{\lambda}\right)^3 C_p \left(\frac{\omega_g}{N_g}\right)^2 = \frac{N_g T_g}{\eta_{dt}} + \left(\frac{B_g N_g}{\eta_{dt}} + \frac{B_r}{N_g}\right)\omega_g.
\end{aligned}
\tag{4.11}
$$

---

[1]This section is captured and reorganized from the paper "Power Improvement of Non-Linear Wind Turbines during Partial Load Operation using Fuzzy Inference Control". The authors' attribution on this paper are given in Appendix C.

Now, assuming operation at the optimal point, it can be shown that,

$$
\frac{N_g T_g}{\eta_{dt}} = 0.5\rho_a A \frac{R^3}{N_g^2 \lambda_{opt}^3} C_{p,max}\omega_g{}^2 - \left(\frac{B_g N_g}{\eta_{dt}} + \frac{B_r}{N_g}\right)\omega_g \Rightarrow
$$
$$
T_g = K_c \omega_{g,s}^2 + K_2 \omega_{g,s}. \tag{4.12}
$$

where, $K_c = 0.5\eta_{dt}\rho_a AR^3 C_{p,max}/(N_g\lambda_{opt})^3$ is the same as the baseline controller gain and $K_2 = -\left(B_g + \eta_{dt}B_r/N_g^2\right)$, where $K_2(Nm/(rad/s))$ is the drive train friction compensation gain. It is obvious that the friction term has reduced the generator torque, where all friction values are constant and in this regard, no assumptions are made. On the other hand, for K_c, it is assumed that the wind turbine is operating at its desired trajectory despite wind speed variation, which is not the case in real situations.

Considering Figures 4.2 and 4.5, it is obvious that the available power in the wind and consequently, the aerodynamic torque, decreases when the wind speed decreases and vice versa. However, because of the slow dynamic response of the wind turbine, the rotor and generator speeds can be high while the wind speed is decreasing with a considerable rate, accordingly, the controller law given in (4.7), still increases the generator torque, whereas the available wind power is decreasing and so the wind turbine will consequently operate at a TSR other than the optimal value. Simulations show that reducing the magnitude of K_c by 20% improves power capture for a wind turbine with large rotor inertia (Hand et al., 2004). On the other hand, when the wind speed is increasing from a lower value, with reduced magnitude of K_c, the control law commands a small generator torque which leads to a reduction in harvested power even though the available power in the wind speed is increasing. So, the fixed magnitude of K_c, will cause the wind turbine to operate outside of its optimal trajectory. It is obvious that the gain K_c, should be tuned with respect to the wind speed variation, without measuring the wind speed accurately. So, it is proposed to use the generator speed and its time derivative as representatives of wind speed variation. In fact, the wind speed value and variation will cause proportional variation of the generator speed. It should be noted that a low pass filter can be utilized to prevent amplifying the noise content in the process. Now, using the generator speed and its time derivative, a FIS can be constructed to generate an appropriate controller gain K_c.

A FIS is a nonlinear mapping from inputs to outputs using some qualitative (linguistic) variables and particular logical rules, which are developed based on expert's knowledge. In fact, to define the rules, the real system behavior should be investigated by conducting considerable amount of experimentation or simulation. In this thesis, a FIS is used to calculate the controller gain K_c according to the appropriate rules, generator speed and its time derivative, as illustrated in Figure 4.12. The generator speed and its time derivative are being fed into the FIS which contains fuzzy

rules and fuzzy membership functions and the controller gain K_{FIS} will being obtained and fed into the controller structure. So, in 4.12, the gain K_c is replaced by K_{FIS}.

It should be noted that an abrupt change in controller gains leads to similar changes in the reference generator torque and this can induce high stresses onto the drive train. So, the fuzzy membership functions of controller gain and generator speed and its derivatives are designed such that the controller gain is changed smoothly by utilizing the Gaussian membership functions (Passino et al., 1998). The Gaussian membership function is defined as,
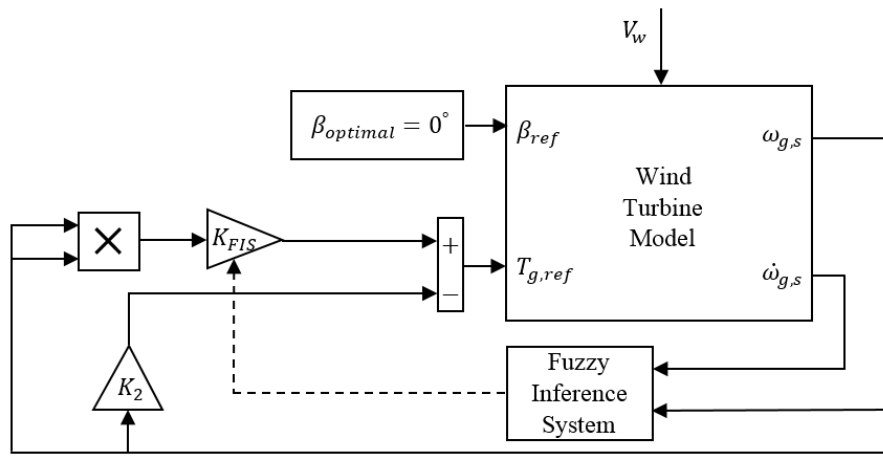
FIGURE 4.12: Baseline partial load controller improvement using FIS.

$$\mu_F\left(x_F, \sigma_F, c_f\right) = e^{-\frac{(x_F - c_F)^2}{2\sigma_F^2}}, \tag{4.13}$$

where μ_F, x_F, σ_F and c_F are the membership function percentage, range of variable, shape parameter and center of membership functions, respectively. The inputs to the FIS are generator speed and its derivative and the output of the FIS is the controller gain K_{FIS}. It should be noted that only the sign of the generator speed derivative, i.e. $\dot{\omega}_{g,s}$, is of interest to consider the generator speed variation. Therefore, the $\dot{\omega}_{g,s}$ membership functions are designed to be small to represent only the sign by selecting small σ_F in the Gaussian membership function (Passino et al., 1998). For $\omega_{g,s}$ and K_{FIS}, to cover the whole range appropriately, five membership functions are used. The membership function parameter values of K_{FIS}, $\omega_{g,s}$ and $\dot{\omega}_{g,s}$ are shown in Tables 4.3-4.5. The range of K_{FIS} is, as stated earlier, in $K_{FIS} = [0.8, 1]Kc$, which leads to $0.9887 \le K_{FIS} \le 1.2359(Nm/(rad/s)^2)$.

On the other hand, the ranges of $\omega_{g,s}$ and $\dot{\omega}_{g,s}$ are found based on the behaviour of the wind turbine model in which different values of generator speed and its time

derivative can be obtained. Indeed, via numerous amounts of simulations and considering the wind turbine as a slow mechanism and the model limitations, these ranges have been set up to cover the whole behaviour of the wind turbine operation (Badihi et al., 2014), as $0 \leq \omega_{g,s} \leq 200 \ (rad/s)$ and $-60 \leq \dot{\omega}_{g,s} \leq 60 (rad/s^2)$. These ranges should be as wide as possible, so as not to let the inputs to the FIS violate the limits, where in this case, the designed FIS will not work properly and the K_{FIS} gain will not be tuned logically. On the other hand, if these ranges are too wide, then the accuracy of the final FIS will reduce considerably. The simulation studies have been accomplished to find these appropriate ranges. Also, a numerical optimization process can be conducted to find the best membership function values, for a given number of membership functions (Habibi et al., 2017d).

The linguistic fuzzy rules can be defined as, "Rule i: if $\omega_{g,s}$ is A_i and $\dot{\omega}_{g,s}$ is B_i, then K_{FIS} is C_i", where A_i, B_i and C_i, are $\omega_{g,s}$, $\dot{\omega}_{g,s}$ and K_{FIS} membership functions, respectively, which are shown in Figures 4.13, 4.14 and 4.15, and their parameters are given in Tables 4.3, 4.4 and 4.5. The fuzzy rules are defined with respect to the idea of adjusting the controller gains based on wind speed variation. On the other hand, the wind speed variation can be found out by monitoring $\omega_{g,s}$ and $\dot{\omega}_{g,s}$ variations and with an expert's knowledge. Then the controller gain K_{FIS} can be tuned. This idea is obtained from the wind turbine behavior as a high inertia mechanism. This behavior can be summarized as follows. Whenever the wind speed has an increasing high value, the $\omega_{g,s}$ will be high and $\dot{\omega}_{g,s}$ will be positive and vice versa.
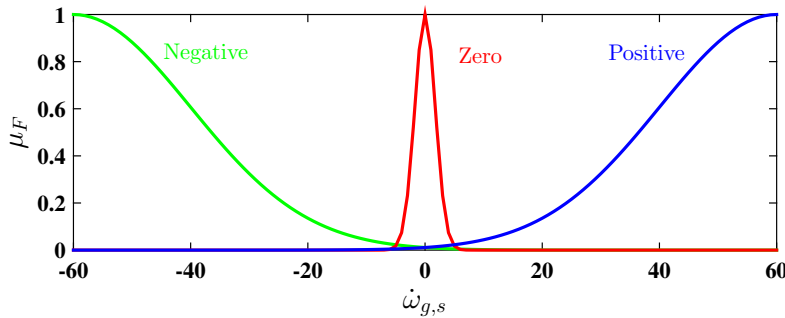
FIGURE 4.13: $\dot{\omega}_{g,s}$ membership functions.

On the other hand, $\omega_{g,s}$ and $\dot{\omega}_{g,s}$ similarly can picture the behavior of wind speed. Accordingly, whenever $\omega_{g,s}$ is high and $\dot{\omega}_{g,s}$ is positive, this implies that the wind speed is an increasing high value, there is high power content and the wind turbine should extract as much power as possible. This can be done by increasing the controller gain K_{FIS} that leads to increasing $T_{g,ref}$ which means demanding more power from the wind turbine. Similarly, for all other membership functions the fuzzy rules can be defined. The fuzzy rules are summarized in Table 4.6, where the K_{FIS} membership functions are in bold face. To finalize the FIS, the Mamdani inference engine was utilized which is one of the most appropriate engines for control

TABLE 4.3: Membership functions for $\omega_{g,s}$.

Membership function	Parameters
Too Small	$c_F = 0$, $\sigma_F = 17$
Small	$c_F = 50$, $\sigma_F = 17$
Medium	$c_F = 100$, $\sigma_F = 17$
Big	$c_F = 150$, $\sigma_F = 17$
Too Big	$c_F = 200$, $\sigma_F = 17$

TABLE 4.4: Membership functions for K_{FIS}.

Membership function	Parameters
Too Small	$c_F = 0.9887$, $\sigma_F = 0.0206$
Small	$c_F = 1.05495$, $\sigma_F = 0.0206$
Medium	$c_F = 1.11229$, $\sigma_F = 0.0206$
Big	$c_F = 1.174085$, $\sigma_F = 0.0206$
Too Big	$c_F = 1.2359$, $\sigma_F = 0.0206$

TABLE 4.5: Membership functions for $\dot{\omega}_{g,s}$.

Membership function	Parameters
Negative	$c_F = -60$, $\sigma_F = 20$
Zero	$c_F = 0$, $\sigma_F = 2$
Positive	$c_F = 60$, $\sigma_F = 20$

TABLE 4.6: Fuzzy rules.

		$\omega_{g,s}$ membership functions				
		Too Small	Small	Medium	Big	Too Big
$\dot{\omega}_{g,s}$ membership functions	Negative	**Too Small**	**Small**	**Small**	**Medium**	**Big**
	Zero	**Small**	**Medium**	**Medium**	**Big**	**Too Big**
	Positive	**Medium**	**Big**	**Big**	**Too Big**	**Too Big**
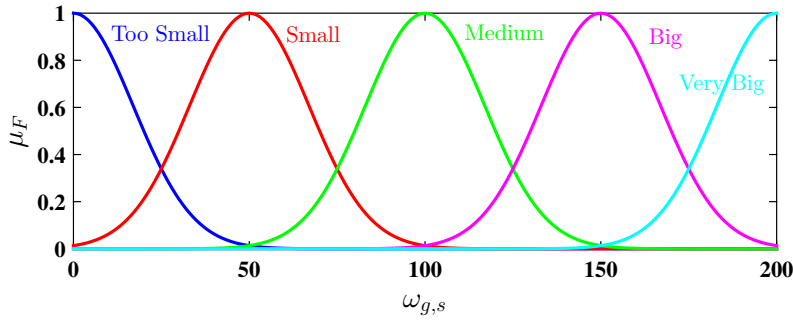
FIGURE 4.14: $\omega_{g,s}$ membership functions.
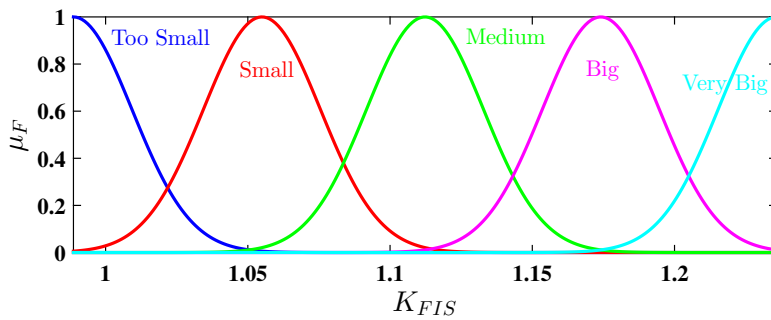
FIGURE 4.15: K_{FIS} membership functions.

processes (Passino et al., 1998). Minimum is used for "And method" and "Implication" while maximum is used for "Or method" and "Aggregation". The centroid is used for "Deffuzification". The corresponding FIS surface using these Fuzzy rules, is shown in Figure 4.16.
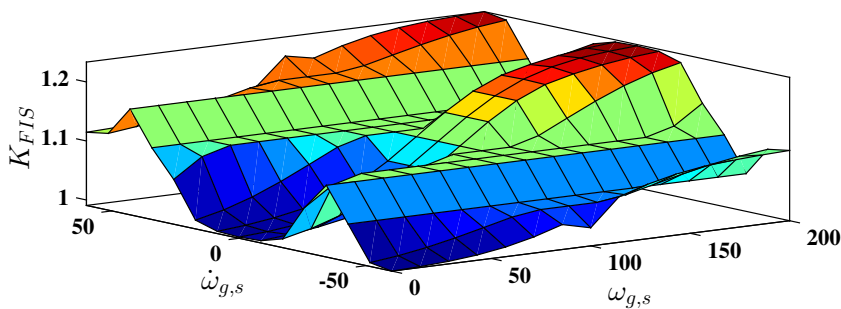
FIGURE 4.16: FIS surface.

Remark 4.1. *In this section it is assumed that the sensor measurements, which are used in the structure of the controller, are fault-free. In Chapter 7, the drive train sensor faults are detected and removed, in a separate manner from the control structure. Indeed, the sensor FDI scheme is designed to remove the fault effect before feeding the sensor measurements into the controller structure.*

TABLE 4.7: Performance criteria values of the improved baseline partial load controller.

Performance criteria	Value
$CC1$	2.924 (GJ)
$CC2$	16.78 $(nrad^2/s)$

TABLE 4.8: Performance criteria values of the baseline partial load controller and the improved one for real wind speed.

Performance criteria	Baseline controller	Improved controller
$CC1$	1.93 (GJ)	1.952 (GJ)
$CC2$	5.92 $(\mu rad^2/s)$	6.27 $(\mu rad^2/s)$

Now, using the designed FIS and the control structure as given in Figure 4.12, the generated power for wind speed shown in Figure 4.2, is illustrated in Figure 4.18. It should be noted that the generated power with the baseline controller, Figure 4.5, is also depicted to compare the results. It is obvious that the extracted power has increased considerably during the initial transient response which is due to including the drive train friction in the controller (4.12). On the other hand, during the steady state response, the use of the FIS has improved the extracted power. Additionally, to compare the overall performance of the proposed controller, the control criteria are also summarized in Table 4.7. It can be concluded that the generated power, in comparison to Table 4.1, has increased about 1.24% while the total induced torsional angle is still of very small magnitude.
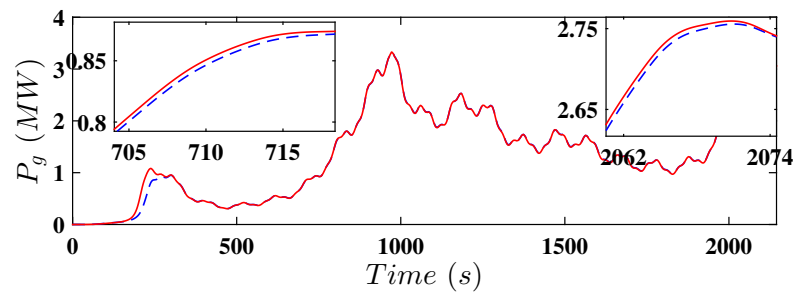
FIGURE 4.17: Comparison between performances of improved (red line) and baseline (blue line) partial load controllers.

Now, to consider the applicability of the proposed controller, a real measured wind speed (Odgaard et al., 2015), shown in Figure 4.18, is used as a disturbance on the nonlinear model of the wind turbine. The results of baseline partial load controller 4.7 and improved one are summarized in Table 4.8.
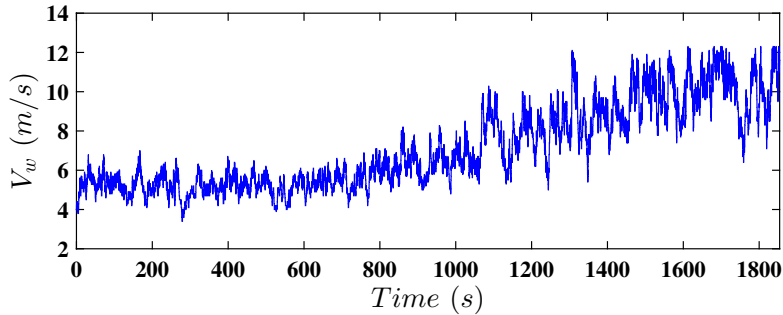
FIGURE 4.18: Real Wind speed profile (Odgaard et al., 2015).

It is obvious that with the improved controller, for the real wind speed, the extracted energy is increased about 1.14% with a consequential 6% increase in total drive train stress. These results show the effectiveness of using the fuzzy logic method to increase the extracted energy and drive train stress in partial load operation.

In this section the baseline partial load controller has been improved using FIS and the performance of both controllers have been compared. In this next, the baseline PID full load controller is improved.

4.4 Improvement of Full Load Baseline Controller

In this section, the baseline full load controller is improved to precisely regulate pitch angle and maintaining the nominal rotor speed, in the presence of wind speed variation and to attenuate model uncertainty, disturbance, and pitch actuator faults. It is aimed to utilize the PID baseline full load controller structure with automatic adaptive gain tuning. Nussbaum type functions were augmented in the adaptive laws to take the unknown control direction into consideration. Finally, stability of the wind turbine model augmented with the proposed controller in the presence of wind speed variation is proved analytically.[2] It should be noted that the proposed controller in this section can be seen as passive FTC. However, the active one will be proposed in Chapter 6. Considering the wind turbine operation, as stated in Chapter 3, it is desirable to keep the drive train torsion angle variation $\dot{\theta}_\Delta$ as close as possible to zero, which, consequently, leads to reduction in drive train stress. Accordingly, $\dot{\theta}_\Delta = 0$ leads to $N_g \omega_r = \omega_g$. So, it is desirable to keep the rotor and generator speeds proportional at the drive train ratio (Tiwari et al., 2016). On the other hand, as generator speed is aimed to be maintained at $\omega_{g,N}$, rotor speed is to be maintained

---

[2]This section is captured and reorganized from the paper "Adaptive PID Control of Wind Turbines for Power Regulation with Unknown Control Direction and Actuator Faults". The authors' attribution on this paper are given in Appendix C.

at $\omega_{g,N}/N_g$ (Boukhezzar et al., 2011). Considering $\dot{\theta}_\Delta = 0$ with zero initial drive train torsion angle, leads to $\theta_\Delta = 0$ as the reduced drive train stress trajectory.

The desirable operational mode of the wind turbine operating at the desired trajectory with reduced drive train stress is as ,

$$\begin{aligned}
\dot{\omega}_r &= a_1\omega_r + a_2\omega_g + a_3T_a, \\
\dot{\omega}_g &= b_1\omega_r + b_2\omega_g + b_3T_g,
\end{aligned} \tag{4.14}$$

where, $a_1 = -(B_{dt} + B_r)/J_r$, $a_2 = B_{dt}/N_gJ_r$, $a_3 = 1/J_r$, $b_1 = \eta_{dt}B_{dt}/N_gJ_g$, $b_2 = \left(-\eta_{dt}B_{dt}/N_g{}^2 - B_g\right)/J_g$, $b_3 = -1/J_g$. Accordingly,

$$\dddot{\omega}_r = c_1\omega_r + c_2\omega_g + c_3T_a + c_4T_g + a_3\dot{T}_a, \tag{4.15}$$

where, $c_1 = a_1{}^2 + a_2b_1$, $c_2 = a_1a_2 + a_2b_2$, $c_3 = a_1a_3$, $c_4 = a_2b_3$, forms the combined rotor dynamic behaviour. Considering (4.15), it is obvious that the rotor speed and generator speed, are controlled by regulation of the pitch angle and consequent aerodynamic torque. Also, T_a is a non-affine function of pitch angle (Jafarnejadsani et al., 2013). One obvious solution is model linearization, which leads to model inaccuracies. So, this problem is solved in this research by utilizing the mean value theorem. As stated earlier, T_a is not a singular function for any triple pair (V_r, ω_r, β) in the operational range of the wind turbine. So, according to the mean value theorem, for any given pair of (V_r, ω_r), there exists $\Xi \in [0, 1]$ such that,

$$T_a\left(V_r, \omega_r, \beta\right) = T_a\left(V_r, \omega_r, \beta^*\right) + \left(\beta - \beta^*\right) \left.\frac{\partial T_a}{\partial \beta}\right|_{(V_r, \omega_r, \beta_k)}, \tag{4.16}$$

where, $\beta_k = \Xi\beta + (1 - \Xi)\beta^*$.

Assumption 4.1. *In this section, it is assumed that the blade aerodynamic characteristics are not varied due to the environmental effect such as debris, ice or dust on the blades. So, $T_a\left(V_r, \omega_r, \beta^*\right)$ and β^* for any given pair (V_r, ω_r), are constant through time. Also, in the case of any potential change, it would be very slow which lies within the yearly scheduled maintenance procedure of the wind turbine and then its effects will be removed soon enough before the occurrence of any significant change. This change will be considered in Chapter 6.*

Remark 4.2. *In Figure 4.6, it is obvious that $-L \leq \partial T_a/\partial \beta \leq -U < 0$, where, $0 < U < L$, which implies that, as wind speed increases, with increasing pitch angle, the aerodynamic torque will decrease, to prevent the rotor from over speeding.*

Considering Assumption 4.1, the time derivative of (4.16) leads to,

$$\dot{T}_a\left(V_w,\ \omega_r,\ \beta\right) = \dot{\beta}\frac{\partial T_a}{\partial \beta} = \dot{\beta}\ T_a)_\beta. \tag{4.17}$$

Now, replacing (4.17) into (4.15), one can obtain,

$$\dddot{\omega}_r = c_1\omega_r + c_2\omega_g + c_3T_a + c_4T_g + a_3\dot{\beta}\ T_a)_\beta. \tag{4.18}$$

Consider pitch actuator dynamic response with dynamic change and actuator fault (3.27). In this section, the wind turbine dynamic states of interest are the vector $x_1 = [\omega_r, \omega_g, \beta, T_g]^T$. Using (4.18) and (3.27) leads to,

$$\dddot{\omega}_r = F(x_1,t) + G(x_1,t)\left(\rho\left(t\right)\beta_{ref} + \Phi\left(t\right)\right) + D(x_1,t) \tag{4.19}$$

where, $F = c_1\omega_r + c_2\omega_g + c_3T_a + c_4T_g - \omega_{n,N}a_3T_a)_\beta\beta/2\xi_N - a_3T_a)_\beta\ddot{\beta}/2\omega_{n,N}\xi_N$, $G = \omega_{n,N}a_3T_a)_\beta/2\xi_N$ and $D = a_3T_a)\Delta\tilde{f}_{PAD}/2\omega_{n,N}\xi_N$.

It is important to be mentioned that in (4.19), the control direction of G is an unknown function, due to existence of $T_a)_\beta$ which depends on wind speed. So, this issue motivates use of the Nussbaum function, which is a well-known tool to cope with unknown control direction issues. F is not completely known, because of the existence of the $T_a)_\beta$ term and noise contents of variable measurements which appear in F. Finally, D is the unknown pitch actuator model uncertainty.

Remark 4.3. *Considering Figure 4.6 and Remark 4.2, it is obvious that $G = \omega_{n,N}a_3T_a)_\beta/2\xi_N$ takes value in $-\omega_{n,N}a_3L/2\xi_N \leq G \leq -\omega_{n,N}a_3U/2\xi_N$ and also $G \neq 0$ for any triple pair (V_r, ω_r, β).*

Assumption 4.2. *Considering the bounded achievable pitch angle and it is allowable variation rate 3.22, it is assumed $|\Phi| \leq \bar{\Phi} \leq \infty$, $|\dot{\rho}| \leq C_{\dot{\rho}} \leq \infty$ and $|\dot{\Phi}| \leq C_{\dot{\Phi}} \leq \infty$, where $\bar{\Phi}$, $C_{\dot{\rho}}$ and $C_{\dot{\Phi}}$ are positive unknown constants (Song et al., 2017).*

Assumption 4.3. *Considering information extraction from system nonlinearities (Song et al., 2016), there is an unknown non-negative constant a_f and computable non-negative function $\varphi_f(x_1)$ such that it satisfies $|F(x_1,t) + \Phi(t)G(x_1,t) + D(x_1,t)| \leq a_f\varphi_f(x_1)$ (Song et al., 2017).*

Now, to construct the proposed controller, the rotor tracking error and its first-time derivative are defined as,

$$\begin{aligned} e_{\omega_r}(t) &= \omega_{r,s}(t) - \omega_{r,N}, \\ \dot{e}_{\omega_r}(t) &= \dot{\omega}_{r,s}(t) - \dot{\omega}_{r,N}. \end{aligned} \tag{4.20}$$

As the nominal values of the wind turbine are assumed constant, so, $\dot{\omega}_{r,N} = 0$. Taking the second time derivative of e_{ω_r}, takes the combined rotor dynamic response (4.19) into consideration, as,

$$\ddot{e}_{\omega_r} = F + G(\rho\beta_{ref} + \Phi) + D. \tag{4.21}$$

To proceed, the tracking error filter is defined as,

$$Z\left(t\right) = 2\lambda_1 e_{\omega_r}(t) + \lambda_1^2 \int_0^t e_{\omega_r}\left(\tau\right) d\tau + \dot{e}_{\omega_r}(t), \tag{4.22}$$

where, λ_1 is a positive design parameter such that the transfer function $s^2 + 2\lambda_1 s + \lambda_1^2$ is Hurwitz. Considering (4.21) and (4.22), it can be easily shown that,

$$\dot{Z} = H(x_1, t) + B\left(x_1, t\right)\beta_{ref}, \tag{4.23}$$

where, $B\left(x_1, t\right) = \rho\left(t\right)G\left(x_1, t\right)$ and $H\left(x_1, t\right) = 2\lambda_1\dot{e}_{\omega_r}(t) + \lambda_1^2 e_{\omega_r}(t) + F\left(x_1, t\right) + \Phi\left(t\right)G\left(x_1, t\right) + D\left(x_1, t\right) + \lambda_1^2\nu_{\omega_r} + 2\lambda_1\nu_{\dot{\omega}_r}$.

Assumption 4.4. *In this section the measurement noise on the variable of Y, i.e. ν_Y, is considered bounded by an unknown bound $\bar{d}_Y$, which is a practical assumption (Tabatabaeipour et al., 2012).*

Now, considering Assumptions 4.3 and 4.4, H is upper bounded as,

$$|H| = 2\lambda_1|\dot{e}_{\omega_r}| + \lambda_1^2|e_{\omega_r}| + a_f\varphi_f(x_1) + \lambda_1^2\bar{d}_{\omega_r} + 2\lambda_1\bar{d}_{\dot{\omega}_r} \le a\varphi(x_1), \tag{4.24}$$

where, $a = \max\{a_f, 2\lambda_1, \lambda_1^2, \lambda_1^2\bar{d}_{\omega_r}, 2\lambda_1\bar{d}_{\dot{\omega}_r}\}$ is an unknown positive constant and $\varphi\left(x_1\right) = \varphi_f\left(x_1\right) + |\dot{e}_{\omega_r}| + |e_{\omega_r}| + 1$. It should be noted $\varphi\left(x_1\right)$ is called a core-function and is a computable scalar function (Song et al., 2017).

It can be proved that boundedness of Z leads to boundedness of e_{ω_r}, $\int_0^t e_{\omega_r}\left(\tau\right) d\tau$ and $\dot{e}_{\omega_r}$. So, the controller is designed to ensure Z is Uniformly Ultimately Bounded (UUB) (Khalil, 1996). In this regard, the following definitions and lemma are stated, on which basis the controller is proposed, and its stability is proved.

Definition 4.1. *The solution of a system $x(t)$ is UUB if, there exists a number $T\left(K, x\left(t_0\right)\right)$, and a $K > 0$ such that for any compact set $\mathcal{S}$ and all $x\left(t_0\right) \in \mathcal{S}$, $||x(t)|| \le K$, for all $t \ge t_0 + T$.*

Definition 4.2. *Any smooth continuous even function $N\left(\xi\left(t\right)\right)$ is called a Nussbaum type function, if $\lim_{r\to\infty}\sup\frac{1}{r}\int_0^r N\left(\xi\right)d\xi = +\infty$ and $\lim_{r\to\infty}\inf\frac{1}{r}\int_0^r N\left(\xi\right)d\xi = -\infty$ (Song et al., 2017).*

Lemma 4.1. *Assume $V(t) > 0$ and $\xi(t)$ are smooth defined functions defined on the time interval $[0\ t_f)$. Also, $N(\xi(t))$ is a selected Nussbaum type function. Then, for any $t \in [0\ t_f)$, if $V(t) < c_0 + e^{-c_1 t} \int_0^t (g(\tau) N(\xi(\tau)) + 1) \dot{\xi} e^{c_1 \tau} d\tau$ holds true, where c_0 and c_1 are positive constants, and $g(\tau)$ represents a time-varying parameter, which takes values in the unknown closed intervals $L \in [l^+,\ l^-]$ with $0 \notin L$, then $V(t)$, $\xi(t)$ and $\int_0^t g(\tau) N(\xi(\tau)) \dot{\xi} e^{c_1 \tau}$ must be bounded on $[0\ t_f)$ (Song et al., 2017).*

Now, considering (4.23), a PID-like pitch angle controller is proposed as,

$$\beta_{ref} = (\lambda_{D_0} + \lambda_D) N(\xi) Z(t), \tag{4.25}$$

where, λ_{D_0} is a positive design parameter, with the following adaptive laws,

$$\begin{aligned}
\lambda_D &= \hat{a}\varphi^2, \\
\dot{\xi} &= (\lambda_{D_0} + \lambda_D) Z^2, \\
\dot{\hat{a}} &= -\sigma_0 \hat{a} + \sigma_1 \varphi^2 Z^2,
\end{aligned} \tag{4.26}$$

where, σ_0 and σ_1 are positive design parameters, and $\hat{a}$ is an estimation of a.

Remark 4.4. *The proposed controller (4.25) can be seen as a combination of two parts, i.e. $Z(t)$ and $(\lambda_{D_0} + \lambda_D) N(\xi)$. Considering (4.22), it is obvious that $Z(t)$ is a PID-like filter of the tracking error and on the other hand, $(\lambda_{D_0} + \lambda_D) N(\xi)$ is auto-updating the gains of $Z(t)$. This is the reason the proposed controller is called a PID-like controller.*

The stability of the wind turbine model using the proposed controller (4.25) is proved via the following theorem.

Theorem 4.1. *Consider the combined rotor dynamic behaviour (4.18), including the presence of a pitch actuator fault and uncertainty. Under Assumptions 4.1-4.4 and the unmeasured wind speed variation, using the proposed pitch angle controller (4.25) with adaptive law (4.26), then,*

(i) Pitch angle controller signal is smooth everywhere,

(ii) All the internal signals are UUB

(iii) The rated rotor speed tracking error is guaranteed to be UUB

The proof of this theorem is given in A.1.

Now, the modified baseline full load controller (4.25) is evaluated via numerical simulations and also, the results are compared to those from the baseline full

load controller (4.10) to demonstrate the performance advantages of the proposed controller with both fault-free and faulty situations.

Although it has been proposed to filter the generator sensor, before feeding it into the baseline controller (4.10) to remove noise content and avoid amplification of noise via controller gain, however, it is obvious that, in the structure of the controller (4.10), the sensor noise $\omega_{g,s}$ is not necessarily attenuated and may be amplified. Also, the pitch actuator uncertainty, i.e. $\Delta \tilde{f}_{PAD}$, is not analytically attenuated in this controller. On the other hand, any possible loss of effectiveness or bias, i.e. $\rho(t)$ and $\Phi(t)$ in (3.27), is not assured to be accommodated. So, it is aimed to improve the baseline full load controller, which has industrial acceptability, to satisfy the desired performance despite the presence of disturbances, uncertainties and faults. This motivates the development of the proposed controller (4.25).

Considering the adaptive laws (4.26), and inequality (4.24), the function φ_f should be selected appropriately. In this regard, considering (4.19) and Assumption 4.3, the φ_f is selected as,

$$
\begin{aligned}
\varphi_f = {} & |c_1 \omega_r| + |c_2 \omega_g| + c_3 \left(\frac{N_g T_{g,max}}{\eta_{dt}} \right) + |c_4 T_g| + \left| \frac{\omega_{n,N} a_3 U \beta}{2 \xi_N} \right| + \\
& \left| \frac{a_3 U \ddot{\beta}}{2 \omega_{n,N} \xi_N} \right| + \left| \frac{\omega_{n,N} a_3 U}{2 \xi_N} \right| + \left| \frac{a_3 U \Delta \left(\tilde{\omega}_n \tilde{\xi} \right) \dot{\beta}}{\omega_{n,N} \xi_N} \right| + \\
& \left| \frac{a_3 U \Delta (\tilde{\omega}_n^2) \left(\beta_{max} - \beta_{min} \right)}{2 \omega_{n,N} \xi_N} \right|,
\end{aligned}
\tag{4.27}
$$

which is obviously a computable scalar function, as a part of the controller structure. Also, in Assumption 4.3, $a_f = max\{1, \Phi, \alpha_{f_1}, \alpha_{f_2}\}$, which is unknown and estimated, considering (4.24) and (4.26). On the other hand, the Nussbaum type function, used in (4.25), is selected as,

$$
N(\xi) = \xi^2 \cos(\xi),
\tag{4.28}
$$

which satisfies Definition 4.2 conditions.

Firstly, the performance of both controllers in normal situations, i.e. without pitch actuator effectiveness loss, bias or dynamic change, are carried out. Then, for each mentioned situation, the wind turbine operation is studied and also, the performance criteria are compared.

The performance of the wind turbine in normal actuation situations using the baseline and improved controllers, under wind speed profile Figure 4.9 are demonstrated and compared in Figures 4.19-4.22. Faults and uncertainty in the pitch actuator are considered as, $\alpha_{f_1} = \alpha_{f_2} = 0$ and consequently $\Delta \tilde{f}_{PAD} = 0$. Also, $\rho = 1$ and

$\Phi = 0$. The numerical performance criteria are summarized in Table 4.9. The first three criteria are significantly decreased compared to the baseline controller, which demonstrates better nominal generator speed and nominal power tracking performance. This result is obvious in Figures 4.19 and 4.20. Also, considering Figure 4.22, the induced drive train torsion angles are similar using both controllers. On the other hand, considering Figure 4.21, which shows the pitch variation using the improved controller, i.e. last two criteria, is increased, which is expected.
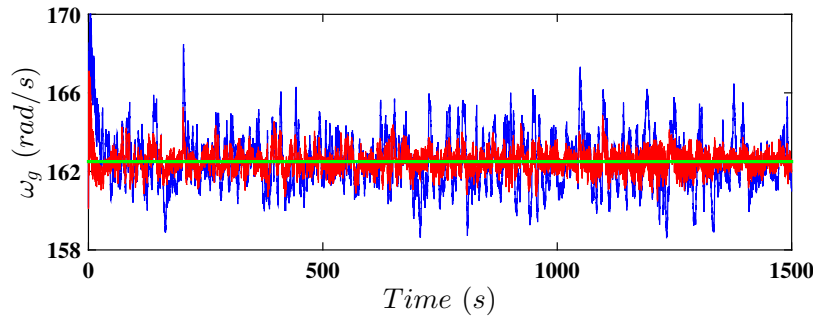
FIGURE 4.19: Generator speed in full load operation using baseline controller (blue line) and improved one (red line), and nominal generator speed (green line).
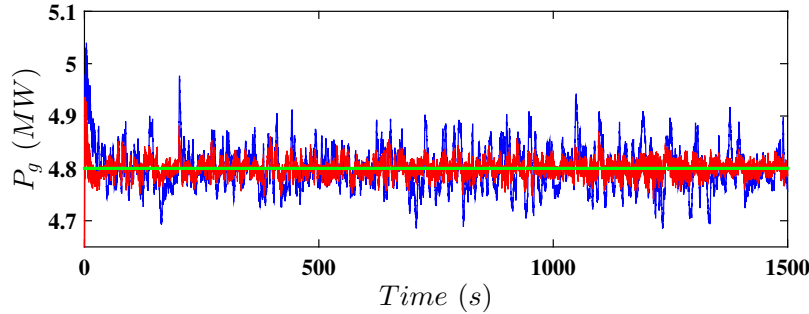
FIGURE 4.20: Generated power in full load operation using baseline controller (blue line) and improved one (red line), and nominal generator speed (green line).

Now, under different pitch actuator faults and dynamic changes, the performance of the wind turbine using both controllers are considered. It should be noted that, to study the effect of each fault accurately, the pitch actuator faults and dynamic changes are considered separately. The pitch actuator bias and effectiveness loss are applied as,

$$\begin{cases} \Phi = 15°, & 200\,(s) \leq t \leq 600(s), \\ \rho = 0.6, & 900\,(s) \leq t \leq 1300(s). \end{cases} \tag{4.29}$$

The generator speed for different time periods, mentioned in (4.29), using the baseline and improved controllers are shown in Figures 4.23-4.26. In Figure 4.23, the
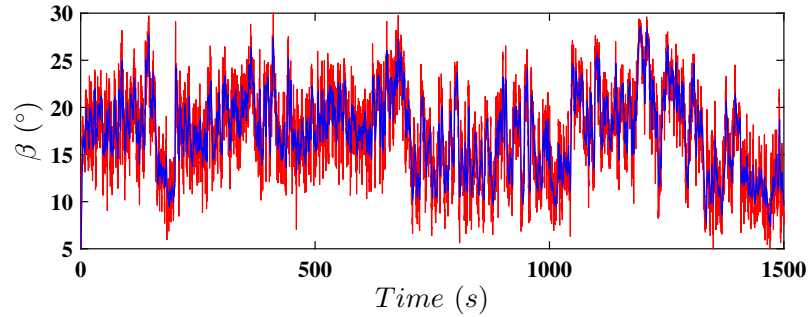
FIGURE 4.21: Pitch angle using baseline controller (blue line) and improved one (red line).
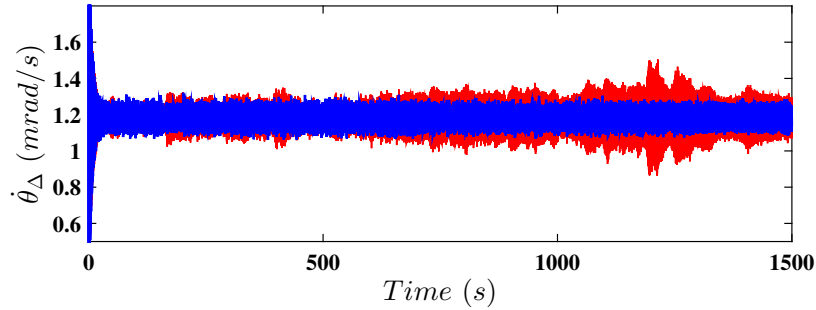
FIGURE 4.22: Drive train torsion angle using baseline controller (blue line) and improved one (red line).

generator speed using the baseline controller in the normal situation and for the pitch bias case, are compared. It is obvious that the pitch bias deviates the generator speed from the nominal one, more so than the normal case. Indeed, the baseline controller is not able to remove the pitch bias effect and operate the same as the normal situation. The same result can be obtained considering Figure 4.24, in which the effective loss of the pitch actuator is applied. Comparing Figure 4.23 and 4.24, it can be seen that the effectiveness loss effect is more severe than the pitch bias. In Figures 4.25 and 4.26, the corresponding improved controller results are illustrated, in which the generator speed with pitch bias and effectiveness loss is obviously kept the same level as the normal one. Also, comparing Figures 4.23 and 4.25 implies that the improved controller, in the pitch bias case, is operating more satisfactorily than the baseline controller. A similar result is obtained by comparing Figures 4.24 and 4.26, in the effectiveness loss case. To verify this outcome, the performance criteria are summarized in Table 4.10.

Now, the effects of the dynamic change in the pitch actuator are considered. To this end, the dynamic changes are applied as,

TABLE 4.9: Performance criteria in normal situation in full load
operation using baseline controller and improved one

Performance criteria	Improved controller	Baseline controller
$CC1$	620.1 $(GW^2 s)$	2819 $(GW^2 s)$
$CC2$	2.110 $(mrad^2/s)$	2.103 $(mrad^2/s)$
$CC3$	270.1 (rad^2/s)	2967 (rad^2/s)
$CC4$	0.0517 (MW)	0.1437 (MW)
$CC6$	29.05 $(°)$	28.42 $(°)$
$CC8$	9.95 $(°/s)$	8.53 $(°/s)$

TABLE 4.10: Performance criteria in pitch bias and effectiveness
loss in full load operation using baseline controller and improved
one

Performance criteria	Improved controller	Baseline controller
$CC1$	643.5 $(GW^2 s)$	4304 $(GW^2 s)$
$CC2$	2.112 $(mrad^2/s)$	2.105 $(mrad^2/s)$
$CC3$	274.8 (rad^2/s)	4669 (rad^2/s)
$CC4$	0.0776 (MW)	0.2087 (MW)
$CC6$	29.45 $(°)$	28.34 $(°)$
$CC8$	10 $(°/s)$	9.05 $(°/s)$
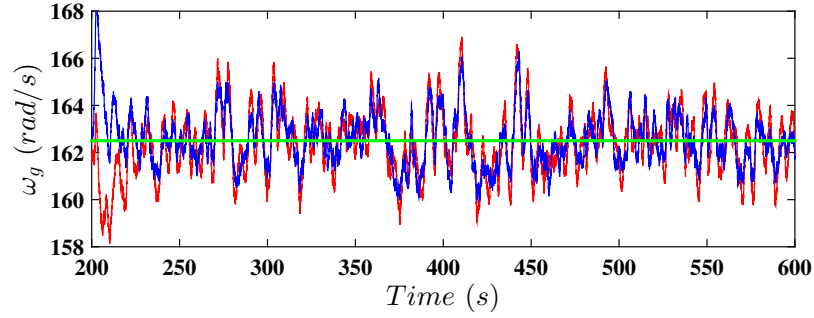
FIGURE 4.23: Generator speed using baseline controller in normal actuation case (blue line) and pitch actuator bias case (red line), and rated generator speed (green line).
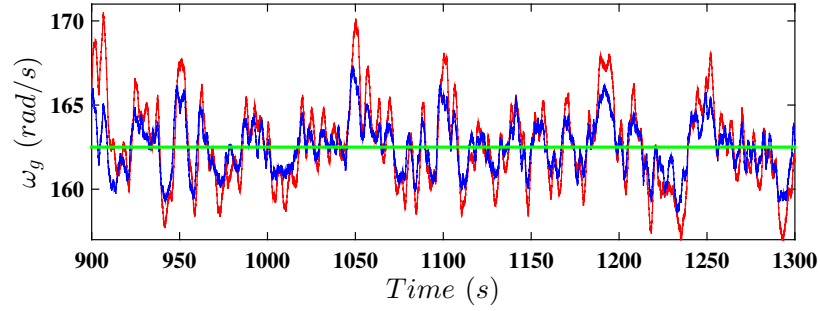
FIGURE 4.24: Generator speed using baseline controller in normal actuation case (blue line) and effectiveness loss case (red line), and rated generator speed (green line).

$$\begin{cases} Pump\ wear, & 400\,(s) \leq t \leq 600(s), \\ Hydraulic\ leak, & 700\,(s) \leq t \leq 900(s), \\ High\ air\ content, & 1000\,(s) \leq t \leq 1200(s). \end{cases} \tag{4.30}$$

Considering Figure 3.8, it is obvious that all the dynamic changes make the pitch actuator about one second slower. This slower time is not obvious in the time span of numerical simulation. So, the difference of the pitch angle between the fault-free case and the pitch angle in the dynamic change case, is considered as the indicator to accurately study the dynamic change effects, defined as,

$$\Delta\beta = \beta_{dc} - \beta_{normal}, \tag{4.31}$$

where, β_{dc} represents the pitch angle in the dynamic change case, using the given controller and β_{normal} is the pitch angle in the normal situation using the same controller. Obviously, as long as this indicator is closer to zero, it means that the considered controller is able to compensate for the dynamic change effects and keep
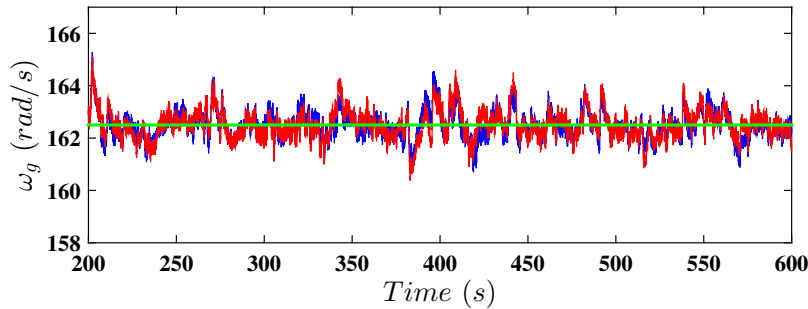
FIGURE 4.25: Generator speed using improved controller in normal actuation case (blue line) and pitch actuator bias case (red line), and rated generator speed (green line).
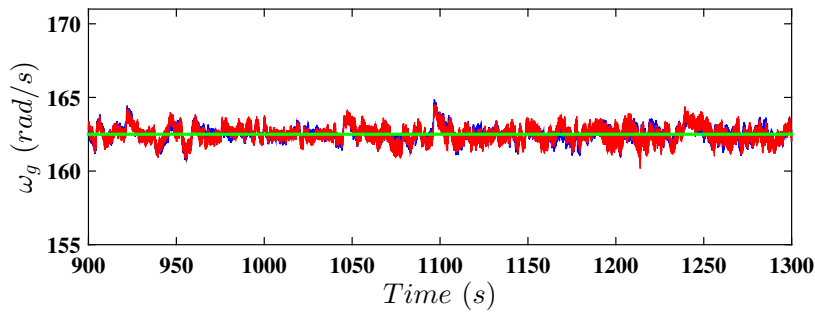
FIGURE 4.26: Generator speed using improved controller in normal actuation case (blue line) and effectiveness loss case (red line), and rated generator speed (green line).

the pitch angle close to the corresponding one in the normal situation. The pitch angle difference using both controllers, with and without the above mentioned dynamic changes (4.31), are demonstrated in Figures 4.27-4.29. It is obvious in each dynamic change case that the pitch difference is closer to zero using the proposed controller than the baseline controller. This means that the proposed controller is able to compensate for the dynamic change in the pitch actuator satisfactorily. Finally, the performance criteria are summarized in Table 4.11, which confirms the aforementioned results, numerically.

In this chapter the baseline controllers of wind turbine operating in both partial and full load regions have been investigated. The performance of the baseline controllers has been considered and, accordingly, the improvements have been developed. In the partial load region, a FIS has been designed to adjust the baseline controller gain based on generator speed variation. The baseline controller augmented with the FIS captured more power compared to the baseline controller. In the full load region, the baseline controller has been improved using adaptive gains to accommodate pitch actuator faults. Also, using the Nussbaum type function, the
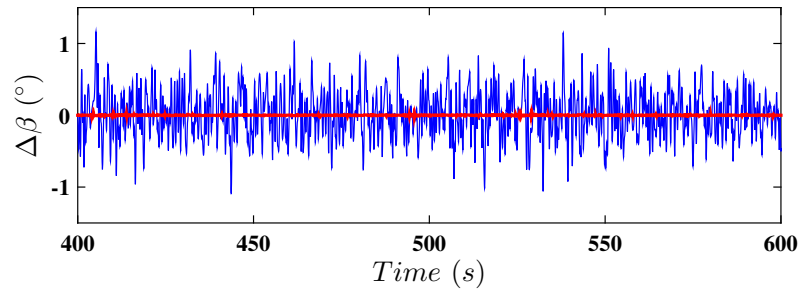
FIGURE 4.27: Pitch angle difference using baseline controller (blue line) and improved one (red line) in pump wear case.
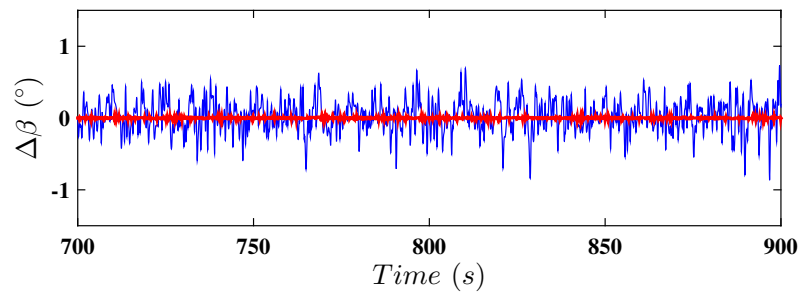
FIGURE 4.28: Pitch angle difference using baseline controller (blue line) and improved one (red line) in hydraulic leak case.

unknown controller problem has been solved. The numerical simulation confirmed that the improved baseline controller was able to handle pitch actuator dynamic change, effectiveness loss and additive bias. It should be noted that, the improved baseline controller partial load is obviously not tolerant against generator actuator faults as well as generator sensor faults. So, in Chapter 5, a new FTC controller is proposed to be tolerant against the generator actuator faults. On the other hand, in Chapter 7, a FDI scheme is proposed to detect and isolate the sensor faults, which can be used alongside the baseline controller. In addition, even though the improved baseline controller full load is able to remove pitch actuator faults, but no fault information is gathered via this controller. In this regard, a new FTC controller is proposed in Chapter 6.
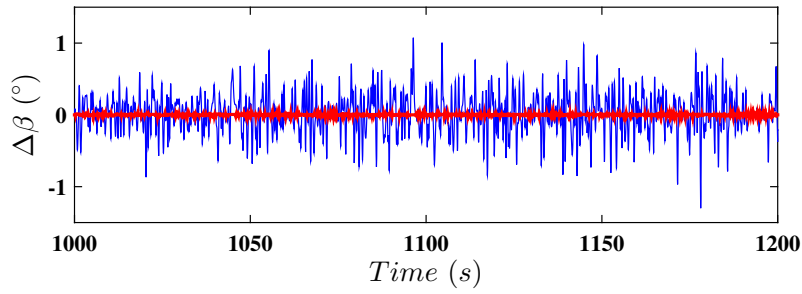
FIGURE 4.29: Pitch angle difference using baseline controller (blue
line) and improved one (red line) in high air content case.

TABLE 4.11: Performance criteria in pitch actuator dynamic change
case in full load operation using baseline controller and improved
one

Performance criteria	Improved controller	Baseline controller
$CC1$	634.8 (GW^2s)	2955 (GW^2s)
$CC2$	2.103 $(mrad^2/s)$	2.103 $(mrad^2/s)$
$CC3$	272.1 (rad^2/s)	3257 (rad^2/s)
$CC4$	0.0714 (MW)	0.1720 (MW)
$CC6$	29.18 $(°)$	28.51 $(°)$
$CC8$	10 $(°/s)$	9.01 $(°/s)$

5 Optimum Efficiency Control with Unknown Desired Trajectory and Actuator Faults

A nonlinear controller is proposed in this chapter to make the wind turbine operate effectively despite the presence of the actuator faults, similar to the fault-free case in partial load operation.[1] The considered actuator faults are pitch and generator actuator biases as well as pitch actuator dynamic change, including, pump wear, hydraulic leakage and high air content in the oil. Also, the wind speed is assumed as an unmeasurable disturbance, and accordingly using GRBFNN, the unknown desired trajectory is reconstructed, so that the captured power is maximized. The proposed controller is shown to be able to keep the wind turbine tracking the reconstructed desired trajectory with sufficient accuracy. Using Lyapunov analysis, the boundedness of the closed-loop system with the proposed controller, is proved. The designed controller is verified via numerical simulations. In comparison with the baseline industrial controller (4.7) results, the effectiveness of the proposed controller is evaluated. It should be noted that the values of controller parameters are given in Section B.3.

Considering the generated power, i.e. $P_a = P_w.C_p\left(\beta, \lambda\right)$ and that the effective wind speed V_r is considered as a disturbance, it can be concluded that if the power coefficient, C_p, is maximized, it will lead to harvesting the most available power from the wind. According to Figure 3.2, it can be seen that $C_{p,max} = 0.48$ which is at $\beta_{opt} = 0$ and $\lambda_{opt} = 8.1$. On the other hand, to keep the power coefficient at its maximum value, the TSR, λ, should be kept at $\lambda_{opt} = 8.1$. Considering $\lambda = R\omega_r/V_r$, the desired rotor speed, i.e. $\omega_{r,desired}$, can be stated as a function of wind speed as, $\omega_{r,desired} = \lambda_{opt}V_r/R$. Considering the presence of V_r in $\omega_{r,desired}$, it is obvious that the desired trajectory is not available. So in this chapter it is reconstructed utilizing GRBFNN. To fulfill the control objective, the load generator torque, $T_{g,ref}$, is controlled such that, via the drive train dynamics, the rotor speed tracks $\omega_{r,desired}$.

---

[1]This chapter is captured and reorganized from the papers "Optimum efficiency control of a wind turbine with unknown desired trajectory and actuator faults", "Power maximization of variable-speed variable-pitch wind turbines using passive adaptive neural fault tolerant control", and "A neuro-adaptive maximum power tracking control of variable speed wind turbines with actuator faults". The authors' attribution on these papers are given in Appendix C.

There may be an operational scheme where the pitch actuator is not active in the partial load operation and the pitch angle has to be fixed at the optimal value, i.e $\beta_{opt} = 0°$, e.g. (4.7) and (4.12). Consequently, there is no need for the pitch controller to be designed. In this regard, it should be noted that the wind speed is a randomly varying disturbance and it cannot be guaranteed that the wind turbine is only operating in the partial load region. The wind turbine operational region can rapidly and continuously vary from the partial to full load region and vice versa. So, it is important to guarantee, regardless of the operation region, that the pitch actuator follows the desired pitch angle accurately, whose dynamic behavior might have changed. Also, due to this excessive operational range variation, a pitch bias may be added into the pitch actuator. So, it is aimed to propose a controller such that, despite the presence of pitch actuator faults, it keeps the pitch angle at the requested value, which is either zero in the partial load region or should be tuned in the full load region, in which a simple industrial PID controller, i.e. (4.10) can be implemented, as studied in Section 4.2. In fact, the proposed pitch controller is readily designed to be used in the full load region, as an extension of this chapter, and so just the desired pitch angle should be constructed, separately.

Now, some technical lemmas are introduced to be used in considering the stability of the proposed controller.

Lemma 5.1. *The state vector of a dynamic system x is UUB for bounded initial condition if there exists a positive definite Lyapunov function $V(x,t)$ satisfying $a_1(\|x\|) \leq V(x,t) \leq a_2(\|x\|)$, such that $dV/dt < -b_1V + b_2$ where b_1 and b_2 are positive constants and a_1 and a_2 are class K-functions. As the time goes by, $V(x,t)$ stays in the set $\Omega = \{V|V \leq b_2/b_1\}$.*

The proof of this lemma is given in A.2.

Lemma 5.2. *Define variable $\tilde{a}$, as $\tilde{a} = \hat{a} - a$, then $-2\sigma_d\tilde{a}\hat{a} \leq -\sigma_d\tilde{a}^2 + \sigma_d a^2$ holds true for any positive constant σ_d.*

The proof of this lemma is given in A.3.

Lemma 5.3. $0 \leq |\xi| - \xi^2/\sqrt{\xi^2 + \gamma^2} < \gamma$ *holds true, for any variable ξ and positive constant γ.*

The proof of this lemma is given in A.4.

In the next section the unknown desired trajectory is constructed via implementing the GRBFNN technique.

5.1 Unknown Desired Trajectory Construction

In this section, the unknown desired trajectory is reconstructed using GRBFNN on which basis, then, the generator torque controller is designed.

As stated earlier, the effective wind speed at the rotor plane, V_r, is not measurable accurately using the anemometer placed at the top of the nacelle, and meanwhile the desired rotor speed, to capture the most possible energy, is stated in terms of wind speed as,

$$\omega_{r,desired} = \frac{\lambda_{opt} V_r}{R},$$
$$\omega_{g,desired} = N_g \omega_{r,desired}. \tag{5.1}$$

So, the desired trajectory is not known a priori. Accordingly, in this section, exploiting the universal approximation capabilities of GRBFNN, the desired trajectory is reconstructed (Song et al., 2017). Considering well-developed approximation theory, the approximated desired trajectory, $\omega_{g,d}^*$ is expressed as a continuous function as,

$$\omega_{g,d}^* = \Psi^{*T}(t)\varphi(t) + \varrho(t), \tag{5.2}$$

where, $\Psi^*, \varphi \in \mathbb{R}^{\varpi \times 1}$ and $\varrho \in \mathbb{R}$ are unknown time varying optimal weights, known basis bounded functions and unknown approximation error, respectively. Also, ϖ is the number of neurons in the neural network. Because Ψ^* and ϱ are unknown, it is obvious that $\omega_{g,d}^*$ is still not utilizable in the controller design procedure. So, the approximated desired trajectory, $\hat{\omega}_{g,d}$, is computed as,

$$\hat{\omega}_{g,d} = \hat{\Psi}^T(t)\varphi(t), \tag{5.3}$$

where, $\hat{\Psi}$ is the estimation of Ψ^* with the estimation error as, $\tilde{\Psi} = \Psi^* - \hat{\Psi}$.

Assumption 5.1. *It is assumed that* $|\varrho| \leq \varrho_1$, $|\dot{\varrho}| \leq \varrho_2$, $\Psi^* \leq \psi_1$ *and* $\dot{\Psi}^* \leq \psi_2$ *where* $0 < \varrho_1, \varrho_2, \psi_1, \psi_2 < \infty$ *are unknown constants (Song et al., 2017), and* $\|\|$ *denotes the Euclidean norm operator for vectors.*

The tracking error and its time derivative, which will be used in the next section to design the generator controller, are defined as, $e_{\omega_g} = \hat{\omega}_{g,d} - \omega_{g,s}$ and $\dot{e}_{\omega_g} = \dot{\hat{\omega}}_{g,d} - \dot{\omega}_{g,s}$, where $\omega_{g,s}$ and $\dot{\omega}_{g,s}$ are the measured generator speed and its derivative sensors, respectively. Also, $\dot{\hat{\omega}}_{g,d}$ is obtained considering (5.3) as,

$$\dot{\hat{\omega}}_{g,d} = \dot{\hat{\Psi}}^T(t)\varphi(t) + \hat{\Psi}^T(t)\dot{\varphi}(t). \tag{5.4}$$

Now, the adaption law for $\hat{\Psi}$ is proposed as,

$$\dot{\hat{\Psi}} = -\sigma\hat{\Psi}(t) + \Lambda\eta(e_{\omega_g}), \tag{5.5}$$

where, σ and Λ are positive design parameters, satisfying $\sigma > \Lambda + 1$, and $\eta(e_{\omega_g}) \in \mathbb{R}^{\varpi \times 1}$ is an arbitrarily selected bounded function, as $\|\eta(e_{\omega_g})\| \leq \eta_1$ where η_1 is an unknown positive constant. Considering (5.5), it can easily be shown that,

$$\ddot{\hat{\Psi}} = \sigma^2\hat{\Psi}(t) - \sigma\Lambda\eta(e_{\omega_g}) + \Lambda\dot{\eta}(e_{\omega_g}), \tag{5.6}$$

where, $\dot{\eta}(e_{\omega_g}) = (\partial\eta/\partial e_{\omega_g})\dot{e}_{\omega_g}$ and $\|\partial\eta/\partial\omega_g\|$ is bounded.

Theorem 5.1. *Considering the adaption law (5.5), $\hat{\Psi}$ and $\dot{\hat{\Psi}}$ are UUB.*

The proof of this theorem is given in A.5.

The desired trajectory construction diagram is illustrated in Figure 5.1. Now,
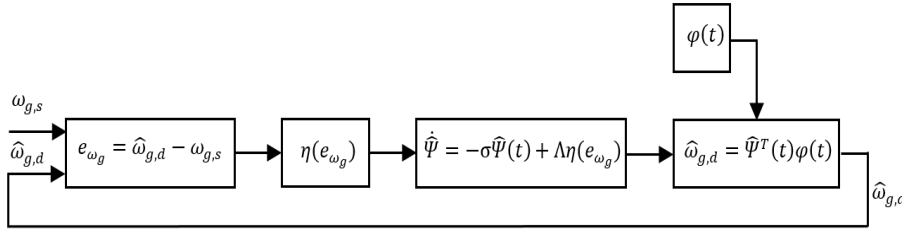
FIGURE 5.1: Desired trajectory construction.

after estimation of the unknown desired trajectory, $\hat{\omega}_{g,d}$, the exact tracking error and its time derivative, i.e. $e^*_{\omega_g}$ and $\dot{e}^*_{\omega_g}$, respectively, are defined as,

$$\begin{aligned} e^*_{\omega_g} &= \omega^*_{g,d} - \omega_{g,s}, \\ \dot{e}^*_{\omega_g} &= \dot{\omega}^*_{g,d} - \dot{\omega}_{g,s}. \end{aligned} \tag{5.7}$$

Taking $e_{\omega_g} = \hat{\omega}_{g,d} - \omega_{g,s}$ and $\dot{e}_{\omega_g} = \dot{\hat{\omega}}_{g,d} - \dot{\omega}_{g,s}$ into consideration, $e^*_{\omega_g}$ and $\dot{e}^*_{\omega_g}$ can be rewritten as,

$$\begin{aligned} e^*_{\omega_g} &= \omega^*_{g,d} - \hat{\omega}_{g,d} + e_{\omega_g} = \tilde{\Psi}^T(t)\varphi(t) + \varrho(t) + e_{\omega_g}, \\ \dot{e}^*_{\omega_g} &= \dot{\tilde{\Psi}}^T(t)\varphi(t) + \tilde{\Psi}^T(t)\dot{\varphi}(t) + \dot{\varrho}(t) + \dot{e}_{\omega_g}. \end{aligned} \tag{5.8}$$

Therefore, considering Theorem 5.1 and Assumption 5.1, it can be concluded that boundedness of e_{ω_g} and $\dot{e}_{\omega_g}$ leads to boundedness of $e^*_{\omega_g}$ and $\dot{e}^*_{\omega_g}$, respectively. So, in the next section, it is aimed to design $T_{g,ref}$ such that $\omega_{g,s}$ tracks as close as possible the estimated desired one, $\hat{\omega}_{g,d}$, such that e_{ω_g} and $\dot{e}_{\omega_g}$ are bounded.

5.2 Generator Torque Controller Design

In this section, the design of the generator torque controller, $T_{g,ref}$, to track the maximum power point, i.e. $\lambda_{opt} = 8.1$, is done based on reducing the tracking error $e_{\omega_g} = \hat{\omega}_{g,d} - \omega_{g,s}$. In order to reduce the torsional angle of twist that may lead to drive train failure, it is desired to keep the generator and rotor speed proportional to each other through the gearbox ratio, accordingly, it is advantageous that $\dot{\theta}_\Delta = 0$. So, the controller is designed on the desirable operational mode of the wind turbine in which $\omega_g = N_g \omega_r$. On this basis, considering (4.14), the second time derivative of generator speed including generator torque bias (3.29) and noises can be obtained as,

$$\dddot{\omega}_g = c_1 \omega_r + c_2 \omega_g + c_3 T_g + c_4 T_a + c_5 T_{g,ref} + d_1 + f_1, \tag{5.9}$$

where, $c_1 = b_1 a_1 + b_2 b_1$, $c_2 = b_1 a_2 + b_2{}^2$, $c_3 = b_2 b_3 - a_g b_3$, $c_4 = b_1 a_3$, $c_5 = b_3 a_g$, $d_1 = c_1 \nu_{\omega_r} + c_2 \nu_{\omega_g} + c_3 \nu_{T_{g,s}}$ and $f_1 = b_3 a_g f_{T_g}$.

Assumption 5.2. *It is assumed that the accumulative fault f_1 is bounded such that $|f_1| \leq \bar{f}_1$, where $\bar{f}_1 \in \mathbb{R}^+$ is an unknown constant (Lan et al., 2018). Indeed, taking into account the maximum possible generator torque, i.e. (3.20), it is assumed that the generator bias, i.e. f_{T_g}, is bounded, before the total failure of the generator in which case the maintenance procedure is inevitable (Sloth et al., 2011). On the other hand, the time derivative of the fault is assumed to be bounded, i.e. $|\dot{f}_1| \leq \rho_{\dot{f}_1}$ where $\rho_{\dot{f}_1} \in \mathbb{R}^+$ is an unknown constant (Lan et al., 2018). Regarding the accumulative disturbance, i.e. d_1, it is assumed that $|d_1| \leq \bar{d}_1$ where $\bar{d}_1 \in \mathbb{R}^+$ is an unknown constant which is a reasonable practical issue (Tabatabaeipour et al., 2012).*

Considering (5.9), it is obvious that the aerodynamic torque is contributing to the generator dynamic behaviour. On the other hand the wind speed is not measurable accurately, on which basis it is difficult to obtain the aerodynamic torque. Although using (5.1) and (5.3), an estimation of wind speed and, consequently, aerodynamic torque, can be reconstructed, but, in this section to avoid computational complexity, a separate aerodynamic torque estimator is implemented. So, in this chapter, the GRBFNN as a class of linearly parameterized neural networks are employed to approximate a smooth and continuous function of aerodynamic torque. In the literature on adaptive control of nonlinear systems, due to their approximation property and the learning capability, neural networks are extensively used for approximation of unknown nonlinearities.

The GRBFNN input vector is selected as, $Z = [T_g, \omega_g, \beta]^T \in \Omega_Z$ and accordingly, the aerodynamic torque is given as,

$$\begin{aligned} T_a(Z) &= \theta^{*T} h(Z) + \varepsilon, \\ T_{a,NN}(Z) &= \theta^T h(Z), \end{aligned} \tag{5.10}$$

where, $T_{a,NN}$ is a GRBFNN approximation of T_a, $\theta^* \in \mathbb{R}^s$ is an unknown optimal weight, $h(Z) = [h_1(Z), h_2(Z), ..., h_s(Z)]^T \in \mathbb{R}^s$, with $s > 1$ being the neural network node number and $h_i(Z)$ is selected as a Gaussian function given by,

$$h_i(Z) = e^{\frac{-(Z-\vartheta_i)^T(Z-\vartheta_i)}{2\varphi_{c,i}^2}}, \tag{5.11}$$

where, $\vartheta_i = [\vartheta_{i,T_g}, \vartheta_{i,\omega_g}, \vartheta_{i,\beta}]^T$ is the center of the ith input and $\varphi_c = [\varphi_{c,1}, ..., \varphi_{c,s}]^T \in \mathbb{R}^s$ is the width of the ith Gaussian function. θ^* is defined as,

$$\theta^* = argmin_{\theta \in \mathbb{R}^s}[sup_{Z \in \Omega_Z}|T_a(Z) - T_{a,NN}(Z)|], \tag{5.12}$$

and also $\varepsilon \in \mathbb{R}$ is an estimation error which is bounded with an unknown bound $\bar{\varepsilon} > 0$, such that, $|\varepsilon| \leq \bar{\varepsilon}$ (Jafarnejadsani et al., 2013).

Now, to design the generator torque controller, a backstepping technique is utilized. A positive definite Lyapunov function is chosen as,

$$V_1^{T_g} = \frac{1}{2}e_{\omega_g}^2, \tag{5.13}$$

where, its time derivative can be written as, $\dot{V}_1^{T_g} = e_{\omega_g}\dot{e}_{\omega_g}$. A variable transformation is defined as, $e_{2,\omega_g} = \alpha_{\omega_g} - \dot{\omega}_{g,s}$, where α_{ω_g} is the virtual control signal, designed as,

$$\alpha_{\omega_g} = \dot{\hat{\omega}}_{g,d} + k_{1,\omega_g}e_{\omega_g}, \tag{5.14}$$

where, k_{1,ω_g} is a positive design parameter. Also, $\dot{\hat{\omega}}_{g,d}$ is obtained using (5.5).

To reduce tracking error of generator speed, the generator torque controller is proposed as,

$$T_{g,ref} = \frac{1}{c_5}\left(g_1 - c_4\hat{T}_a - \hat{f}_1 + \frac{e_{2,\omega_g}}{\sqrt{e_{2,\omega_g}^2 + \eta_{d_1}^2}}\hat{d}_1 + k_{2,\omega_g}e_{2,\omega_g}\right), \tag{5.15}$$

where, η_{d_1} and k_{2,ω_g} are positive design parameters, and $\hat{f}_1$ and $\hat{d}_1$ are estimations of f_1 and d_1, respectively. Also, $g_1 = e_{\omega_g} + \dot{\alpha}_{\omega_g} - c_1\omega_{r,s} - c_2\omega_{g,s} - c_3T_{g,s}$, $\hat{T}_a = \hat{\theta}^T h$ and $\hat{\theta}$ is the estimated weight of θ^*. Also, the adaptive laws are defined as,

$$\dot{\hat{d}}_1 = \frac{e_{2,\omega_g}^2}{\sqrt{e_{2,\omega_g}^2 + \eta_{d_1}^2}} - \sigma_{d_1}\hat{d}_1,$$

$$\dot{\hat{\theta}} = \Gamma\left(-c_4 e_{2,\omega_g}h - \sigma_c\hat{\theta}\right), \tag{5.16}$$

$$\dot{\hat{f}}_1 = -e_{2,\omega_g} - \sigma_{f_1}\hat{f}_1,$$

$$\dot{\hat{\rho}}_{\tilde{f}_1} = -\sigma_{\tilde{f}_1}\hat{\rho}_{\tilde{f}_1},$$

where, σ_{d_1}, σ_c, σ_{f_1} and $\sigma_{\tilde{f}_1}$ are positive design parameters. $\Gamma \in \mathbb{R}^{s \times s}$ is the design matrix such that $\Gamma = \Gamma^T > 0$. NN weight and disturbance estimation errors are as,

$$
\begin{aligned}
\tilde{\theta} &= \hat{\theta} - \theta^*, \\
\tilde{d}_1 &= \hat{d}_1 - D,
\end{aligned}
\tag{5.17}
$$

respectively, where D is a positive unknown constant satisfying $0 < c_4 \bar{\varepsilon} + \bar{d}_1 \leq D$. Fault estimation error is given as,

$$
\tilde{f}_1 = \hat{f}_1 - f_1,
\tag{5.18}
$$

which is assumed to be bounded as $\left| \tilde{f}_1 \right| < \rho_{\tilde{f}_1}$ where $\rho_{\tilde{f}_1}$ is a positive unknown constant (Lan et al., 2018). So, estimation of $\rho_{\tilde{f}_1}$ is defined as $\hat{\rho}_{\tilde{f}_1}$ and its estimation error is as,

$$
\tilde{\rho}_{\tilde{f}_1} = \hat{\rho}_{\tilde{f}_1} - \rho_{\tilde{f}_1}.
\tag{5.19}
$$

The stability and boundedness of the wind turbine equipped with a generator torque controller (5.15), is considered in the following theorem.

Theorem 5.2. *Consider the wind turbine model (3.23) and the proposed generator torque controller (5.15) with adaption laws (5.16). Let the initial conditions of the drive train and generator dynamics be bounded. Then for all pitch angles, generator speed tracking error, i.e. e_{ω_g}, and its time derivative, i.e. $\dot{e}_{\omega_g}$, are UUB.*

The proof of this theorem is given in A.6.

In Figure 5.2, a schematic diagram of the proposed generator torque controller is illustrated. Note that, considering (5.15), larger controller design parameters, leads to higher drive train torsion angle and generator torque variation, which can be seen as negative effects. So, the design parameters are selected in such a way to keep the drive train torsion angle and generator torque variation at a reasonable level compared to the baseline controller values.

5.2.1 Generator torque bias estimation

Considering $f_1 = b_3 a_g f_{T_g}$, and the estimated fault in (5.16), $\hat{f}_1$, the generator bias can be obtained as,

$$
\hat{f}_{T_g} = \frac{\hat{f}_1}{b_3 a_g},
\tag{5.20}
$$

where, $\hat{f}_{T_g}$ is the estimated generator torque bias. Indeed, the benefit of the proposed controller is that the fault effect is handled and no controller reconfiguration is needed. On the other hand, the estimated fault signal is generated which can be
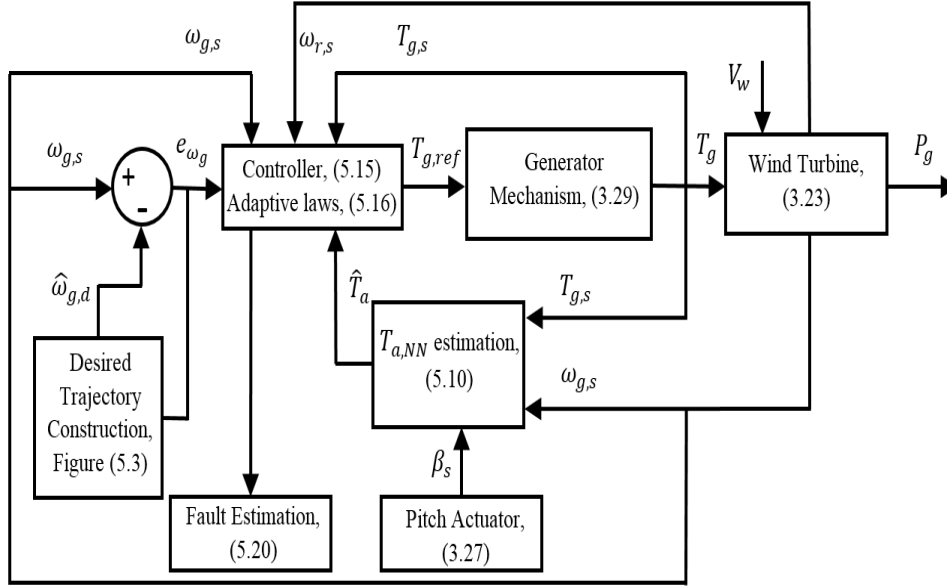
FIGURE 5.2: Generator torque controller diagram.

used for many purposes, such as supervisory condition monitoring schemes as well as in the manual maintenance procedures.

In this section, the generator torque controller has been proposed to accommodate the generator torque bias and also, to steer the wind turbine toward the desired trajectory. Also, the generator torque bias has been estimated which might be used for maintenance purposes. In the next section the pitch actuator controller is designed.

5.3 Pitch Actuator Controller Design

The pitch controller is designed in this section to fulfil the next control objective, i.e. keeping the pitch angle close to zero despite the presence of pitch actuator bias. Also, an estimation of pitch actuator dynamic change, is obtained which can be implemented on the well-known baseline controller in the full load region, (Lan et al., 2018) to remove fault effects. The pitch tracking error is constructed as, $e_\beta = \beta_d - \beta_s$, where β_d is the desired pitch angle. Considering (3.27), the pitch actuator dynamic behavior can be rewritten as,

$$\ddot{\beta} = -\omega_{n,N}{}^2\beta - 2\omega_{n,N}\xi_N\dot{\beta} + \omega_{n,N}{}^2\beta_{ref} + f_2 + d_2, \qquad (5.21)$$

where, $d_2 = -\omega_{n,N}{}^2\nu_\beta - 2\omega_{n,N}\xi_N\nu_{\dot{\beta}}$ and $f_2 = \Delta\tilde{f}_{PAD} + \omega_{n,N}{}^2\Phi$. β_d is zero in the partial load operation. Also, β_d is variable and should be tuned in the full load region, in which a simple industrial baseline controller, i.e. (4.10), can be used.

It should be noted that, in this chapter the pitch actuator effectiveness loss is not considered, because for the case of $\beta_d = 0°$, the effectiveness loss is not effective at all. This fault will be considered in Chapter 6.

Assumption 5.3. *The accumulative fault, f_2, is assumed to be bounded such that $|f_2| \leq \bar{f}_2$ where $\bar{f}_2 \in \mathbb{R}^+$ is an unknown constant. In fact, Φ is considered as a constant, or slowly varying additive step applied at the unknown fault time, i.e. t_Φ. On the other hand, $\Delta \tilde{f}_{PAD}$, with respect to the limited actuator input and achievable states, is bounded (Schulte et al., 2015). Also, the time derivative of the fault is assumed to be bounded, i.e. $\left| \dot{f}_2 \right| \leq \rho_{\dot{f}_2}$ (Lan et al., 2018), where $\rho_{\dot{f}_2} \in \mathbb{R}^+$ is unknown. Also, with the accumulative disturbance, d_2, it is assumed that $|d_2| \leq \bar{d}_2$ where $\bar{d}_2$ is an unknown constant (Tabatabaeipour et al., 2012).*

Now, to design the pitch actuator controller, a positive definite Lyapunov function is chosen as,

$$V_1^\beta = \frac{1}{2} e_\beta^2, \tag{5.22}$$

where, its time derivative can be written as, $\dot{V}_1^\beta = e_\beta \dot{e}_\beta$. A variable transformation can be defined as, $e_{2,\beta} = \alpha_\beta - \dot{\beta}_s$, where α_β is the virtual control signal which is chosen as,

$$\alpha_\beta = \dot{\beta}_d + k_{1,\beta} e_\beta, \tag{5.23}$$

where, $k_{1,\beta}$ is a positive constant design parameter. Now, the pitch actuator controller is designed as,

$$\beta_{ref} = \frac{1}{\omega_{n,N}^2} \left(g_2 - \hat{f}_2 + \frac{e_{2,\beta}}{\sqrt{e_{2,\beta}^2 + \eta_{d_2}^2}} \hat{d}_2 + k_{2,\beta} e_{2,\beta} \right), \tag{5.24}$$

where, η_{d_2} and $k_{2,\beta}$ are positive constant design parameters, and $\hat{f}_2$ and $\hat{d}_2$ are estimations of f_2 and d_2, respectively. Also, $g_2 = e_\beta + \dot{\alpha}_\beta + \omega_{n,N}^2 \beta_s + 2\omega_{n,N} \xi_N \dot{\beta}_s$ and the adaptive laws are defined as,

$$\begin{aligned}
\dot{\hat{d}}_2 &= \frac{e_{2,\beta}^2}{\sqrt{e_{2,\beta}^2 + \eta_{d_2}^2}} - \sigma_{d_2} \hat{d}_2, \\
\dot{\hat{f}}_2 &= -e_{2,\beta} - \sigma_{f_2} \hat{f}_2, \\
\dot{\hat{\rho}}_{\tilde{f}_2} &= -\sigma_{\tilde{f}_2} \hat{\rho}_{\tilde{f}_2},
\end{aligned} \tag{5.25}$$

where, σ_{d_2}, σ_{f_2} and $\sigma_{\tilde{f}_2}$ are positive constant design parameters. The estimation errors are defined as,

$$\begin{aligned}
\tilde{d}_2 &= \hat{d}_2 - \bar{d}_2, \\
\tilde{f}_2 &= \hat{f}_2 - f_2.
\end{aligned} \tag{5.26}$$

Also it is assumed that $\left|\tilde{f}_2\right| < \rho_{\tilde{f}_2}$ (Lan et al., 2018) with unknown $\rho_{\tilde{f}_2} \in \mathbb{R}^+$. Estimation of $\rho_{\tilde{f}_2}$ is defined as $\hat{\rho}_{\tilde{f}_2}$ and its estimation error as,

$$\tilde{\rho}_{\tilde{f}_2} = \hat{\rho}_{\tilde{f}_2} - \rho_{\tilde{f}_2}. \tag{5.27}$$

The stability and boundedness of the pitch actuator equipped with the pitch angle controller (5.24), is considered in the following theorem.

Theorem 5.3. *Consider the pitch actuator (5.21) and proposed pitch controller (5.24) with adaptive laws (5.25). Let the initial conditions of the pitch actuator be bounded. Then, for all generator torque, e_β and $\dot{e}_\beta$ are UUB.*

The proof of this theorem is given in A.7.

In Figure 5.3, the schematic diagram of the proposed pitch angle controller is illustrated.
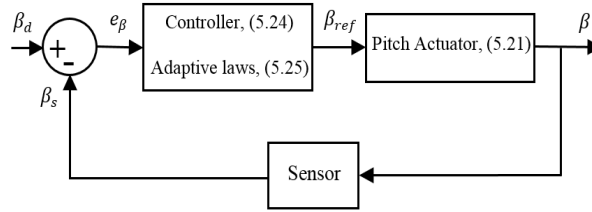
FIGURE 5.3: Pitch angle controller diagram.

5.3.1   Pitch actuator bias and dynamic change estimation

Now, the pitch actuator bias and dynamic change are going to be approximated. The auxiliary signals for different cases of pitch actuator dynamic change are calculated and compared with the estimated fault $\hat{f}_2$ to detect and isolate dynamic change.

Considering (3.27) and Table 3.1, the auxiliary signals are calculated as,

$$
\begin{aligned}
f_{auxiliary,\ fault\ free} &= 0\Delta(\tilde{\omega}_n{}^2)\beta_s - 0\Delta\left(\tilde{\omega}_n\tilde{\xi}\right)\dot{\beta}_s + 0\Delta(\tilde{\omega}_n{}^2)\beta_{ref} \\
&= 0, \\
f_{auxiliary,\ pump\ wear} &= -0.6316\Delta(\tilde{\omega}_n{}^2)\beta_s - 0.59376\Delta\left(\tilde{\omega}_n\tilde{\xi}\right)\dot{\beta}_s \\
&\quad + 0.6316\Delta(\tilde{\omega}_n{}^2)\beta_{ref}, \\
f_{auxiliary,\ hydraulic\ leak} &= -\Delta(\tilde{\omega}_n{}^2)\beta_s - 1.75706\Delta\left(\tilde{\omega}_n\tilde{\xi}\right)\dot{\beta}_s \\
&\quad + \Delta(\tilde{\omega}_n{}^2)\beta_{ref}, \\
f_{auxiliary,\ high\ air} &= -0.81083\Delta(\tilde{\omega}_n{}^2)\beta_s - 2\Delta\left(\tilde{\omega}_n\tilde{\xi}\right)\dot{\beta}_s \\
&\quad + 0.81083\Delta(\tilde{\omega}_n{}^2)\beta_{ref},
\end{aligned}
\tag{5.28}
$$

where, in $f_{auxiliary,\ X}$, X represents the dynamic change type and is replaced with either fault-free, pump wear, hydraulic leakage or high air content. Also, β_s and $\dot{\beta}_s$ are measured pitch angle and its rate, respectively, and β_{ref} is defined in (5.24). The other parameters are defined in (3.27). To proceed with fault estimation of the pitch actuator, first, the dynamic change case is indicated and it is assumed that there is no pitch actuator bias. Considering $f_2 = \Delta\tilde{f}_{PAD} + \omega_{n,N}{}^2\Phi$, in the absence of Φ, it can be seen that $f_2 = \Delta\tilde{f}_{PAD}$. So, using all auxiliary signals $f_{auxiliary,\ X}$, as (5.28), the most similar one to the estimated accumulative fault, $\hat{f}_2$, is selected as the dynamic change case. So, similarity indices are utilized on which basis the fault isolation is conducted. The Root Mean Squared Error (RMSE) and the Variance Accounted For (VAF) indices are used in this paper, which are defined as,

$$
\begin{aligned}
RMSE_X &= \sqrt{\frac{1}{t_{exe}}\int_0^{t_{exe}}\left(f_{auxiliary,X} - \hat{f}_2\right)^2 dt}, \\
VAF_X &= \left(1 - \frac{var\left(f_{auxiliary,X} - \hat{f}_2\right)}{var\left(f_{auxiliary,X}\right)}\right) \times 100
\end{aligned}
\tag{5.29}
$$

where, X represents the dynamic change type and t_{exe} is the execution time. In the ideal fault detection case, RMSE and VAF should be zero and 100%, respectively. Indeed, using (5.29), the case X which leads to RMSE and VAF indices close to zero and 100%, respectively, is selected as the corresponding dynamic change case, i.e. $\hat{X}$. It should be noted that pitch bias Φ is considered as an added constant on the accumulative fault. So, even in the presence of pitch bias with dynamic change, only RMSE index deviates significantly from zero, but the VAF index still indicates the correct dynamic change properly. Now, after indicating $\hat{X}$, the pitch actuator bias is estimated. Considering $f_2 = f_{auxiliary,\hat{X}} + \omega_{n,N}{}^2\Phi$, where $f_{auxiliary,\hat{X}}$ is the calculated auxiliary signal using (5.29) for the indicated dynamic change $\hat{X}$, the

estimation of pitch actuator bias, $\hat{\Phi}$, is as,

$$\hat{\Phi} = \frac{f_{auxiliary,\hat{X}} - \hat{f}_2}{\omega_{n,N}{}^2}.$$ (5.30)

In this section, the pitch actuator controller has been proposed to accommodate the pitch actuator bias and dynamic change, to guarantee that the pitch angle tracks the desired pitch angle. Also, the pitch angle bias and dynamic change have been estimated which might be used for maintenance purposes. In the next section the numerical results, using both proposed generator torque and pitch angle controllers, are investigated.

5.4   Numerical Evaluation

In this section, the proposed controllers, (5.15) and (5.24), are evaluated and the results are compared to baseline controller (4.7) values. It should be noted that more accurate desired trajectory tracking, taking wind speed variation into account, leads to increasing drive train torsion angle of twist. So, there should be a trade-off between efficiency and drive train torsion angle, accordingly, in this chapter it is expected to increase efficiency while keeping drive train torsion angle at a reasonable level compared to baseline controller values, which has industrial acceptability. Firstly, the fault-free situation is studied using both the proposed controller and baseline controller via considering various control criteria. Then, the fault detection of the proposed controller for the pitch mechanism is evaluated and also, its fault tolerant capability is considered. The generator controller response, including fault detection and fault effect removal, is studied. The effectiveness of the proposed controller for a real wind speed profile is evaluated. Finally, the simulation results are discussed.

5.4.1   Fault-free situation

The simulation results of the generated power augmented with the baseline controller and the proposed controller, using wind speed shown in Figure 5.4, are illustrated in Figure 5.5. It is assumed that there is no dynamic change or pitch bias in the pitch mechanisms and no torque bias in the generator. Figure 5.5 shows that at some times, where the wind speed reduces after a high value, the generated power is more than the optimal one, because the stored kinetic energy is being converted to electrical energy. Also, power coefficients using both controllers are shown in Figure 5.6. It is obvious that the initial response using the proposed controller is

faster than the corresponding one from the baseline controller. Considering the effect of this variation on the wind turbine, the induced drive train torsion angle, $\dot{\theta}_\Delta$, is shown in Figure 5.7, for both controllers. It is obvious that the induced gearbox torsion angle for both controllers is in the same order. It also confirms the assumption which was made in keeping $\dot{\theta}_\Delta$ as close to zero as possible, in the generator torque control design. The tracking error and generator torque for both controllers are shown in Figures 5.8 and 5.9, respectively. Finally, the estimated wind speed is calculated using (5.1) and (5.3), which is shown in Figure 5.10. High variation of produced power using the proposed controller, as illustrated in Figure 5.5, is due to the desired trajectory construction and the aerodynamic torque estimation based on GRBFNN. Indeed, considering Figure 5.10, the fluctuation of the estimated wind speed around the actual one is obvious. The desired trajectory has been constructed using (5.3), in which radial basis functions form the basis functions. Accordingly, using (5.1), the wind speed is estimated. Both the constructed desired trajectory and estimated aerodynamic torque have been utilized in the generator torque controller, see (5.15). So, the fluctuation of the constructed desired trajectory and estimated aerodynamic torque, leads to high variation of generator torque and consequently, considering the produced power, i.e. $P_a = \eta_g T_g \omega_g$, causes high variation of power. So, reconsidering Figure 5.5, the produced power has fluctuated in the same manner as the estimated wind speed. To compare the results of the two controllers, the values of the control criteria are compared in Table 5.1. It can be seen that more power is extracted using the proposed controller compared to the reference one, although, this is not the main purpose of the proposed controller, which is its FTC capabilities, considered in the next section.
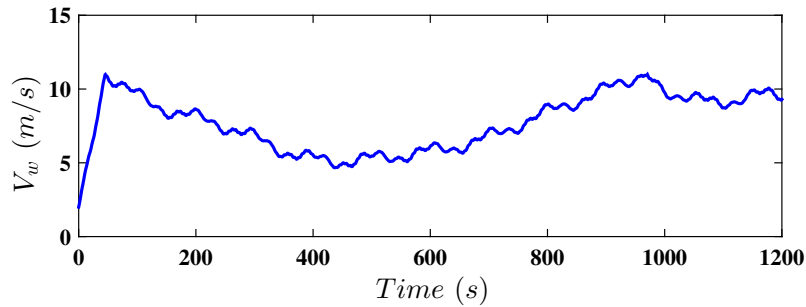
FIGURE 5.4: Wind speed profile in partial load region.

5.4.2 FTC evaluation

The FTC capabilities of the proposed controllers, are evaluated in this section. Also, the faults are augmented in the baseline controller to show the effect of the considered faults, and the results are compared with those from the proposed controller.
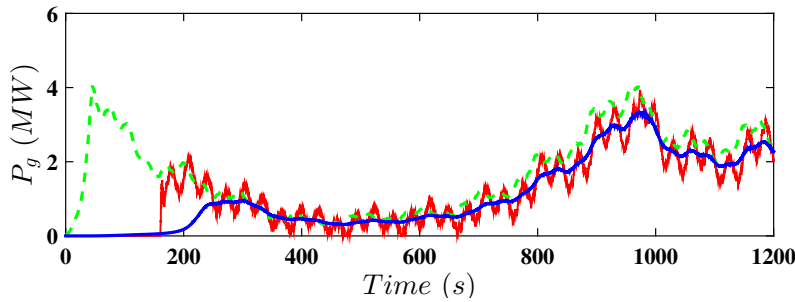
FIGURE 5.5: Generated power using the proposed controller (red line) and baseline controller (blue line), and optimal extractable wind power (green dashed line).
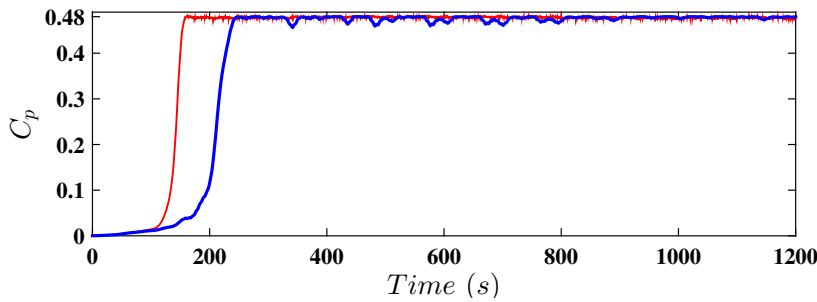
FIGURE 5.6: Power coefficient using the proposed controller (red line) and baseline controller (blue line).

Pitch actuator fault detection

In this section, the fault detection of the pitch actuator system is considered using the proposed controller, (5.24). In this regard, firstly the dynamic change of the pitch actuator is considered. To avoid a trivial response, an abrupt nonzero time varying input is applied to the pitch system for a small time interval to study its behaviour. For 6 seconds a sinusoidal wave is used as $\beta_d = 1sin(t)$ (Casau et al., 2015). The pitch sensor output for the fault-free case, pump wear, high air content and hydraulic leak cases are shown in Figure 5.11. It is obvious that the pitch actuator response is very similar in all situations which is the case in Figure 3.7, where the time delay for each case changes by 0.5 seconds at the most. Also, in each case, the estimated fault and calculated auxiliary signals are shown, on which basis the detection indices, (5.29), are calculated and shown in Table 5.2. According to Table 5.2, for each fault case, using the estimated accumulated fault, $\hat{f}_2$, and comparing the indices for each auxiliary signal, it is expected that RMSE and VAF values would be close to zero and 100, respectively. So, comparing all calculated indices, the auxiliary signal which leads to smallest RMSE and closest VAF to 100, is selected as the detected dynamic change case of the pitch actuator. In
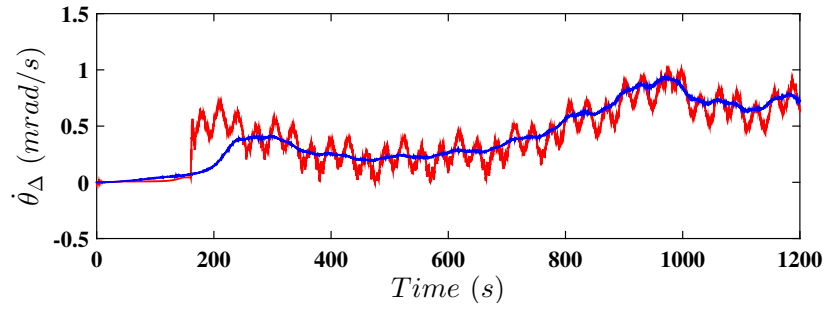
FIGURE 5.7: Torsion angle of drive train using the proposed controller (red line) and baseline controller (blue line).
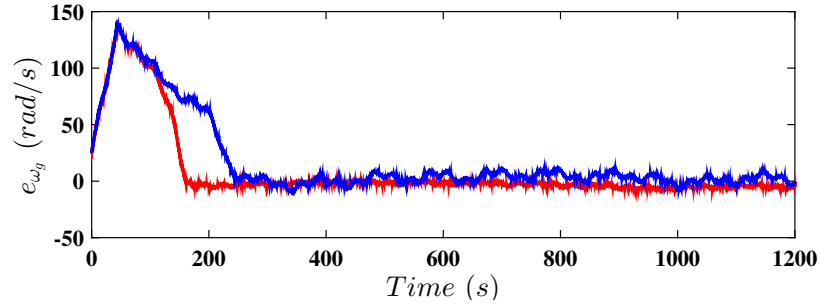
FIGURE 5.8: Tracking error using the proposed controller (red line) and baseline controller (blue line).

the last column of Table 5.2, the detected fault is represented, which shows that the proposed fault detection accurately detects all pitch actuator dynamic change cases. Now to evaluate the detection of pitch actuator bias, $\Phi = 10$, is added to the pitch dynamic response and using (5.28), the estimated pitch bias, $\hat{\Phi}$, is shown in Figure 5.12. The reference pitch angle is set to $\beta_{ref} = 1\sin(t)$, the same as the dynamic change detection. In Figure 5.12 it is obvious that Φ is accurately estimated.

Pitch actuator FTC

Firstly, the proposed pitch actuator controller, (5.24), is evaluated, where the dynamic changes due to pump wear, hydraulic leak and high air content in the oil are introduced. Also, the pitch actuator bias is added to the pitch mechanism. Additionally, sensor measurement is contaminated with noise. Accordingly, to only consider the dynamic change, sensor noise and pitch bias are removed, which will be considered afterward. Indeed, the sensor noise and pitch bias have more effect on pitch angle than the dynamic change, which reduces the visibility of the dynamic change, in the case of $\beta_d = 0°$. Actually, it is just for the sake of consideration. Also,
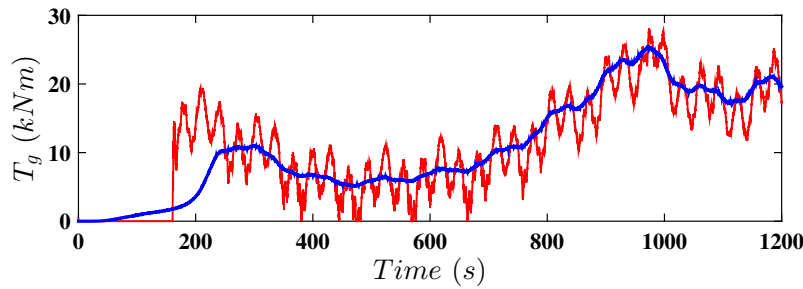
FIGURE 5.9: Generator torque using the proposed controller (red line) and baseline controller (blue line).
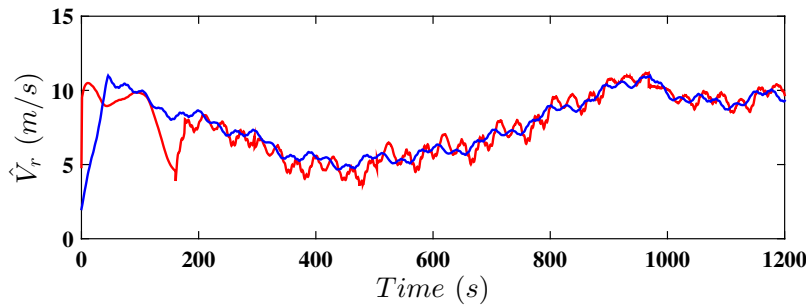
FIGURE 5.10: Estimated (red line) and actual wind speed (blue line).

the initial pitch angle is selected as $5°$, to let the delay in response be distinguishable. The results are illustrated in Figure 5.13. It is obvious that using the proposed pitch controller reduces the delays due to the induced dynamic change significantly, where the response is even better than the fault-free case with no controller. Now, to consider all types of faults altogether, pitch sensor noise, ν_β and pitch bias Φ, i.e. $10°$, are introduced to the model and it is expected that the pitch bias is removed and meanwhile the noise should not cause instability and should be reduced. In Figure 5.14, the proposed pitch controller results, in the presence of ν_β and Φ, for pump wear, hydraulic leak and high air situations, are illustrated, where the reference pitch angle is $0°$. It is obvious that in each of the three cases, the pitch bias is removed. Also, considering the dynamic change, it is obvious that the response of the pitch actuator using the proposed controller is similar to the fault-free one, comparing Figures 5.13 and 5.14. Finally, it can be stated that the proposed pitch controller is able to handle the pitch dynamic change and pitch bias. Although in partial load operation the pitch angle is enough to be set to $0°$, by using the proposed controller it is guaranteed that this aim is met using the sensor measurement which is contaminated with noise or else the pitch actuator may introduce the pitch bias. Also, this controller is readily capable of being used in full load operation, where the reference pitch angle is not fixed anymore and should be tuned to keep

TABLE 5.1: Values of the control criteria for fault-free situation

Performance criteria	Proposed controller	Baseline controller
$CC1$	1.486 (GJ)	1.394 (GJ)
$Efficiency$	70%	65%
$CC2$	47.06 $(\mu rad^2/s)$	0.6154 $(\mu rad^2/s)$
$CC5$	17.88 (MNm)	0.3694 (MNm)
$CC6$	28.10 (kNm)	25.30 (kNm)
$CC7$	7.32 (kNm)	7.27 (kNm)

TABLE 5.2: Pitch actuator dynamic change fault detection indices

	Calculated auxiliary signal								Decision
	Fault free		Pump wear		Hydraulic leak		High air content		
Fault free	RMSE	VAF	RMSE	VAF	RMSE	VAF	RMSE	VAF	No fault
	0.13	**95.3**	3.88	2.71	3.918	3.01	1.83	7.78	
Pump wear	RMSE	VAF	RMSE	VAF	RMSE	VAF	RMSE	VAF	Pump wear
	8.40	0.82	**0.45**	**99.69**	2.58	94.35	1.38	96.41	
Hydraulic leak	RMSE	VAF	RMSE	VAF	RMSE	VAF	RMSE	VAF	Hydraulic leak
	40.85	0.05	17.00	50.02	**5.60**	**97.64**	13.51	76.04	
High air content	RMSE	VAF	RMSE	VAF	RMSE	VAF	RMSE	VAF	High air content
	56.81	0.08	2.24	86.17	3.35	79.65	**0.78**	**97.13**	

the generated power at its nominal one. Indeed, via the proposed controller, the results show that the pitch angle is guaranteed to track the reference one, whether it is fixed, i.e. in partial load operation which is of interest in this chapter, or not, i.e. in full load operation, despite the presence of pitch bias, dynamic change and pitch noise. Also, in full load operation, using the proposed controller, the dynamic change of the pitch actuator can be detected. However, the dynamic change, in the case of the zero degree fixed pitch angle, is not very effective, considering Figure 5.13. So, in the next section only the pitch actuator bias is considered.

Wind turbine FTC using both generator and pitch controllers

The generator torque controller, (5.15), alongside the pitch controller, (5.24), are applied to the wind turbine model, and it is expected that despite the generator bias, i.e. f_{T_g}, pitch actuator bias, i.e. Φ and wind speed variation which is shown in Figure 5.4, the power coefficient is being kept at its maximum value and accordingly the generated power tracks the maximum one. Also, the considered faults are applied to the baseline, to study the effects of faults on the wind turbine behavior. The fault scenario is summarized in Table 5.3. In this fault scenario, to study the effect of the generator fault, which is more likely in partial load operation (Badihi et al.,
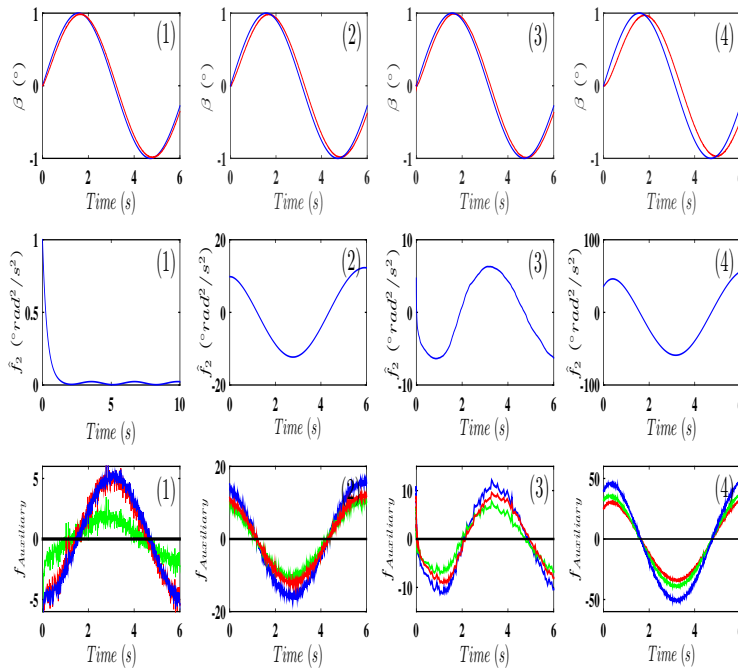
FIGURE 5.11: Fault detection in pitch actuator due to dynamic change. (First row) Reference pitch (blue line) and pitch sensor output (red line). (1) Fault-free case, (2) pump wear case, (3) high air content case, and (4) hydraulic leak case. (Second row) Estimated fault signal. (1) Fault-free case, (2) pump wear case, (3) high air content case, and (4) hydraulic leak case. (Third row) Calculated auxiliary signal for fault-free (black), pump wear (red), hydraulic leak (blue), and high air content (green). (1) Fault-free case, (2) pump wear case, (3) high air content case, and (4) hydraulic leak case.

2014), two different generator biases are introduced. Also, to evaluate the fault tolerance capability accurately, a consecutive pitch bias is considered which starts at $900(s)$, exactly when the second generator bias ends. In Figures 5.15 and 5.16, the power coefficient and generated power using the proposed controller and baseline controller, are shown, respectively. It is obvious that the proposed controller keeps the power coefficient at its maximum one, while the reference control results are significantly decreased in faulty periods. It is obvious that this power curve is similar to the fault-free one, in Figure 5.6, using the proposed controller. The tracking error, reference generator torque, reference pitch angle and drive train torsion angle are illustrated in Figures 5.17-5.20, respectively. It can be seen that the tracking error using the proposed controller is similar to the fault-free situation, in Figure 5.8. Also, the generator torque is kept at the same value unlike the corresponding result
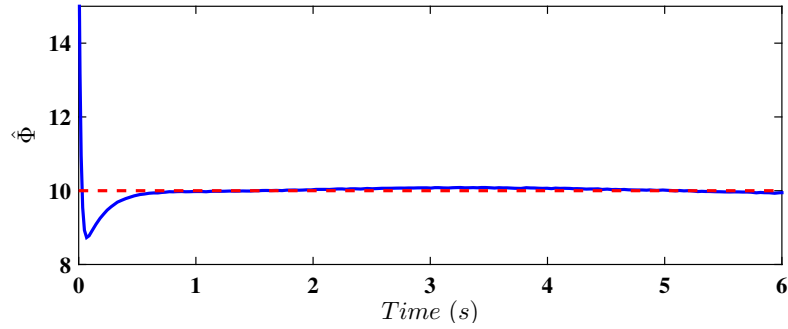
FIGURE 5.12: Estimated pitch actuator bias (blue line) and actual one (red line).
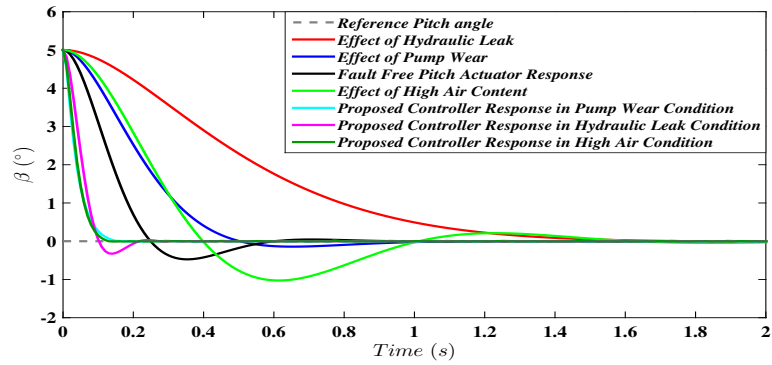
FIGURE 5.13: Pitch actuator controller response without sensor bias and noise, fault-free with no controller (black line), pump wear condition (blue line), hydraulic leak condition (red line), high air condition (light green line), pump wear with controller (light blue line), hydraulic leak with controller (pink line) and high air in the oil with controller (dark green).

from the baseline controller. At $300(s)$ and $700(s)$, when the generator biases are applied, sudden deviations from the fault-free case are obvious, after which their effects are completely removed using the proposed controller. Also, the same result can be obtained considering Figure 5.19, in which using the proposed pitch angle controller, the effect of pitch bias is removed. The estimated generator and pitch biases, are depicted in Figures 5.21 and 5.22, respectively. Considering the tracking error, the initial deviation of the estimated generator bias should not be taken into consideration, because at this time period, the desired trajectory tracking error has not been reduced yet, after which the generator biases are accurately estimated. On the other hand, because of the fast response of the pitch actuator, the pitch bias is estimated precisely over the whole simulation time. Also, the resulting control criteria are shown in Table 5.4. It is obvious that the efficiency from using the proposed controller is kept the same as the fault-free one, while the corresponding result using the baseline controller is decreased significantly. On the other hand, the induced
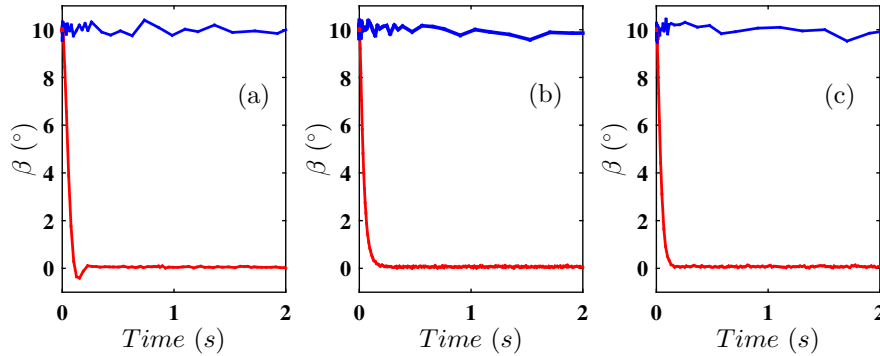
FIGURE 5.14: Pitch actuator controller response (red line) and without controller (blue line) in (a) hydraulic leak, (b) pump wear and (c) high air content conditions with sensor noise and pitch bias.

TABLE 5.3: First Fault scenario.

Fault scenario 1	Value	Period
Generator bias	$f_{T_g} = 2000\ (Nm)$	$300 - 500\ (s)$
Generator bias	$f_{T_g} = 5000\ (Nm)$	$700 - 900\ (s)$
Pitch bias	$\Phi = 10°$	$900 - 1100\ (s)$

drive train torsion stress remains in the same order using the proposed controller, but considering the corresponding result using the baseline controller, this criterion is about 54 times larger than the fault-free one. Also, considering the other criteria, the advantage of the proposed controller can be concluded.   To further investigate
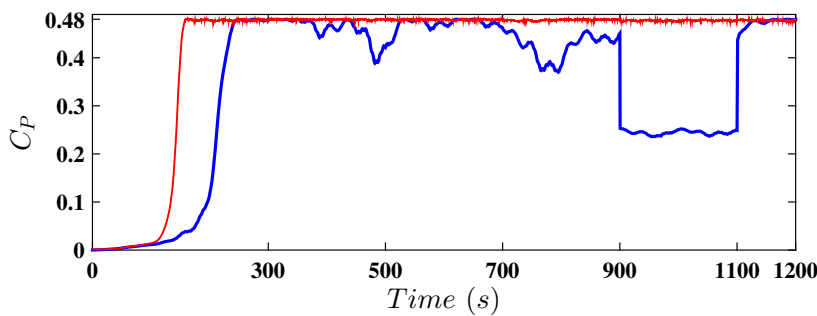
FIGURE 5.15: Power coefficient using the proposed controller (red line) and baseline controller (blue line).

the proposed controller's performance, a realistic wind speed profile, as shown in Figure 4.18, with mean wind speed 7.08 m/s is fed into the wind turbine including the fault scenarios shown in Table 5.5. The control criteria are summarized in Tables 5.6 and 5.7. It is obvious that the same results can be obtained considering
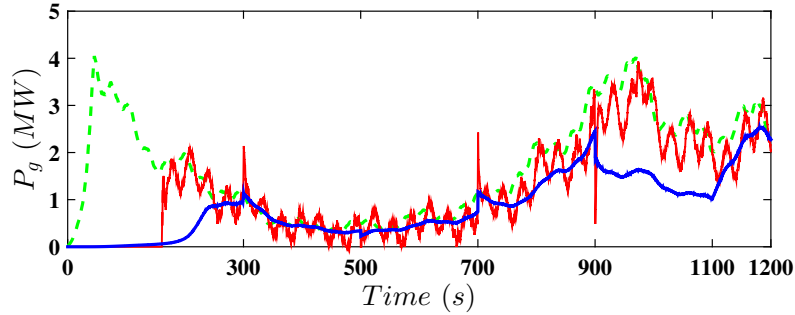
FIGURE 5.16: Generated power using the proposed controller (red line) and baseline controller (blue line), and optimal extractable wind power (green line).
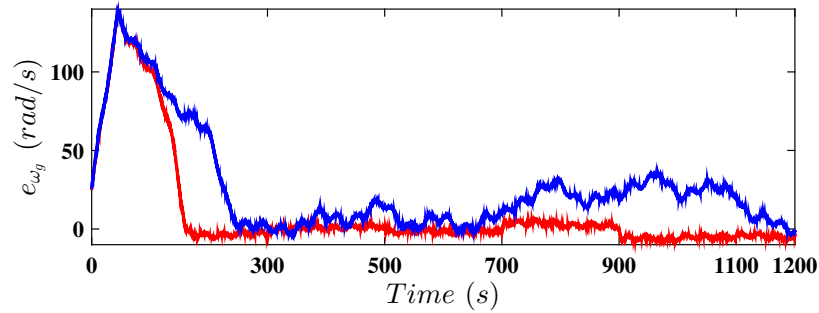
FIGURE 5.17: Tracking error using the proposed controller (red line) and baseline controller (blue line).

the performance of the proposed controller in both fault-free and faulty situations compared to the corresponding results when using the baseline controller.

5.5 Discussion

In the simulations, for the fault-free case, obviously the initial response from using the proposed controller has been improved, as shown in Figures 5.5 and 5.6. Also, the fluctuations of generated power, induced torsion angle and generator torque, can be seen in Figures 5.5, 5.7 and 5.9, respectively. In fact, the adaptive structure of the controller and high variation of the GRBFNN output, which was used to estimate the unknown desired trajectory, i.e. Figure 5.10, and also variation of $\hat{T}_a$ used in (5.15), have led to this phenomenon. So, considering Table 5.1, it is obvious that high fluctuation of the generator torque, has caused more drive train torsion angle fluctuations and generator torque variation, compared to the corresponding ones for the baseline controller. Nevertheless, considering Figures 5.7 and 5.9, it is obvious that the induced torsion angle and generator torque are in the same order as

TABLE 5.4: Values of the control criteria with first fault scenario.

Performance criteria	Proposed controller	Baseline controller
$CC1$	1.483 (GJ)	1.1 (GJ)
$Efficiency$	69.5%	52%
$CC2$	68.8 $(\mu rad^2/s)$	32.55 $(\mu rad^2/s)$
$CC5$	18.49 (MNm)	0.3539 (MNm)
$CC6$	28.14 (kNm)	22.42 (kNm)
$CC7$	7.38 (kNm)	5.88 (kNm)

TABLE 5.5: Second Fault scenario.

Fault scenario 1	Value	Period
$Generator\ bias$	$f_{T_g} = 5000\ (Nm)$	$100 - 300\ (s)$
$Pitch\ bias$	$\Phi = 5°$	$500 - 700\ (s)$
$Generator\ bias$	$f_{T_g} = 7000\ (Nm)$	$900 - 1100\ (s)$
$Pitch\ bias$	$\Phi = 10°$	$1300 - 1500\ (s)$

TABLE 5.6: Values of the control criteria for real wind profile in
fault-free case.

Performance criteria	Proposed controller	Baseline controller
$CC1$	1.852 (GJ)	1.785 (GJ)
$Efficiency$	77%	74%
$CC2$	212.3 $(\mu rad^2/s)$	20.95 $(\mu rad^2/s)$
$CC5$	42.74 (MNm)	0.5268 (MNm)
$CC6$	30.52 (kNm)	28.67 (kNm)
$CC7$	12.28 (kNm)	7.65 (kNm)

TABLE 5.7: Values of the control criteria second fault scenario.

Performance criteria	Proposed controller	Baseline controller
$CC1$	1.847 (GJ)	1.374 (GJ)
$Efficiency$	76%	57%
$CC2$	299.3 $(\mu rad^2/s)$	264.4 $(\mu rad^2/s)$
$CC5$	42.53 (MNm)	75.44 (MNm)
$CC6$	35.30 (kNm)	35.3 (kNm)
$CC7$	12.49 (kNm)	11.23 (kNm)
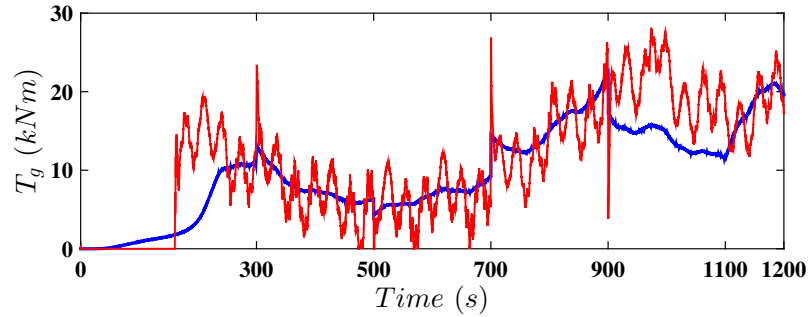
FIGURE 5.18: Generator torque using the proposed controller (red line) and baseline controller (blue line).
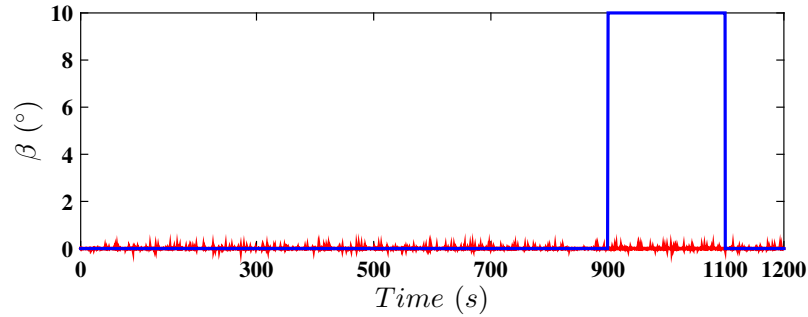
FIGURE 5.19: Pitch angle using the proposed controller (red line) and baseline controller (blue line).

the baseline controller results. So, it can be concluded that the proposed controller has similar performance in the fault-free case, as the baseline controller, while the efficiency has been increased. The advantage of the proposed controller can be exploited in the faulty case, considering Tables 5.3 and 5.4, in which the efficiency has been retained in the same order, while this number has been decreased about 13% for the baseline controller. Also, the stress has been increased just 1.47 times more than the fault-free case, but this ratio is about 52.89, for the baseline controller. Also, the actuator fault has been estimated, which can be used for maintenance purposes. The pitch actuator dynamic change, for nonzero desired pitch angle, β_d, was studied and it was shown that the dynamic change can be accurately detected, as shown in Table 5.2 and Figure 5.11. Also, the response of the pitch actuator under dynamic change was considered and it was illustrated that the pitch angle has tracked the desired one, using the proposed controller, faster than any other condition, either with or without dynamic change, as shown in Figures 5.13 and 5.14. It should be clearly pointed out that because of the negligible effect of the pitch actuator dynamic change in the partial load operation, where $\beta_d = 0(^\circ)$, this case is not considered in Section 5.4.2, where just the effect of pitch bias has been studied. In fact, the proposed pitch controller, is readily able to follow the β_d, whether fixed or variable, and detect dynamic change. So, this controller is applicable in full
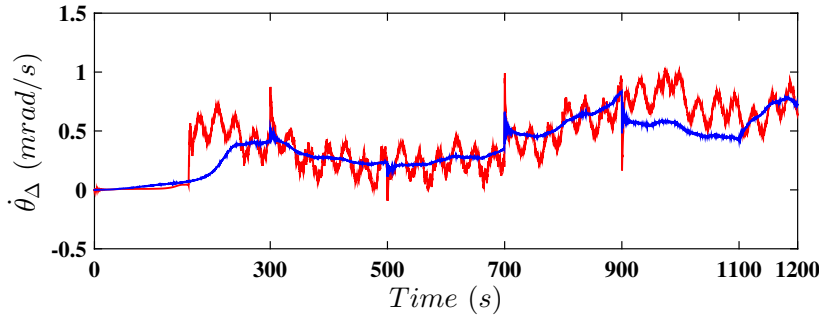
FIGURE 5.20: Torsion angle of drive train using the proposed con-
troller (red line) and baseline controller (blue line).
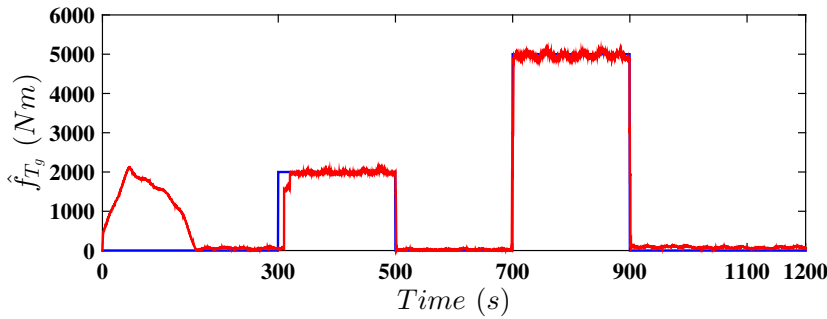
FIGURE 5.21: Estimated (red line) and actual (blue line) generator
bias.

load region, where the β_d can be simply tuned via a PID controller , which has not been considered in this chapter. In the selection of the controller parameters, a compromise should be taken between the boundedness of the controller behaviour and tracking performance. For example, because the GRBFNN weight estimation, $\hat{\theta}$, is the sliding surface function, small σ_c will cause large estimation weights. On the other hand, small σ_{d_1} and σ_{d_2}, may make large adapting disturbance parameters, and thus decrease the robustness to disturbances. In addition, large k_{2,ω_g} and $k_{2,\beta}$, may lead to saturated control input, i.e. pitch and generator torque. Actually, numerous offline response studies should be conducted to make the trade-off satisfactorily, between the various contradictory objectives.

The optimum power point tracking of the nonlinear wind turbine, using a nonlinear FTC in the presence of actuator faults, has been studied in this chapter. It was aimed to propose a new controller having functionality to fulfil the control objectives in both fault-free and faulty situations, satisfactorily. The wind speed and, accordingly, desired operational trajectory, at which wind turbines capture the most available energy, have been considered as unknown and so the desired trajectory has been reconstructed using a neural network scheme embedded into the proposed
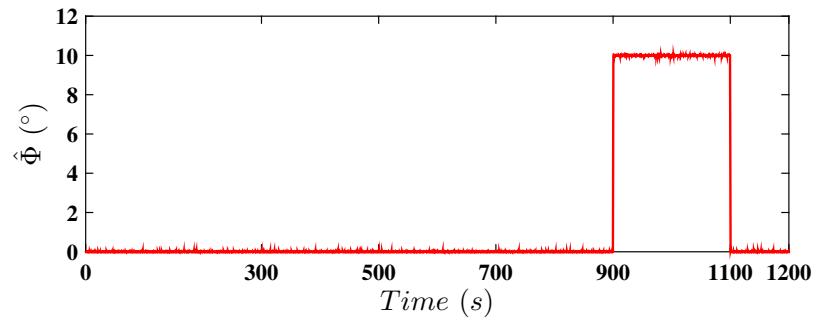
FIGURE 5.22: Estimated (red line) and actual (blue line) pitch bias.

controller. Utilising the Lyapunov analysis, the boundedness of the closed-loop system behavior with the proposed controller has been guaranteed. The performance of the proposed controller was studied via numerical simulations in which the baseline controller, i.e. constant gain controller, was used to evaluate the proposed controller results. The results showed that the proposed controller, contrary to the constant gain controller, was able to track the optimum power trajectory in both fault-free and faulty cases with very close performance indices. Additionally, the actuator faults were accurately estimated, which can be used for effective management of the required maintenance procedures.

6 Power Regulation with Unknown Control Direction using Neuro Adaptive Constrained FTC

In full load operation, the power regulation is vital to prevent the wind turbine from over speeding resulting in catastrophic operation, and for keeping the produced power at the nominal level. Otherwise, if the wind turbine speeds up and violates the predefined limit, the mechanical brakes, located on the rotor, are engaged. This leads to generated power reduction considerably less than the nominal one. Also, fatigue load on the rotor is increased (Tiwari et al., 2016). Therefore, it is beneficial to guarantee that the produced power is kept within the safe-to-operate constraint, around the nominal power and, consequently, to avoid the engagement of the mechanical brake. The power regulation is fulfilled by adjusting the blade's pitch angle via the pitch actuator, to adjust the applied aerodynamic torque, and consequently, the generated power. The aerodynamic torque is a nonlinear function of the blade pitch angle (Li et al., 2017). Meanwhile, the wind speed, as another variable which affects the aerodynamic torque, is highly stochastic and, consequently, an unmeasurable disturbance. So, it can be stated that the control function, from pitch angle to aerodynamic torque, is not completely known. This leads to the unknown control direction problem. Accordingly, it is very challenging to retain the generated power exactly at the nominal one (Boukhezzar et al., 2011). The achievable pitch angle is bounded. Hence, the practical operational range of the pitch actuator is limited. So, the high wind speed variation may lead to the pitch actuator saturation, which consequently causes violation of the constrained power regulation. So, in the pitch angle controller design, it is desirable to avoid any abrupt and long-lasting saturation, and smoothly pass any possible saturation period.

The modern wind turbines are designed to be larger and are often located in remote places, i.e. offshore, to increase the produced power. Operation in harsh remote places in the presence of the high wind speed variation, may lead to pitch actuator faults, and consequently, poor power regulation and catastrophic operation. These faults can be considered as pitch actuator bias, effectiveness loss and dynamic change. The last one causes slow pitch actuator response (see Figure 3.8), which consequently leads to degraded power regulation. Also, the debris build-up and blade erosion changes the aerodynamic characteristics of the blades. So, it is

desirable to integrate the fault tolerance capability into the pitch angle controller to keep the performance at the desired level.

Considering the abovementioned issues, this chapter presents a novel adaptive neural-based FTC design for wind turbines with unknown dynamics and unknown wind speed. By utilizing the Barrier Lyapunov Function (BLF) in the analysis of the Lyapunov direct method, the constrained behavior of the system is provided in which the rotor speed and its variation remain in their bounds. Furthermore, the computational cost of the controller is reduced by exploiting the Dynamic Surface Control (DSC) in the proposed analytical algorithms. Input saturation, in terms of smooth pitch actuator bounding is considered. In addition, by introducing a Nussbaum type function and adaptive laws, together with utilizing GRBFNN, a robust adaptive FTC scheme is advanced without the need for precise information about the wind turbine model nor the pitch actuator faults. The effectiveness of the theoretical results is illustrated using numerical simulations.[1] It should be noted that the values of controller parameters are given in Section B.4.

6.1   Pitch Actuator Saturation

Considering the physically bounded achievable pitch angle, the operational range of the pitch actuator is limited, as (3.22). So, the pitch actuator saturation phenomenon should be considered in the pitch angle controller design. Considering (3.26), for the given wind turbine model the pitch actuator saturation $H\left(\beta_u\right)$ is as,

$$H(\beta_u) = \begin{cases} \beta_{max}, & \beta_u > \beta_{max}, \\ \beta_u, & \beta_{min} \leq \beta_u \leq \beta_{max}, \\ \beta_{min}, & \beta_u < \beta_{min}, \end{cases} \tag{6.1}$$

where, $\beta_{max} = 30(°)$ and $\beta_{min} = -2(°)$. $H(\beta_u)$ is illustrated in Figure 6.1. So, this actuation saturation function is integrated into the pitch actuator mechanism (3.21) as,

$$\ddot{\beta} = -\omega_n{}^2\beta - 2\omega_n\xi\dot{\beta} + \omega_n{}^2 H\left(\beta_u\right). \tag{6.2}$$

Obviously, this saturation function of the pitch angle is non-smooth with sharp saturation behavior, which may cause pitch actuator failure (Zhao et al., 2016). So, it is desirable to approximate this saturation function by a smooth function and

---

[1]This chapter is captured and reorganized from the papers "Backstepping Nussbaum Gain Dynamic Surface Control for a Class of Input and State Constrained Systems with Actuator Faults", and "Constrained control of wind turbines for power regulation in full load operation". The authors' attribution on these papers are given in Appendix C.
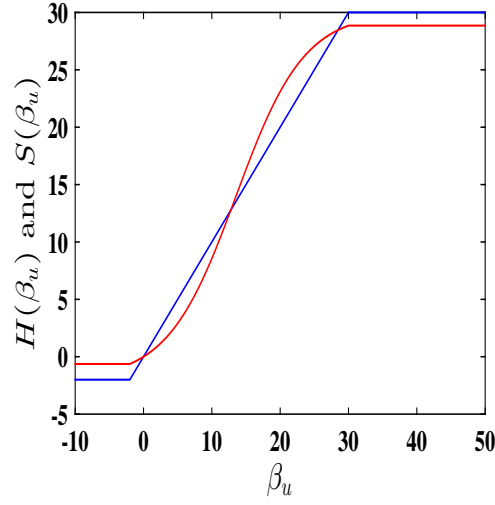
FIGURE 6.1: Pitch actuator saturation (blue line) and its smooth estimation (red line).

to pass from each saturation period fluently. In this regard, the following smooth saturation function is proposed as,

$$S\left(\beta_u\right) = \frac{\bar{\varrho}P - \underline{\varrho}P^{-1}}{P + P^{-1}}, \tag{6.3}$$

where, $\underline{\varrho} = 2$, $\bar{\varrho} = 30$, $P = e^{\epsilon + \eta\beta_u}$, $\epsilon = 0.5 \ln\left(\underline{\varrho}/\bar{\varrho}\right)$, and η is a positive constant to be selected. $S\left(\beta_u\right)$ is always in $\left(-\underline{\varrho}, \bar{\varrho}\right)$ for all $\beta_u \in \mathbb{R}$. $S\left(\beta_u\right)$ is illustrated in Figure 6.1, for $\eta = 0.1$. Then, $H\left(\beta_u\right)$ can be expressed as,

$$H\left(\beta_u\right) = S\left(\beta_u\right) + D(\beta_u), \tag{6.4}$$

where $D(\beta_u)$ is the difference between $S\left(\beta_u\right)$ and $H\left(\beta_u\right)$. The bounded property of the function $S\left(\beta_u\right)$ and saturation function $H\left(\beta_u\right)$, yields the function $D(\beta_u)$ to be bounded as, $|D(\beta_u)| \leq \bar{D}_1$, where $\bar{D}_1$ is a positive and unknown constant. For the pitch actuator controller design, the mean value theorem is employed on function $S\left(\beta_u\right)$ to get,

$$S\left(\beta_u\right) = S\left(\beta_0\right) + \left.\frac{\partial S}{\partial \beta_u}\right|_{\beta_m} \left(\beta_u - \beta_0\right), \tag{6.5}$$

where, $\beta_m = m\beta_u + (1 - m)\beta_0$ and $m \in (0, 1)$. By choosing $\beta_0 = 0$ and using the fact that $S\left(0\right) = 0$, (6.5) becomes,

$$S\left(\beta_u\right) = \left.\frac{\partial S}{\partial \beta_u}\right|_{\beta_m} \beta_u = S_{\beta_u}\beta_u, \tag{6.6}$$

where, $S_{\beta_u} = \left. \frac{2\eta\left(\bar{\varrho}+\varrho\right)}{(P+P^{-1})^2} \right|_{\beta_m}$. $S_{\beta_u} \in (0.2,\ 1.65)$ for $\beta_m \in (-\varrho,\ \bar{\varrho})$. Then, S_{β_u} is a positive variable. Now, considering (6.2), (6.4) and (6.6), the pitch actuator dynamic behavior with smooth saturation function can be written as,

$$\ddot{\beta} = -\omega_n{}^2\beta - 2\omega_n\xi\dot{\beta} + \omega_n{}^2\left(S_{\beta_u}\beta_u + D\left(\beta_u\right)\right). \tag{6.7}$$

6.2   Desired Operational Mode with Pitch Actuator Faults and Aerodynamic Characteristics Change

The pitch actuator dynamic change is considered as an uncertainty which should be attenuated by the pitch angle controller. Also, the pitch actuator output can be corrupted by an unanticipated fault, modelled as an additive bias and/or effectiveness loss. So, the pitch actuator dynamic behavior (6.7), associated with dynamic change, pitch actuator bias and effectiveness loss, can be rewritten as,

$$\ddot{\beta} = -\omega_{n,N}{}^2\beta - 2\omega_{n,N}\xi_N\dot{\beta} + \omega_{n,N}{}^2\left(S_{\beta_u}\rho\left(t\right)\beta_{ref} + S_{\beta_u}\Phi\left(t\right) + D(\beta_u)\right) + \Delta\tilde{f}_{PAD}. \tag{6.8}$$

The wind turbine operation in the presence of rain, snow and dirt, leads to debris build-up on the blades or erosion, which in turn, leads to the blade aerodynamic efficiency reduction. Consequently, the captured aerodynamic power is decreased. On the other hand, the power regulation by the blade pitch control is not satisfactorily achieved due to the changed blade aerodynamic profile. The debris build-up effect is modelled as an aerodynamic change $\Delta T_a|_{\Delta C_p}$, due to a change in power coefficient as $\tilde{C}_p = C_p + \Delta C_p$. So, it is very important to foresee this potential change in the controller design. It is worth noting that debris build-up is difficult to detect, as it is hard to identify if the blade's debris is the reason for the reduced power generation or simply that the wind speed has reduced (Borcehrsen et al., 2014). As debris build-up happens slowly on the blades, it is mostly assumed that this changes within the annual maintenance/inspection, and the blades can be simply cleaned/replaced. So, in this chapter it is aimed to design the pitch controller to be insensitive to debris build-up and to retain desired operation up to next annual maintenance/inspection of the blades. In regard to aerodynamic characteristics change, taking the time derivative of (4.16), yields

$$\dot{T}_a\left(V_w,\ \omega_r,\ \beta\right) = \Delta T_a|_{\Delta C_p} + \dot{\beta}\frac{\partial T_a}{\partial \beta} = \Delta T_a|_{\Delta C_p} + \dot{\beta}\ T_a)_\beta, \tag{6.9}$$

where, $\Delta T_a|_{\Delta C_p} = \frac{dT_a(V_r, \omega_r, \beta^*)}{dt} + (\beta - \beta^*) \frac{d}{dt} \left.\frac{\partial T_a}{\partial \beta}\right|_{(V_r, \omega_r, \beta_k)} - \frac{d\beta^*}{dt} \left.\frac{\partial T_a}{\partial \beta}\right|_{(V_r, \omega_r, \beta_k)}$ and $\frac{\partial T_a}{\partial \beta} = T_a)_\beta$. $\Delta T_a|_{\Delta C_p}$ is due to ΔC_p, which is the result of blade aerodynamic characteristic changes. The debris build-up happens slowly in time within the annual timeframe of blade maintenance. So, all terms which are contributing to $\Delta T_a|_{\Delta C_p}$ are assumed to be bounded, then $\Delta T_a|_{\Delta C_p}$ is bounded as, $\left| \Delta T_a|_{\Delta C_p} \right| \leq \bar{k}_1$, where $\bar{k}_1$ is an unknown positive constant. Also, it should be noted that the wind speed is not accurately measurable. So, $T_a)_\beta$ in (6.9) is an unknown variable.

Substituting (6.9) into (4.15) leads to,

$$\ddot{\omega}_r = c_1 \omega_r + c_2 \omega_g + c_3 T_a + c_4 T_g + a_3 \left(\Delta T_a|_{\Delta C_p} + \dot{\beta} \, T_a)_\beta \right). \tag{6.10}$$

Now, by considering (6.8), the rotor dynamic behavior, (6.10), can be rewritten as,

$$\begin{aligned}
\ddot{\omega}_r = {}& c_1 \omega_r + c_2 \omega_g + c_3 T_a + c_4 T_g - \frac{a_3 \omega_{n,N} \beta \, T_a)_\beta}{2\xi_N} - \frac{a_3 \ddot{\beta} \, T_a)_\beta}{2\omega_{n,N}\xi_N} \\
& + \frac{a_3 S_{\beta_u} \omega_{n,N} \rho \, T_a)_\beta}{2\xi_N} \beta_{ref} + \frac{a_3 \omega_{n,N} D \, T_a)_\beta}{2\xi_N} + a_3 \, \Delta T_a|_{\Delta C_p} \\
& + \frac{a_3 \, T_a)_\beta}{2\xi_N} \left(\frac{\Delta \tilde{f}_{PAD}}{\omega_{n,N}} + S_{\beta_u} \omega_{n,N} \Phi \right).
\end{aligned} \tag{6.11}$$

This captures the wind turbine rotor dynamic behaviour, operating on the desired operational mode, associated with pitch actuator dynamic change, pitch bias, effectiveness loss and blade aerodynamic change. Also, smooth pitch angle saturation is considered.

As mentioned earlier in Section 4.2, in the full load region it is desirable to keep P_g at the nominal value $P_{a,N}$, to keep the wind turbine structurally safe, to avoid over speeding and consequent brake engagement. As the wind speed is a highly stochastic variable, the accurate nominal power generation is very challenging, and in the case of improper controller design, it may lead to over speeding and braking. So, it is very beneficial to guarantee the generated power and speed so as to not violate the given constraint, within which the mechanical brake is not engaged. It should be noted that for the wind turbine power regulation considered in this chapter, the generator torque controller is not active. Accordingly, the faults in the generator are not considered and it is assumed that these faults have already been accommodated using the generator torque controller (5.15).

The controller is designed to regulate the reference pitch angle β_{ref} in (6.11) and maintain the rotor speed as close as possible to the nominal one, i.e. $\omega_{r,N}$, never violating the given constraint, in the presence of wind speed variation, disturbance, and pitch actuator faults and saturation. The primary objective of this chapter is to satisfy the above-mentioned requirements.

6.3   Constraint FTC Design and Stability Analysis

In this section, the constrained FTC is designed to guarantee that the generated power is kept within given constraints, in the presence of wind speed variation, disturbance, pitch actuator faults and saturation. The stability of the wind turbine closed-loop system equipped with the proposed controller is proved. Firstly, the technical preliminaries, which are going to be used in the controller design are given.

6.3.1   Technical preliminaries

The wind speed is considered as an unmeasurable disturbance. Accordingly, the aerodynamic torque T_a is not available. On the other hand, T_a is contributing in the rotor dynamic response (6.11). So, T_a should be estimated to be used in the proposed controller structure. In this chapter, a GRBFNN is designed to estimate aerodynamic torque. In this regard T_a is approximated as (5.10).

Now, the following definition and lemmas are given, which will be used in the proposed controller design. As $T_a)_\beta$, is an unknown variable, contributing to the gain of β_{ref} in (6.11), this leads to the unknown control direction problem. To tackle this problem in the controller design, the Nussbaum type function is utilized, which is defined in Definition 4.2.

The BLF function is defined as follows, which is used in the constraint control construction.

Definition 6.1. *A scalar function $V(x)$ is a BLF if it is a positive definite continuous scalar function, defined with respect to the system $\dot{x} = f(x)$ on an open region $\mathcal{D}$, containing the origin. In addition, $V(x)$ has continuous first order partial derivatives within all $\mathcal{D}$, and approaches to infinity as x approaches to the boundary of the region $\mathcal{D}$. Finally, $V(x)$ satisfies $V(x) \leq m$, $\forall t \geq 0$ along the solution of $\dot{x} = f(x)$ for $x(0) \in \mathcal{D}$, and some positive constant m (Rahimi et al., 2018b).*

The following lemma is given for stability analysis of the closed-loop system.
Lemma 6.1. *For variable ψ in $|\psi| < 1$, $\tan(\pi\psi^2/2) < \pi\psi^2 sec^2(\pi\psi^2/2)$ holds true (Rahimi et al., 2018a).*

Lemma 6.2. *For any variable Ψ and any positive constant γ, $0 < |\Psi| - \Psi tanh\left(\Psi/\gamma\right) < K\gamma$ holds true, where K satisfies $= e^{-(K+1)}$, accordingly, $= 0.2785$. Also, as $\Psi tanh\left(\Psi/\gamma\right) > 0$, then for any variable $Z < -1$, $Z\Psi tanh(\Psi/\gamma) < -\Psi tanh(\Psi/\gamma)$ holds (Rahimi et al., 2018a).*

6.3.2 Controller design procedure

The main objective of the proposed controller is to keep the rotor speed and acceleration within constraints, which in turn leads to bounded power generation around the nominal one. To initiate the proposed controller design, the rotor speed tracking error and its time derivatives are defined as,

$$
\begin{aligned}
e_{\omega_r} &= \omega_{r,s} - \omega_{r,d}, \\
e_{\dot{\omega}_r} &= \dot{\omega}_{r,s} - z_2,
\end{aligned}
\tag{6.12}
$$

respectively, where, $\omega_{r,d}$ is the desired rotor speed. As stated earlier, $\omega_{r,d}$ in the full load region is $\omega_{r,N}$. z_2 is a virtual control. Here, to avoid repetitive differentiation of z_2, which increases the implementation complexity, the DSC technique is utilized, by introducing filtering of z_2 via α_D which is a stabilizing function to be designed. Let α_D pass through a first order filter with a time constant τ_2 as,

$$
\tau_2 \dot{z}_2 + z_2 = \alpha_D, z_2\left(0\right) = \alpha_D(0).
\tag{6.13}
$$

The output error of the first-order filter is defined as, $\chi_2 = z_2 - \alpha_D$ where its first-time derivative yields $\dot{z}_2 = -\chi_2/\tau_2$.

A positive definite Lyapunov function is chosen as,

$$
V_1 = \frac{k_{e_1}^2}{\pi} tan\Lambda_1 + \frac{1}{2}\chi_2^2,
\tag{6.14}
$$

where, $\Lambda_1 = \pi\xi_1^2/2$, $\xi_1 = e_{\omega_r}/k_{e_{\omega_r}}$ and $k_{e_{\omega_r}}$ is considered a constraint on e_{ω_r}. It should be noted that V_1 is continuous in the set $\Omega_{e_{\omega_r}} = \left\{ e_{\omega_r} : -k_{e_{\omega_r}} < e_{\omega_r} < k_{e_{\omega_r}} \right\}$. The Lyapunov function V_1 is positive definite, in which the first term captures the BLF characteristics of the modified tracking error ξ_1, according to Definition 6.1. The time derivative of ξ_1 is obtained as,

$$
\dot{\xi}_1 = \frac{\dot{e}_{\omega_r}}{k_{e_{\omega_r}}} = \frac{e_{\dot{\omega}_r} + \chi_2 + \alpha_D}{k_{e_{\omega_r}}}.
\tag{6.15}
$$

First-time derivative of (6.14) can be obtained as,

$$\dot{V}_1 = e_{\omega_r} e_{\dot{\omega}_r} sec^2 \Lambda_1 + e_{\omega_r} \chi_2 sec^2 \Lambda_1 + e_{\omega_r} \alpha_D sec^2 \Lambda_1 - \frac{\chi_2^2}{\tau_2} - \dot{\alpha}_D \chi_2. \qquad (6.16)$$

The virtual control α_D is designed as,

$$\alpha_D = -\gamma_1 e_{\omega_r} - e_{\omega_r} sec^2 \Lambda_1, \qquad (6.17)$$

where, γ_1 is a positive design parameter. Substitution of (6.17) into (6.16) yields,

$$\dot{V}_1 = e_{\omega_r} e_{\dot{\omega}_r} sec^2 \Lambda_1 + e_{\omega_r} \chi_2 sec^2 \Lambda_1 - \gamma_1 e_{\omega_r}^2 sec^2 \Lambda_1 - e_{\omega_r}^2 sec^4 \Lambda_1 - \frac{\chi_2^2}{\tau_2} - \dot{\alpha}_D \chi_2. \quad (6.18)$$

Considering Young's inequality,

$$\begin{aligned} e_{\omega_r} e_{\dot{\omega}_r} sec^2 \Lambda_1 &\le \frac{1}{2} e_{\omega_r}^2 sec^4 \Lambda_1 + \frac{1}{2} e_{\dot{\omega}_r}^2, \\ e_{\omega_r} \chi_2 sec^2 \Lambda_1 &\le \frac{1}{2} e_{\omega_r}^2 sec^4 \Lambda_1 + \frac{1}{2} \chi_2^2. \end{aligned} \qquad (6.19)$$

Since α_D is a function of ω_r, $\omega_{r,d}$ and $\dot{\omega}_{r,d}$, it can be shown that,

$$\dot{\alpha}_D = \frac{\partial \alpha_D}{\partial \omega_r} \dot{\omega}_r + \frac{\partial \alpha_D}{\partial w_{r,d}} \dot{\omega}_{r,d} + \frac{\partial \alpha_D}{\partial \dot{w}_{r,d}} \ddot{\omega}_{r,d}. \qquad (6.20)$$

Considering (6.20), $\dot{\alpha}_D$ is a continuous function. Then, given $\delta_{\omega_{r,d}}$ and any positive number δ_1, the set $\Omega_{\omega_{r,d}} := \{\omega_{r,d} \in \mathbb{R} : \omega_{r,d}^2 + \dot{\omega}_{r,d}^2 + \ddot{\omega}_{r,d}^2 < \delta_{\omega_{r,d}}\}$ for all initial conditions satisfying $\Omega_1 := \{[e_{\omega_r}, \chi_2]^T : (k_{e_{\omega_r}}^2 tan\Lambda_1)/\pi + \chi_2^2/2 < \delta_1\}$ is compact. Thus, $\dot{\alpha}_D$ has a maximum constant value M_1 in the compact set $\Omega_{\omega_{r,d}} \times \Omega_1$, for given initial conditions (Zhao et al., 2016). So, based on Young's inequality,

$$|\dot{\alpha}_D \chi_2| \le \frac{1}{2} \chi_2^2 + \frac{1}{2} M_1^2. \qquad (6.21)$$

According to (6.21) and (6.19), (6.18) can be rewritten as,

$$\dot{V}_1 < -\gamma_1 e_{\omega_r}^2 sec^2 \Lambda_1 - \frac{1}{2} \chi_2^2 \left(\frac{2}{\tau_2} - 2 \right) + \frac{1}{2} M_1^2 + \frac{1}{2} e_{\dot{\omega}_r}^2. \qquad (6.22)$$

The parameter τ_2 is selected as $\tau_2 < 1$, to satisfy $(2/\tau_2 - 2) > 0$. Also, considering Lemma 6.1, $-\gamma_1 e_{\omega_r}^2 sec^2 \Lambda_1 < -\gamma_1 (k_{e_{\omega_r}}^2 \, tan\Lambda_1)/\pi$ holds true. Consequently, (6.22) is rewritten as,

$$\dot{V}_1 < -\sigma_{1,1} V_1 + \sigma_{1,2} + \frac{1}{2} e_{\dot{\omega}_r}^2, \qquad (6.23)$$

where, $\sigma_{1,1} = \min\{\gamma_1, (2/\tau_2 - 2)\}$ and $\sigma_{1,2} = M_1^2/2$.

Considering the measurement noise and the GRBFNN estimation of aerodynamic torque (5.10), the rotor dynamic response (6.11) can be rewritten as,

$$\ddot{\omega}_r = g_1 + c_3 \theta^{*T} h - \frac{a_3 \omega_{n,N} \beta \, T_a)_\beta}{2\xi_N} - \frac{a_3 \ddot{\beta} \, T_a)_\beta}{2\omega_{n,N}\xi_N} + G\beta_{ref} + \frac{a_3 \, T_a)_\beta}{2\xi_N} f + d, \quad (6.24)$$

where, $g_1 = c_1\omega_r + c_2\omega_g + c_4 T_g$, $d = c_1\nu_{\omega_r} + c_2\nu_{\omega_g} + c_4\nu_{T_g} + c_3\varepsilon + a_3\omega_{n,N} \, T_a)_\beta \nu_\beta/2\xi_N + a_3 \, T_a)_\beta \nu_{\ddot{\beta}}/2\omega_{n,N}\xi_N + a_3\omega_{n,N} D \, T_a)_\beta /2\xi_N + a_3\Delta T_a|_{\Delta C_p}$, $G = a_3 S_{\beta_u}\omega_{n,N}\rho \, T_a)_\beta /2\xi_N$ and $f = \Delta\tilde{f}_{PAD}/\omega_{n,N} + S_{\beta_u}\omega_{n,N}\Phi$.

Assumption 6.1. *Considering the limited achievable β, $\dot{\beta}$ and β_u, the boundedness of $\Delta\tilde{f}_{PAD}$, S_{β_u} and Φ are concluded. This, in turn, leads to the bounded fault term f in (6.24), considered as $|f| \leq \bar{f}$, where $\bar{f}$ is an unknown positive constant. Also, the time derivative of f is assumed to be bounded, i.e. $|\dot{f}| \leq \rho_{\dot{f}}$, where $\rho_{\dot{f}}$ is an unknown positive constant (Lan et al., 2018). Indeed, it is assumed that the applied fault is a slowly varying function of time. Besides, the sensor noise contents are assumed limited which is a reasonable practical issue. Accordingly, by considering Figure 4.6 and $|\varepsilon| \leq \bar{\varepsilon}$, the disturbance d is bounded as $|d| \leq \bar{D}$, where $\bar{D}$ is a positive unknown constant. Finally, it is easily seen that G is unknown but bounded, due to the presence of $T_a)_\beta$.*

Now the proposed pitch angle controller is designed as,

$$\beta_{ref} = N(\zeta_1)\upsilon_1, \qquad (6.25)$$

with,

$$\dot{\zeta}_1 = e_2 sec^2 \Lambda_2 \upsilon_1,$$

$$\upsilon_1 = g_1 + \frac{\chi_2}{\tau_2} + c_3 \hat{\theta}^T h + \frac{a_3 \omega_{n,N} \beta L}{2\xi_N} \tanh\left(\frac{e_{\dot{\omega}_r} \beta sec^2 \Lambda_2}{\eta_1}\right)$$

$$+ \frac{a_3 \ddot{\beta} L}{2\omega_{n,N}\xi_N} \tanh\left(\frac{e_{\dot{\omega}_r} \ddot{\beta} sec^2 \Lambda_2}{\eta_2}\right) + \hat{d} \tanh\left(\frac{e_{\dot{\omega}_r} sec^2 \Lambda_2}{\eta_3}\right) \qquad (6.26)$$

$$+ \frac{a_3 L \hat{f}}{2\xi_N} \tanh\left(\frac{e_{\dot{\omega}_r} sec^2 \Lambda_2}{\eta_4}\right) + \gamma_2 e_{\dot{\omega}_r},$$

associated with the adaptive laws,

$$\dot{\hat{f}} = \frac{e_{\dot{\omega}_r} a_3 L}{2\xi_N} sec^2 \Lambda_2 \tanh\left(\frac{e_{\dot{\omega}_r} sec^2 \Lambda_2}{\eta_4}\right) - \sigma_f \hat{f},$$

$$\dot{\hat{\theta}} = \Gamma\left(e_{\dot{\omega}_r} c_3 sec^2 \Lambda_2 h - \sigma_c \hat{\theta}\right), \qquad (6.27)$$

$$\dot{\hat{d}} = e_{\dot{\omega}_r} sec^2 \Lambda_2 \tanh\left(\frac{e_{\dot{\omega}_r} sec^2 \Lambda_2}{\eta_3}\right) - \sigma_d \hat{d},$$

to estimate the fault, GRBFNN weights and disturbance, respectively, where, η_1, η_2, η_3, η_4, γ_2, σ_f, σ_c, σ_d are positive design parameters. Also, $\Gamma \in \mathbb{R}^s$ is the design matrix such that $\Gamma = \Gamma^T > 0$. Accordingly, the estimation errors are defined as,

$$\tilde{f} = \hat{f} - f,$$

$$\tilde{d} = \hat{d} - \bar{D}, \qquad (6.28)$$

$$\tilde{\theta} = \hat{\theta} - \theta^*.$$

To accurately estimate the fault, the estimation error is to be bounded as $|\tilde{f}| \leq \rho_{\tilde{f}}$, where $\rho_{\tilde{f}}$ is an unknown positive variable (Lan et al., 2018). So, an adaptive law is used to estimate $\rho_{\tilde{f}}$ as,

$$\dot{\hat{\rho}}_{\tilde{f}} = -\sigma_{\tilde{f}} \hat{\rho}_{\tilde{f}}, \qquad (6.29)$$

where, $\sigma_{\tilde{f}}$ is a positive design parameter, with estimation error,

$$\tilde{\rho}_{\tilde{f}} = \hat{\rho}_{\tilde{f}} - \rho_{\tilde{f}}. \qquad (6.30)$$

Now, a positive definite Lyapunov function is selected as,

$$V_2 = \frac{k_{e_{\dot{\omega}_r}}^2}{\pi} tan\Lambda_2 + \frac{1}{2}\tilde{f}^2 + \frac{1}{2}\tilde{d}^2 + \frac{1}{2}\tilde{\theta}^T \Gamma^{-1}\tilde{\theta} + \frac{1}{2}\tilde{\rho}_{\tilde{f}}^2, \qquad (6.31)$$

where, $\Lambda_2 = \pi\xi_2^2/2$, $\xi_2 = e_{\dot{\omega}_r}/k_{e_{\dot{\omega}_r}}$ and $k_{e_{\dot{\omega}_r}}$ is a considered constraint on $e_{\dot{\omega}_r}$. It should be noted that V_2 is continuous in the set $\Omega_{e_{\dot{\omega}_r}} = \{e_{\dot{\omega}_r} : -k_{e_{\dot{\omega}_r}} < e_{\dot{\omega}_r} < k_{e_{\dot{\omega}_r}}\}$.

The Lyapunov function V_2 is positive definite, in which the first term captures the BLF characteristics of the modified tracking error ξ_2, according to Definition 6.1. The time derivative of ξ_2 is obtained as,

$$\dot{\xi}_2 = \frac{\ddot{\omega}_r + \frac{\chi_2}{\tau_2}}{k_{e_{\dot{\omega}_r}}}. \tag{6.32}$$

First-time derivative of (6.31) can be obtained as,

$$\begin{aligned}
\dot{V}_2 = {} & \tilde{f}(\dot{\hat{f}} - \dot{f}) + \tilde{d}\dot{\hat{d}} + \tilde{\theta}^T \Gamma^{-1} \dot{\hat{\theta}} + \tilde{\rho}_{\tilde{f}} \dot{\hat{\rho}}_{\tilde{f}} \\
& + e_{\dot{\omega}_r}\Big(g_1 + c_3 \theta^{*T} h - \frac{a_3 \omega_{n,N} \beta T_a)_\beta}{2\xi_N} \\
& - \frac{a_3 \ddot{\beta}.T_a)_\beta}{2\omega_{n,N}\xi_N} + G\beta_{ref} + \frac{a_3.T_a)_\beta}{2\xi_N} f + d + \frac{\chi_2}{\tau_2}\Big) sec^2 \Lambda_2.
\end{aligned} \tag{6.33}$$

Substituting (6.25)-(6.27) and (6.29) in (6.33) leads to,

$$\dot{V}_2 = GN\left(\zeta_1\right)\dot{\zeta}_1 + \dot{\zeta}_1 + \sum_{i=1}^{6} \Pi_i, \tag{6.34}$$

where,

$\Pi_1 = -(e_{\dot{\omega}_r} a_3 \omega_{n,N} \beta\, T_a)_\beta \, sec^2 \Lambda_2)/2\xi_N - e_{\dot{\omega}_r} a_3 \omega_{n,N} \beta L sec^2 \Lambda_2 tanh(\beta e_{\dot{\omega}_r} sec^2 \Lambda_2/\eta_1)\,/2\xi_N$,

$\Pi_2 = -(e_{\dot{\omega}_r} a_3 \ddot{\beta}\, T_a)_\beta \, sec^2 \Lambda_2)/2\omega_{n,N}\xi_N - e_{\dot{\omega}_r} a_3 \ddot{\beta} L sec^2 \Lambda_2 tanh\left(e_{\dot{\omega}_r} \ddot{\beta} sec^2 \Lambda_2/\eta_2\right)/2\omega_{n,N}\xi_N$,

$\Pi_3 = d e_{\dot{\omega}_r} sec^2 \Lambda_2 + \tilde{d} e_{\dot{\omega}_r} sec^2 \Lambda_2 tanh(e_{\dot{\omega}_r} sec^2 \Lambda_2/\eta_3) - \sigma_d \hat{d}\tilde{d} - \hat{d} tanh(e_{\dot{\omega}_r} sec^2 \Lambda_2/\eta_3) e_{\dot{\omega}_r} sec^2 \Lambda_2$,

$\Pi_4 = (e_{\dot{\omega}_r} a_3\, T_a)_\beta\, f sec^2 \Lambda_2)/2\xi_N - e_{\dot{\omega}_r} a_3 L f sec^2 \Lambda_2 tanh(e_{\dot{\omega}_r} sec^2 \Lambda_2/\eta_4)/2\xi_N - \sigma_f \hat{f}\tilde{f} - \tilde{f}\dot{f} - \sigma_{\tilde{f}} \hat{\rho}_{\tilde{f}} \tilde{\rho}_{\tilde{f}}$, $\Pi_5 = -\sigma_c \tilde{\theta}^T \hat{\theta}$, $\Pi_6 = -\gamma_2 e_{\dot{\omega}_r}^2 sec^2 \Lambda_2$.

Considering Remark 4.2 and the inequality $0 \le |e_{\dot{\omega}_r}|\,|\beta|\, sec^2 \Lambda_2$ leads to $(|T_a)_\beta||e_{\dot{\omega}_r}||\beta|sec^2\Lambda_2)/L \le |e_{\dot{\omega}_r}||\beta|sec^2\Lambda_2$. Accordingly, based on Lemmas 5.2 and 6.2, one can obtain,

$$\begin{aligned}
\Pi_1 \le {} & \frac{a_3 \omega_{n,N} L}{2\xi_N}\left(|e_{\dot{\omega}_r}|\,|\beta|\, sec^2 \Lambda_2 - e_{\dot{\omega}_r} \beta sec^2 \Lambda_2 \tanh\left(\frac{e_{\dot{\omega}_r} \beta sec^2 \Lambda_2}{\eta_1}\right)\right) \\
\le {} & \frac{a_3 \omega_{n,N} L}{2\xi_N} K \eta_1.
\end{aligned} \tag{6.35}$$

Similarly, considering $|T_a)_\beta||e_{\dot{\omega}_r}||\ddot{\beta}|sec^2\Lambda_2/L \le |e_{\dot{\omega}_r}||\ddot{\beta}|sec^2\Lambda_2$, leads to

$$\Pi_2 \leq \frac{a_3 L}{2\omega_{n,N}\xi_N} \left(|e_{\dot{\omega}_r}| \left| \dddot{\beta} \right| sec^2\Lambda_2 - e_{\dot{\omega}_r}\dddot{\beta} sec^2\Lambda_2 \tanh\left(\frac{e_{\dot{\omega}_r}\dddot{\beta} sec^2\Lambda_2}{\eta_2} \right) \right)$$
$$\leq \frac{a_3 L}{2\omega_{n,N}\xi_N} K\eta_2. \tag{6.36}$$

Also, with the aid of Lemma 6.2, the following inequality can be obtained.

$$\Pi_3 \leq \bar{D} |e_{\dot{\omega}_r}| sec^2\Lambda_2 - \bar{D}e_{\dot{\omega}_r} sec^2\Lambda_2 \tanh\left(\frac{e_{\dot{\omega}_r} sec^2\Lambda_2}{\eta_3} \right) - \sigma_d \hat{d}\tilde{d}$$
$$\leq \bar{D}K\eta_3 - \frac{\sigma_d}{2}\tilde{d}^2 + \frac{\sigma_d}{2}\bar{D}^2,$$
$$\Pi_4 \leq \frac{a_3 L\bar{f}}{2\xi_N} \left(|e_{\dot{\omega}_r}| sec^{2\Lambda_2} - e_{\dot{\omega}_r} sec^2\Lambda_2 \tanh\left(\frac{e_{\dot{\omega}_r} sec^{2\Lambda_2}}{\eta_4} \right) \right) - \frac{\sigma_f}{2}\tilde{f}^2 + \frac{\sigma_f}{2}\bar{f}^2$$
$$- \frac{\sigma_{\tilde{f}}}{2}\tilde{\rho}_{\tilde{f}}^2 + \frac{\sigma_{\tilde{f}}}{2}\rho_{\tilde{f}}^2 + \rho_f\rho_{\tilde{f}}$$
$$\leq -\frac{\sigma_f}{2}\tilde{f}^2 - \frac{\sigma_{\tilde{f}}}{2}\tilde{\rho}_{\tilde{f}}^2 + \frac{a_3 L\bar{f}}{2\xi_N}K\eta_4 + \frac{\sigma_f}{2}\bar{f}^2 + \frac{\sigma_{\tilde{f}}}{2}\rho_{\tilde{f}}^2 + \rho_f\rho_{\tilde{f}},$$
$$\Pi_5 \leq \frac{-\sigma_c}{2}||\tilde{\theta}||^2 + \frac{\sigma_c}{2}||\theta^*||^2 \leq \frac{-\sigma_c}{2\lambda_{max}(\Gamma^{-1})}\tilde{\theta}^T\Gamma^{-1}\tilde{\theta} + \frac{\sigma_c}{2}||\theta^*||^2,$$

$$\tag{6.37}$$

where, $\lambda_{max}(\Gamma^{-1})$ is the maximum eigenvalue of Γ^{-1}. Finally, considering Lemma 6.1, leads to

$$\Pi_6 < -\gamma_2 \frac{k_{\dot{\omega}_r}^2}{\pi} tan\Lambda_2. \tag{6.38}$$

Using (6.35)-(6.38) in (6.34) yields,

$$\dot{V}_2 < GN(\zeta_1)\dot{\zeta}_1 + \dot{\zeta}_1 - \sigma_{2,1}V_2 + \sigma_{2,2}, \tag{6.39}$$

where, $\sigma_{2,1} = \min\{\gamma_2, \sigma_f, \sigma_d, \sigma_c/\lambda_{max}(\Gamma^{-1}), \sigma_{\tilde{f}}\}$ and $\sigma_{2,2} = a_3\omega_{n,N}LK\eta_1/2\xi_N + a_3LK\eta_2/2\omega_{n,N}\xi_N + \bar{D}K\eta_3 + \sigma_d\bar{D}^2/2 + a_3L\bar{f}K\eta_4/2\xi_N + \sigma_f\bar{f}^2/2 + \sigma_{\tilde{f}}\rho_{\tilde{f}}^2/2 + \rho_f\rho_{\tilde{f}} + \sigma_c||\theta^*||^2/2$.

Now, the main property of the designed pitch controller is given in the following theorem.

Theorem 6.1. *Consider the wind turbine rotor dynamic model (6.11), with non-smooth input saturation (6.1) approximated with (6.4), including pitch actuator bias, effectiveness loss, dynamic changes and blade aerodynamic change, under Assumption 6.1. If initial conditions satisfy $e_{\omega_r}(0) \in \{e_{\omega_r} : |e_{\omega_r}(0)| < k_{e_{\omega_r}}\}$ and*

$e_{\dot{\omega}_r}(0) \in \{e_{\dot{\omega}_r} : |e_{\dot{\omega}_r}(0)| < k_{e_{\dot{\omega}_r}}\}$, *via utilizing control inputs* (6.25), (6.26) *with filter* (6.13), *virtual control* (6.17) *adaption laws* (6.27) *and* (6.29), *then the following objectives are obtained.*

(i) All states of the closed-loop system are bounded

(ii) The constraint sets $\Omega_{e_{\omega_r}} = \{e_{\omega_r} : |e_{\omega_r}| < k_{e_{\omega_r}}\}$ and $\Omega_{e_{\dot{\omega}_r}} = \{e_{\dot{\omega}_r} : |e_{\dot{\omega}_r}| < k_{e_{\dot{\omega}_r}}\}$ are not violated for $i = 1, 2$

(iii) The tracking error e_{ω_r} can be made small by the proper choice of the design parameters.

The proof of this theorem is given in A.8.

6.4 Fault Identification

In this section, a scheme is given to identify the pitch actuator fault, including pitch bias Φ, effectiveness loss ρ, dynamic change $\Delta \tilde{f}_{PAD}$, and aerodynamic characteristic change $\Delta T_a|_{\Delta C_p}$. For this aim, the auxiliary signals are calculated and compared with the estimated fault $\hat{f}$ to identify dynamic change cases. Considering Table 3.1, the auxiliary signals are defined as (5.28). Now to finalize the pitch actuator fault identification scheme, first, the dynamic change case is considered, assuming no pitch actuator bias. Considering $f = \Delta \tilde{f}_{PAD}/\omega_{n,N} + S_{\beta_u}\omega_{n,N}\Phi$, in absence of Φ, it can be obtained that $f = \Delta \tilde{f}_{PAD}/\omega_{n,N}$. So, using the auxiliary signals $f_{auxiliary, X}$, the most similar one to $\hat{f}$, is identified as the dynamic change case. So, similarity indices are needed, on which basis the fault identification is conducted. The indices adopted in this chapter are RMSE and VAF defined as,

$$
\begin{aligned}
RMSE_X &= \sqrt{\frac{1}{t_{exe}} \int_0^{t_{exe}} \left(f_{auxiliary,X} - \hat{f} \right)^2 dt}, \\
VAF_X &= \left(1 - \frac{var\left(f_{auxiliary,X} - \hat{f} \right)}{var\left(f_{auxiliary,X} \right)} \right) \times 100\%.
\end{aligned}
\tag{6.40}
$$

In the ideal fault identification case, RMSE and VAF indices are zero and 100%, respectively. Accordingly, the case X with RMSE and VAF indices close to zero and 100%, respectively, is selected as the corresponding dynamic change case, i.e. $\hat{X}$. The pitch bias Φ is considered as an added constant on the accumulative fault f. So, even in the presence of pitch bias with dynamic change, only the RMSE index deviates significantly from zero, but the VAF index still indicates the correct dynamic change properly. Now, after indicating $\hat{X}$, the pitch actuator bias is estimated. Considering $f = f_{auxiliary,\hat{X}}/\omega_{n,N} + S_{\beta_u}\omega_{n,N}\Phi$, where $f_{auxiliary,\hat{X}}$ is the

calculated auxiliary signal using (5.28) for the indicated dynamic change $\hat{X}$, the estimation of pitch actuator bias, $\hat{\Phi}$, is as,

$$\hat{\Phi} = \frac{\omega_{n,N}\hat{f} - f_{auxiliary,\hat{X}}}{S_{\beta_u}\omega_{n,N}^2}.$$
(6.41)

Finally, if neither dynamic change case nor pitch actuator bias is identified, and meanwhile, the fault-free case is not identified, then it can be concluded that the faulty case is either pitch actuator effectiveness loss or aerodynamic characteristic change. Considering (6.24), it is clear that the aerodynamic characteristic change is seen as an additive disturbance, and attenuated by the proposed controller. On the other hand, the effectiveness loss is contributing in the control gain, i.e. G. So, the estimated fault $\hat{f}$ is affected by the effectiveness loss and is insensitive to the aerodynamic characteristic change. Accordingly, consider the given period, in which no pitch actuator dynamic change, bias or fault-free cases are identified. Then if $\hat{f}$ is considerably disturbed from zero, this leads to effectiveness loss identification. Otherwise, the aerodynamic characteristic change is identified.

6.5   Numerical Evaluation and Comparison

In this section, the numerical simulations are studied to evaluate the performance of the proposed controller (6.25), both in fault-free and faulty situations. Also, a comparison is made to the industrial baseline controller (4.10) to illustrate the superiority of the proposed controller, considering the numerical criteria Table 3.3. It should be noted that different fault scenarios, including separated and simultaneous ones, and wind speed variations are introduced to investigate the robustness of the proposed controller.

The parameter values of the proposed controller are given in Section B.4. The constraints on the rotor speed and its time derivative are selected as, $k_{e_1} = 0.02\,(rad/s)$, $k_{e_2} = 0.04\,(rad/s^2)$, respectively. So, it can be concluded that the inequalities $|\omega_r - \omega_{r,N}| \leq 0.02\,(rad/s)$ and $|\dot{\omega}_r| \leq 0.04\,(rad/s^2)$ are to be satisfied. Consequently, considering the desired operational mode leads to the constraints on generator shaft speed and generated power as, $|\omega_g - \omega_{g,N}| \leq 1.9\,(rad/s)$ and $|P_g - P_{g,N}| \leq 0.056\,(MW)$, respectively. As it is obvious in (6.25), a Nussbaum type function is needed. In this chapter the Nussbaum function $N(\zeta_1) = \zeta_1^2\cos(\zeta_1)$ is used which complies with Definition 4.2.

6.5.1 Fault-free situation

Firstly, the performance of the proposed controller in the fault-free situation under wind speed variation with mean $19.84\ (m/s)$ and standard deviation $1.94\ (m/s)$, illustrated in Figure 6.2, is studied for $1500\ (s)$. It is expected that the mentioned constraints are not violated, the pitch angle saturation is smoothly avoided, and that the performance is to be improved compared to the baseline controller.
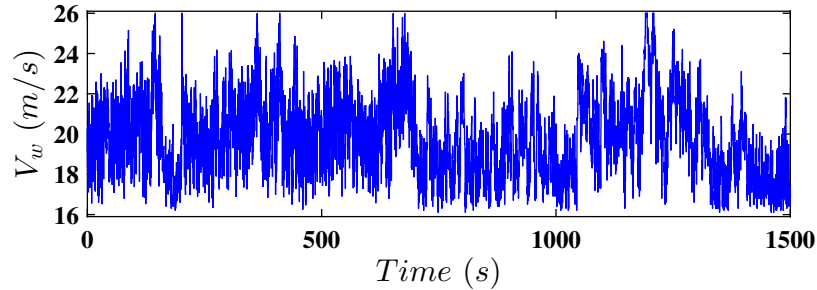
FIGURE 6.2: Free wind speed profile.

The corresponding rotor speed, rotor acceleration, generator speed and generated power, using the proposed controller, are shown in Figures 6.3-6.6, respectively. It is obvious that the considered constraints are not violated. Also, using the same wind speed, the baseline controller results are given in Figures 6.3-6.6. It is obvious that the baseline controller is not able to keep the corresponding outputs within the considered constraints, in the presence of the wind speed variation. Also, the designed reference pitch angle using both controllers are compared in Figure 6.7, in which it is obvious that using the baseline controller has caused the pitch actuator saturation. In contrast, the proposed controller has smoothly avoided the saturation. It should be noted that, as the proposed controller has kept the rotor speed within the constraints, despite the high wind speed variation, more pitch angle variation is requested, compared to the baseline one. As mentioned in Section 6.2, the proposed controller is designed on the desired trajectory of the wind turbine, on which the drive train torsion angle is reduced. In this regard, to investigate this issue, the induced drive train torsion angle using the proposed and baseline controllers are depicted in Figure 6.8. It is obvious that the induced drive train torsion angle using the proposed controller has been kept in the same order as the baseline one. This implies that the proposed controller has not considerably increased drive train torsion and, consequently, stress, despite the wind speed variation and more accurate nominal power tracking. As it is obvious in the proposed controller structure, the unknown aerodynamic torque is estimated by the GRBFNN. This estimation is shown in Figure 6.9, in which the actual aerodynamic torque is illustrated to evaluate the estimation efficiency. It is obvious that the aerodynamic torque is estimated accurately-enough and has been kept around the nominal one, same as

the actual aerodynamic torque. Finally, to accurately compare the results, the performance criteria using both controllers are summarized in Table 6.1. Evidently, the performance criteria $CC1$, $CC2$ and $CC3$ have been considerably reduced via using the proposed controller. These results comply with the Figures 6.3, 6.5 and 6.6. Also, the criterion $CC4$ shows the same induced drive train torsion angle rate, as has been illustrated in Figure 6.8. The criterion $CC6$ shows the advantage of using the smooth pitch angle saturation, as depicted in Figure 6.7. As mentioned earlier, the more accurate nominal power tracking needs higher pitch angle change, in the presence of high wind speed variation. This issue can be seen considering criterion $CC8$. So, it can be concluded that the proposed controller improves the wind turbine performance in the fault-free case compared to the industrial baseline controller.
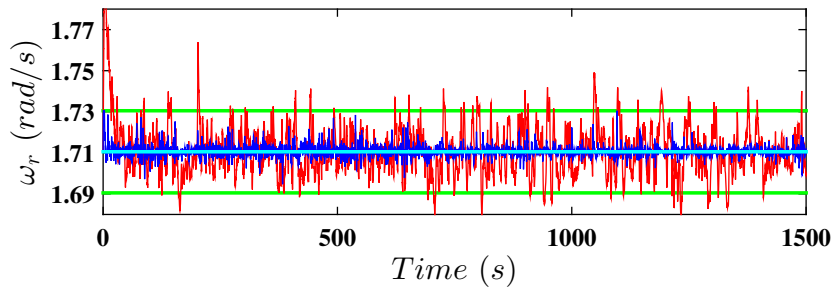
FIGURE 6.3: Rotor speed using the proposed controller (dark blue line), baseline controller (red line), nominal rotor speed (light blue line), and constraints (green line), in fault-free situation.

FIGURE 6.4: Rotor acceleration using the proposed controller (dark blue line), baseline controller (red line), and constraints (green line), in fault-free situation.

6.5.2   Faulty situation

In this section, in the presence of the faults, the fault tolerance capability of the proposed controller is evaluated. It is expected that the mentioned constraints are

FIGURE 6.5: Generator speed using the proposed controller (dark blue line), baseline controller (red line), nominal generator speed (light blue line), and constraints (green line), in fault-free situation.

FIGURE 6.6: Generated power using the proposed controller (dark blue line), baseline controller (red line), nominal power (light blue line), and constraints (green line), in fault-free situation.

not violated and the fault effects are attenuated. Also, the estimated fault is examined to accurately identify the considered faults. The results using the baseline controller are given to study the effect of each fault as well as to signify the benefit of the proposed controller. The considered fault scenario is defined in Table 6.2. The fault periods are separated to accurately study the effect of each fault. Also, the wind speed, shown in Figure 6.2, is used again to compare the results to the corresponding fault-free ones. In Figures 6.10-6.13, the rotor speed, rotor acceleration, generator speed and generated power associated with corresponding constraints are illustrated, respectively, using both proposed and baseline controllers. Compared to Figures 6.3-6.6, it is obvious that the baseline controller performance is deteriorated, while the proposed controller is able the attenuate the fault effects and keep the considered outputs within the corresponding constraints. The designed reference pitch angle using both controllers are compared in Figure 6.14, in which it is obvious that using the baseline controller has caused the pitch actuator saturation, while, the saturation is smoothly avoided using the proposed controller. It should be noted, as the proposed controller is trying to remove the pitch actuator dynamic change, while the dynamic change has reduced the speed of the pitch actuator, it has led to slightly more pitch angle variation compared to the fault-free case, in

FIGURE 6.7: Reference pitch angle using the proposed controller (dark blue line) and baseline controller (red line), in fault-free situation.
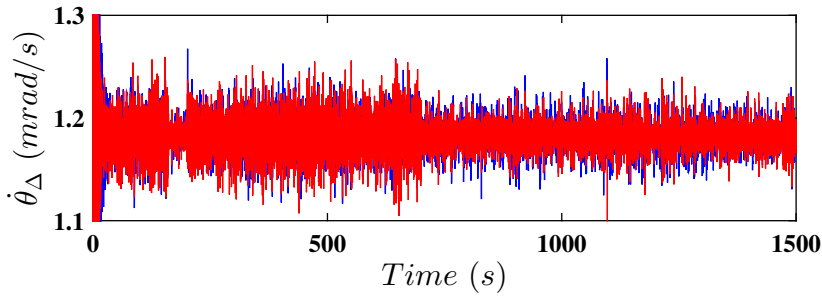
FIGURE 6.8: Induced drive train torsion angle rate using the proposed controller (dark blue line) and baseline controller (red line), in fault-free situation.

the dynamic change periods. Consequently, the induced drive train torsion angle using the proposed controller, has been increased in the mentioned time periods, as illustrated in Figure 6.15.

Now, to accurately, study the effect of the considered faults, compared to the fault-free case, the change in all variables with respect to the fault-free one is considered, which is defined as follows.

$$\delta X = X_{ff} - X_{fa}, \tag{6.42}$$

where, δX is the change in the considered variable X, X_{ff} is the fault-free value and X_{fa} is the value in the faulty situation. In Figures 6.16-6.18, δP_g, $\delta \omega_g$ and $\delta \omega_r$, are illustrated respectively, for both proposed and baseline controllers. It is obvious that the pitch actuator bias and effectiveness loss have led to considerable change in the baseline controller performance. However, these changes are significantly attenuated using the proposed controller. Also, the effect of the considered blade aerodynamic change, i.e. $\Delta T_a|_{\Delta C_p} = 5\%$, has led to less variation. It should be noted that in the pitch actuator dynamic change situations, as the pitch actuator response becomes slower, the performance difference is less obvious, among

TABLE 6.1: Values of the performance criteria for fault-free situation

Performance criteria	Proposed controller	Baseline controller
$CC1$	400.7 $(GW^2 s)$	2256 $(GW^2 s)$
$CC2$	1331 $(\mu rad^2/s)$	1416 $(\mu rad^2/s)$
$CC3$	138.9 (rad^2/s)	2266 (rad^2/s)
$CC4$	0.056 (MW)	0.2937 (MW)
$CC6$	29.37 $(°)$	30 $(°)$
$CC8$	10 $(°/s)$	9.79 $(°/s)$

TABLE 6.2: First Fault scenario.

Fault type	Fault effect	Fault period
Pitch actuator pump wear	$\alpha_{f_1} = 0.6316$, $\alpha_{f_2} = 0.29688$	$200 - 300$ (s)
Pitch actuator hydraulic leak	$\alpha_{f_1} = 1$, $\alpha_{f_2} = 0.87853$	$400 - 500$ (s)
Pitch angle bias	$\Phi = 5°$	$600 - 700$ (s)
Pitch actuator high air	$\alpha_{f_1} = 0.81083$, $\alpha_{f_2} = 1$	$800 - 900$ (s)
Pitch actuator effectiveness loss	$\rho = 0.7$	$1000 - 1100$ (s)
Aerodynamic characteristic change	$\Delta T_a\|_{\Delta C_p} = 5\%$	$1200 - 1300$ (s)
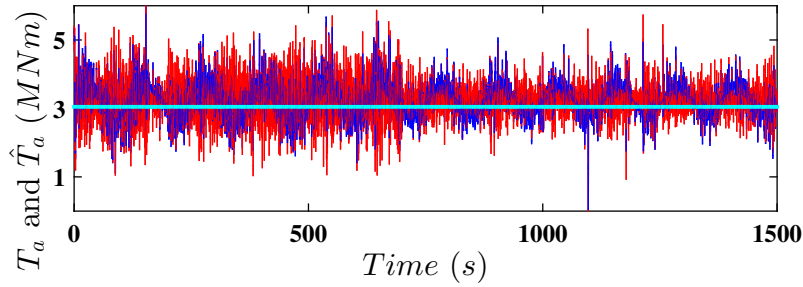
FIGURE 6.9: Actual aerodynamic torque (red line), estimated one
(dark blue line), and nominal one (light blue line).
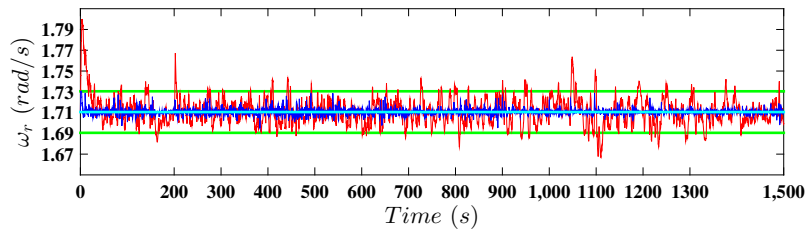
FIGURE 6.10: Rotor speed using the proposed controller (dark blue
line), baseline controller (red line), nominal rotor speed (light blue
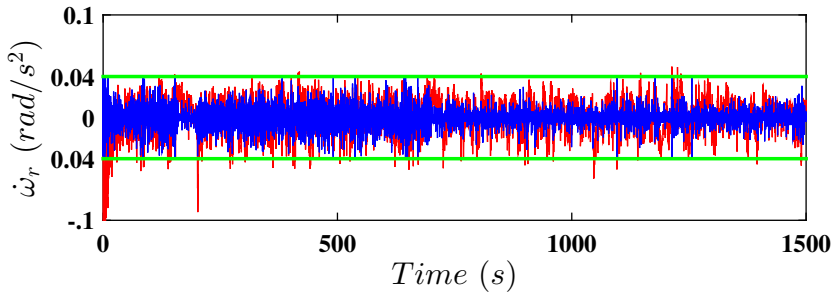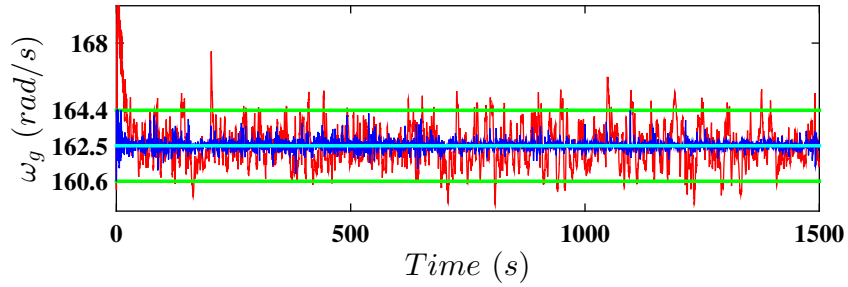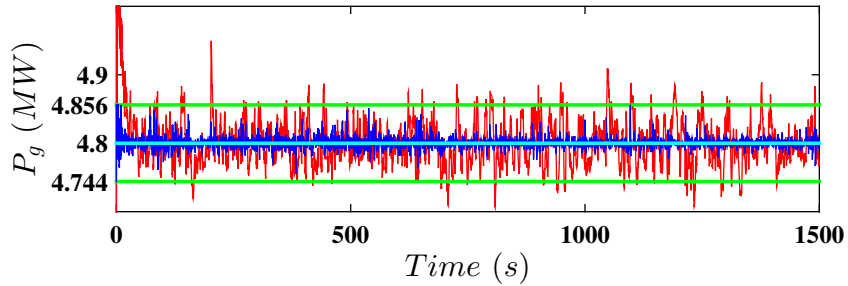line), and constraints (green line), under first fault scenario.

which the hydraulic leak has notable effects. To accurately study the effect of faults
on the pitch actuator response, $\delta\beta$ is depicted in Figure 6.19. Evidently, the pitch
actuator dynamic changes have been considerably attenuated using the proposed
controller, while the slower pitch actuator and consequent difference, are obvious
in the baseline controller performance. Also, the effect of pitch actuator bias, is
completely removed, in which at the beginning and end of the corresponding bias
period, the estimated bias is subtracted abruptly to remove its effect. This effect is
obvious considering the baseline performance. The same result is obtained consid-
ering the effectiveness loss period. In the blade aerodynamic change period, both
controllers have led to the same trend in $\delta\beta$, while the variation using the baseline
controller is significantly higher. Even though, this fault is removed from the blade
after $1300\,(s)$, but its effect has yet disturbed the baseline controller performance.

Finally, to numerically compare the performance of the controllers, the criteria
are summarized in Table 6.3. It can be pointed out that the performance of the
proposed controller remained very similar to the fault-free case, as this is the main
objective of FTC design.
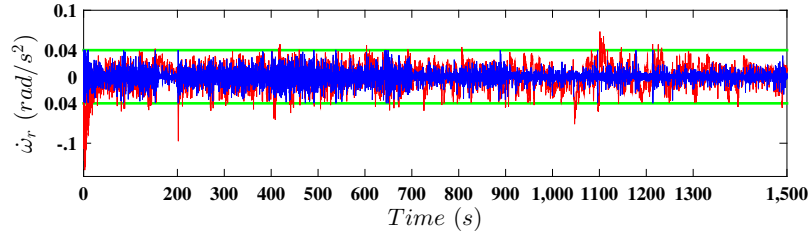
FIGURE 6.11: Rotor acceleration using the proposed controller (dark blue line), baseline controller (red line), and constraints (green line), under first fault scenario.
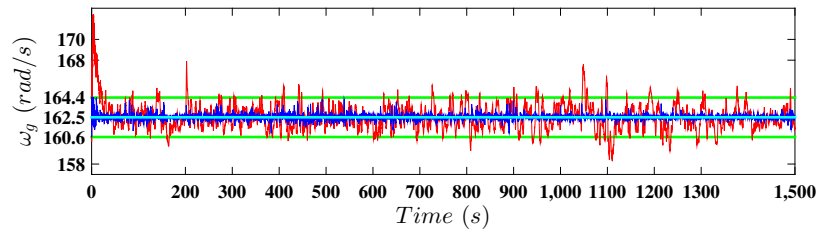
FIGURE 6.12: Generator speed using the proposed controller (dark blue line), baseline controller (red line), nominal generator speed (light blue line), and constraints (green line), under first fault scenario.

Fault identification

In this section, with aid of the estimated fault $\hat{f}$ and calculated auxiliary signals (5.28), the faults are identified, using the similarity indices (6.40). The identification includes detection of the presence of the fault and the fault type. Consequently, the estimated pitch actuator bias $\hat{\Phi}$ is obtained using (6.41), in which S_{β_u} is calculated using $2\eta(\bar{\varrho} + \underline{\varrho})/(P + P^{-1})^2|_{\beta_s}$. It should be noted that these indices and the estimated fault should be obtained and compared in every time step of operation, to

TABLE 6.3: Values of the performance criteria under first fault scenario

Performance criteria	Proposed controller	Baseline controller
$CC1$	414.8 (GW^2s)	2506 (GW^2s)
$CC2$	1349 $(\mu rad^2/s)$	1438 $(\mu rad^2/s)$
$CC3$	155 (rad^2/s)	2552 (rad^2/s)
$CC4$	0.056 (MW)	0.2941 (MW)
$CC6$	29.26 $(°)$	30 $(°)$
$CC8$	10 $(°/s)$	10 $(°/s)$
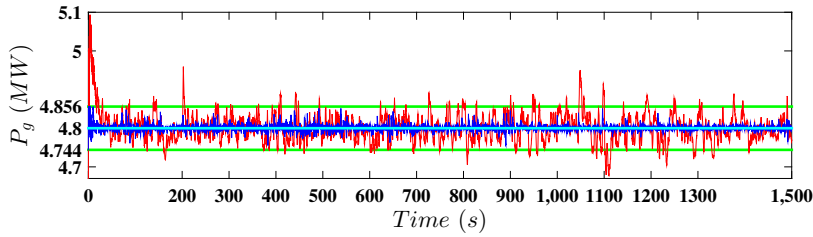
FIGURE 6.13: Generated power using the proposed controller (dark blue line), baseline controller (red line), nominal power (light blue line), and constraints (green line), under first fault scenario.
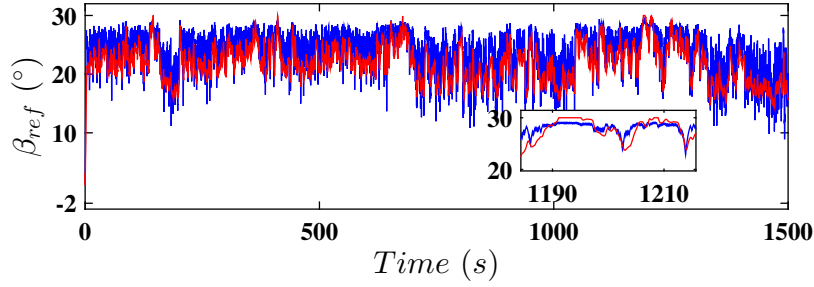

FIGURE 6.14: Reference pitch angle using the proposed controller (dark blue line) and baseline controller (red line), under first fault scenario.

accurately identify the fault. However, in this section, for the sake of clear explanation and investigation of the mentioned approach, the comparison is conducted in each fault period. Also, as the calculated auxiliary signal for fault-free case, i.e. $f_{auxiliary, \, fault \, free}$, is always zero, then the $VAF_{fault \, free}$ in (6.40) is calculated as $var(\hat{f}) \times 100\%$. Now, to investigate the fault identification capability of the proposed controller, the obtained $\hat{f}$ is illustrated in Figure 6.20. Also, the calculated auxiliary signals (5.28) are depicted in Figure 6.21. Also, with aid of fault identification indices of (6.40), which are summarized in Table 6.4, the estimated pitch actuator bias is shown in Figure 6.22. As mentioned earlier, for the fault identification, the case in which the RMSE and VAF indices have close values to zero and 100%, respectively, is selected as the fault case. Considering Table 6.4, it is obvious that in each fault-free period, the indices are indicating the fault-free case. Also, the estimated pitch actuator bias is zero. In pitch actuator dynamic change cases, it is obvious that the selected indices lead to the accurate identification of corresponding actual dynamic change case. In all dynamic change cases, the estimated pitch actuator bias is zero. So, the dynamic change cases are clearly distinguished from pitch actuator bias. Evidently, in the pitch actuator bias period, no indices satisfy the given conditions to be selected. On the other hand, the pitch actuator bias is precisely estimated. Now consider the pitch actuator effectiveness loss and aerodynamic characteristic change periods. Obviously, neither the dynamic change case nor the fault-free case is selected, as the corresponding indices do not satisfy the given conditions. On the other hand, pitch actuator bias is estimated as zero. So,
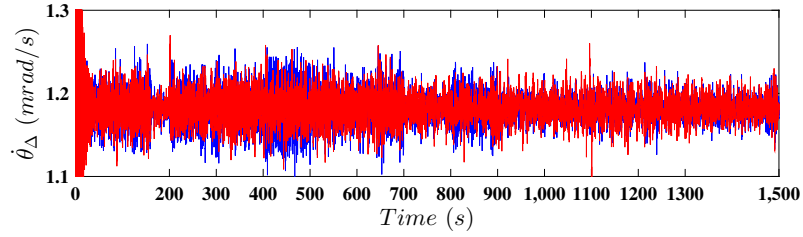
FIGURE 6.15: Induced drive train torsion angle rate using the proposed controller (dark blue line) and baseline controller (red line), under first fault scenario.

FIGURE 6.16: δP_g using the proposed controller (dark blue line) and baseline controller (red line), under first fault scenario.

it can be concluded that these two periods represent the pitch actuator effectiveness loss and/or aerodynamic characteristic change. Now to identify these two cases, firstly consider the estimated fault, i.e. Figure 6.20. Now, considering (6.24), it is obvious that aerodynamic characteristic change is treated as an additive disturbance, while the effectiveness loss is contributing in the control gain, i.e. G. The proposed controller has proved to be insensitive to the considered disturbances. Accordingly, the estimated fault is affected by the effectiveness loss and it is insensitive to the aerodynamic characteristic change. So, in $1000 - 1100(s)$, as the estimated fault is not zero, the effectiveness loss case is identified. Also, in $1200 - 1300(s)$, as the estimated fault is zero, the aerodynamic characteristic change case is identified.

6.5.3 Further robustness evaluation

In this section, the proposed controller is further evaluated in terms of robustness to different wind speed and fault scenarios. The wind speed is shown in Figure 6.23, with mean 20.41 (m/s) and standard deviation 3.01 (m/s) for $1100(s)$. Compared to the former wind speed profile, i.e. Figure 6.2, the current one is more varying. So, it is more challenging for the controller to satisfy the objectives. Also, in the fault scenario, which is summarized in Table 6.5, the faults are introduced simultaneously for a longer period. Also, the pitch actuator bias and aerodynamic characteristic change values are increased. On the other hand, the pitch actuator effectiveness

TABLE 6.4: Fault identification indices for first fault scenario.

Time (s)	Fault type	High Air Content		Hydraulic Leak	
		RMSE	VAF	RMSE	VAF
0-200	Fault-Free	0.37	-788	0.36	-842
200-300	Pump Wear	3.25	50.94	1.94	66.65
300-400	Fault-Free	0.31	-890	0.31	-932
400-500	Hydraulic Leak	2.40	75.01	**0.19**	**99.26**
500-600	Fault-Free	0.35	-921	0.34	-963
600-700	Pitch Bias	27.82	-41.85	21.99	-32.33
700-800	Fault-Free	6.24	-93370	6.20	-68300
800-900	High Air Content	**0.42**	**97.50**	1.81	76.41
900-1000	Fault-Free	0.53	-866	0.41	-923
1000-1100	Effectiveness Loss	19.14	-8903	18.7	-5800
1100-1200	Fault-Free	1.71	-8870	1.67	-5990
1200-1300	Aerodynamic change	0.29	-751.6	0.28	-807.95
1300-1500	Fault-Free	0.46	-755	0.46	-811

Time (s)	Fault type	Pump Wear		Fault-Free		mean ($\hat{\Phi}$)
		RMSE	VAF	RMSE	VAF	
0-200	Fault-Free	0.39	-5916	**0.43**	**99.98**	0
200-300	Pump Wear	**0.15**	**98.91**	1.46	215.12	0
300-400	Fault-Free	0.33	-6291	**0.37**	**97.65**	0
400-500	Hydraulic Leak	67.99	2.4	2.54	575.7	0
500-600	Fault-Free	0.37	-6420	**0.41**	**99.86**	0
600-700	Pitch Bias	18.67	-24.33	87.62	4.05	**5**
700-800	Fault-Free	6.24	-182000	**6.35**	**97.85**	0
800-900	High Air Content	1.64	79.01	1.95	383.6	0
900-1000	Fault-Free	0.44	-6309	**0.05**	**99.89**	0
1000-1100	Effectiveness Loss	19.56	-16700	21.05	1100	0
1100-1200	Fault-Free	1.75	-17300	**1.88**	**99.17**	0
1200-1300	Aerodynamic change	0.31	-5770	0.34	11.89	0
1300-1500	Fault-Free	0.49	-5790	**0.54**	**98.38**	0
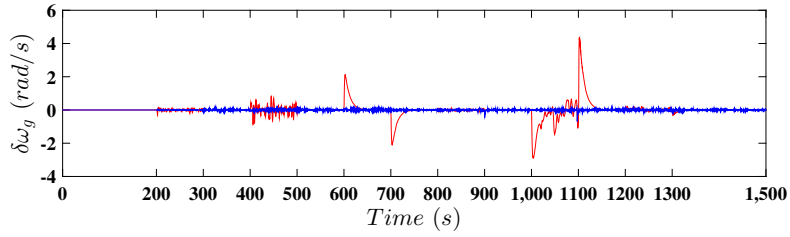
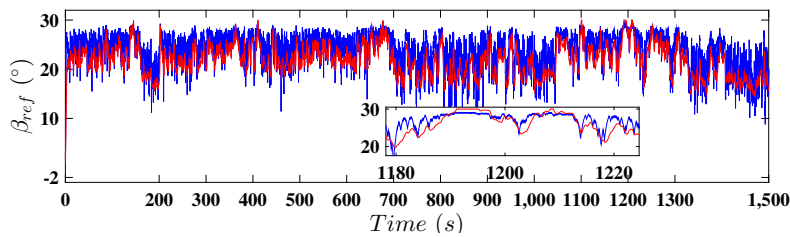FIGURE 6.17: $\delta\omega_g$ using the proposed controller (dark blue line) and baseline controller (red line), under first fault scenario.
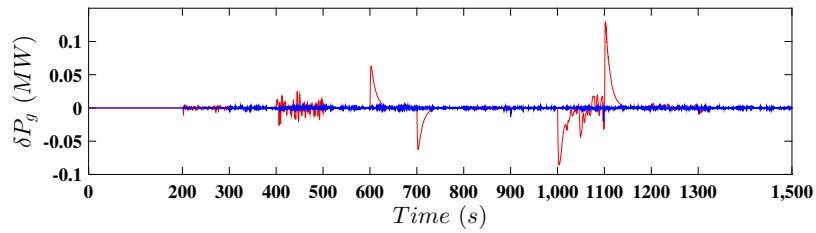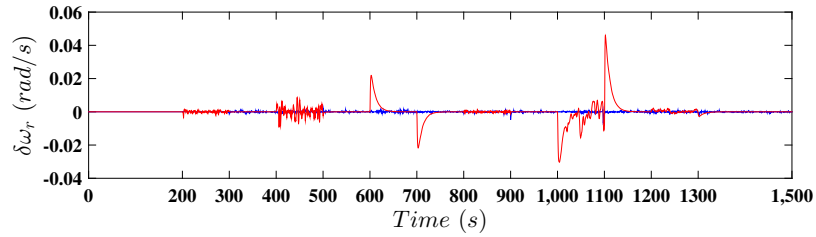

FIGURE 6.18: $\delta\omega_r$ using the proposed controller (dark blue line) and baseline controller (red line), under first fault scenario.

is decreased. To avoid the repetitive studies, only the generated power in fault-ree and fault cases, using both controllers are considered, for the sake of brevity. Also, the performance criteria are compared. The generated power in both fault-free and faulty situations are illustrated in Figures 6.24 and 6.25, respectively. It is obvious that in both situations, the generated power is maintained within the given constraints. The performance criteria are summarized in the Tables 6.6 and 6.7, which further confirm that, despite the baseline controller, the proposed controller can successfully maintain reliable performance under faulty condition.

TABLE 6.5: Second Fault scenario.

Fault type	**Fault effect**	**Fault period**
Pitch actuator pump wear	$\alpha_{f_1} = 0.6316, \ \alpha_{f_2} = 0.29688$	$100 - 300 \ (s)$
Pitch actuator effectiveness loss	$\rho = 0.5$	$100 - 300 \ (s)$
Pitch actuator hydraulic leak	$\alpha_{f_1} = 1, \ \alpha_{f_2} = 0.87853$	$400 - 600 \ (s)$
Pitch angle bias	$\Phi = 10°$	$400 - 600 \ (s)$
Pitch actuator high air	$\alpha_{f_1} = 0.81083, \ \alpha_{f_2} = 1$	$800 - 1000 \ (s)$
Aerodynamic characteristic change	$\Delta T_a|_{\Delta C_p} = 10\%$	$800 - 1000 \ (s)$

TABLE 6.6: Values of the performance criteria in fault-free situation
with second wind speed

Performance criteria	Proposed controller	Baseline controller
$CC1$	465 $(GW^2 s)$	1817 $(GW^2 s)$
$CC2$	1299 $(\mu rad^2/s)$	1371 $(\mu rad^2/s)$
$CC3$	212.5 (rad^2/s)	1762 (rad^2/s)
$CC4$	0.056 (MW)	0.2094 (MW)
$CC6$	29.12 $(°)$	30 $(°)$
$CC8$	10 $(°/s)$	7.46 $(°/s)$

TABLE 6.7: Values of the performance criteria under second fault
scenario with second wind speed

| Performance criteria	Proposed controller	Baseline controller
$CC1$	544.9 $(GW^2 s)$	3549 $(GW^2 s)$
$CC2$	1421 $(\mu rad^2/s)$	1376 $(\mu rad^2/s)$
$CC3$	304.2 (rad^2/s)	3747 (rad^2/s)
$CC4$	0.056 (MW)	0.2214 (MW)
$CC6$	29.40 $(°)$	30 $(°)$
$CC8$	10 $(°/s)$	10 $(°/s)$
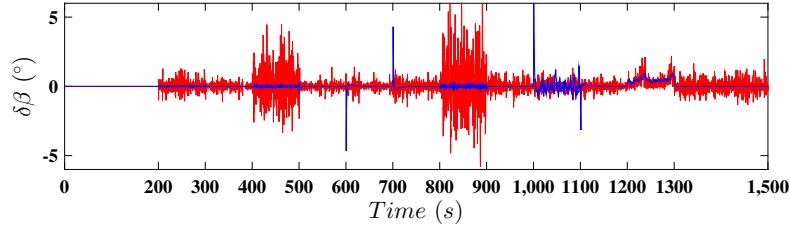
FIGURE 6.19: $\delta\beta$ using the proposed controller (dark blue line) and baseline controller (red line), under first fault scenario.
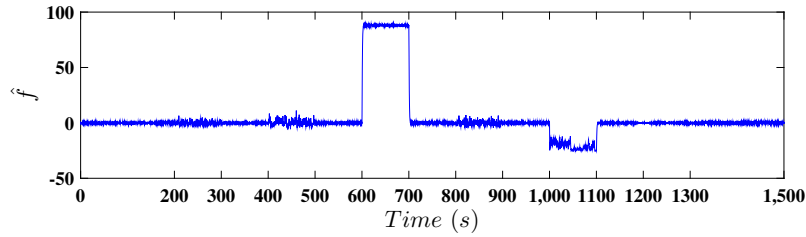
FIGURE 6.20: Estimated fault for first fault scenario.

6.6   Discussion

Considering the simulation results in fault-free and first fault scenario, i.e. Table 6.2, using the same wind speed profile, i.e. Figure 6.2, it can be pointed out the proposed controller is able to keep the wind turbine performance in the same level. Firstly, it is obvious that the generated power never violates the given bound. It should be noted that this bound is appropriately selected by the wind turbine manufacturer. Indeed, this bound represents the safe-to-operate bound in full load operation without the mechanical brake engagement. On the other hand, the mechanical braking increases the induced fatigue load on the drive train. Also, as the rotor acceleration is constrained, it leads to less stress on the rotor shaft. So, it can be concluded that via utilizing the proposed controller, less fatigue load and stress are induced to the drive train. One obvious benefit of the proposed controller is that harsh long-lasting pitch actuator saturation is avoided. In fact, using the smooth pitch actuator saturation function, the speed of the pitch actuator response is increase before the saturation, as it is obvious in Figure 6.1. This characteristic has led to the improved power regulation. On the other hand, the smooth saturation bounds have been kept smaller in value than the actual ones. It has been illustrated that the induced drive train torsion angle rate, has been kept in the same level as the baseline controller one. So, considering industrial acceptability of the baseline controller, the proposed controller can be approved by industry, in terms of applied torsional stress. It is evident that the estimated aerodynamic torque is fluctuating around the nominal one, due to the inherent features of GRBFNN and the Gaussian basis functions. However, as mentioned in the controller design procedure, the estimation error is
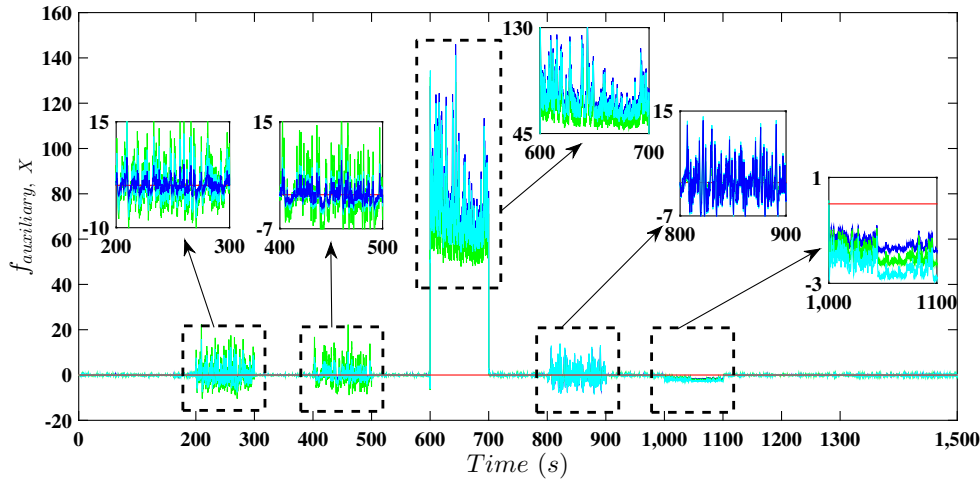
FIGURE 6.21: Auxiliary signal in the case of fault-free (red line), pump wear (dark blue line), high air content (green line), and hydraulic leak (light blue line).
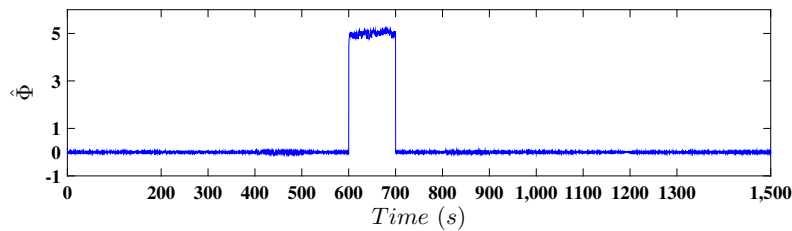
FIGURE 6.22: Estimated pitch actuator bias for first fault scenario.

bounded. This is obvious when comparing the actual aerodynamic torque and the estimated one. As mentioned earlier, the pitch actuator dynamic change, leads to slower response of the pitch actuator and consequently poor power regulation. This phenomenon is obvious in Figures 6.16 and 6.19. Nevertheless, the proposed controller has been shown to be able to attenuate this effect, same as the effects of the pitch actuator bias, using the properly-designed fault estimator. On the other hand, the effects of the pitch actuator effectiveness loss and debris build-up are mitigated appropriately, satisfying the performance objectives. Also, using the fault estimator information alongside the proposed fault identification scheme, different faults are identified. Similar outcomes are obtained, considering the results for the more severe instantaneous faults and higher wind speed variation.

In this chapter, a new adaptive constrained control methodology was proposed for wind turbines in power regulation subject to actuation failures as well as unknown system dynamics. Using BLF in conjunction with the concept of DSC a constrained control structure was developed that ensured stable tracking while reducing
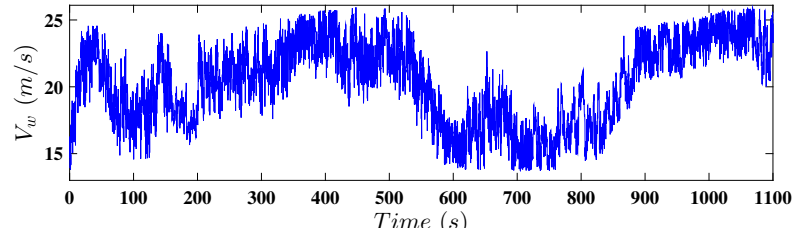
FIGURE 6.23: Second free wind speed profile.
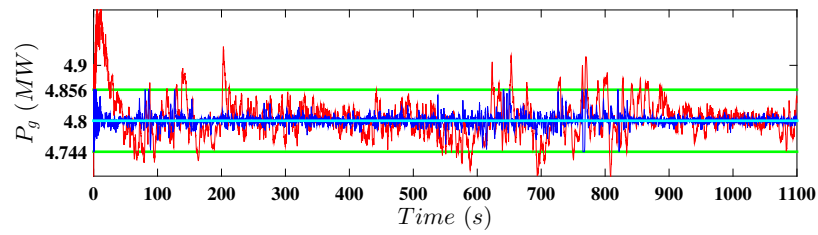
FIGURE 6.24: Generated power using the proposed controller (dark blue line), baseline controller (red line), nominal power (light blue line), and constraints (green line), in fault-free situation, with second wind speed.

the computational cost. In addition, utilizing GRBFNN together with a proper fault-tolerant scheme, the precise wind turbine mathematical model and actuation faults were not required. In contrast to previous works where the unknown wind speed observer/estimator was needed, using the Nussbaum-type function, the proposed method handled the unpredictable wind speed variation effects in the control design without requiring wind speed measurement. Numerical simulations were performed to validate the effectiveness of the reported theoretical developments.
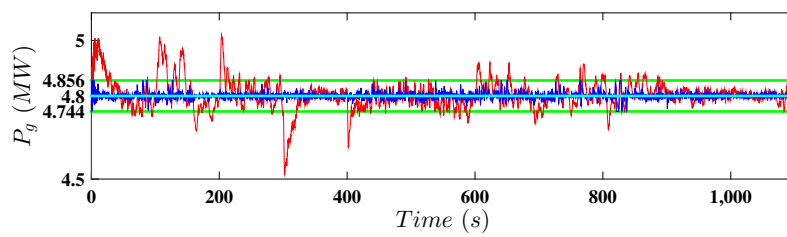
FIGURE 6.25: Generated power using the proposed controller (dark blue line), baseline controller (red line), nominal power (light blue line), and constraints (green line), under second fault scenario, with second wind speed.

7 Drive Train Sensor FDI and FTC Design

In this chapter, using a novel UIO design associated with a Kalman filter, the faults in rotor and generator sensors are detected and accommodated. In the FD step, using Kalman filter outputs, the need for thresholds is eliminated.[1] Additionally, in the Bayesian setting, the fault probability is calculated which will be used for FDI. Also, via an auxiliary signal and by checking the updated residual and fault probability, the isolation of the fault in each sensor is accomplished without the need for any redundant physical sensor. The baseline controller is used in both the fault-free and faulty situation, as well. It should be noted that the proposed controller, designed in Chapters 5 and 6, can be used along side with the designed FDI. On the other hand, to avoid any repetitive explanations, this chapter is only focused in the partial load operation. Although, the designed FDI, can be easily augmented on the controller in full load region controller. Accordingly, for sake of consideration, the baseline controller (4.7) is used in this chapter. It should be noted that instead of reconfiguring the controller which increases the complexity and cost of the final design, the VSA scheme is used to allow the baseline controller to be applicable in faulty situations, which needs accurate identification of fault size. The rotor and generator sensor faults are considered in this chapter, because they are fed into the baseline controller and have a major effect on the performance of the wind turbine. Also, to cover a wide family of fault types, the sensor fault is modelled as a multiplicative fault, i.e. (3.30). Different numerical Recursive Least Square (RLS) methods are proposed and compared to remove noise from the estimated fault size, including the regular, windowed and exponentially weighted estimates. It should be noted that the values of FDI scheme parameters are given in Section B.5.

---

[1]This chapter is captured and reorganized from the papers "Bayesian Fault Probability Estimation; Application inWind Turbine Drive train Sensor Fault Detection", and "Bayesian Sensor Fault Detection in a Markov Jump System". The authors' attribution on these papers are given in Appendix C.

7.1   Fault Detection, Isolation and Identification

This section focuses on the detection of the sensor faults, the probability of fault occurrence, the location of the faults that should be isolated and finally, identifying the size of the detected faults to be used in the FTC procedure.

7.1.1   FD scheme

The FD step comprises two different indices including residual signal and fault probability. As it will be shown, because the residual signal is constructed based on the Kalman estimated states, it only deviates significantly from zero at the moment the fault occurs. Additionally, the residual detects any variation of the sensor coefficient. In fact, if the sensor coefficient varies from a number other than one, to one, which is the fault-free case, the residual deviates from zero, again. So, to find the accurate fault period and to see which residual deviation is indicating the fault, the fault probability is used, which along with the residual, accurately indicates the fault moment and period.

Residual signal

In this section, an optimal observer, namely a Kalman filter, is used on one well-known linear part of a wind turbine, i.e. the drive train (3.15), to estimate the signals and, accordingly, the residual signal will be constructed. Additionally, as the sensor signal is manipulated by noise, the residual signal can have nonzero value even in fault-free situations. Indeed, the noise can be mistakenly seen as a fault on the residual. Accordingly, to reduce the number of false alarms, where there is no fault on the system but yet the FD scheme indicates the fault, an appropriate threshold should be chosen and compared to the residual to check if the FD scheme can conclude that the fault is present. Too small a threshold will lead to false alarms. On the other hand, if the threshold is chosen to be too large, some faults, with minor effects on the residual, will not be detected and accordingly will be missed, even though these faults may have some severe consequences on the wind turbine performance. So, the threshold should be designed adaptively. In the case of the wind turbine, in which the system is noisy, a harsh disturbance such as the wind, acting on it, and given that an accurate model of the whole system is not available, it may be too challenging to design an appropriate adaptive threshold. Instead, a novel approach, i.e. using the signals which are estimated by the observer, will be used to detect the presence of faults in the sensors, because the observer is an optimal one and the effect of noise on the estimated signal is minimized. As stated before, this observer is designed only for the drive train whose dynamic model is accurately available from the manufacturer and its model is linear. The sensor FD is

completed by checking the estimated generator speed, ω_g and rotor speed, ω_r, to see if their ratio is exactly equal to the drive train ratio or not. This exact number and non-noisy estimated signal eliminate the need for the threshold. As it will be shown later, this ratio will actually change at the time of the fault. The observer diagram is illustrated in the Figure 7.1. It should be noted that the estimated state vector is $\hat{x} = \begin{bmatrix} \hat{\omega}_g \ \hat{\omega}_r \ \hat{\theta}_\Delta \end{bmatrix}^T$. Additionally, $\hat{y} = \begin{bmatrix} \hat{\omega}_g \ \hat{\omega}_r \end{bmatrix}^T$, is the estimated output such that a part of it, i.e. $\hat{\omega}_r$, will be fed back into the observer and another part, i.e. $\hat{\omega}_g$ will be used in the fault identification step. Using the drive train model (3.15), the observer dynamic can be stated as follows,

$$
\begin{aligned}
\dot{\hat{x}} &= A_{dt}\hat{x} + Bu + K(\omega_r - \hat{\omega}_r), \\
\hat{y} &= C\hat{x}, \\
A_{dt} &= \begin{bmatrix} \dfrac{-(\frac{\eta_{dt}B_{dt}}{N_g^2}+B_g)}{J_g} & \dfrac{\eta_{dt}B_{dt}}{N_gJ_g} & \dfrac{\eta_{dt}K_{dt}}{N_gJ_g} \\[2mm] \dfrac{B_{dt}}{N_gJ_r} & \dfrac{-(B_{dt}+B_r)}{J_r} & \dfrac{-K_{dt}}{J_r} \\[2mm] \dfrac{-1}{N_g} & 1 & 0 \end{bmatrix}, \\
B &= \begin{bmatrix} \dfrac{-1}{J_g} & 0 \\[1mm] 0 & \dfrac{1}{J_r} \\[1mm] 0 & 0 \end{bmatrix}, \\
C &= \begin{bmatrix} 1 & 0 & 0 \\ 0 & 1 & 0 \end{bmatrix}, \\
u &= \begin{bmatrix} T_g \\ T_a \end{bmatrix},
\end{aligned}
\tag{7.1}
$$

where, K is observer gain.
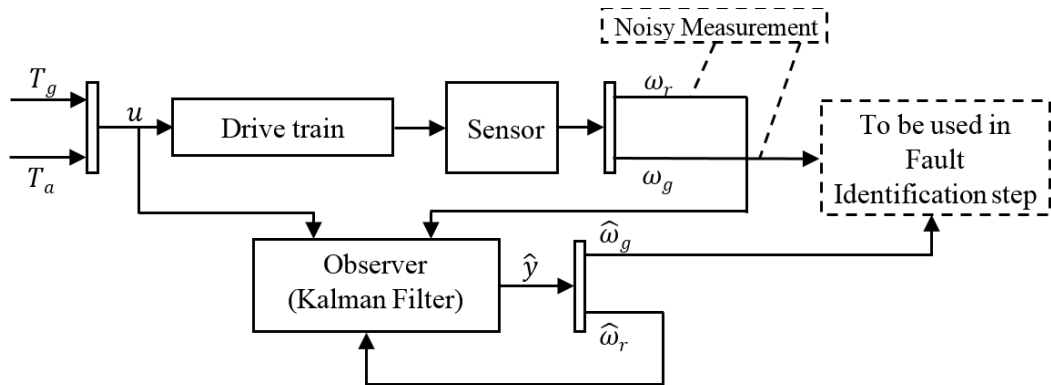
FIGURE 7.1: Drive train observer diagram.

It should be noted that the generator speed measurement, ω_g, could be fed into the Kalman filter and there would not be any major difference, but in the wind turbine mechanism the rotor speed, ω_r, is much noisier than ω_g (Sloth et al., 2009), and ω_g

will be used in fault identification. Accordingly, the accuracy of the identified fault size will be increased.

As it is obvious from Figure 7.1, the drive train input, u, which is fed into the Kalman filter, includes the generator torque, T_g and aerodynamic torque, T_a. T_g is generated by the controller (4.7), and it is available via measurement, but the challenging issue of wind turbines is that the wind speed, on which basis the T_a will be calculated, cannot be measured precisely using the anemometer located on the top of the hub, due to the temporal and spatial distribution of the wind over the plane of the blades. To overcome this issue, an estimation of aerodynamic torque should be fed into the Kalman filter. It is obvious that when the wind turbine is working in the fault-free situation at its stationary points, i.e. the controller is trying to keep the wind turbine operating at these points, the generator torque should be proportional to aerodynamic torque, i.e. $T_a = N_g T_g$. On the other hand, due to wind speed variation and faults, this relation can be violated. So, T_a can be estimated as $N_g T_g$ and, meanwhile, a PID controller, whose gains are K_{PO}, K_{IO} and K_{DO}, is designed and added to take the effects of wind speed variation and faults into consideration and to keep the estimated aerodynamic torque, $\hat{T}_a$, as close as possible to the actual one. Accordingly, the Kalman filter will have the same input as the drive train and optimality and accuracy of estimated signals will be guaranteed. The modified observer diagram is illustrated in Figure 7.2, where the ideal estimate of T_a, which is $N_g T_g$, and PID controller are added to the previous schematic shown in Figure 7.1.

Remark 7.1. *In Chapters 5 and 6 RBFNN was used to estimate wind speed and aerodynamic torque. One may say that this estimation could be used here in the observer structure of Figure 7.1. It should be noted that, in Chapters 5 and 6, it was assumed that the sensor measurements are fault-free and they were then fed into the RBFNN to estimate aerodynamic torque. So, in this chapter, another wind speed estimator is designed to be used in the observer structure, to separate the sensor FD from Chapters 5 and 6 objectives.*

In Figure 7.2, the PID controller is used to decrease the difference between the actual rotor speed and the estimated one, whilst the Kalman filter, in case of the same input as the drive train, i.e. $u = \hat{u}$, will be trying to eliminate noise from the sensor measurements. Consequently, when $\omega_r \approx \hat{\omega}_r$, as the main goal of the Kalman filter, the PID output will approach zero and the estimated aerodynamic torque, $\hat{T}_a$, will be $N_g T_g$, which is the condition of wind turbine operation at its stationary points, because the controller will generate T_g to guarantee operation at the expected operating trajectory. The Kalman filter equation can then be modified as,

$$\dot{\hat{x}} = A_{dt}\hat{x} + B\hat{u} + K\left(\omega_r - \hat{\omega}_r\right). \tag{7.2}$$
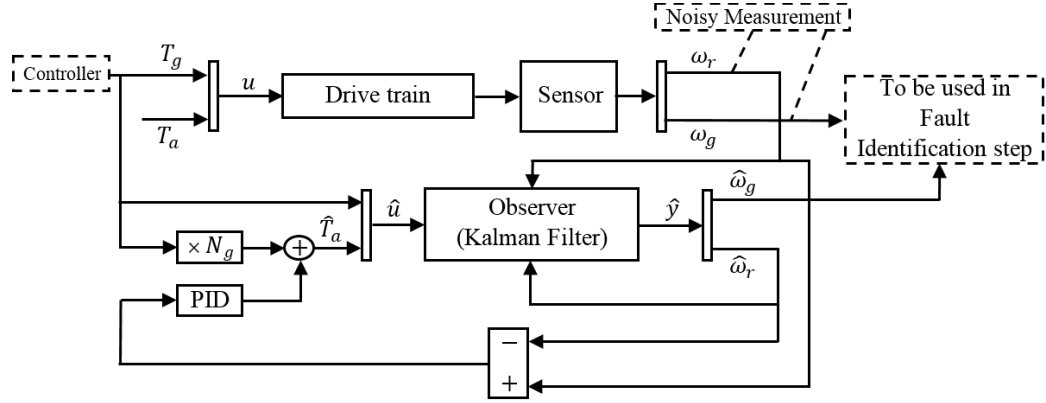
FIGURE 7.2: Modified drive train observer diagram.

The estimated aerodynamic torque for the wind speed shown in Figure 4.2, is illustrated in Figure 7.3 and compared to the actual one and, because these two signals are very close, the relative estimation error, i.e. $(\hat{T}_a - T_a)/T_a$, is depicted in Figure 7.4. To finalize FD, the residual will be constructed as,

$$d = \hat{\omega}_g - N_g \hat{\omega}_r. \tag{7.3}$$

As stated before, because the noise is minimized in the estimated estates, $\hat{\omega}_g$ and $\hat{\omega}_r$ and the PID controller guarantees $\omega_r = \hat{\omega}_r$, the residual d only deviates meaningfully from zero when a fault occurs. As the output of one sensor will be manipulated by the fault, $d \approx 0$ will not hold any more at the fault moment.

It should be noted that the PID controller used in the observer diagram, always tries to keep $\hat{\omega}_r$ as close as possible to ω_r and, consequently, $\hat{\omega}_g$ which is estimated by the Kalman filter, is very close to $N_g \hat{\omega}_r$, except at the fault moment. Indeed, the PID controller has a limited range of rising and settling times and the wind turbine dynamic response is very slow, due to the large mass moment of inertia of the rotor and blades. So when a fault occurs, it always takes a limited period of time for the PID controller to reduce the difference between $\hat{\omega}_r$ and ω_r, and to make $\hat{\omega}_g = N_g \hat{\omega}_r$, again. So this limited time period can be utilized to detect the fault.

The benefit of the proposed algorithm is that the estimated states from which noise has been minimized, are being used to construct the residual and to subsequently detect the fault. Therefore, compared to the residuals which are constructed using noisy sensor outputs, false alarms, in small threshold cases, and missed faults, in large threshold cases, will be reduced. Finally, FD can be summarized as, $d = \hat{\omega}_g - N_g \hat{\omega}_r$, which deviates from zero at the fault time and then returns to zero again. To illustrate FD, a case study is shown where the coefficient of the ω_r sensor is doubled after $t_f = 1500(s)$ and the proposed residual using estimated states, i.e. (7.3), and traditional residual using sensor outputs, i.e. $d_T = \omega_g - N_g \omega_r$, are compared. The same comparison is done when the coefficient of the ω_g sensor

coefficient is doubled after $t_f = 1500(s)$. It should be noted that the noises added to ω_g and ω_r sensors were: $\nu_{\omega_r} \sim N(0, (0.004 \times 2 \times \pi)^2)$ and $\nu_{\omega_g} \sim N(0, 0.05^2)$ (Sloth et al., 2009). These illustrations are shown in Figures 7.5-7.8. It is obvious that when using d_T, the fault-free situation can be translated to the fault due to the noise content of sensors, while the residual d, except at the fault moment, is extremely close to zero compared to its value at the fault moment, which is not the case for d_T.
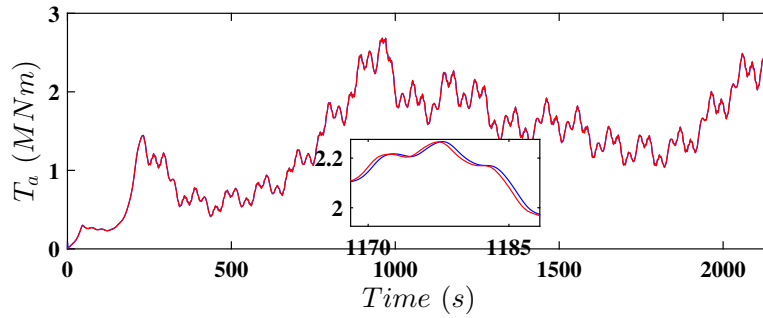
FIGURE 7.3: Estimated aerodynamic torque (blue line) and Actual aerodynamic torque (red line).
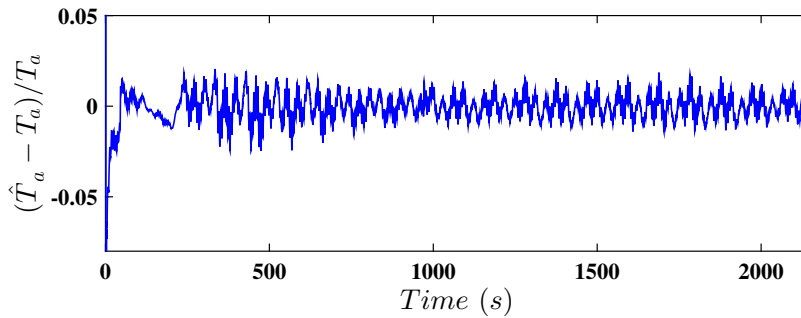
FIGURE 7.4: The relative estimation error of aerodynamic torque.

Fault probability

In this section, under a Bayesian setting, the probability of fault occurrence for the sensor fault problem is studied. Consider the sensor measurement as, $y_t = \alpha_t x_t + \varepsilon_t$, where, y_t is sensor output, x_t is the measured state coming from nonlinear dynamic $x_t = h(x_{t-1}, u_t)$, ε_t is measurement noise and α_t is measurement coefficient, which is $\alpha_t = 1$ in fault-free case and $\alpha_t \neq 1$ after fault occurs. Two important criteria to detect the fault are first the Bayesian estimates of regression coefficient, i.e. $E(\alpha_t | \hat{\alpha}_t)$, where, $\hat{\alpha}_t$ is estimation of α_t. Since $\hat{\alpha}_t$ is a sufficient statistic,
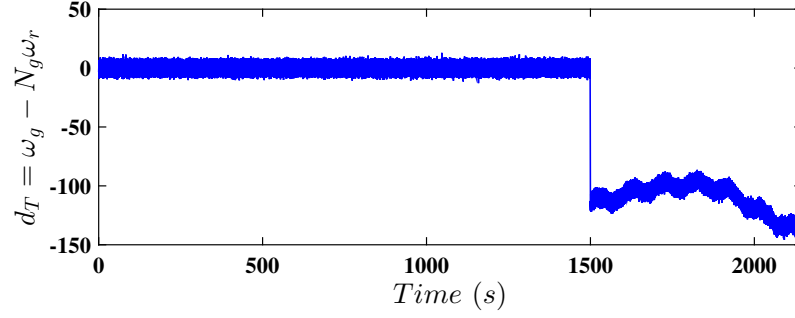
FIGURE 7.5: Traditional residual using sensor outputs when ω_r is doubled after $t_f = 1500(s)$.
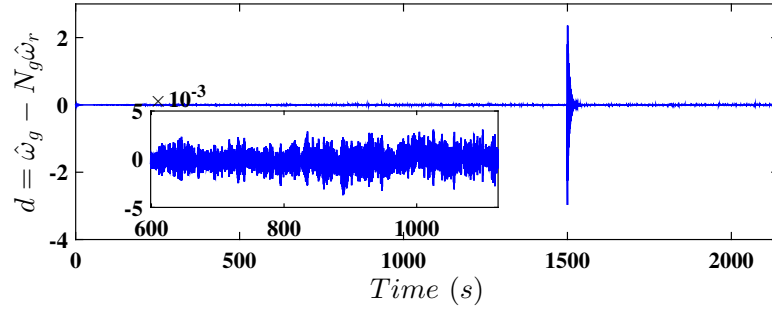
FIGURE 7.6: Residual using observer outputs when ω_r is doubled after $t_f = 1500(s)$.

it is used in the Bayesian estimation instead of the whole data. the second criterion is the probability of appearance of a special configuration $(j_1, \ldots, j_t)$, i.e. $P(J_t = j_t, \ldots, J_1 = j_1 | \hat{\alpha}_t)$. Here, $j_k = 0, 1$, $k = 1, \ldots, t$. For example, for $j_t = 1, j_{t-1} = 0, \ldots, j_1 = 0$, it is the posterior probability of facing the first fault at time t. However, since $\hat{\alpha}_t$ is really sensitive to sensor noise contents, therefore the fault probability is used in this chapter. To find the probability of the fault, two fundamental approaches using particle filtering and Expectation-Maximization (EM) algorithm are used.

The Bayesian method needs a prior which, in this chapter, the Yao's prior structure, (Yao, 1984), is selected, which is given as follows,

$$\alpha_t = (1 - J_t) \alpha_{t-1} + J_t z_t, \qquad (7.4)$$

It is assumed that ε_t and z_t are independent and identically distributed (*iid*). Although, this may be generalized to any distribution of ε_t and z_t, since the particle
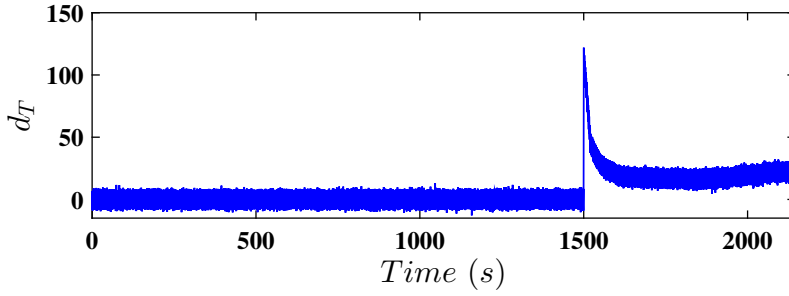
FIGURE 7.7: Traditional residual using sensor outputs when ω_g is doubled after $t_f = 1500(s)$.
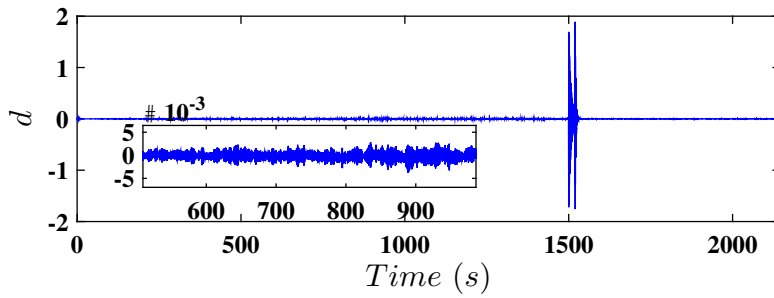
FIGURE 7.8: Residual using observer outputs when ω_g is doubled after $t_f = 1500(s)$.

filtering is applicable for all non-normal distribution. However, for descriptive purposes normal distributions are chosen. The probability of the fault is given as,

$$p_t = P\left(J_t = j_t,\ J_{t-1} = j_{t-1}, \ldots,\ J_1 = j_1 | \hat{\alpha}_t\right). \tag{7.5}$$

The following proposition is useful for calculating the probability of fault using a Bayesian setting.

Proposition 7.1. *Let* $\mu_i = E(\alpha_i | J_i = j_i, \ldots, J_1 = j_1)$, $\sigma_i^2 = var(\alpha_i | J_i = j_i, \ldots, J_1 = j_1)$, *and given* $J_{max(i,k)} = j_{max(i,k)}, \ldots, J_1 = j_1$, $\sigma_{ik} = cov(\alpha_i, \alpha_k)$ *for* $i, k \geq 1$. *The distribution of* $\hat{\alpha}_t$ *given* $J_t = j_t, \ldots, J_1 = j_1$ *is normal with the mean* $E(\hat{\alpha}_t | J_t = j_t, \ldots, J_1 = j_1) = \sum_{i=1}^{t} \lambda_{it} \mu_i$, *and variance* $var(\hat{\alpha}_t | J_t = j_t, \ldots, J_1 = j_1) = \sum_{i=1}^{t} \sum_{j=1}^{t} \lambda_{it} \lambda_{jt} \sigma_{ij} + \sigma_\varepsilon^2 / \sum_{i=1}^{t} x_i^2$, *where* $\lambda_{it} = x_i^2 / \sum_{j=1}^{t} x_j^2$, $1 \leq i \leq t \leq n$.

The proof of this proposition is given in A.9.

However, in this chapter, to approximate the fault probability, considering Proposition 7.1, two fundamental approaches based on particle filtering and EM algorithm are used.

Particle filtering

A natural extension of Kalman filtering to the cases of non-normal disturbances and nonlinear equations is particle filtering. The particle filtering method was introduced in (Gordon et al., 1993) by combining the sequential Monte Carlo and importance sampling techniques together. The Particle Filtering Framework (PFF) algorithm, (Zhou et al., 2008), is given in Algorithm 7.1. Here, p and P stand for density function and probability, respectively.

Algorithm 7.1: PFF for state X and measurement Y

Result: Calculate $\hat{p}_t(X_t)$

1 Initialization. Sample $\{X_0^i\}_{i=1}^N$ *iid* from initial distribution p_0. Set $t = 1$.
2 Importance sampling. Sample X_t^i from $p(X_t|X_{t-1}^i)$, $i = 1, 2, \ldots, N$. Set $t \geq 2$.
3 Bayesian updating. Let $\hat{p}_t(X_t) = \sum_{i=1}^N w_t^i \delta(X_t - X_t^i)$, where δ is the Dirac delta function. Weights are calculated as $w_t^i \propto p(Y_t|X_t^i)$, $i = 1, 2, \ldots, N$, and normalized.
4 Re-sampling. Sample $\{X_t^i\}_{i=1}^N$ *iid* from $\hat{p}_t(X_t)$ and go to step 2.

Algorithm 7.1 is used to calculate the probability of fault $P(J_t = j_t, \ldots, J_1 = j_1|\hat{\alpha}_t)$ for each t and for every configuration $(j_t, \ldots, j_1)$ in which $(J_t, \ldots, J_1)$ and $\hat{\alpha}_t$ play the roles of X and Y, respectively. Also, since vector $(J_t, \ldots, J_1)$ is not a Markov property, step 2 of Algorithm 7.1 is removed in Algorithm 7.2. Consider the following algorithm.

Algorithm 7.2: PFF algorithm for probability of fault

Result: Calculate $P(J_t = j_t, \ldots, J_1 = j_1|\hat{\alpha}_t)$

1 Fix $t \geq 1$. Extract L samples $(j_t, \ldots, j_1)_l$, $l = 1, \ldots, L$ from $(J_t, \ldots, J_1)$.
2 For each $l = 1, \ldots, L$, compute the density of $\hat{\alpha}_t$ given $(J_t, \ldots, J_1) = (j_t, \ldots, j_1)_l$ and particle filtering weights are computed, as Proposition 7.1.
3 Using weights of step 2, configurations are re-sampled B times, using the weighted bootstrap method, to obtain re-samples $(j_t^*, \ldots, j_1^*)_b$, $b = 1, \ldots, B$.
4 The Empirical distribution of $(j_t^*, \ldots, j_1^*)_b$, $b = 1, \ldots, B$ estimates distribution of $P(J_t = j_t, \ldots, J_1 = j_1|\hat{\alpha}_t)$.

Remark 7.2. *A fast approach to derive the* $var(\sum_{i=1}^t x_i^2 \alpha_i)$ *is using a standard Monte Carlo method, given* $J_t = j_t, \ldots, J_1 = j_1$.

Although, the particle filtering (Algorithm 7.2) provides the probability of the fault, however, characterization of the probability of a fault for every configuration is time-consuming work. A shortcut solution to this problem is to compute the $P(J_t = j_t|\hat{\alpha}_t)$ for every t. Indeed, the length of configuration is reduced. On the

other hand, computationally, it is easy to calculate $P\left(J_t = j_t | \hat{\alpha}_s, s \leq t\right)$. As well as, since a recursive relation exists for $\hat{\alpha}_t$, it is better to calculate $P\left(J_t = j_t | \hat{\alpha}_t, \hat{\alpha}_{t-1}\right)$ which is proportional to the product of likelihood and prior, i.e. $P(\hat{\alpha}_t | J_t = j_t, \hat{\alpha}_{t-1}) \times P(J_t = j_t)$. Thus, to run the particle filtering Algorithm 7.2, it is enough to substitute $(j_t, \ldots, j_1), (j_t^*, \ldots, j_1^*)$, $(J_t, \ldots, J_1)$ with j_t, j_t^*, J_t, respectively, in all steps and to substitute the conditional density of $\hat{\alpha}_t$ given $J_t = j_t, \ldots, J_1 = j_1$ with $p(\hat{\alpha}_t | J_t = j_t, \hat{\alpha}_{t-1})$ in step 2 of Algorithm 7.2. To compute the last density, recursive relations are useful. As follows, the distribution of $\hat{\alpha}_t$ given $J_t = j_t$ and $\hat{\alpha}_{t-1}$ is derived and the particle filtering method is applied to compute the $p_t = P\left(J_t = j_t | \hat{\alpha}_t, \hat{\alpha}_{t-1}\right)$.

Proposition 7.2. *The distribution of $\hat{\alpha}_t$ given $J_t = j_t$ and $\hat{\alpha}_{t-1}$, is normal with $mean = (1 - \lambda_t)\,\hat{\alpha}_{t-1} + \lambda_t\,(1 - j_t)\,\hat{\alpha}_{t-1} + \lambda_t j_t \mu_z$ and $variance = \lambda_t^2 \sigma_\varepsilon^2 / x_t^2 + \lambda_t^2 j_t \sigma_z^2$, where $\lambda_t = x_t^2 / \sum_{j=1}^t x_j^2$.*

The proof of this proposition is given in A.10.

In order to reduce the computational load and complexity, beside the shortcut $p(\hat{\alpha}_t | J_t = j_t, \hat{\alpha}_{t-1})$, there are other solution which is to use the other types of estimation of $\hat{\alpha}_t$. Also, it is beneficial to use very recent observations and forget the very past ones to check the existence of the fault. This new estimation is given via utilization of EM algorithm, which is described in the next section.

EM algorithm

Here the EM algorithm is reviewed briefly, to obtain a recursive relation for the estimation of measurement coefficient $\hat{\alpha}_t$, to be used in Algorithm 7.2. Let the θ be an unknown parameter, X be observed and Z be missing data. Let $f(X, Z; \theta)$ be the joint density of X and Z. The EM algorithm consists of two steps. First, the expectation $E_{Z|X, \theta = \theta_t}(log\,p(X, Z; \theta)) = Q(\theta, \theta_t)$ is calculated. Then, $Q(\theta, \theta_t)$ is maximized with respect to θ. As $t \to \infty$, θ_t converges in probability to the actual maximum likelihood of θ which is not computable directly, since the Z is missing. Next, to apply the EM algorithm to the problem of Bayesian FD, first Lemma 7.1 is proposed. Let $n(x, \mu, \sigma^2)$ be the density of normal distribution with mean μ and variance σ^2 and $log(n\,(x, \mu, \sigma^2))$ be its natural logarithm.

Lemma 7.1. *Let $0 < q < 1$, $\theta^* = \sigma_2^2 / \sigma_1^2$ and define, $f(x) = q.log\,(n\,(x, \mu_1, \sigma_1^2)) + (1 - q).log\,(n\,(x, \mu_2, \sigma_2^2))$. Then, f attains its maximum at $x = (q\mu_1\theta^* + (1 - q)\mu_2)/(q\theta^* + (1 - q))$.*

The proof is straightforward and omitted. □

To implement the EM algorithm, let $\hat{d}_t = \hat{\alpha}_t - (1 - \lambda_t)\,\hat{\alpha}_{t-1} = \lambda_t\,(y_t/x_t) = \lambda_t\,(\alpha_t + \varepsilon_t/x_t)$. Here, the $\hat{\alpha}_t$ is the least square estimate of α_t.

Proposition 7.3. *Let* $k_2(J_t) = (1 - \lambda_t)^2 J_t \sigma_z^2 + \lambda_t^2 \sigma_\varepsilon^2 / x_t^2, \theta = k_2(J_t = 0)/k_2(J_t = 1)$ *and* $\gamma = p\theta/(p\theta + (1 - p))$. *The EM algorithm Bayesian recursive relation for* α_t *is given by,* $\hat{\alpha}_t^{EM} = \hat{d}_t + (1 - \lambda_t)\left(\gamma \mu_z + (1 - \gamma)\hat{\alpha}_{t-1}^{EM}\right)$.

The proof of this proposition is given in A.11.

Since the recursive relation for EM estimate of $\hat{\alpha}_t$ *is* found, thus the probability of fault is computable. The following proposition gives the conditional distribution of $\hat{\alpha}_t^{EM}$ given $J_t = j_t$.

Proposition 7.4. *The distribution of* $\hat{\alpha}_t^{EM}$ *given* $J_t = j_t$ *and* $\hat{\alpha}_{t-1}^{EM}$ *is normal with mean* $\lambda_t \alpha_t + (1 - \lambda_t)\left(\gamma^* \mu_z + (1 - \gamma^*)\hat{\alpha}_{t-1}^{EM}\right)$ *and variance* $\lambda_t^2 \sigma_\varepsilon^2 / x_t^2$.

The proof is straightforward and omitted. □

The fault probability calculation procedure using EM algorithm is illustrated in Figure 7.9. Now, using this algorithm, the corresponding fault probability for faults shown in Figures 7.5-7.8, are illustrated in Figures 7.10 and 7.11. It is obvious that after the fault moment, the fault probability is accurately changed to one. It should be noted that in the simulation the sampling time is $0.01(s)$. Also, to run the Algorithm 7.2, $L = 100$ and $B = 1000$ are selected.
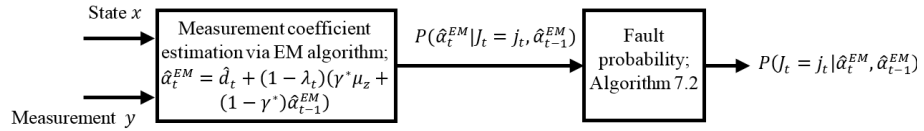
FIGURE 7.9: EM algorithm procedure for fault probability calculation.
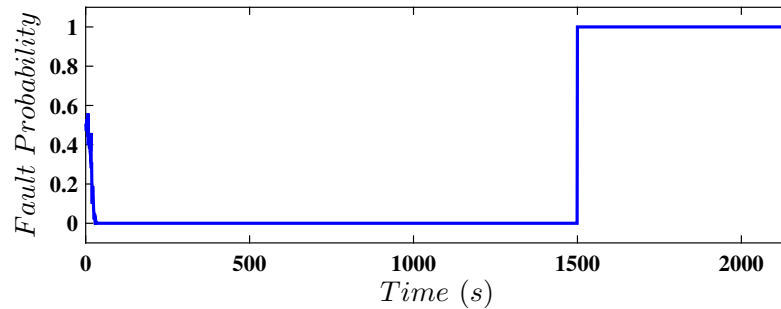
FIGURE 7.10: Fault probability when ω_g is doubled after $t_f = 1500(s)$.
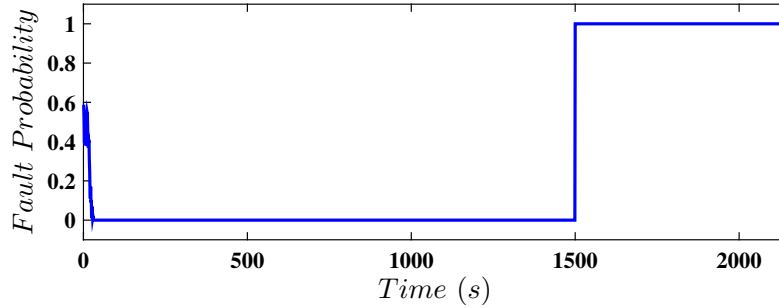
FIGURE 7.11: Fault probability when ω_r is doubled after $t_f = 1500(s)$.

7.2 Drive Train Sensor Fault Model

The fault is modeled as an unknown abrupt sensor coefficient jump or latent jump, in which the coefficient of the sensor equation will change at an unknown time and with an unknown size. For example, considering (3.24), the rotor speed sensor is rewritten as,

$$\omega_{r,s} = \alpha_{\omega_r}\omega_r + \nu_{\omega_r}, \qquad (7.6)$$

where α_{ω_r} is the coefficient of measurement equation. It should be noted that before the unknown fault moment t_f, $\alpha_{\omega_r} = 1$ and after t_f, $\alpha_{\omega_r} = \alpha_1$, where α_1 is unknown. Similar consideration can be made for generator speed sensor to 7.6, but for sake of explanation, only the rotor speed sensor is considered in this section. Four different fault types commonly happen in a sensor including, proportional error (multiplicative fault), bias error (additive fault), no output and fixed output. Indeed, via this fault model, all types of sensor faults can be considered. For sensor bias,

$$\omega_{r,s} = \omega_r + Bias_{\omega_r} + \nu_{\omega_r} = \alpha_1\omega_r + \nu_{\omega_r}. \qquad (7.7)$$

where, $\alpha_1 = 1 + Bias_{\omega_r}/\omega_r$. So, the sensor bias, i.e. $Bias_{\omega_r}$, can be considered as a coefficient change α_{ω_r} to α_1. In fact, it is considered as a time variable coefficient that can cover a wide range family of biases. On the other hand, for the sensor fixed output,

$$\omega_{r,s} = \omega_{rConstant} = \alpha_1\omega_r. \qquad (7.8)$$

where, $\alpha_1 = \omega_{rConstant}/\omega_r$. Also, there is another method to detect the fixed output by considering the probability of the fixed output from a noisy sensor with white Gaussian distribution of noise for several consecutive time steps (Sloth et al., 2009).

It should be noted that the zero-output situation cannot be considered as a fixed output because this implies that $\alpha_1 = 0$, meaning that the fault cannot be identified. If the anemometer, which is located at the top of the hub to measure wind speed roughly, denotes the nonzero value of wind speed, because the wind speed provides

the motivating force that makes the wind turbine operate, neither of ω_r or ω_g can be zero. If so, the zero sensor output fault can be concluded. Although, one zero sensor output and one nonzero sensor output, can indicate the fault on the zero one, but, in the case that both sensor outputs are zero, using only the anemometer signal can lead to FD. For no output situations, the controller, which changes the generator torque, and the Kalman filter will detect the fault. Indeed, if the ω_r sensor generates no output, because it has been fed into the observer diagram, the Kalman filter will alarm this type of fault. On the other hand, if the ω_g sensor generates no output, the main controller 4.7, into which ω_g has been fed, will generate the alarm.

7.3 Effect of Fault on Kalman Filter

In the fault-free situation, the Kalman filter is able to minimize the noise from measured signals and estimate them appropriately in an optimal manner. Now, it should be taken into consideration what happens if the sensor whose output is manipulated by faults, is fed into the Kalman filter. Indeed, this will provide the basic logic for FII, as well. Suppose that the fault occurs at time step t_f and sensor coefficient of system, i.e. matrix C in (7.1), before and after fault are $\begin{bmatrix} 1 & 0 & 0 \\ 0 & 1 & 0 \end{bmatrix}$ and $\begin{bmatrix} 1 & 0 & 0 \\ 0 & \alpha_1 & 0 \end{bmatrix}$, respectively. Indeed, it is assumed that the coefficient of the ω_r sensor is changed from one to α_1. Although, considering the ω_g sensor fault with a similar procedure can be used to consider its effect on the Kalman filter. In fact, the fault in the ω_r sensor will lead to estimation of $\hat{\omega}_g$ dissimilar to ω_g because the faulty ω_r sensor is used in the Kalman filter. On the other hand, the fault in the ω_g sensor will cause instantaneous deviation of ω_r from the estimated one, $\hat{\omega}_r$, because ω_g is utilized as input to the controller which changes the generator torque. After the fault occurs, it is assumed that the matrix C is $\begin{bmatrix} 1 & 0 & 0 \\ 0 & \alpha_1 & 0 \end{bmatrix}$. α_1 is unknown and should be identified. Because the fault in the sensor is latent, so the matrix C of the sensor is assumed to still be $\begin{bmatrix} 1 & 0 & 0 \\ 0 & 1 & 0 \end{bmatrix}$. In fact, one cannot directly apply the coefficient α_1 in matrix C of the Kalman filter, because the accurate size of the fault is not yet known, which will be estimated in the fault identification step. On the other hand, to hold $\omega_r = \hat{\omega}_r$, as the goal of the Kalman filter, the latent coefficient α_1 should be applied in matrix C of the Kalman filter. Accordingly, the Kalman filter equation should be written as follows to satisfy $\omega_r = \hat{\omega}_r$, giving,

$$\dot{\hat{x}} = A_{dt}\hat{x} + B\hat{u} + K\left(\omega_r - \alpha_1\hat{\omega}_r\right). \tag{7.9}$$

So, by selecting the appropriate estimator gain, K, the estimated rotor speed, i.e. $\hat{\omega}_r$, will be close optimally to the term of ω_r/α_1 (Habibi et al., 2017a). Consequently, it can be concluded that $\hat{\omega}_r$ cannot be similar to ω_r, but rather to the ω_r/α_1 term where

the coefficient α_1 is contributing. In other words, $\hat{\omega}_r$ will be similar to the affected ω_r by the fault (Isermann, 2006). This shows the applicability of the Kalman filter for state estimation for the unknown coefficient jump. The same thing will hold when the fault occurs in the ω_g sensor. In Figures 7.12 and 7.13 the sensors and corresponding Kalman estimations are illustrated when the ω_r sensor coefficient is doubled after $t_f = 1500(s)$.
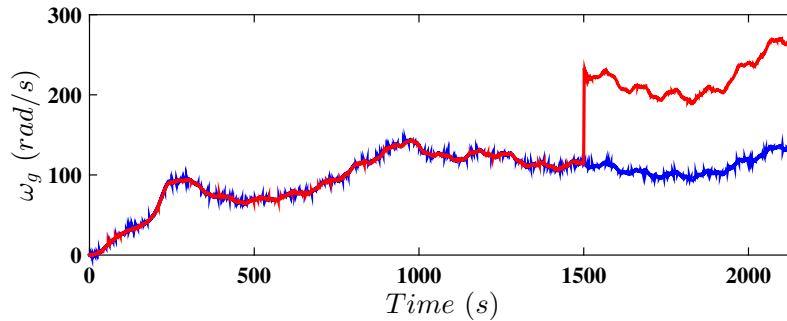
FIGURE 7.12: ω_g (blue line) and $\hat{\omega}_g$ (red line) when ω_r sensor coefficient is doubled after $t_f = 1500(s)$.
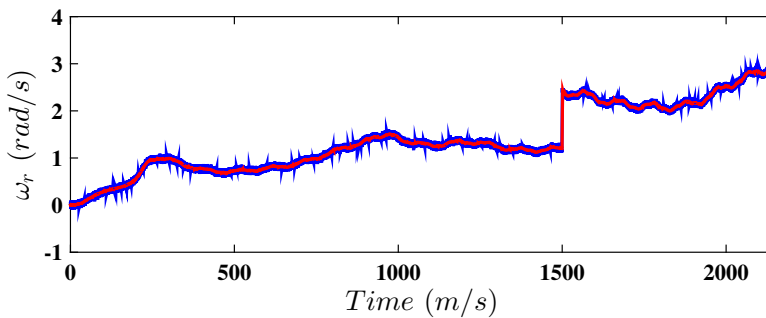
FIGURE 7.13: ω_r (blue line) and $\hat{\omega}_r$ (red line) when ω_r sensor coefficient is doubled after $t_f = 1500(s)$.

7.4   Fault Isolation

In the fault isolation step, the source of the fault should be detected. Indeed, it should be determined which actual sensor is faulty. The fault can be isolated utilizing and comparing the measured and estimated signals to locate the fault source. It should be noted that due to the presence of the PID controller in the observer diagram, $\omega_r = \hat{\omega}_r$ always holds, and whether the ω_r or ω_g sensor is faulty, only a change in comparing ω_g and $\hat{\omega}_g$ is obvious. In Figures 7.12 and 7.13, it can be seen that when the ω_r sensor is faulty, i.e. ω_r sensor coefficient is doubled after

$t_f = 1500(s)$, disregarding noise contents, only the ω_g sensor is different from $\hat{\omega}_g$. The same results can be found when the ω_g sensor is faulty. So, it seems that despite the fault source, using the proposed FD scenario, it always indicates that the ω_g sensor is faulty. Let either the rotor or generator sensor coefficients change from one to α at t_f. The question remains then about how to isolate the ω_r sensor fault? The point is that when only using information from two sensors, the fault in each sensor cannot be isolated directly (Isermann, 2006). In most of the literature, it has been proposed to use hardware redundancy (Chen et al., 2011b). The novel approach used in this chapter is in designing an auxiliary signal in the FTC step. Indeed, the PID controller always makes the residual $d = \hat{\omega}_g - N_g\hat{\omega}_r$ zero except at the fault moment when d deviates from zero significantly and the fault probability becomes one. After the fault occurrence, despite the fault source, as discussed in Section 7.3, $\omega_g/\hat{\omega}_g = \hat{\alpha}$, accordingly, the ω_g sensor can be multiplied by $1/\hat{\alpha}$ to remove the fault effect from this signal which is being fed into the controller. The auxiliary signal can then be designed by accommodating the fault and signal correction of the ω_g sensor, which will be described in the next section, after which it is expected that d and the fault probability will return to zero. Consequently, if this is the case, it can be concluded that the fault source was correctly selected as the ω_g sensor. Otherwise, if still $d \neq 0$ and the fault probability is around one, at exactly the moment that the ω_g signal was corrected, it can evidently be pointed out that the fault source was the ω_r sensor and this fault should be accommodated.

It can be pointed out that in this fault isolation procedure, if the $\omega_{g,s}$ signal is mistakenly corrected by multiplying by $1/\hat{\alpha}$, then it may lead to dangerous operation and even instability. Indeed, this correction can be seen as a sudden change K_c in (4.7), to $K_c/\hat{\alpha}^2$. Firstly, it should be noted that the stability of the controller gain K_c is considered using gain and phase margins and, as wind turbines are operating in dangerous harsh environment, these margins are selected to be considerably large. So, a mistakenly small change of $\hat{\alpha}$, will not lead to dangerous operation or instability. However, this issue should be considered in the isolation procedure. Accordingly, the marginal safety gains K_{M1} and K_{M2} can be defined by the designer to guarantee safe operation, such that $K_{M1} \leq K_c/\hat{\alpha}^2 \leq K_{M2}$. So, as long as the estimated fault size lies within $\sqrt{K_c/K_{M2}} \leq \hat{\alpha} \leq \sqrt{K_c/K_{M1}}$, corresponding correction of $\omega_{g,s}$ will not lead to dangerous operation. On the other hand, in (Zhang et al., 2011), it is proposed to detect the fault in $\omega_{g,s}$, using the wind turbine generated power (3.19). Accordingly, it is proposed to estimate generator speed using measured generated power, i.e. $P_{g,s}$, via $\omega_{ge} = P_{g,s}/\eta_g T_g$. Then comparing ω_{ge} and $\omega_{g,s}$ the fault in generator sensor is estimated as $\omega_{g,s}/\omega_{ge} = \hat{\alpha}_e$. Although, due to the presence of noise in $P_{g,s}$ and $\omega_{g,s}$, $\hat{\alpha}_e$ is not accurately equal to $\hat{\alpha}$. So, for small fault size, this criterion may not be able to accurately detect the fault and it only operates properly for considerable large $\hat{\alpha}$. This complementary criterion is utilized here to fulfil the fault isolation. In this regard, after $\hat{\alpha}$ is obtained, it is compared with $\hat{\alpha}_e$. So, if $|\hat{\alpha} - \hat{\alpha}_e| \leq \varepsilon_d$, where ε_d is a small design parameter, and $\sqrt{K_c/K_{M2}} \leq \hat{\alpha} \leq \sqrt{K_c/K_{M1}}$, then the $\omega_{g,s}$ is the fault

source and it is corrected. Then the fault probability is recalculated to guarantee the selected fault source. If it is not zero, then $\omega_{r,s}$ is the fault source and it is corrected. This fault isolation is given in Algorithm 7.3 and illustrated in Figure 7.14.

Algorithm 7.3: Fault isolation algorithm

Result: Find the sensor fault source

1 Sample estimated states using (7.2).
2 Calculate fault probability via Algorithm 7.2. If the Fault probability is zero,
3 Terminate this algorithm. Otherwise,
4 Calculate $\hat{\alpha}$.
5 Calculate $\hat{\alpha}_e = \omega_{g,s}\eta_g T_g / P_{g,s}$. If $|\hat{\alpha} - \hat{\alpha}_e| \leq \varepsilon_d$ and
  $\sqrt{K_c/K_{M2}} \leq \hat{\alpha} \leq \sqrt{K_c/K_{M1}}$, then,
6 Inserting corrected $\omega_{g,corrected}$ into the controller as, $\omega_{g,corrected} = \omega_{g,s}/\hat{\alpha}$.
  Otherwise,
7 Inserting corrected $\omega_{r,corrected}$ into the observer as, $\omega_{r,corrected} = \omega_{r,s} \times \hat{\alpha}$.
8 Go to step 1.

Remark 7.3. *In Algorithm 7.3, step 4, the calculation of $\hat{\alpha}$ is needed. It is obvious that this calculation, using $\omega_g/\hat{\omega}_g$, will be noisy due to noise in the ω_g signal. So, in this section, for the sake of explanation, it is assumed that this calculation of $\hat{\alpha}$ is satisfactorily accurate and then, after constructing the fault isolation and fault accommodation scenarios, further analysis will continue to remove noise content from $\hat{\alpha}$ in the fault identification step.*

One benefit of this proposed algorithm for fault isolation, i.e. designing an auxiliary signal, is that the $\hat{\alpha}$, calculated using the measured ω_g and estimated $\hat{\omega}_g$, will be used for FA in both ω_g and ω_r sensors, which is described in the next section. In fact, there will be no need for further calculation algorithms for each fault source and using the one step calculation, both faults can be accommodated.

Remark 7.4. *It should be noted that it is assumed that the main rotor and generator sensor pair are fed into Algorithm 7.3. However, if the redundant sensor pair is available, then Algorithm 7.3 can be separately used to detect the faults in those sensors.*

Remark 7.5. *In this chapter, the faults in drive train sensors are considered because in partial load operation, these sensor measurements are fed into the baseline controller. Although there are other sensors in wind turbine systems which are also prone to failure. The pitch angle is kept at its optimal value while its sensor fault can be accommodated passively (Sloth et al., 2011). On the other hand, in the case of the generated power sensor fault, the generator torque and generator speed sensors can be used in which the generator torque sensor is passively robust against faults (Sloth et al., 2010). Finally, faults in the wind speed sensor are not studied, because the baseline controller is not constructed based on the measured wind*
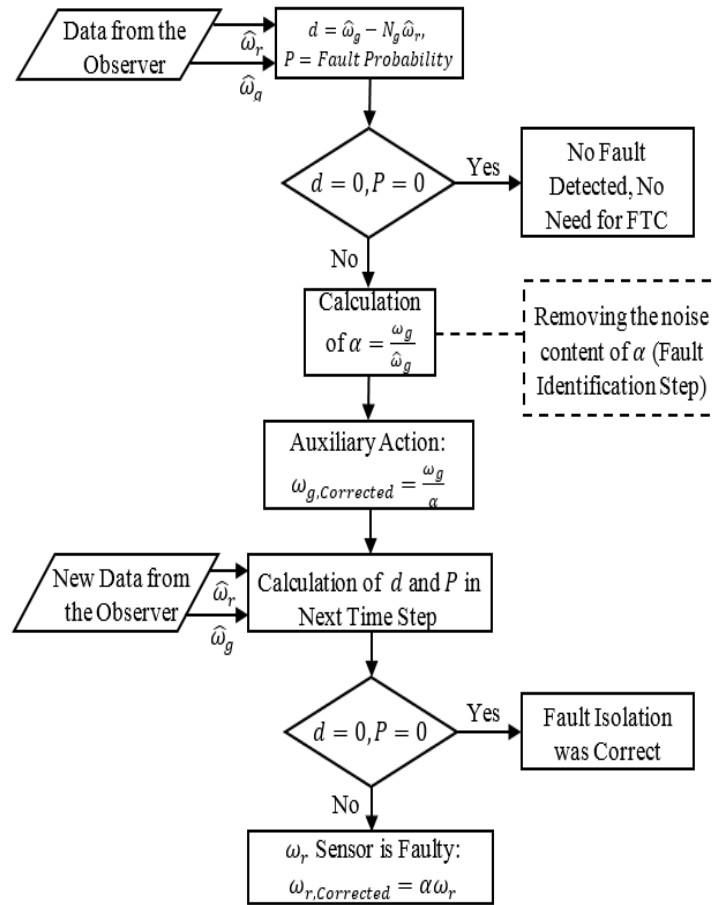
FIGURE 7.14: Fault isolation algorithm.

speed. Also, it should be noted that, the proposed algorithms can be simply used for pitch and generator sensors FDI with Kalman filter estimation without the need for UIO design. In both pitch and generator actuator dynamic models, there are no unknown inputs. So, to avoid any repetitive study, this chapter is only focused on drive train sensor FDI design, which are more challenging than the other sensors.

7.5 Drive Train Sensors FA

It should be noted that in the FTC procedure, FII is prior to the FA, but for sake of readability, the FA scheme is considered firstly, and the fault identification is considered in detail in the next section. In this chapter, so-called virtual sensor accommodating method or signal correction, is used to accommodate sensor faults and remove their effects from the system and keep the baseline controller working and the system performing as close as possible to the fault-free condition (Badihi et

al., 2014). In the virtual sensor method, the sensor signal is fed into a virtual sensor module, such that the fault effect is mitigated and then, this corrected signal will be fed into the controller. The benefit of this FTC method is that the baseline controller can be utilized in both fault-free and faulty conditions and there will be no need for CR which is one of the major issues in FTC research (Blanke et al., 2006). When the signal is being corrected, because the baseline controller has already been designed for fault-free situations and this controller is going to be utilized again in the faulty situation, then there is no need to be concerned regarding final controller stability and performance, which have already been considered in the fault-free condition.

7.5.1 Remedial action

Remedial action can be seen as part of FA in which any action that should be taken regarding FTC, will be designed for any fault type. Based on the fault type which has been described in Section 7.2, several actions can be considered. The design approach here is to use as least different actions as possible to reduce the complexity and increase the applicability of the final proposed FTC. As discussed in Section 7.2, proportional, bias and nonzero fixed output errors, can be considered as multiplicative faults. So, the sensor coefficient should be estimated via the fault identification step using measured and estimated signals and improving its accuracy and removing noise from it through the use of RLS estimate. As discussed in earlier sections, the only two signals which are different after the fault occurrence, are ω_g and $\hat{\omega}_g$. The generator speed sensor is as,

$$\omega_{g,s} = \alpha_{\omega_g} + \nu_{\omega_g}. \tag{7.10}$$

As discussed in Section 7.3,

$$\hat{\alpha} \approx \frac{\omega_g}{\hat{\omega}_g} \approx \frac{\omega_g}{95\hat{\omega}_r}. \tag{7.11}$$

So, to eliminate the fault effect from the measured signal, either ω_g should be divided by $\hat{\alpha}$ or $\hat{\omega}_r$ should be multiplied by $\hat{\alpha}$, which depends on the fault source. Accordingly, in the latter case, in which $\hat{\omega}_r$ should be multiplied by $\hat{\alpha}$, keeping $\omega_g/\hat{\omega}_g$ at one can be done by multiplying the ω_r signal by $\hat{\alpha}$ before it is fed into the observer, because, based on the observer diagram, $\hat{\omega}_r$ always tracks the ω_r, then $\omega_g/\hat{\omega}_g$ can be one by changing ω_r appropriately. In summary, disregarding noise content, the ratio $\omega_g/\hat{\omega}_g$ should be one unless a fault occurs in either the ω_g or the ω_r sensors. On this basis, whenever the ω_g sensor is detected as the fault source, then, the ω_g signal should be divided by $\hat{\alpha}$ before it is fed into the baseline controller and, on the other hand, when the FD scheme indicates the ω_r sensor as the faulty component, then ω_r signal should be multiplied by $\hat{\alpha}$. One benefit of this algorithm is that the fault size with different sources, i.e. either the ω_g or ω_r sensor,

can be identified with only one calculation step which comprises the calculation of $\hat{\alpha}$ accurately. This issue reduces complexity of the algorithm and increases its applicability.

For zero fixed output or no output conditions, there is no choice except CR. In fact, the modern wind turbines have been equipped with duplicated sensors, i.e. using two or three sensors with identical structure and signals, to be used for FD as well as FTC. Accordingly, in zero fixed output or no output conditions, the second identical sensor can be replaced. In this chapter, it is suggested to utilize the proposed algorithm instead of redundant sensors. Accordingly, for the two above-mentioned conditions, to eliminate the need for redundant sensors, it is suggested that the lost signals be replaced by the estimated ones. In (Sloth et al., 2009), it has been proposed to use the other fault-free signals instead of the lost one, but this leads to some major problems. First of all, for instance, using the $N_g\omega_r$ signal instead of the lost ω_g signal, increases the noise content of the signal, because ω_r is much noisier than ω_g (Sloth et al., 2009), and multiplying it by N_g, further increases the noise content amplitude, which is not desirable. Additionally, in case of the simultaneous loss of both sensor signals, there will be no signal to be replaced. In the other solution, ω_g can be estimated by $P_{g,s}/(\eta_g T_{g,s})$, in which the two noises of P_g and T_g sensors are contributing (Sloth et al., 2009), this estimation is not applicable. The FA and remedial action are summarized in Algorithm 7.4 and is illustrated in Figure 7.15. Of course, it does not eliminate the need for CR, because the signals which had already been fed into the controller or observer, have to be replaced by estimated ones and this issue raises the need for switching the signals that can be translated as CR in the FTC field. However, using estimated signals will not add any further noise to the system and also it is applicable in the case of simultaneous loss of both sensor signals.

Algorithm 7.4: FA and remedial action algorithm

Result: Remove the effect of drive train sensor faults

1 Obtain fault isolation information.

2 Calculate $\hat{\alpha}$.

3 If the fault source is $\omega_{g,s}$, correct $\omega_{g,s}$ as $\omega_{g,s}/\hat{\alpha}$ before feeding into the controller.

4 If the fault source is $\omega_{r,s}$, correct $\omega_{r,s}$ as $\omega_{r,s} \times \hat{\alpha}$ before feeding into the observer.

5 If there are no sensor measurements, switch the estimated signals into the controller or observer structure.

7.5.2 Fault identification and RLS estimation

This section seeks to identify the accurate size of the fault and the removal of noise from the calculated $\hat{\alpha}$. To improve α estimation the least squares method is used
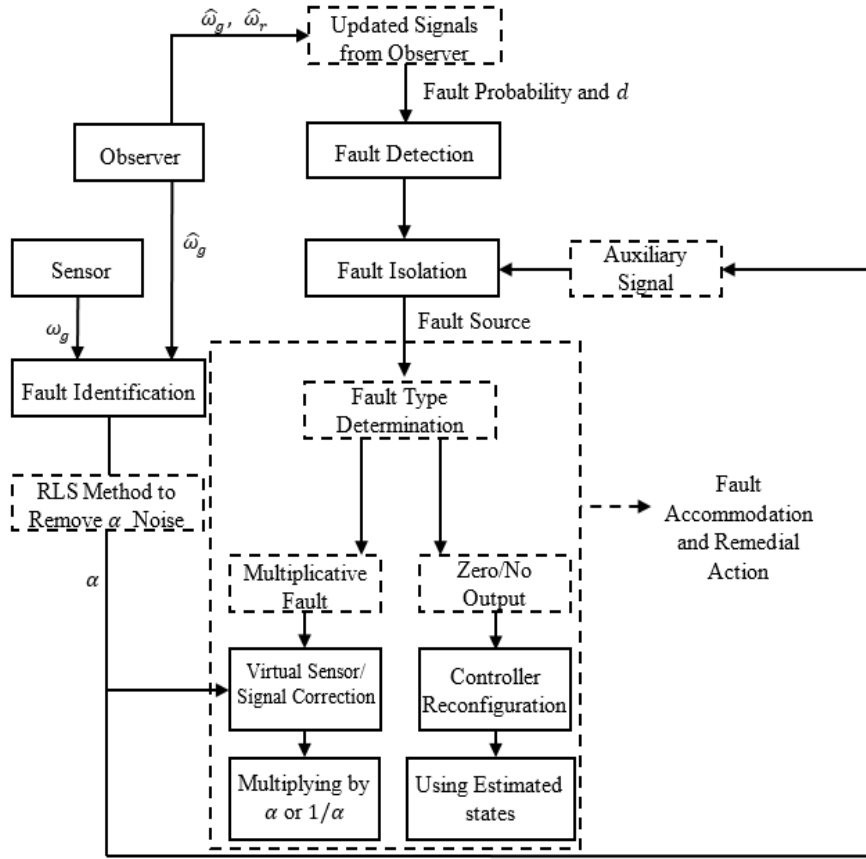
FIGURE 7.15: Fault accommodation and remedial action.

to mitigate noise. Consider sensor measurement as, $y_t = \alpha_t x_t + \varepsilon_t$, where, without loss of generality, it is assumed that ε_t are *iid* normally distributed random variables with zero mean and variance σ_ε^2. For a time span $\{1, 2, \ldots, t\}$, the null hypothesis implies that there is no fault among observations up until time t. The least square estimate of α_t is the minimizer of $\sum_{i=1}^{t} (y_i - \alpha_t x_i)^2$, which is given by $\hat{\alpha}_t = \sum_{i=1}^{t} x_i y_i / \sum_{i=1}^{t} x_i^2$, to minimize the noise effect. $\hat{\alpha}_t$ is normally distributed as $N\left(\alpha_t, \sigma_\varepsilon^2 / \sum_{i=1}^{t} x_i^2\right)$, under the null hypothesis of no fault up to time t. This distribution plays the role of observation equation density. There is a recursive formula for $\hat{\alpha}_t$ derived as follows,

$$
\begin{aligned}
\hat{\alpha}_t &= \frac{\sum_{i=1}^{t-1} x_i y_i + x_t y_t}{\sum_{i=1}^{t} x_i^2} \\
&= \frac{(\sum_{i=1}^{t-1} x_i^2)\hat{\alpha}_{t-1} + x_t y_t}{\sum_{i=1}^{t} x_i^2} \\
&= (1 - \pi_t)\hat{\alpha}_{t-1} + \pi_t \left(\frac{y_t}{x_t}\right),
\end{aligned}
\tag{7.12}
$$

where, $\pi_t = x_t^2 / \sum_{i=1}^{t} x_i^2$. (7.12) defines the RLS filter of α_t. Because of the strength of past data, it is seen that the RLS has a delay to distinguish the fault size, therefore, some modifications on this estimator are given. The exponentially weighted version of this estimator for some forgetting factor $\lambda_e \in (0,1)$ is also given by,

$$\hat{\alpha}_{t,\lambda_e} = \frac{\sum_{i=1}^{t} \lambda_e^{t-i} x_i y_i}{\sum_{i=1}^{t} \lambda_e^{t-i} x_i^2}. \tag{7.13}$$

Suitable values for λ_e belong to the interval $(0.95, 0.99)$. The recursive formula for $\hat{\alpha}_{t,\lambda_e}$ is given by,

$$\hat{\alpha}_t = (1 - \pi_{t,\lambda_e})\hat{\alpha}_{t-1} + \pi_{t,\lambda_e}\left(\frac{y_t}{x_t}\right), \tag{7.14}$$

where, $\pi_{t,\lambda_e} = x_t^2 / \sum_{i=1}^{t} \lambda_e^{t-i} x_i^2$. The ordinary least square estimator $\hat{\alpha}_t$ based on the r-current observations (with suitable select for r) is given by,

$$\hat{\alpha}_{t,r} = \frac{\sum_{i=t-r+1}^{t} x_i y_i}{\sum_{i=t-r+1}^{t} x_i^2}. \tag{7.15}$$

It is referred to as the windowed least square estimate, in the literature. One may use a hybrid estimator by combining the weighted and windowed formula. It should be noted that there is a tradeoff between the length of the window r and the accuracy of the windowed estimator and the cost of data gathering will be considerable. Indeed, using exponentially weighted or windowed least square estimates, it is expected to utilize the most recent data, instead of using all data, which is the case for $\hat{\alpha}_t$. So, the accuracy of fault size estimation should be increased, as discussed in the simulation section.

A useful tool for fault size identification, visually, especially in offline settings, is the scatter plot of the measured signal, y_t, against the estimated state $\hat{x}_t$. If the estimated state is time ordered, i.e. an increasing function of time, then the model is changed to a piecewise line regression and this plot clarifies the fault size very well. However, this is not always the case. To overcome this problem, let z_t be an increasing sequence across time t. Then, the following regression model has increasing independent variable z_t, that is,

$$y_t^* = \frac{z_t}{x_t}y_t = \alpha_t z_t + \frac{z_t}{x_t}\varepsilon_t = \alpha_t z_t + \varepsilon_t^*. \tag{7.16}$$

Notice that $var\left(\varepsilon_t^*\right) = z_t^2 \sigma_\varepsilon^2 / x_t^2$. To avoid heteroscedasticity problems, it is necessary to use the weighted least square,

$$\hat{\alpha}_{w,t} = \frac{\sum_{i=1}^{t} w_t z_t y_t^*}{\sum_{i=1}^{t} w_t z_t^2}, \tag{7.17}$$

where, $w_t = x_t^2/z_t^2$. The scatter plot of (z_t, y_t^*) works better than this plot based on coordinates (x_t, y_t). To find z_t, let

$$z_t = x_t + bh_t \left(z_{t-1} - x_t \right), b \geq 1, \; z_1 = x_1, \qquad (7.18)$$

where,

$$h_t = \begin{cases} 0, & x_t \geq z_{t-1}, \\ 1, & x_t < z_{t-1}, \end{cases} \qquad (7.19)$$

When $b = 1$, then, $z_t = max(z_{t-1}, x_t)$. This choice has a problem that if for some t, z_{t-1} is larger that z_s, $s \geq t$, then the trend of regression is removed. To solve this problem, a modified version of this method is,

$$z_t = max(z_{t-1}, x_t) + \delta, \qquad (7.20)$$

where, δ is a small number like 0.005. It should be noted that similar to the ordinary least square estimate $\hat{\alpha}_t$, the exponentially weighted and windowed least square estimates can be rewritten for sorted state and measurements, i.e. z_t and y_t^*, such that w_t appears in the numerator and denominator of exponentially weighted and windowed estimate formulas, which are going to be used in this work, as follows,

$$\begin{aligned} \hat{\alpha}_{w,t,r} &= \frac{\sum_{i=t-r+1}^{t} w_t z_t y_t^*}{\sum_{i=t-r+1}^{t} w_t z_t^2}, \\ \hat{\alpha}_{w,t,\lambda_e} &= \frac{\sum_{i=1}^{t} \lambda_e^{t-i} w_t z_t y_t^*}{\sum_{i=1}^{t} \lambda_e^{t-i} w_t z_t^2}. \end{aligned} \qquad (7.21)$$

The $\hat{\alpha}_t = \omega_g/\hat{\omega}_g$ graph is illustrated in Figure 7.16, in which the ω_g sensor coefficient is doubled at $t = 1500(s)$. It is obvious that despite the rapid change in Figure 7.17, the fault size is not clearly identified. The $\hat{\alpha}_{w,t}$ is shown in Figure 7.17. Also, exponentially weighted and windowed least square estimates are shown in Figures 7.18 and 7.19, respectively.   It is obvious that, comparing Figures 7.16-7.19, the
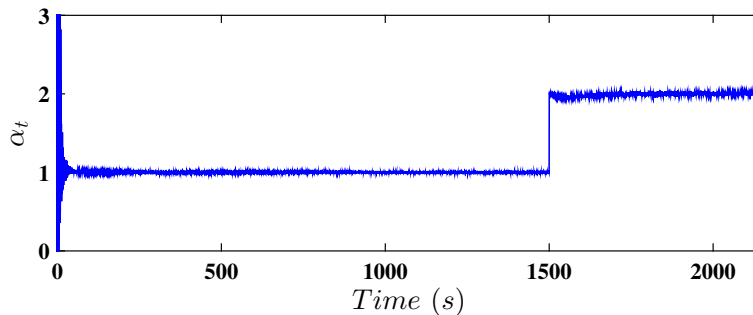
FIGURE 7.16: $\hat{\alpha}_t = \omega_g/\hat{\omega}_g$.
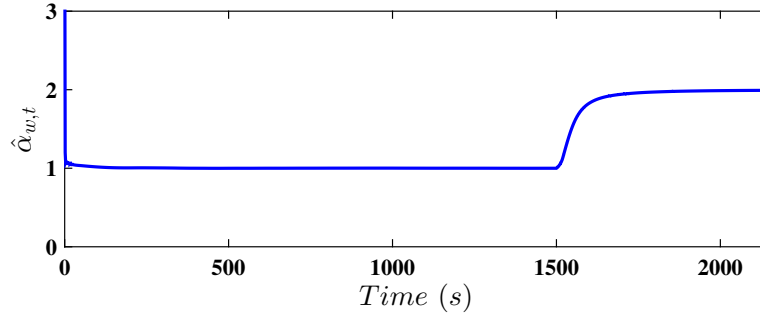
FIGURE 7.17: $\hat{\alpha}_{w,t}$.
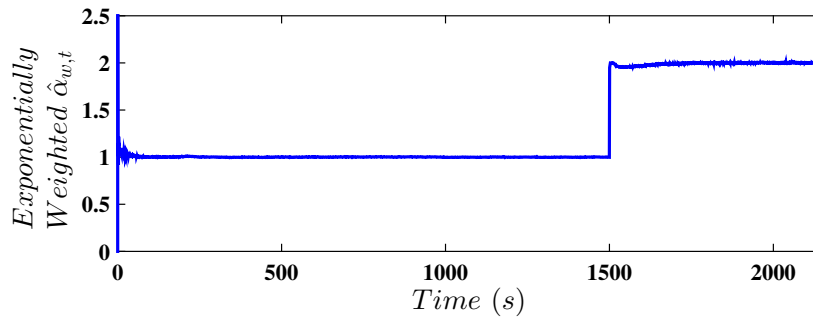
FIGURE 7.18: Exponentially weighted $\hat{\alpha}_{w,t,\lambda_e}$ for $\lambda_e = 0.95$.

noise is removed from $\hat{\alpha}_{w,t}$, while there is a considerable delay in fault size identification. So, using exponentially weighted and windowed least square estimates, this delay is eliminated. It should be noted that, via simulation study, windowed estimates are less time consuming and, by adjusting window length, the noise effect is completely removed from the estimated fault size.

To compare the different estimations numerically, the RMSE and VAF indices are used, which are as follows (Badihi et al., 2014),

$$
\begin{aligned}
RMSE &= \sqrt{\frac{1}{N} \sum_{i=1}^{N} (\alpha_{it} - \hat{\alpha}_{et})^2}, \\
VAF &= 1 - \frac{var(\alpha_{it} - \hat{\alpha}_{et})}{var(\alpha_{it})},
\end{aligned}
\tag{7.22}
$$

where, N is data number, α_{it} is ideal fault size which should be estimated and $\hat{\alpha}_{et}$ is estimated one.

Corresponding RMSE and VAF indices for Figures 7.16-7.19, are compared in Table 7.1. It is obvious that the exponentially weighted and windowed estimates are more accurate while the windowed method is less time consuming than the exponential one.
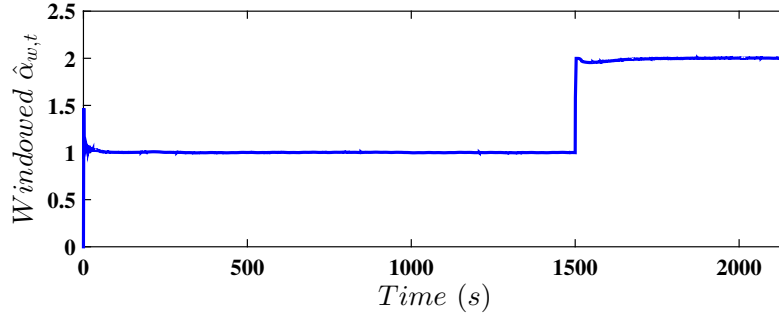
FIGURE 7.19: Windowed $\hat{\alpha}_{w,t,r}$ for $r = 1000$.

TABLE 7.1: RMSE and VAF indices for different identification methods

Estimation Method		RMSE	VAF
$\hat{\alpha}_t = \omega_g/\hat{\omega}_g$		44.43	9387.9
$\hat{\alpha}_{w,t}$		40.39	9381.4
Windowed $\hat{\alpha}_{w,t,r}$	$r = 1000$	0.027	0.9964
	$r = 3000$	0.33	0.9948
	$r = 5000$	0.057	0.9846
Exponentially weighted $\hat{\alpha}_{w,t,\lambda_e}$	$\lambda_e = 0.95$	0.076	0.722

Now, to accurately evaluate the proposed fault identification algorithm for multiple faults, which is the case in the simulation section, the fault scenario, which is given as follows, is designed such that several consecutive faults with different sizes and sources appear,

$$\alpha_t \; of \; \omega_g \; sensor = \begin{cases} 1, & 0 \le t < 300, \\ 2, & 300 \le t < 800, \\ 1, & 800 \le t < 1000, \\ 0.5, & 1000 \le t < 1300, \\ 1, & 1300 \le t \le 2145, \end{cases}$$

$$\alpha_t \; of \; \omega_r \; sensor = \begin{cases} 1, & 0 \le t < 1700, \\ 0.25, & 1700 \le t < 2100, \\ 1, & 2100 \le t \le 2145. \end{cases}$$

Considering this fault scenario, regardless of fault source, the expected estimate of fault sizes, which are going to be identified via the proposed algorithm, should be as follows. Considering the ω_g sensor coefficients, it is easy to conclude that

between $300 \leq t < 800$ and $1000 \leq t < 1300$, the ω_g sensor output is 2 and 0.5 times the estimated one, respectively. On the other hand, between, $1700 \leq t < 2100$, the ω_r sensor output is multiplied by 0.25 and because of PID, such that $\omega_r = \hat{\omega}_r$, and the ω_g sensor output will be 4 times the estimated one,

$$expected\ fault\ size\ estimation:\ \hat{\alpha}_t = \begin{cases} 1, & 0 \leq t < 300, \\ 2, & 300 \leq t < 800, \\ 1, & 800 \leq t < 1000, \\ 0.5, & 1000 \leq t < 1300, \\ 1, & 1300 \leq t < 1700, \\ 4, & 1700 \leq t < 2100, \\ 1, & 2100 \leq t \leq 2145. \end{cases}$$

First of all, the residual, on which basis the fault is detected, using the estimated states, is shown in Figure 7.20. It should be noted that each change of sensor coefficient is precisely detected as a fault, for instance, at $t = 1300(s)$, at which the coefficient of ω_g sensor is changed from 0.5 to 1, the residual deviates considerably from zero, even though the coefficient 1 is a fault-free situation. The fault probability, on which basis the fault periods can be found, because this section is about fault size estimation, are not shown, but will be considered in the simulation section. Additionally, the estimated fault sizes are shown in Figures 7.21-7.23, including $\hat{\alpha}_t = \omega_g / \hat{\omega}_g$, $\hat{\alpha}_{w,t}$ and the windowed $\hat{\alpha}_{w,t,r}$. It should be noted that the exponentially weighted estimate is omitted here, because it takes too much computation time while the windowed one is more accurate, as discussed earlier in this section.
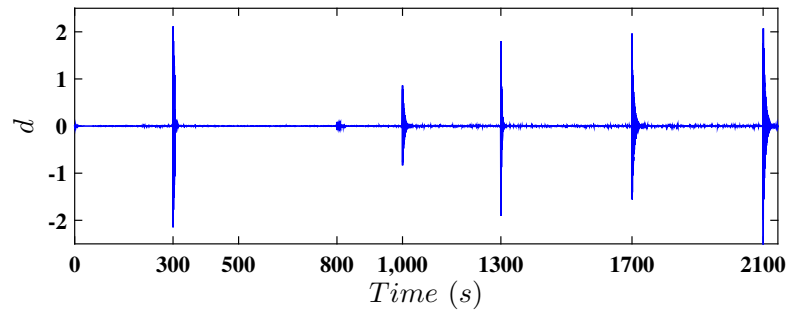
FIGURE 7.20: Residual for multiple fault scenario.

It is obvious that $\hat{\alpha}_{w,t}$ the estimated fault size has a delay and the size 0.5 is not estimated at all. On the other hand, the windowed $\hat{\alpha}_{w,t,r}$ has accurately estimated the fault size as well as fault time, and the noise content, which is obvious in
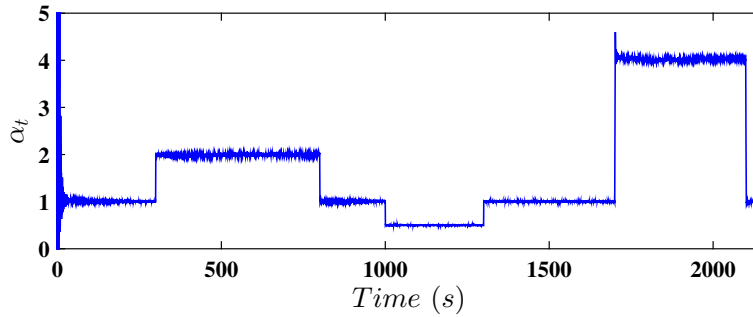
FIGURE 7.21: $\hat{\alpha}_t = \omega_g/\hat{\omega}_g$ for multiple fault scenario.
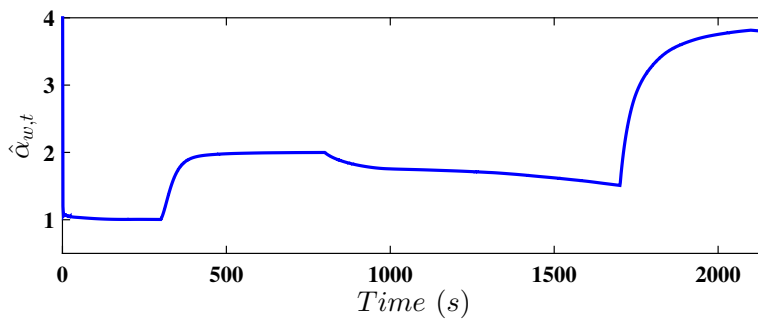
FIGURE 7.22: $\hat{\alpha}_{w,t}$ for multiple fault scenario.

$\hat{\alpha}_t = \omega_g/\hat{\omega}_g$, is satisfactorily removed. The corresponding RMSE and VAF indices are shown in Table 7.2.

7.6   FTC Simulation Results

In this section, using a real measured wind speed shown in Figure 4.18, proposed FD and FTC algorithms are evaluated, with the aim of the baseline controller (4.7). It should be noted that the proposed controller (5.15) is implantable here, but just for the sake of consideration, the baseline controller is used.

TABLE 7.2: RMSE and VAF indices for several consecutive faults

Estimation Method		RMSE	VAF
$\hat{\alpha}_t = \omega_g/\hat{\omega}_g$		44.8970	1395.22
$\hat{\alpha}_{w,t}$		44.241	1393.64
Windowed $\hat{\alpha}_{w,t,r}$	$r = 1000$	0.088	0.9938
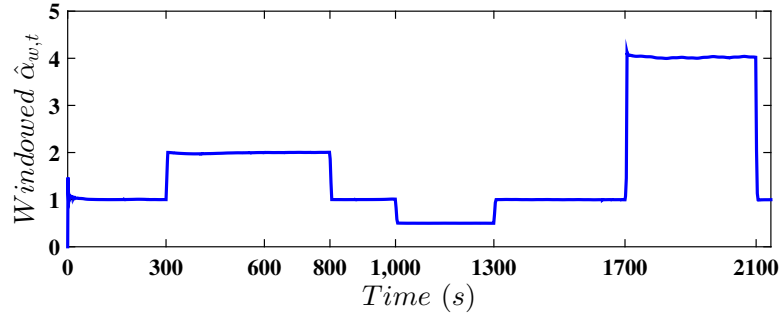
FIGURE 7.23: Windowed $\hat{\alpha}_{w,t,r}$ for multiple fault scenario $r = 1000$.

7.6.1 Multiplicative fault scenario

In this section the multiplicative fault scenario is investigated, which is as follows,

$$First\ fault\ scenario: \alpha_t\ of\ \omega_g sensor = \begin{cases} 1, & 0 \leq t < 600, \\ 4, & 600 \leq t < 800, \\ 1, & 800 \leq t \leq 1800, \end{cases}$$

$$\alpha_t\ of\ \omega_r\ sensor = \begin{cases} 1, & 0 \leq t < 1400, \\ 0.5, & 1400 \leq t < 1600, \\ 1, & 1600 \leq t \leq 1800, \end{cases}$$

and the expected fault size is,

$$expected\ fault\ size\ estimation: \hat{\alpha}_t = \begin{cases} 1, & 0 \leq t < 600, \\ 4, & 600 \leq t < 800, \\ 1, & 800 \leq t < 1400, \\ 2, & 1400 \leq t < 1600, \\ 1, & 1600 \leq t < 1800. \end{cases}$$

The generated power with this fault scenario, is compared to the fault-free one, in Figure 7.24. It can be seen that the generated power is less than the fault-free one over the range from $600 \leq t < 1100$, although the ω_g sensor fault is only between $600 \leq t < 800$. Indeed, the system is still under the effect of the sensor fault $300(s)$ after the fault has removed. Also, as it was stated in the proposed controller section, the generated power is not affected by the ω_r sensor fault, because this sensor measurement is not fed into the proposed controller, but because it is fed into

the Kalman filter, it deviates the residual from zero, so it should be accommodated.

FIGURE 7.24: Comparison between generated power under first fault scenario (red line) and fault-free one (blue line).

Fault detection

The residual and fault probability of the considered fault are shown in Figures 7.25 and 7.26. It is obvious that according to the residual, the fault moments are accurately detected. On the other hand, as shown in Figure 7.26, the fault periods are satisfactorily shown.
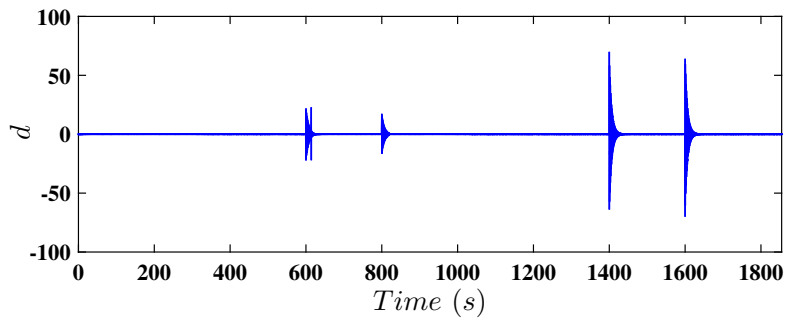
FIGURE 7.25: The residual for first fault scenario.

Fault isolation

Utilizing fault sizes, which are going to be identified in the next section, remedial action and fault accomodation scenarios, the location of each fault is determined. It should be noted that, in this proposed FTC scheme, the fault isolation and identification happen simultaneously, but for sake of explanation, are described separately. So, in this step, for fault isolation purposes, the expected values of fault size are
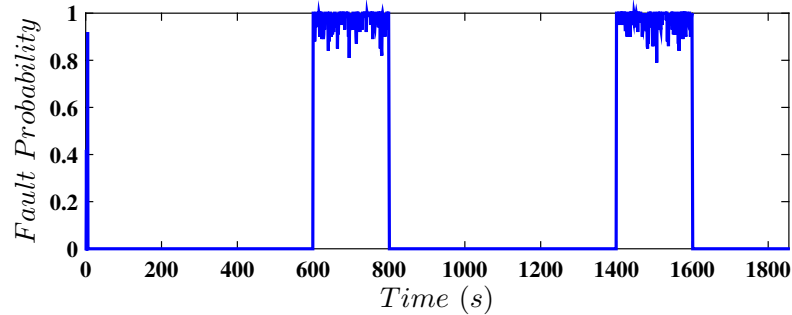
FIGURE 7.26: The fault probability for first fault scenario.

used, which is not the case in practice. Firstly, between $600 \leq t < 800$, the ω_g sensor output is divided by 4 before it is fed into the controller and then, is divided by 2 between $1400 \leq t < 1600$. At each step, it is expected that the corresponding residual and fault probability are zero, otherwise, it can be concluded that the ω_r sensor is faulty and its output is multiplied by the fault size. In Figures 7.27 and 7.28, the residual and fault probability, for fault isolation purposes are shown, respectively.

It is obvious that during $600 \leq t < 800$, the fault effect was removed, so it was correctly decided that the fault source was the ω_g sensor, while at $t = 1400(s)$ the residual and fault probability are deviated from zero significantly, so the fault source was not the ω_g sensor, rather it was the ω_r sensor, so that after this decision and multiplying the ω_r sensor output by the fault size which was 2, the residual and fault probability are zero, again.
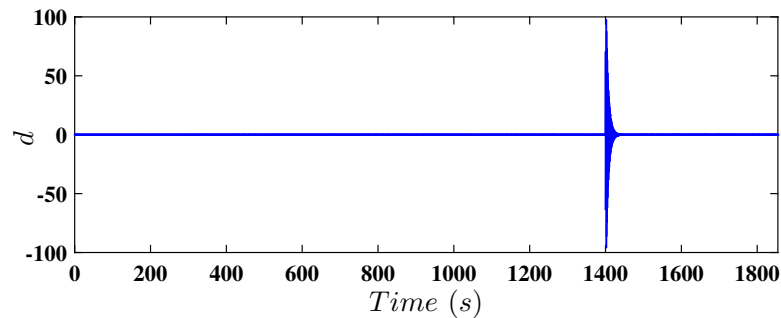
FIGURE 7.27: The residual for fault isolation under first fault scenario.

Fault identification

Now, using the proposed algorithms, the fault size is identified, as shown in Figures 7.29 and 7.30. It should be noted that $\hat{\alpha}_{w,t}$ and the exponentially weighted estimate,
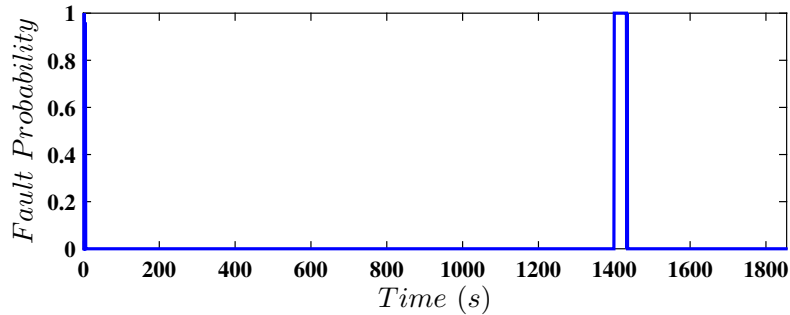
FIGURE 7.28: The fault probability for fault isolation under first
fault scenario.

are not shown as the windowed one satisfactorily estimate the fault size and the
estimation delay and noise have been eliminated.
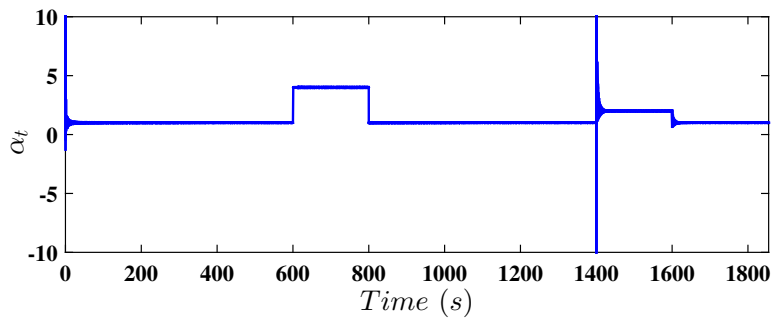
FIGURE 7.29: $\alpha_t = \omega_g/\hat{\omega}_g$ for first fault scenario.

Fault accommodation

Using the estimated fault size and the proposed FTC basis, which is the virtual sensor and the isolated fault source, the fault effect has been eliminated. It should be noted, as stated in the fault isolation section, that all steps are implemented simultaneously to evaluate the proposed FTC scheme practically. In accommodating the fault effect, it is assumed that the source of the fault is not yet isolated and it is done at the same time as the fault accommodation. The resulting generated power is shown in Figure 7.31 and a comparison with the fault-free and faulty situations, is made. It is obvious that at $t = 1400(s)$, when mistakenly the ω_g sensor is isolated as the fault source, the generated power deviated from the fault-free one, which is inevitable because this is a necessary part of the fault isolation step. After this time, it was decided that the ω_r sensor was the fault source and, consequently, the generated power returns to be the same as the fault-free one. Additionally, in Table 7.3, the generated power and induced torsion angle of twist for the fault-free and faulty
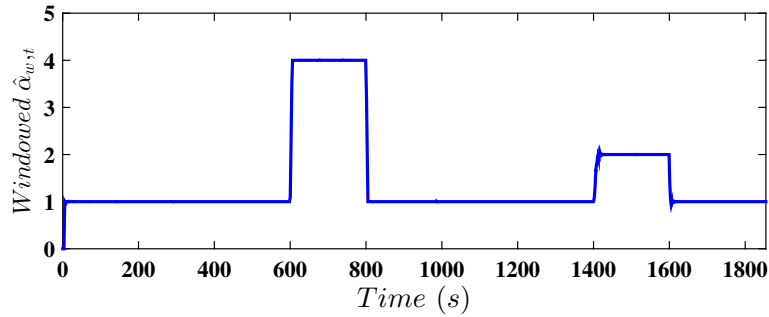
FIGURE 7.30: Windowed $\hat{\alpha}_{w,t,r}$ for multiple fault scenario $r = 1000$ for first fault scenario.

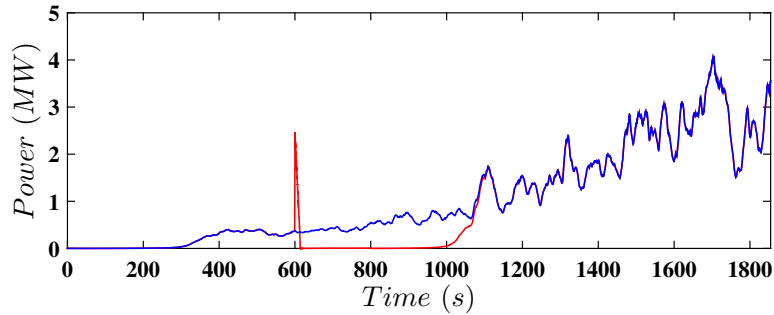

FIGURE 7.31: Comparison between generated power under first fault scenario with FTC (red line) and fault-free one (blue line).

situation with/without FTC are compared numerically, to evaluate the effect of the proposed FTC algorithm.

It can be concluded that, despite the energy loss at the fault isolation time, the captured energy with FTC is very close to the fault-free one. Additionally, via FTC algorithm, the induced torsion angle on the drive train is kept at a reasonable level compared to the operation without FTC.

TABLE 7.3: Control Criteria values for first fault scenario

Performance criteria	Fault-free situation	Faulty situation without FTC	Faulty situation with FTC
$CC1$	1.93 (GJ)	1.724 (GJ)	1.926 (GJ)
$CC2$	5.92 $(\mu rad^2/s)$	586.37 $(\mu rad^2/s)$	83.06 $(\mu rad^2/s)$

7.6.2   Additive (bias) and fixed output fault scenario

In this section, to investigate the proposed FTC algorithm for the fixed sensor output or the biased one, the fault scenario is defined as follows, and its effects are shown in Figures 7.32 and 7.33. Second fault scenario: ω_g sensor output is fixed at $80(rad/s)$ in $1000 \leq t < 1200$ and ω_r sensor output is biased $2(rad/s)$ in $500 \leq t < 700$.

It is obvious that ω_g and ω_r sensor outputs are fixed and biased in corresponding time periods, respectively. Also, in Figure 7.34, the generated power under the second fault scenario is shown, which deviated from the fault-free one when the ω_g sensor is faulty. Although the ω_r sensor has no effect on the generated power, it still increases the induced torsion angle of shaft twist and should be accommodated.
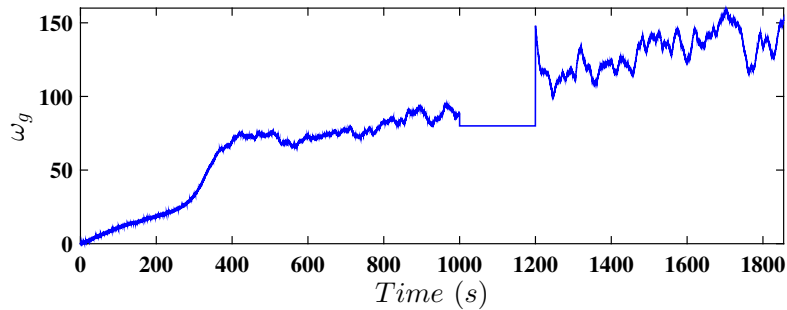
FIGURE 7.32: ω_g sensor output under second fault scenario.
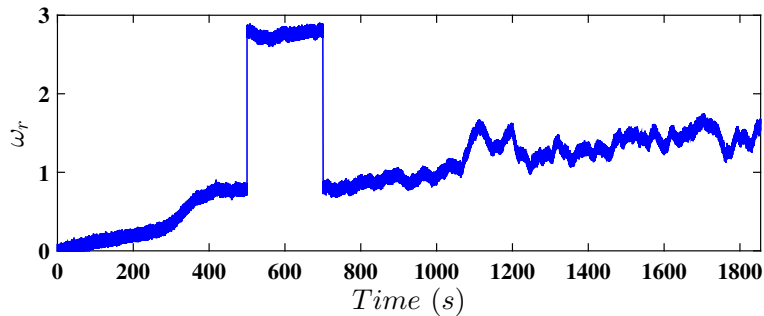
FIGURE 7.33: ω_r sensor output under second fault scenario.

Fault detection

The residual and fault probability, for obtaining fault moments and periods, are shown in Figures 7.35 and 7.36, respectively. It is obvious, considering these two indices, that the faults are accurately detected.
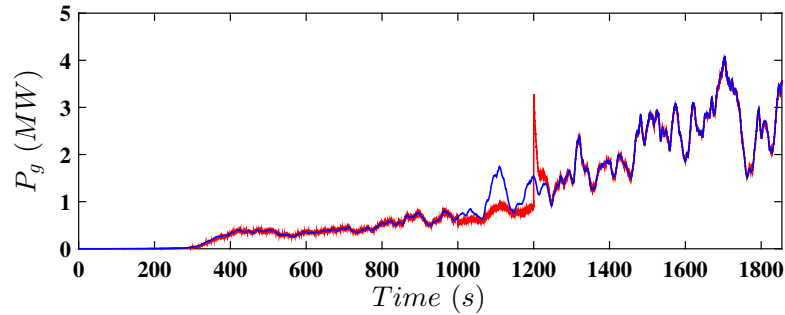
FIGURE 7.34: Comparison between generated power under second fault scenario (red line) and fault-free one (blue line).
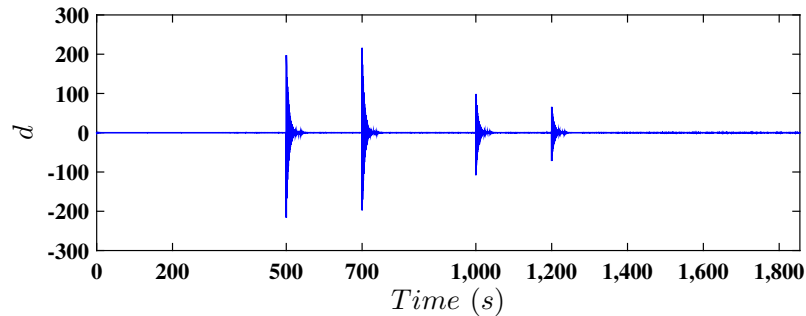
FIGURE 7.35: The residual for second fault scenario.

Fault isolation, identification and accommodation

In this section, the second fault scenario is identified with windowed RLS, as shown in Figure 7.37. It should be noted that because the fixed and biased fault is considered as a multiplicative fault with variable coefficient, the ideal fault size cannot be predicted prior to the fault identification, which is the case in real FTC of dynamic systems.

The fault isolation and accommodation are done simultaneously, because there is no fault size expectation to consider these two steps separately, such as in the multiplicative fault scenario section. Even for the multiplicative fault scenario, the fault isolation and accommodation are conducted at the same time, but for sake of explanation and because the ideal fault size was well known prior to fault identification, they were addressed separately. The updated residual and fault probability are shown in Figures 7.38 and 7.39, respectively, in which it is obvious that at $t = 500$ (s), it was mistakenly decided that the ω_g sensor was faulty and actually, the ω_r sensor was the fault source. Accordingly, using the estimated fault size, Figure 7.37, the ω_r sensor output was corrected. On the other hand, at $t = 1000$ (s), according to Figure 7.38 and 7.39, it can be concluded that the fault source was correctly selected as the ω_g sensor whose sensor output was corrected prior to feeding
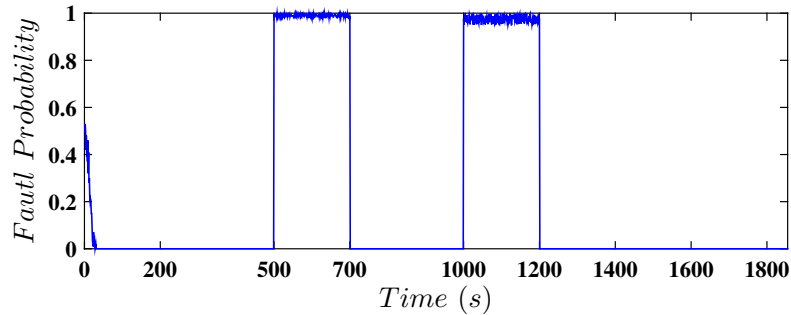
FIGURE 7.36: The fault probability for second fault scenario.

TABLE 7.4: Control Criteria values for second fault scenario

Performance criteria	Fault-free situation	Faulty situation without FTC	Faulty situation with FTC
$CC1$	1.93 (GJ)	1.882 (GJ)	1.929 (GJ)
$CC2$	5.92 $(\mu rad^2/s)$	51.52 $(\mu rad^2/s)$	25.79 $(\mu rad^2/s)$

it into the controller. Also, in Figure 7.40, the generated power is compared to the fault-free one, which confirms the above mentioned result.
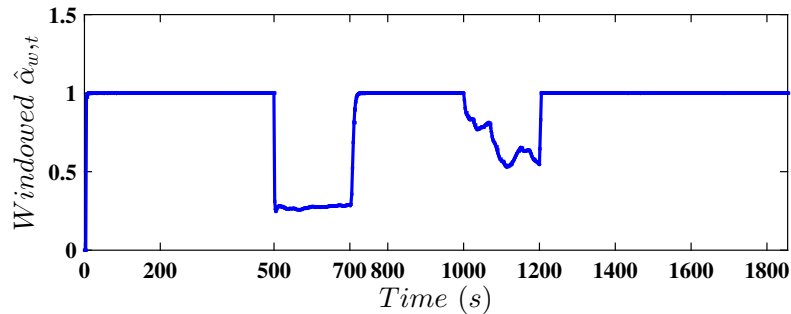
FIGURE 7.37: Windowed $\hat{\alpha}_{w,t,r}$, $r = 1000$ for second fault scenario.

In Table 7.4, the control criteria for the fault-free situation and the fault with/without FTC are given to evaluate the proposed algorithm numerically. It is obvious that, despite the fact that the generated power in the fault situation with FTC is very close to the fault-free one, the induced torsion angle of twist is considerably less than the corresponding value for the faulty situation without FTC because of the accommodation of the sensor fault.

In this chapter, a FTC scheme, to accommodate drive train sensor faults, was proposed. To detect sensor faults, a Kalman filter procedure was designed such that it was sensitive to faults and the aerodynamic torque was also estimated by utilizing
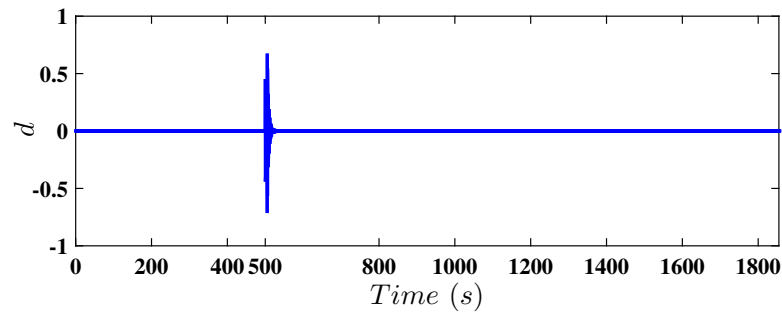
FIGURE 7.38: The residual for fault isolation under second fault scenario.
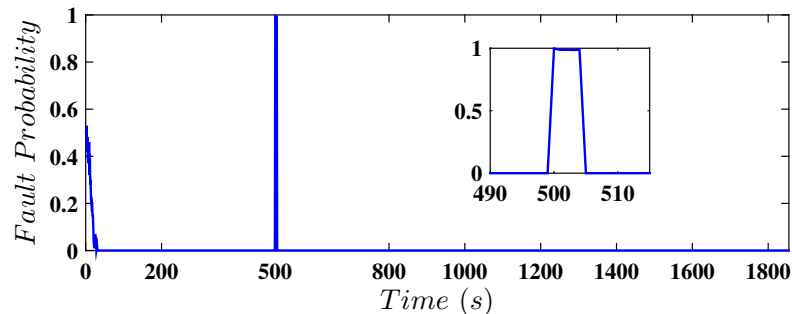
FIGURE 7.39: The fault probability for fault isolation under second fault scenario.

a PID controller prior to the Kalman filter. The sensor faults were modelled as a multiplicative fault which represents a change in coefficient of the measurement equation to cover several different faults simultaneously. The residual, constructed by estimated states, was investigated for several fault scenarios and consequently, to isolate the fault source, an auxiliary signal was designed. Additionally, the fault probability using the Bayesian setting was calculated to be used as part of FDI and meanwhile, to diagnose the fault periods. The recursive least square methods and its two modifications, were used to eliminate the noise from the estimated fault size which was then fed into the fault accommodating scheme to remove the fault effects. The windowed RLS fault size estimation, because of its inherent updating characteristics, showed better fault size estimation when using the RMSE index for several consecutive faults. Utilizing the virtual sensor and signal correction concept, the baseline controller was demonstrated to be useable in both fault-free and faulty situations which was a desirable property for this proposed controller. All proposed algorithms and the baseline controller, were evaluated with two different fault scenarios including multiplicative, biased and fixed faults. The results showed satisfying accommodation of the considered faults and the total generated power and induced torsion angle of twist on the drive train as control criteria, and showed the ability of this algorithm to keep the wind turbine operating very close to the
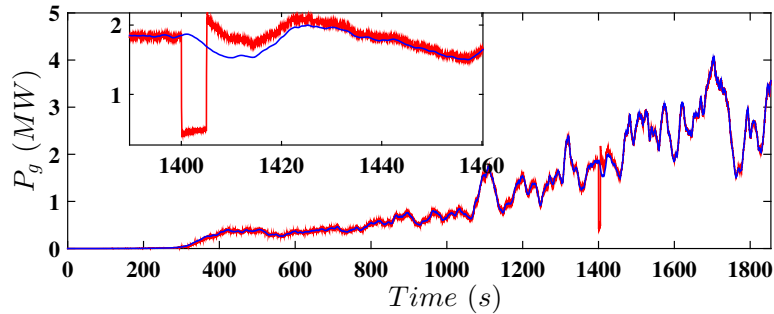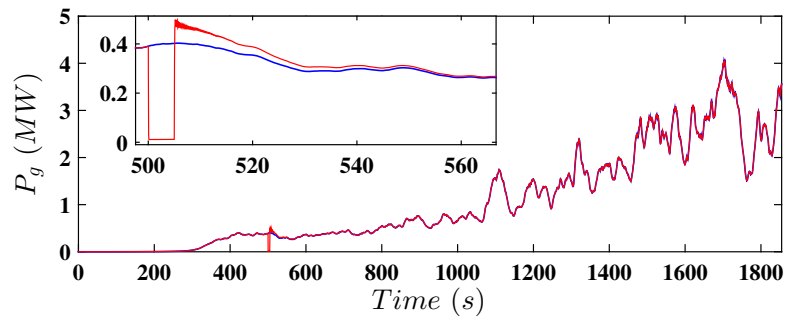
FIGURE 7.40: Comparison between generated power under second
fault scenario with FTC (red line) and fault-free one (blue line).

desirable trajectory in faulty situations compared to the fault-free one, which is the
major aim of FTC.

8 Conclusions

In this chapter, the concluding remarks of this thesis are discussed. Also, based on the given discussion, some of the future study trends of the current research are proposed.

8.1 Concluding Remarks

In this thesis MBFDI and FTC design approaches of a wind turbine benchmark model were sought, as the most recent solutions to have sustainable and reliable wind energy production. These approaches are shown to be profitable in the case of offshore wind farms, which are currently dominating this industry. This arises from the fact that long-term operation in harsh remote environment with less maintenance plans, due to reachability difficulty, increase the possibility of the presence of faults on the wind turbines, and consequently, power generation is degraded, requisite downtime is longer and increased maintenance cost is expected. As the wind turbine MBFDI and FTC designs have recently been introduced, there exist numerous studies on this field. Accordingly, to have a contributive research, an accurate and comprehensive review on the wind turbine MBFDI and FTC designs was presented in Chapter 2. On this regard, the different methods, which have been adopted to fulfil the fault tolerance capability on wind turbines, were introduced in detail, and their application on wind turbines components, was evaluated. This led to accurately adopting the methods to be utilized in the rest of this thesis.

A necessary step in MBFDI and FTC design, is accurate wind turbine modeling. So, in Chapter 3, the HAWT model was accurately introduced, including different fault sources, which have been considered afterwards. Also, the HAWT operational modes and desirable trajectories were introduced, on which basis, numerical operational criteria were defined. These criteria were widely used in the following chapters to investigate the fault tolerance capability of the proposed controllers in comparison to the available industrial baseline controllers. Consequently, these baseline controllers were introduced in Chapter 4 and their performance on the wind turbine are investigated. As a side outcome, satisfactory operation using the baseline controller could lead to wind turbine model verification. In both partial load and full load operations, the baseline controllers are constant gain ones, assuming the wind turbine is operating on the desired operational mode, which is not the case in

practice. Accordingly, in Chapter 4, initial improvements of the baseline controllers were proposed. In partial load operation the baseline controller was equipped with FIS to tune the controller gain properly, with respect to corresponding wind speed variation. The results showed the increased captured power. On the other hand, a PID-like controller is designed with adaptive gains for full load operation, to take advantage of structural simplicity, while providing a better performance, compared to the baseline PID controller. Also, the Nussbaum-type function was adopted in adaptive laws, to tackle the unknown control direction problem, which stemmed from unknown wind speed variation. On the other hand, the proposed controller was passively tolerant against the pitch actuator faults and dynamic change.

Throughout this thesis, the proposed controllers were designed separately for different operational regions of wind turbines. The reason for this approach, is that, there exist some available wind turbines in operation which have been designed for only one operation region. On the other hand, the integration of the proposed controller into one controller to function in the whole operational region of the wind turbine is not challenging. Indeed, via adoption of some appropriate switching schemes, the proposed controller can be integrated into one controller, which was considered in this thesis. Accordingly, in chapter 5, for partial load operation, a nonlinear FTC was proposed to keep the wind turbine operating with maximum efficiency, in the presence of pitch angle bias, dynamic change and generator torque bias, similar to the fault-free case. Also, the wind speed was assumed as an unmeasurable disturbance, and accordingly using GRBFNN, the unknown desired trajectory was reconstructed, so that the captured power was maximized. The proposed controller was shown to be able to keep the wind turbine tracking the reconstructed desired trajectory with sufficient accuracy. Results were compared with the baseline controller ones, which showed superiority of the proposed controller in both fault-free and faulty cases. Also, the considered faults were estimated adaptively, and fault information was gathered which can be used in maintenance procedures.

In Chapter 6, the constrained FTC was designed for the full load region. The idea was to avoid the possible and frequent use of mechanical brakes which are located on the rotor shaft. The use of these brakes is to prevent the rotor shaft from over speeding and keep the wind turbine structurally safe. On the other hand, mechanical brake engagement leads to increased applied stress on the drive train. The baseline controller was shown not to be able to guarantee that the rotor speed does not violate the predefined and safe-to-operate limit. So, via adoption of constrained control this objective was achieved. Also, the proposed controller was robust against pitch actuator faults, dynamic change and aerodynamic characteristics change due to debris build-up. The pitch actuator saturation was smoothly avoided. The Nussbaum-type function was utilized to resolve the unknown control direction problem. The fault information was estimated adaptively. Finally, the unknown aerodynamic torque, was approximated using GRBFNN. The numerical comparison was made with respect to baseline controller results, considering the defined performance criteria,

which showed the effectiveness of the proposed controller.

In Chapter 7, the drive train sensor MBFDI scheme was designed. This scheme was shown to be able to detect and isolate the faults in both rotor speed and generator speed sensors, using a UIO with a Kalman filter structure. This was done to avoid using the wind speed estimation, which was given in Chapter 5, because, in that estimation the sensors measurements were already used. So, in the case of sensor faults this estimation is not accurate anymore. Accordingly, it is aimed to keep the structure of the proposed scheme separated from the proposed schemes in the Chapters 5 and 6. On the other hand, within the Bayesian framework, the fault probability was calculated with the aim of particle filtering and EM algorithm, to be used in both FD and FII, without the need for any redundant sensor. It should be mentioned that both controllers proposed in Chapter 5 and 6, were utilizable here, but just for sake of consideration the baseline partial load controller was used. To let the controller be usable in both fault-free and faulty conditions, the VSA scheme was adopted to remove the sensor fault effects. An accurate fault size estimation was given which was used in the FA step. Also, a wide family of sensor faults, including multiplicative fault, bias and fixed output, were numerically considered and the results illustrated that the proposed FTC scheme was able to perform satisfactorily even in the presence of faults. Finally, it should be noted that the proposed scheme is applicable in the case of pitch and generator sensor faults. However, it is less challenging for the pitch actuator and generator sensors, as there is no unknown input acting on these two subsystems. Accordingly, this chapter was focused only on the drive train sensors, on which an unknown input, i.e. wind speed, is being applied.

8.2 Closing Points, Future Perspective and Trends

Wind turbine FDI and FTC have recently emerged to support reliable wind energy conversion. Different FDI schemes are available, which can rely on the accurate modelling, among which fuzzy T-S and LPV are common descriptions. However, it is always desirable to design FDI schemes for the nonlinear model. Effective FDI is the main step in the active FTC, so it should be well matured before practical implementation. The MBFDI methods applied to the drive train are still limited to signal-based methodologies. The blade aerodynamic change due to debris build-up and erosion can be detected more accurately at the farm level, compared to the individual wind turbine scale. The adoption of hardware redundancy is still an effective and desirable approach for industrial FDI purpose, in which the rate of false/missed alarms are decreased. For FTC, the VSA approach is more commonly adopted to compensate for the wind turbine sensor faults. This approach has attracted most of the industrial interest due to its simple implementation. The CR strategy has been

considered for accommodating the wind turbine actuator faults. However, accurate fault information is needed. In contrast to active FTC, the passive solutions are designed in a conservative manner, to remove the need for fault detection, and meanwhile to keep the wind turbine working in faulty situations with an accepted performance level, only in specific considered fault situations.

Finally, by considering the issues above, future trends on wind turbines FDI and FTC are suggested as follows.

- Expert's knowledge can be included in the design phase, using soft computing approaches, e.g. fuzzy if-then rules, neural networks or Bayesian frameworks.

- High-fidelity simulators are required for both wind turbine and wind farm systems.

- More realistic fault scenarios need to be implemented and analyzed, especially multiple and simultaneous actuator faults.

- Accurate performance analysis, verification and validation tools applied to the developed FDI and FTC strategies are required.

- The practical implementation of the designed schemes needs to be assessed in experimental-scale wind turbines and industrial applications.

- Most of the studies have been focused on FDI, rather than FTC design. Moreover, the proposed solutions are mostly developed for a given operational region of the wind turbine. Accordingly, the focus should be on FTC systems, since the FDI task is a by-product. Moreover, the requirements of Industry 4.0 lead to the consideration of adaptive and real-time methodologies, working for the whole operational region of the wind turbine.

- Some faults are better dealt with at the wind farm control level, e.g. blade debris build-up, erosion and slowly developing faults, but the literature is still scarce. So, new schemes for detection, isolation and accommodation of faults at the wind farm level should be investigated.

- Some faults, such as the ones affecting the drive train, are detected only via signal-based approaches (e.g. vibration or frequency analysis tools); active schemes should be analyzed for this wind turbine component.

A Proofs

In this appendix, the proofs of the theorems which have been stated in this thesis are given, in order of the appearances of the theorems.

A.1 Proof of Theorem 4.1

Let the Lyapunov function V be selected as,

$$V = \frac{1}{2}Z^2 + \frac{1}{2\sigma_1}\tilde{a}^2, \tag{A.1}$$

where, $\tilde{a}$ is estimation error of a, defined as $\tilde{a} = a - \hat{a}$. The time derivative of (A.1), considering (4.23) and (4.25), is derived as,

$$\dot{V} = Z\dot{Z} - \frac{1}{\sigma_1}\tilde{a}\dot{\hat{a}} = ZH + B(\lambda_{D_0} + \lambda_D)N(\xi)Z^2 + \frac{\sigma_0}{\sigma_1}\hat{a}\tilde{a} - \tilde{a}\varphi^2 Z^2. \tag{A.2}$$

Considering the trivial inequality $(\tilde{a} - a)^2 \geq 0$, it can be easily shown that $\hat{a}\tilde{a} \leq a^2/2 - \tilde{a}^2/2$. Also, considering (A.2), $ZH < |Z|\,a\varphi < a\varphi^2 Z^2 + a/4$ holds true. So, $\dot{V}$ can be bounded as,

$$\dot{V} \leq a\varphi^2 Z^2 + \frac{a}{4} + BN(\xi)\dot{\xi} + \frac{\sigma_0}{\sigma_1}\frac{a^2}{2} - \frac{\sigma_0}{\sigma_1}\frac{\tilde{a}^2}{2} - \tilde{a}\varphi^2 Z^2. \tag{A.3}$$

The right hand side of (A.3) is equal to $(\hat{a}\varphi^2 + \lambda_{D_0})Z^2 + a/4 + B(\cdot)N(\xi)\dot{\xi} + \sigma_0 a^2/2\sigma_1 - \sigma_0\tilde{a}^2/2\sigma_1 - \lambda_{D_0}Z^2$. Also considering $\lambda_D = \hat{a}\varphi^2$ and $\dot{\xi} = (\lambda_{D_0} + \lambda_D)Z^2$, yields,

$$\begin{aligned}
\dot{V} &\leq \dot{\xi} + B(\cdot)N(\xi)\dot{\xi} + \frac{a}{4} + \frac{\sigma_0}{\sigma_1}\frac{a^2}{2} - \frac{\sigma_0}{\sigma_1}\frac{\tilde{a}^2}{2} - \lambda_{D_0}Z^2 \\
&< \dot{\xi} + B(\cdot)N(\xi)\dot{\xi} - c_1 V + c_2,
\end{aligned} \tag{A.4}$$

where, $c_2 = \min\{\sigma_0, 2\lambda_{D_0}\}$ and $c_2 = a/4 + \sigma_0 a^2/2\sigma_1$ and both are positive. Multiplying (A.4) by $e^{c_1 t} > 0$, yields,

$$\frac{d\left(Ve^{c_1 t}\right)}{dt} \leq \dot{\xi}e^{c_1 t} + B\left(\cdot\right)N\left(\xi\right)\dot{\xi}e^{c_1 t} + c_2 e^{c_1 t}, \tag{A.5}$$

and integrating both sides of (A.5) over $[0\ t]$, leads to,

$$V < e^{-c_1 t}\int_0^t \left(B\left(\cdot\right)N\left(\xi\right) + 1\right)\dot{\xi}e^{c_1 \tau}d\tau + \left(V\left(0\right) - \frac{c_2}{c_1}\right)e^{-c_1 t} + \frac{c_2}{c_1}. \tag{A.6}$$

It is obvious that $0 < e^{-c_1 t} \leq 1$, so, inequality (A.6) is rewritten as,

$$V < e^{-c_1 t}\int_0^t \left(B\left(\cdot\right)N\left(\xi\right) + 1\right)\dot{\xi}e^{c_1 \tau}d\tau + c_0, \tag{A.7}$$

where, $c_0 = c_2/c_1 + V\left(0\right)$ is a positive constant. Considering Lemma 4.1 and Remark 4.3, it is concluded from (A.7) that V, ξ and $\int_0^t \left(B\left(\cdot\right)N\left(\xi\right) + 1\right)\dot{\xi}e^{c_1 \tau}d\tau$ are bounded on $[0\ t_f)$. As stated in (Ryan, 1991), if the closed-loop system solution is bounded, then t_f approaches to $+\infty$. Boundedness of V leads to boundedness of Z and $\tilde{a}$. Because a is bounded and $\tilde{a} = a - \hat{a}$, then $\hat{a}$ is bounded. Since, $V\left(0\right)$ is bounded, it is obvious that $\lim_{t\to+\infty} Z^2/2 \leq c_2/c_1$; i.e. $|Z|$ converges to set $\Omega = \{|Z|\ ||Z| < \sqrt{2c_2/c_1}\}$ as $t \to +\infty$. On the other hand, boundedness of Z ensures boundedness of e_r, $\int_0^t e_r\left(\tau\right)d\tau$ and $\dot{e}_r$, and consequently, ω_r, ω_g, φ are bounded (Khalil, 1996). Therefore, from (4.23), (4.25) and (4.26), it can be stated that β_{ref}, $\dot{\hat{a}}$, $\dot{Z}$ and λ_D are bounded. Taking the time derivative of β_{ref}, (4.25), can be written as,

$$\dot{\beta}_{ref} = \frac{\partial\beta_{ref}}{\partial Z}\dot{Z} + \frac{\partial\beta_{ref}}{\partial N}\frac{\partial N}{\partial \xi}\dot{\xi} + \frac{\partial\beta_{ref}}{\partial \varphi}\dot{\varphi} + \frac{\partial\beta_{ref}}{\partial \hat{a}}\dot{\hat{a}}, \tag{A.8}$$

where, $\partial\beta_{ref}/\partial Z = (\lambda_{D_0} + \lambda_D)N(\xi)$, $\partial\beta_{ref}/\partial N = (\lambda_{D_0} + \lambda_D)Z\left(t\right)$, $\partial\beta_{ref}/\partial\varphi = 2\hat{a}\varphi N(\xi)Z\left(t\right)$, $\dot{\varphi} = (\partial\varphi/\partial x_1)\dot{x}_1 + (\partial\varphi/\partial e)\dot{e}$ and $\partial\beta_{ref}/\partial\hat{a} = \varphi^2 N(\xi)Z\left(t\right)$. Note that Z, $\dot{Z}$, ξ, $\dot{\xi}$, $\hat{a}$, $\dot{\hat{a}}$, φ, $N(\xi)$ and, consequently, $\partial N/\partial\xi$ are all bounded and continuous, and accordingly so are all terms in (A.8). So, $\dot{\beta}_{ref}$ is bounded and continuous, which leads to smooth β_{ref}. This ends the proof. $\qquad\square$

A.2   Proof of Lemma 5.1

Multiplying both sides of $dV/dt < -b_1 V + b_2$ by $e^{b_1 t}$ leads to $e^{b_1 t}dV/dt < -e^{b_1 t}b_1 V + b_2 e^{b_1 t}$ which is equivalent to $d(e^{b_1 t}V)/dt < e^{(b_1 t)}b_2$. Now, taking the integral with respect to time from both sides, leads to $e^{b_1 t}V - V(0) < e^{b_1 t}b_2/b_1 - b_2/b_1$. Multiplying by $e^{-b_1 t}$, gives $V < b_2/b_1 + e^{-b_1 t}(V(0) - b_2/b_1)$. On the other hand, for bounded

initial condition and consequent bounded $V(0)$, V is bounded. Consequently, $\boldsymbol{x}$ is bounded since V includes a positive term as a function of states. On the other hand, as the time goes by, $e^{-b_1 t}$ approaches to zero. So, V satisfies $V < b_2/b_1$. $\square$

A.3   Proof of Lemma 5.2

Considering $(\tilde{a} + a)^2 \geq 0$ leads to $\tilde{a}^2 + a^2 \geq -2\tilde{a}a$. Replace $-2\tilde{a}a$ with $-2\tilde{a}(\hat{a} - \tilde{a})$ and multiply both sides by σ_d. Consequently, $-2\sigma_d \tilde{a}\hat{a} \leq -\sigma_d \tilde{a}^2 + \sigma_d a^2$ can be obtained. $\square$

A.4   Proof of Lemma 5.3

Consider the inequality $\xi^4 \leq \xi^2 \gamma^2 + \xi^4$ and take the square root from both sides. Consequently, it proves the left side of the inequality. To prove the right-hand side, consider $0 \leq 2|\xi|\gamma$ and add $\xi^2 + \gamma^2$ to both sides. Taking the square root of the resulting inequality leads to $\sqrt{\xi^2 + \gamma^2} \leq \gamma + |\xi|$. Accordingly, it can be obtained that $-1/\sqrt{\xi^2 + \gamma^2} \leq -1/(\gamma + |\xi|)$ which leads to $|\xi| - \xi^2/\sqrt{\xi^2 + \gamma^2} \leq |\xi| - \xi^2/(\gamma + |\xi|)$. Finally, considering $|\xi| - \xi^2/(\gamma + |\xi|) = \gamma|\xi|/(\gamma + |\xi|)$ and $\gamma|\xi|/(\gamma + |\xi|) < \gamma$, it can be seen that $|\xi| - \xi^2/\sqrt{\xi^2 + \gamma^2} < \gamma$. $\square$

A.5   Proof of Theorem 5.1

Choose a positive definite Lyapunov function $V^{\omega_{g,d}}$ as,

$$V^{\omega_{g,d}} = \frac{1}{2}\tilde{\Psi}^T \tilde{\Psi}. \tag{A.9}$$

The time derivative of $V^{\omega_{g,d}}$ can be obtained as,

$$\dot{V}^{\omega_{g,d}} = \tilde{\Psi}^T \dot{\Psi}^* + \sigma \tilde{\Psi}^T \Psi^* - \sigma \tilde{\Psi}^T \tilde{\Psi} - \Lambda \tilde{\Psi}^T \eta. \tag{A.10}$$

Considering the inequality for the two vectors $A, B \in R^{n \times 1}$ as, $\pm A^T B \leq (A^T A + B^T B)/2$ and, $A^T A = \|A\|$, the following can be derived from (A.10), as,

$$\dot{V}^{\omega_{g,d}} \leq \frac{\tilde{\Psi}^T \tilde{\Psi} + \dot{\Psi}^{*T} \dot{\Psi}^*}{2} + \sigma \frac{(\tilde{\Psi}^T \tilde{\Psi} + \Psi^{*T} \Psi^*)}{2} - \sigma \tilde{\Psi}^T \tilde{\Psi} + \Lambda \frac{(\tilde{\Psi}^T \tilde{\Psi} + \eta^T \eta)}{2}$$

$$\leq \frac{\tilde{\Psi}^T \tilde{\Psi}}{2} - \sigma \frac{\tilde{\Psi}^T \tilde{\Psi}}{2} + \Lambda \frac{\tilde{\Psi}^T \tilde{\Psi}}{2} + \|\dot{\Psi}^*\|^2 + \sigma \|\Psi^*\|^2 + \Lambda \|\eta\|^2$$

$$< -\Upsilon_1 V + \Upsilon_2,$$

$$(A.11)$$

where, $\Upsilon_1 = -1 + \sigma - \Lambda$ and $\Upsilon_2 = \sigma \psi_1^2 + \psi_2^2 + \Lambda \eta_1^2$. Since $0 < \sigma$, $0 < \Lambda$, and according to $\sigma > \Lambda + 1$, then $0 < \Upsilon_1$ and $0 < \Upsilon_2$. Now, considering Lemma 5.1, $\tilde{\Psi}$ and $\hat{\Psi}$ are UUB. Also, considering (5.5) and Assumption 5.1, it can be seen that $\dot{\hat{\Psi}}$ and consequently $\dot{\tilde{\Psi}}$ are UUB. □

A.6   Proof of Theorem 5.2

Choose a positive definite Lyapunov function as,

$$V^{T_g} = V_1^{T_g} + \frac{1}{2}e_{2,\omega_g}^2 + \frac{1}{2}\tilde{d}_1^2 + \frac{1}{2}\tilde{\theta}^T \Gamma^{-1} \tilde{\theta} + \frac{1}{2}\tilde{f}_1^2 + \frac{1}{2}\tilde{\rho}_{\tilde{f}_1}^2 + V^{\omega_{g,d}}. \qquad (A.12)$$

Taking the time derivative of (A.12) obtains, $\dot{V}^{T_g} = \dot{V}_1^{T_g} + e_{2,\omega_g}\dot{e}_{2,\omega_g} + \tilde{d}_1\dot{\tilde{d}}_1 + \tilde{\theta}^T \Gamma^{-1}\dot{\tilde{\theta}} + \tilde{f}_1 \dot{\tilde{f}}_1 + \tilde{\rho}_{\tilde{f}_1}\dot{\tilde{\rho}}_{\tilde{f}_1} + \dot{V}^{\omega_{g,d}}$, which can be rewritten as,

$$\dot{V}^{T_g} = \sum_{i=1}^{4} \Pi_i^{T_g} - k_{1,\omega_g}e_{\omega_g}^2 - k_{2,\omega_g}e_{2,\omega_g}^2 + \dot{V}^{\omega_{g,d}}, \qquad (A.13)$$

where, $\Pi_1^{T_g} = -e_{2,\omega_g}c_4\varepsilon - e_{2,\omega_g}d_1 + (\tilde{d}_1 - \hat{d}_1)e_{2,\omega_g}^2/\sqrt{e_{2,\omega_g}^2 + \eta_{d_1}^2} - \sigma_{d_1}\hat{d}_1\tilde{d}_1$, $\Pi_2^{T_g} = -c_4 e_{2,\omega_g}(\tilde{\theta}^T + \theta^{*T} - \hat{\theta}^T)h - \sigma_c\tilde{\theta}^T\hat{\theta}$, $\Pi_3^{T_g} = -e_{2,\omega_g}(-\hat{f}_1 + f_1 + \tilde{f}_1) - \sigma_{f_1}\hat{f}_1\tilde{f}_1 - \dot{f}_1\tilde{f}_1$

and $\Pi_4^{T_g} = -\sigma_{\tilde{f}_1}\hat{\rho}_{\tilde{f}_1}\tilde{\rho}_{\tilde{f}_1}$. According to Lemmas 5.2 and 5.3, it can be shown that,

$$
\begin{aligned}
\Pi_1^{T_g} &< \left|e_{2,\omega_g}\right|\left(c_4\bar{\varepsilon} + \bar{d}_1\right) - \frac{e_{2,\omega_g}^2}{\sqrt{e_{2,\omega_g}^2 + \eta_{d_1}^2}}D \\
&= \left(\left|e_{2,\omega_g}\right| - \frac{e_{2,\omega_g}^2}{\sqrt{e_{2,\omega_g}^2 + \eta_{d_1}^2}}\right)D - \sigma_{d_1}\hat{d}_1\tilde{d}_1 \\
&< \eta_{d_1}D - \frac{\sigma_{d_1}}{2}\tilde{d}_1^2 + \frac{\sigma_{d_1}}{2}D^2, \\
\Pi_2^{T_g} &< -\frac{\sigma_c}{2}\tilde{\theta}^T\tilde{\theta} + \frac{\sigma_c}{2}\theta^{*T}\theta^* \\
&< -\frac{\sigma_c}{2\lambda_{max}(\Gamma^{-1})}\tilde{\theta}^T\Gamma^{-1}\tilde{\theta} + \frac{\sigma_c}{2}\theta^{*T}\theta^*, \\
\Pi_3^{T_g} &< -\frac{\sigma_{f_1}}{2}\tilde{f}_1^2 + \frac{\sigma_{f_1}}{2}\bar{f}_1^2 + \rho_{\dot{f}_1}\rho_{\tilde{f}_1}, \\
\Pi_4^{T_g} &< -\frac{\sigma_{\tilde{f}_1}}{2}\tilde{\rho}_{\tilde{f}_1}^2 + \frac{\sigma_{\tilde{f}_1}}{2}\rho_{\tilde{f}_1}^2.
\end{aligned}
\tag{A.14}
$$

where, $\lambda_{max}\left(\Gamma^{-1}\right)$ is the maximum eigenvalue of Γ^{-1}. Finally, considering (A.11), (A.13) and (A.14), it can be shown that,

$$
\dot{V}^{T_g} < -b_1^{T_g}V^{T_g} + b_2^{T_g},
\tag{A.15}
$$

where, $b_1^{T_g} = min\{2k_{1,\omega_g}, 2k_{2,\omega_g}, \sigma_{\tilde{f}_1}, \sigma_{f_1}, \sigma_{d_1}, \sigma_c/\lambda_{max}(\Gamma^{-1}), 2\Upsilon_1\}$ and $b_2^{T_g} = \eta_{d_1}D + \sigma_{d_1}D^2/2 + \sigma_{f_1}\bar{f}_1^2/2 + \rho_{\dot{f}_1}\rho_{\tilde{f}_1} + \sigma_{\tilde{f}_1}\rho_{\tilde{f}_1}^2/2 + \sigma_c\|\theta^*\|^2/2 + \Upsilon_2$. Here, $\lambda_{max}(\Gamma^{-1})$ represents the maximum eigenvalue of matrix Γ^{-1}. It is obvious that b_1 and b_2 are positive. Now, Considering Lemma 5.1, it can be stated that e_{ω_g} and $\dot{e}_{\omega_g}$ are UUB. $\square$

A.7 Proof of Theorem 5.3

Choose a positive definite Lyapunov function as,

$$
V^\beta = V_1^\beta + \frac{1}{2}e_{2,\beta}^2 + \frac{1}{2}\tilde{d}_2^2 + \frac{1}{2}\tilde{f}_2^2 + \frac{1}{2}\tilde{\rho}_{\tilde{f}_2}^2.
\tag{A.16}
$$

Taking the time derivative of (A.16) obtains, $\dot{V}^\beta = \dot{V}_1^\beta + e_{2,\beta}\dot{e}_{2,\beta} + \tilde{d}_2\dot{\tilde{d}}_2 + \tilde{f}_2\dot{\tilde{f}}_2 + \tilde{\rho}_{\tilde{f}_2}\dot{\tilde{\rho}}_{\tilde{f}_2}$, which can be rewritten as,

$$
\dot{V}^\beta = \sum_{i=1}^3 \Pi_i^\beta - k_{1,\beta}e_\beta^2 - k_{2,\beta}e_{2,\beta}^2,
\tag{A.17}
$$

where, $\Pi_1^\beta = e_{2,\beta}\left(\hat{f}_2 - f_2 - \tilde{f}_2\right) - \sigma_{f_2}\hat{f}_2\tilde{f}_2 - \dot{f}_2\tilde{f}_2$,
$\Pi_2^\beta = -e_{2,\beta}d_2 + e_{2,\beta}^2\left(\tilde{d}_2 - \hat{d}_2\right)/\sqrt{e_{2,\beta}^2 + \eta_{d_2}^2} - \sigma_{d_2}\hat{d}_2\tilde{d}_2$ and $\Pi_3^\beta = -\sigma_{\tilde{f}_2}\hat{\rho}_{\tilde{f}_2}\tilde{\rho}_{\tilde{f}_2}$.
According to Lemmas 5.2 and 5.3, it can be shown that,

$$\Pi_1^\beta < -\frac{\sigma_{f_2}}{2}\widetilde{f}_2^2 + \frac{\sigma_{f_2}}{2}\bar{f}_2^2 + \rho_{\dot{f}_2}\rho_{\widetilde{f}_2},$$

$$\Pi_2^\beta < \bar{d}_2\left(|e_{2,\beta}| - \frac{e_{2,\beta}^2}{\sqrt{e_{2,\beta}^2 + \eta_{d_2}^2}}\right) - \sigma_{d_2}\hat{d}_2\widetilde{d}_2$$

$$< \bar{d}_2\eta_{d_2} - \frac{\sigma_{d_2}}{2}\widetilde{d}_2^2 + \frac{\sigma_{d_2}}{2}\bar{d}_2^2,$$

$$\Pi_3^\beta < -\frac{\sigma_{\tilde{f}_2}}{2}\widetilde{\rho}_{\tilde{f}_2}^2 + \frac{\sigma_{\tilde{f}_2}}{2}\rho_{\tilde{f}_2}^2. \tag{A.18}$$

Accordingly, it can be shown that,

$$\dot{V}^\beta < -b_1^\beta V^\beta + b_2^\beta, \tag{A.19}$$

where, $b_1^\beta = min\{2k_{1,\beta}, 2k_{2,\beta}, \sigma_{\tilde{f}_2}, \sigma_{f_2}, \sigma_{d_2}\}$ and $b_2^\beta = \sigma_{f_2}\bar{f}_2^2/2 + \rho_{\dot{f}_2}\rho_{\tilde{f}_2} + \bar{d}_2\eta_{d_2} + \sigma_{d_2}\bar{d}_2^2/2 + \sigma_{\tilde{f}_2}\rho_{\tilde{f}_2}^2/2$. Now, considering Lemma 5.1, it can be stated that e_β and $\dot{e}_\beta$ are UUB. $\qquad\square$

A.8   Proof of Theorem 6.1

Multiplying both sides of (6.39) by $e^{\sigma_{2,1}t}$ yields,

$$\frac{d\left(V_2(t)\,e^{\sigma_{2,1}t}\right)}{dt} < \left(GN\left(\zeta_1\right)\dot{\zeta}_1 + \dot{\zeta}_1 + \sigma_{2,2}\right)e^{\sigma_{2,1}t}. \tag{A.20}$$

Thus, integration of (A.20) over $[0,t]$, becomes,

$$V_2(t) < \frac{\sigma_{2,2}}{\sigma_{2,1}} + \left(V_2(0) - \frac{\sigma_{2,2}}{\sigma_{2,1}}\right)e^{-\sigma_{2,1}t} + e^{-\sigma_{2,1}t}\int_0^t \left(GN\left(\zeta_1\right)+1\right)\dot{\zeta}_1 e^{\sigma_{2,1}\tau}d\tau. \tag{A.21}$$

Furthermore, considering $\sigma_{2,2}/\sigma_{2,1} > 0$ and $\lim_{t\to\infty} e^{-\sigma_{2,1}t} = 0$, (A.21) becomes,

$$V_2(t) < c_{1,1} + e^{-\sigma_{2,1}t}\int_0^t \left(GN\left(\zeta_1\right)+1\right)\dot{\zeta}_1 e^{\sigma_{2,1}\tau}d\tau. \tag{A.22}$$

where, $c_{1,1} = \sigma_{2,2}/\sigma_{2,1} + V_2(0)$. Also, G satisfies the conditions in Lemma 4.1. Accordingly, considering (A.22), it can be stated that V_2 and ζ_1 are bounded. Consequently, according to (6.31), $(k_{e_{\dot{\omega}_r}}^2 \tan\Lambda_2)/\pi$, $\tilde{f}, \tilde{d}, \tilde{\theta}$ and $\tilde{\rho}_{\tilde{f}}$ are bounded, which implies $e_{\dot{\omega}_r}$ belongs to set $\Omega_{e_{\dot{\omega}_r}} = \left\{e_{\dot{\omega}_r} : |e_{\dot{\omega}_r}| < k_{e_{\dot{\omega}_r}}\right\}$ and accordingly is bounded.

Then one can obtain that

$$\frac{1}{2}e_{\dot{\omega}_r}^2 \le m_{1,1}, \tag{A.23}$$

where, $m_{1,1} = 0.5 max \left(e_{\dot{\omega}_r}^2 (\tau) \right)$, for $\tau \in [0, t]$. Now, considering (A.23), (6.23) is rewritten as,

$$\dot{V}_1(t) < -\sigma_{1,1}V_1(t) + c_{1,2}, \tag{A.24}$$

where, $c_{1,2} = \sigma_{1,2} + m_{1,1}$. According to Lemma 5.1, V_1 is bounded and considering (6.14), $(k_{e_{\omega_r}}^2 tan\Lambda_1)/\pi$ and χ_2 are bounded, which implies e_{ω_r} belongs to set $\Omega_{e_{\omega_r}} = \left\{ e_{\omega_r} : |e_{\omega_r}| < k_{e_{\omega_r}} \right\}$. From the abovementioned analysis, the objectives (i), (ii) and (iii) are achieved as follows.

(i) Consider the boundedness of V_1, V_2, $e_{\dot{\omega}_r}$ and e_{ω_r}. Therefore ω_r and $\dot{\omega}_r$ are bounded. Now from the boundedness of $\tilde{f}$, $\tilde{d}$, $\tilde{\theta}$ and $\tilde{\rho}_{\tilde{f}}$, the boundedness of α_D, ζ_1, υ_1, $\hat{f}$, $\hat{d}$, $\hat{\theta}$, $\hat{\rho}_{\tilde{f}}$, and consequently β_{ref} is concluded.

(ii) As a part of the closed-loop system analysis, it is shown that the tracking errors e_{ω_r} and $e_{\dot{\omega}_r}$, always stay in the sets $\Omega_{e_{\omega_r}} = \left\{ e_{\omega_r} : |e_{\omega_r}| < k_{e_{\omega_r}} \right\}$ and $\Omega_{e_{\dot{\omega}_r}} = \left\{ e_{\dot{\omega}_r} : |e_{\dot{\omega}_r}| < k_{e_{\dot{\omega}_r}} \right\}$, respectively.

(iii) Multiplying both sides of (A.24) by $e^{\sigma_{1,1}t}$ yields,

$$d \left(V_1(t) e^{\sigma_{1,1}t} \right) /dt < c_{1,2}e^{\sigma_{1,1}t}. \tag{A.25}$$

Thus, integration of (A.25) over $[0, t]$, becomes,

$$V_1(t) < \mathfrak{D}, \tag{A.26}$$

where, $\mathfrak{D} = (V_1(0) - c_{1,2}/\sigma_{1,1}) e^{-\sigma_{1,1}t} + c_{1,2}/\sigma_{1,1}$. From the definition of V_1, it can be shown that,

$$|e_{\omega_r}| < \mathcal{O}. \tag{A.27}$$

where, $\mathcal{O} = k_{e_{\omega_r}} \sqrt{2tan^{-1} \left(\pi\mathfrak{D}/k_{e_{\omega_r}}^2 \right) /\pi}$. If $V_1(0) = c_{1,2}/\sigma_{1,1}$, then, it holds $|e_{\omega_r}| < k_{e_{\omega_r}} \sqrt{2tan^{-1} \left(\pi c_{1,2}/k_{e_{\omega_r}}^2 \sigma_{1,1} \right) /\pi}$. If $V_1(0) \ne c_{1,2}/\sigma_{1,1}$, it can be concluded that given any $\mathcal{O} > k_{e_{\omega_r}} \sqrt{2tan^{-1} \left(\pi c_{1,2}/k_{e_{\omega_r}}^2 \sigma_{1,1} \right) /\pi}$, there exists T such that for any $t > T$, it has $|e_{\omega_r}| < \mathcal{O}$. As, $t \to \infty$, $|e_{\omega_r}| < k_{e_{\omega_r}} \sqrt{2tan^{-1} \left(\pi c_{1,2}/k_{e_{\omega_r}}^2 \sigma_{1,1} \right) /\pi}$, which implies e_{ω_r} can be made arbitrarily small by selecting the design parameters appropriately.

Considering Definition 4.1, and objectives (i), (ii) and (iii), it is guaranteed that the closed-loop system is UUB. □

A.9   Proof of Proposition 7.1

It is easy to see that $\hat{\alpha}_t = \left(\sum_{i=1}^{t} x_i^2 \alpha_i + \sum_{i=1}^{t} x_i \varepsilon_i\right) / \sum_{i=1}^{t} x_i^2$. Given $J_t = j_t, \ldots, J_1 = j_1$, then $\alpha_i = (1 - j_i) \alpha_{i-1} + j_i z_i$ with $\alpha_1 = a_1$. Therefore, α_i is a linear combination of independent normal variables $z_j (j \leq i)$. Thus, it is normally distributed with $\mu_i = (1 - j_i) \mu_{i-1} + j_i \mu_z$, $\sigma_i^2 = var(\alpha_i) = (1 - j_i) \sigma_{i-1}^2 + j_i \sigma_z^2$, $\mu_1 = a_1$ and $\sigma_1^2 = 0$. The covariance of α_i and α_j, i.e. $\sigma_{ij} = cov(\alpha_i, \alpha_j)$, is easy to derive. For example, $\sigma_{i,i-1} = (1 - j_i) \sigma_{i-1}^2$ or $\sigma_{i+h,i} = (1 - j_{i+h}) (1 - j_i) \sigma_{i+h-1,i-1}$. Also, variables $\sum_{i=1}^{t} x_i^2 \alpha_i$ and $\sum_{i=1}^{t} x_i \varepsilon_i$ are independent. Let $\lambda_{it} = x_i^2 / \sum_{i=1}^{t} x_i^2$. Notice that $var(\hat{\alpha}_t) = var(\sum_{i=1}^{t} x_i^2 \alpha_i) / \left(\sum_{i=1}^{t} x_i^2\right)^2 + \sigma_\varepsilon^2 / \sum_{i=1}^{t} x_i^2$ and $var(\sum_{i=1}^{t} x_i^2 \alpha_i) / \left(\sum_{i=1}^{t} x_i^2\right)^2 = cov(\sum_{i=1}^{t} x_i^2 \alpha_i, \sum_{j=1}^{t} x_j^2 \alpha_j) / \left(\sum_{i=1}^{t} x_i^2\right)^2 = \sum_{i=1}^{t} \sum_{j=1}^{t} x_i^2 x_j^2 \sigma_{ij} / \left(\sum_{i=1}^{t} x_i^2\right)^2$. □

A.10   Proof of Proposition 7.2

Notice that $\hat{\alpha}_t = (1 - \lambda_t) \hat{\alpha}_{t-1} + \lambda_t (y_t/x_t)$, $y_t/x_t = \alpha_t + \varepsilon_t/x_t$ and $\alpha_t = (1 - j_t) \alpha_{t-1} + j_t z_t \approx (1 - j_t) \hat{\alpha}_{t-1} + j_t z_t$. Combining these relations leads to $\hat{\alpha}_t = (1 - \lambda_t) \hat{\alpha}_{t-1} + \lambda_t \varepsilon_t/x_t + \lambda_t (1 - j_t) \hat{\alpha}_{t-1} + \lambda_t j_t z_t$. This completes the proof. □

A.11   Proof of Proposition 7.3

Notice that $\hat{d}_t = \lambda_t y_t/x_t = \lambda_t (\alpha_t + \varepsilon_t/x_t)$. Then, $\hat{d}_t = \alpha_t - (1 - \lambda_t) \alpha_t + \lambda_t \varepsilon_t/x_t$. Since, $\alpha_t = (1 - J_t) \alpha_{t-1} + J_t z_t$, then $\hat{d}_t = \alpha_t - (1 - \lambda_t) (1 - J_t) \alpha_{t-1} - (1 - \lambda_t) J_t z_t + \lambda_t \varepsilon_t/x_t$. The conditional density of $\hat{d}_t$ given J_t, α_t and α_{t-1} is, $f_{\hat{d}_t|J_t,\alpha_t,\alpha_{t-1}}(d) = n(d, k_1(J_t), k_2(J_t))$, where, $k_1(J_t) = \alpha_t - (1 - \lambda_t) (1 - J_t) \alpha_{t-1} - (1 - \lambda_t) J_t \mu_z$ and $k_2(J_t) = (1 - \lambda_t)^2 J_t \sigma_z^2 + \lambda_t^2 \sigma_\varepsilon^2 / x_t^2$.

Considering α_t and α_{t-1} as deterministic variables, the expectation of the logarithm of $f_{\hat{d}_t|J_t,\alpha_t,\alpha_{t-1}}(d)$ is,

$E_{J_t}\left(\log(f_{\hat{d}_t|J_t,\alpha_t,\alpha_{t-1}}(d))\right) = p \log(n(d, k_1(J_t = 1), k_2(J_t = 1)))$
$+ (1 - p) \log(n(d, k_1(J_t = 0), k_2(J_t = 0))) = p \log(n(d, \alpha_t - (1 - \lambda_t) \mu_z, k_2(J_t = 1))) + (1 - p) \log(n(d, \alpha_t - (1 - \lambda_t) \alpha_{t-1}, k_2(J_t = 0)))$.

Notice that $n(x, \mu + a, \sigma^2) = n(\mu, x - a, \sigma^2)$, thus, $E_{J_t}\left(\log\left(f_{\hat{d}_t|J_t,\alpha_t,\alpha_{t-1}}(d)\right)\right) = p \log(n(\alpha_t, d + (1 - \lambda_t) \mu_z, k_2(J_t = 1))) + (1 - p) \log(n(\alpha_t, d + (1 - \lambda_t) \alpha_{t-1}, k_2(J_t = 0)))$.

According to the Lemma 7.1, the $E_{J_t}\left(\log(f_{\hat{d}_t|J_t,\alpha_t,\alpha_{t-1}}(d))\right)$ attains its maximum at $\alpha_t^{EM} = \hat{d}_t + (1 - \lambda_t) \left(\gamma \mu_z + (1 - \gamma) \alpha_{t-1}^{EM}\right)$, where $\gamma = p\theta/(p\theta + (1 - p))$ and $\theta = k_2(J_t = 0)/k_2(J_t = 1)$. □

B Design Parameters

In this appendix, the numerical values of model and designed schemes, which have been used in this thesis, are given.

B.1 Wind Turbine Model Parameters

The wind turbine benchmark model parameters are given in this section, separately for each subsystems in Tables B.1-B.7. It should be noted that the pitch actuator dynamic parameters are given in Table 3.1

B.2 Design Parameters Used in Chapter 4

In this section the design parameters of baseline partial load and full load baseline and improved full load controllers, which have been designed in Chapter 4, are given in Tables B.8-B.10. It should be noted that the parameters of the improved partial load controller have been given in Section 4.3.

B.3 Design Parameters Used in Chapter 5

In this section the design parameters of nonlinear partial load FTC, which have been designed in Chapter 5, are given here.

Firstly, the GRBFNN structures which have been used to reconstruct the unknown desired trajectory and estimate the aerodynamic torque are given. It should be noted that as in partial load operation, both desired trajectory and aerodynamic

TABLE B.1: Aerodynamic model parameters.

Density	Swept area	Blade length
$\rho_a = 1.225 (kg/m^3)$	$A = 10381.625 (m^2)$	$R = 57.5 (m)$

TABLE B.2: Drive train model parameters.

Rotor inertia	Generator inertia	Rotor damping
$J_r = 390(kgm^2)$	$J_g = 55(Mkgm^2)$	$B_r = 27.8(kNm/rad/s)$
Generator damping	**Gearbox ratio**	**Torsional stiffness**
$B_g = 3.034(Nm/rad/s)$	$N_g = 95$	$K_{dt} = 2.7(GNm/rad)$

Torsional damping	Gearbox efficiency
$B_{dt} = 945(kNm/rad/s)$	$\eta_{dt} = 0.97$

TABLE B.3: Tower model parameters.

Nacelle mass	Tower Damping	Tower elasticity
$M_t = 484(ton)$	$B_t = 66.7(N/m/s)$	$K_t = 2.55(MN/m)$

TABLE B.4: Generator model parameters.

Time constant	Generator delay	Generator efficiency
$\tau_g = 0.02(s)$	$t_{g,d} = 0.01(s)$	$\eta_g = 0.92$
Minimum rate	**Maximum rate**	**Minimum torque**
$\dot{T}_{g,min} = -50(MNm/s)$	$\dot{T}_{g,max} = 50(MNm/s)$	$T_{g,min} = 0(Nm)$

Maximum torque
$T_{g,max} = 35.3(kNm)$

TABLE B.5: Pitch actuator parameters.

Time delay	Maximum rate	Minimum rate
$t_{p,d} = 0.01(s)$	$\dot{\beta}_{max} = 10(°/s)$	$\dot{\beta}_{min} = -10(°/s)$

Maximum pitch	Minimum pitch
$\beta_{max} = 30(°)$	$\beta_{min} = -2(°)$

TABLE B.6: Sensors noise content.

Pitch angle	Rotor speed	Generator speed
$\nu_\beta \sim N(0, 0.2)(°)$	$\omega_r \sim N(0, (0.008\pi)^2)(rad/s)$	$\omega_g \sim N(0, 0.05^2)(rad/s)$

Generator torque
$\nu_{T_g} \sim N(0, 90)(Nm)$

TABLE B.7: Operational parameters.

Cut-in wind speed	Cut-out wind speed	Nominal wind speed
$V_{r,cut-in} = 3(m/s)$	$V_{r,cut-out} = 25(m/s)$	$V_{r,N} = 12.3(m/s)$
Nominal power	**Nominal torque**	**Nominal rotor speed**
$P_{a,N} = 4.8(MW)$	$T_{g,N} = 32(kNm)$	$\omega_{r,N} = 1.71(rad/s)$
Nominal generator speed	**Optimal pitch**	**optimal TSR**
$\omega_{g,N} = 162.5(rad/s)$	$\beta_{opt} = 0(°)$	$\lambda_{opt} = 8.1$

Maximum power coefficient
$C_{p,max} = 0.48$

TABLE B.8: Partial load baseline controller parameters.

K_c	K_2
$1.2353(Nm/(rad/s)^2)$	$-6.022(Nm/rad/s)$

TABLE B.9: Full load baseline controller parameters.

K_P	K_I	K_D
1	4	0

TABLE B.10: Full load improved controller parameters.

λ_1	λ_{D_0}	σ_0	σ_1	U	L
0.1	1	0.1	1	100000	700000

TABLE B.11: GRBFNN parameters in partial load operation.

σ and σ_c	Λ	$\eta(e_{\omega_g})$	Γ
$0.1I_{5\times5}$	0.1	$sin(e_{\omega_g})Ones(5,1)$	$I_{5\times5}$

TABLE B.12: Generator torque controller parameters.

$k_{1,\omega g}$	η_{d_1}	$k_{2,\omega g}$	σ_{d_1}	σ_{f_1}	$\sigma_{\tilde{f}_1}$
10	0.1	1	1	5	1

torque are functions of unknown wind speed, then the GRBFNN structures are designed similarly for both unknown desired trajectory reconstruction and aerodynamic torque estimation. In this regard, the neuron numbers are selected as $\varpi = s = 10$. Also $\varphi(t) = [\varphi_1(Z), ..., \varphi_\varpi(Z)]^T$ and $h(t) = [h_1(Z), ..., h_s(Z)]^T$, where $Z = [T_g, \omega_g, \beta]^T$ and $\varphi_i(Z) = h_i(Z) = exp(-(Z - \vartheta_i)^T(Z - \vartheta_i)/2\varphi_{c,i}^2)$, for $i = 1, ..., s$. $\vartheta_i = [\vartheta_{i,T_g}, \vartheta_{i,\omega_g}, \vartheta_{i,\beta}]^T$ is the center of the ith input and $\varphi_c = [\varphi_{c,1}, ..., \varphi_{c,s}]^T \in \mathbb{R}^s$ is the width of the ith Gaussian function. The center matrix and width vector are selected as follows.

$$\vartheta = \begin{bmatrix} 0 & 3567 & 7134 & 10702 & 14269 & 17837 & 21404 & 24972 & 28539 & 32107 \\ 0 & 18.05 & 36.11 & 54.16 & 72.22 & 90.27 & 108.33 & 126.39 & 144.44 & 162.5 \\ -2 & 0.67 & 1.33 & 2 & 2.66 & 3.33 & 4 & 4.66 & 5.33 & 6 \end{bmatrix},$$

$\varphi = 10ones(s,1)$.

The other design parameters are given in Table B.11.

The generator torque and pitch actuator controller parameters are given in Tables B.12 and B.13, respectively.

B.4   Design Parameters Used in Chapter 6

In this section the design parameters of neuro adaptive constrained FTC control, which have been designed in Chapter 6, are given.

TABLE B.13: Pitch controller parameters.

$k_{1,\beta}$	η_{d_2}	$k_{2,\beta}$	σ_{d_2}	σ_{f_2}	$\sigma_{\tilde{f}_2}$
2	0.1	1	1	1	0.1

TABLE B.14: Constrained controller parameters.

τ_2	γ_1	γ_2	η_1	η_2	η_3
0.1	10	5	1	1	1

η_4	σ_f	σ_c	σ_d	$\sigma_{\tilde{f}}$	Γ
1	1	1	5	5	$I_{10 \times 10}$

TABLE B.15: PID controller gains in observer structure.

K_{PO}	K_{IO}	K_{DO}
1.17×10^7	4.34×10^5	0

The structure of GRBFNN, which has been used to estimate the aerodynamic torque, is given. This structure is similar to one, which was defined in (5.10) and (5.11) with $s = 10$. Also, the centers and width of the GRBFNN are as follows.

$$\vartheta = \begin{bmatrix} 30907 & 31207 & 31507 & 31807 & 32107 & 32407 & 32707 & 33007 & 33307 & 33607 \\ 90 & 110 & 120 & 140 & 162.5 & 180 & 190 & 210 & 220 & 230 \\ -2 & 1.5 & 5.11 & 8.66 & 12.22 & 15.77 & 19.33 & 22.88 & 26.44 & 30 \end{bmatrix},$$

$\varphi = 10 ones(s, 1).$

The other control parameter values are given in Table B.14.

B.5 FDI Design Parameters Used in Chapter 7

In this section, the design parameters, which have been used in the observer structure and fault isolation are given. In Table B.15 the PID controller gains, which have been adopted in Figure 7.2, are given. On the other hand, the design parameters of the fault isolation algorithm 7.3, are given in Table B.16.

TABLE B.16: Fault isolation design parameters.

K_{M_1}	K_{M_2}	ε_d
0.1	7	0.01

C Co-authors' Attribution statements

In this appendix, the signed co-authors' attribution statements are given and signed by the co-authors.

Co-author Attribution Approval Statement

Hereby, I, Dr Hamed Rahimi Nohooji, confirm that the following papers are my joint papers with Hamed Habibi. I, as a co-author, endorse that the level of all authors' contribution is accurately and appropriately addressed in the following tables. I also consent these papers to be used in the thesis "Wind Turbine Reliability Improvement by Fault Tolerant Control", submitted for the Degree of PhD in Mechanical Engineering of Curtin University.

Paper: Hamed Habibi, Hamed Rahimi Nohooji, and Ian Howard, "Adaptive PID Control of Wind Turbines for Power Regulation with Unknown Control Direction and Actuator Faults", IEEE Access, Vol. 6, pp. 37464-37479, 2018.
Author's affiliation (in order of appearance in submitted version of paper):
1- Hamed Habibi, Faculty of Science and Engineering, School of Civil and Mechanical Engineering, Curtin University, Perth, Australia.
2- Hamed Rahimi Nohooji, Center for Research in Mechatronics, Institute of Mechanics, Materials and Civil Engineering, Université catholique de Louvain, Belgium.
3- Ian Howard, Faculty of Science and Engineering, School of Civil and Mechanical Engineering, Curtin University, Perth, Australia.

		Attributions						
		Conception and design	Acquisition of method	Data manipulation	Interpretation & discussion	Paper drafting	Paper revising	Final approval
Authors	Hamed Habibi	✕	✕	✕	✕	✕	✕	✕
	Hamed Rahimi		✕		✕		✕	✕
		I acknowledge that these represent my contribution to the above research output. Signed... _Rahimi_ ... Date......10/.10/.18......................						
	Ian Howard		✕		✕		✕	✕

Paper: Hamed Habibi, Hamed Rahimi Nohooji, and Ian Howard, "Optimum efficiency control of a wind turbine with unknown desired trajectory and actuator faults", Journal of Renewable and Sustainable Energy, Vol. 9, No. 6, p. 063305, 2017.
Author's affiliation (in order of appearance in submitted version of paper):
1- Hamed Habibi, Faculty of Science and Engineering, School of Civil and Mechanical Engineering, Curtin University, Perth, Australia.
2- Hamed Rahimi Nohooji, Faculty of Science and Engineering, School of Civil and Mechanical Engineering, Curtin University, Perth, Australia.
3- Ian Howard, Faculty of Science and Engineering, School of Civil and Mechanical Engineering, Curtin University, Perth, Australia.

		Attributions						
		Conception and design	Acquisition of method	Data manipulation	Interpretation & discussion	Paper drafting	Paper revising	Final approval
Authors	Hamed Habibi	✕	✕	✕	✕	✕	✕	✕
	Hamed Rahimi		✕		✕		✕	✕
		I acknowledge that these represent my contribution to the above research output. Signed.._Rahimi_ .... Date......10/.10/.18......................						
	Ian Howar		✕		✕		✕	✕

	d							

Paper: Hamed Habibi, Hamed Rahimi Nohooji, and Ian Howard, "Power maximization of variable-speed variable-pitch wind turbines using passive adaptive neural fault tolerant control", Frontiers of Mechanical Engineering, Vol. 12, No. 3, pp. 377-388, 2017.

Author's affiliation (in order of appearance in submitted version of paper):

1- Hamed Habibi, Faculty of Science and Engineering, School of Civil and Mechanical Engineering, Curtin University, Perth, Australia.
2- Hamed Rahimi Nohooji, Faculty of Science and Engineering, School of Civil and Mechanical Engineering, Curtin University, Perth, Australia.
3- Ian Howard, Faculty of Science and Engineering, School of Civil and Mechanical Engineering, Curtin University, Perth, Australia.

		Attributions						
		Conception and design	Acquisition of method	Data manipulation	Interpretation & discussion	Paper drafting	Paper revising	Final approval
Authors	Hamed Habibi	×	×	×	×	×	×	×
	Hamed Rahimi		×		×		×	×
		I acknowledge that these represent my contribution to the above research output. Signed.. _Rahimi_ .... Date....|2/.10./.|.8.........................						
	Ian Howard		×		×		×	×

Paper: Hamed Habibi, Hamed Rahimi Nohooji, and Ian Howard, "Constrained control of wind turbines for power regulation in full load operation", proceedings of 11th Asian Control Conference (ASCC), pp. 2813-2818, 2017.

Author's affiliation (in order of appearance in submitted version of paper):

1- Hamed Habibi, Faculty of Science and Engineering, School of Civil and Mechanical Engineering, Curtin University, Perth, Australia.
2- Hamed Rahimi Nohooji, Faculty of Science and Engineering, School of Civil and Mechanical Engineering, Curtin University, Perth, Australia.
3- Ian Howard, Faculty of Science and Engineering, School of Civil and Mechanical Engineering, Curtin University, Perth, Australia.

		Attributions						
		Conception and design	Acquisition of method	Data manipulation	Interpretation & discussion	Paper drafting	Paper revising	Final approval
Authors	Hamed Habibi	×	×	×	×	×	×	×
	Hamed Rahimi		×		×		×	×
		I acknowledge that these represent my contribution to the above research output. Signed. _Rahimi_ .... Date......|2/.10./.|.8.....................						
	Ian Howard		×		×		×	×

Paper: Hamed Habibi, Hamed Rahimi Nohooji, and Ian Howard, "A neuro-adaptive maximum power tracking control of variable speed wind turbines with actuator faults", proceedings of Australian and New Zealand Control Conference (ANZCC), pp. 63-68, 2017.

Author's affiliation (in order of appearance in submitted version of paper):

1- Hamed Habibi, Faculty of Science and Engineering, School of Civil and Mechanical Engineering, Curtin University, Perth, Australia.
2- Hamed Rahimi Nohooji, Faculty of Science and Engineering, School of Civil and Mechanical Engineering, Curtin University, Perth, Australia.
3- Ian Howard, Faculty of Science and Engineering, School of Civil and Mechanical Engineering, Curtin University, Perth, Australia.

		Attributions						
		Conception and design	Acquisition of method	Data manipulation	Interpretation & discussion	Paper drafting	Paper revising	Final approval
Authors	Hamed Habibi	X	X	X	X	X	X	X
	Hamed Rahimi		X		X		X	X
		I acknowledge that these represent my contribution to the above research output. Signed...Rahimi....S............ Date...|9/.|2./.|8...................						
	Ian Howard		X		X		X	X

Paper: Hamed Habibi, Hamed Rahimi Nohooji, and Ian Howard "Backstepping Nussbaum Gain Dynamic Surface Control for a Class of Input and State Constrained Systems with Actuator Faults", submitted to Information Sciences.

Author's affiliation (in order of appearance in submitted version of paper):

1- Hamed Habibi, Faculty of Science and Engineering, School of Civil and Mechanical Engineering, Curtin University, Perth, Australia.
2- Hamed Rahimi Nohooji, Center for Research in Mechatronics, Institute of Mechanics, Materials and Civil Engineering, Université catholique de Louvain, Belgium.
3- Ian Howard, Faculty of Science and Engineering, School of Civil and Mechanical Engineering, Curtin University, Perth, Australia.

		Attributions						
		Conception and design	Acquisition of method	Data manipulation	Interpretation & discussion	Paper drafting	Paper revising	Final approval
Authors	Hamed Habibi	X	X	X	X	X	X	X
	Hamed Rahimi	X			X		X	X
		I acknowledge that these represent my contribution to the above research output. Signed...Rahimi....S............ Date.....\9.|2./.|8...................						
	Ian Howard		X		X		X	X

Co-author Attribution Approval Statement

Hereby, I, Professor Silvio Simani, confirm that the following paper is my joint paper with Hamed Habibi. I, as a co-author, endorse that the level of all authors' contribution is accurately and appropriately addressed in the following table. I also consent this paper to be used in the thesis "Wind Turbine Reliability Improvement by Fault Tolerant Control", submitted for the Degree of PhD in Mechanical Engineering of Curtin University.

Paper: Hamed Habibi, Ian Howard, and Silvio Simani, "Wind Turbine Reliability Improvement using Model-based Fault Detection and Fault Tolerant Control: a review", submitted to Renewable Energy.

Author's affiliation (in order of appearance in submitted version of paper):

1- Hamed Habibi, Faculty of Science and Engineering, School of Civil and Mechanical Engineering, Curtin University, Perth, Australia.

2- Ian Howard, Faculty of Science and Engineering, School of Civil and Mechanical Engineering, Curtin University, Perth, Australia.

3- Silvio Simani, Department of Engineering, University of Ferrara, Ferrara, Italy.

		Attributions						
		Conception and design	Acquisition of method	Data manipulation	Interpretation & discussion	Paper drafting	Paper revising	Final approval
Authors	Hamed Habibi	×	×	×	×	×	×	×
	Ian Howard			×	×		×	×
	Silvio Simani		×		×		×	×

I acknowledge that these represent my contribution to the above research output.
Signed………Silvio Simani…………
Date: October 10, 2018 ……………

Department of Mechanical
Engineering
Level 4, Building 204
GPO Box U1987
Perth, Australia

Co-author Attribution Approval Statement

Hereby, I, Professor Aghil Yousefi Koma, confirm that the following paper is my joint publication with Hamed Habibi. I, as a co-author, endorse that the level of all authors' contribution is accurately and appropriately addressed in the following table. I also consent this paper to be used in the thesis "Wind Turbine Reliability Improvement by Fault Tolerant Control", submitted for the Degree of PhD in Mechanical Engineering of Curtin University.

Paper: Hamed Habibi, Aghil Yousefi Koma, and Ian Howard, "Power Improvement of Non-Linear Wind Turbines during Partial Load Operation using Fuzzy Inference Control", Control Engineering and Applied Informatics, Vol. 19, No. 2, pp. 31-42, 2017.

Author's affiliation (in order of appearance in published version of paper):
1- Hamed Habibi, Faculty of Science and Engineering, School of Civil and Mechanical Engineering, Curtin University, Perth, Australia
2- Aghil Yousefi Koma, Centre of Advanced Systems and Technologies (CAST), School of Mechanical Engineering, College of Engineering, University of Tehran, Tehran, Iran.
3- Ian Howard, Faculty of Science and Engineering, School of Civil and Mechanical Engineering, Curtin University, Perth, Australia.

		Attributions						
		Conception and design	Acquisition of method	Data manipulation	Interpretation & discussion	Paper drafting	Paper revising	Final approval
Authors	Hamed Habibi	X	X	X	X	X	X	X
	Aghil Yousefi Koma	X	X				X	X
		I acknowledge that these represent my contribution to the above research output Signed.. Aghil...Yousefi–Koma Date.............10/10/2018						
	Ian Howard			X	X		X	X

Curtin University

Department of Mechanical
Engineering
Level 4, Building 204
GPO Box U1987
Perth, Australia

Co-author Attribution Approval Statement

Hereby, I, Dr Reza Habibi, confirm that the following papers are my joint publications with Hamed Habibi. I, as a co-author, endorse that the level of all authors' contribution is accurately and appropriately addressed in the following tables. I also consent these papers to be used in the thesis "Wind Turbine Reliability Improvement by Fault Tolerant Control", submitted for the Degree of PhD in Mechanical Engineering of Curtin University.

Paper: Hamed Habibi, Ian Howard, and Reza Habibi, "Bayesian Sensor Fault Detection in a Markov Jump System", Asian Journal of Control, Vol. 19, No. 4, pp. 1465-1481, 2017.
Author's affiliation (in order of appearance in published version of paper):
1- Hamed Habibi, Faculty of Science and Engineering, School of Civil and Mechanical Engineering, Curtin University, Perth, Australia.
2- Ian Howard, Faculty of Science and Engineering, School of Civil and Mechanical Engineering, Curtin University, Perth, Australia.
3- Reza Habibi, Iran Banking Institute, Central Bank of Iran, Tehran, Iran.

		Attributions						
		Conception and design	Acquisition of method	Data manipulation	Interpretation & discussion	Paper drafting	Paper revising	Final approval
Authors	Hamed Habibi	×	×	×	×	×	×	×
	Ian Howard			×	×		×	×
	Reza Habibi	×	×				×	×
		I acknowledge that these represent my contribution to the above research output. Signed.. Date..						

Oct. 9. 2018   Habibi

Paper: Hamed Habibi, Ian Howard, and Reza Habibi, "Bayesian Fault Probability Estimation; Application in Wind urbine Drive train Sensor Fault Detection", Asian Journal of Control, In Press.
Author's affiliation (in order of appearance in published version of paper):
1- Hamed Habibi, Faculty of Science and Engineering, School of Civil and Mechanical Engineering, Curtin University, Perth, Australia.
2- Ian Howard, Faculty of Science and Engineering, School of Civil and Mechanical Engineering, Curtin University, Perth, Australia.
3- Reza Habibi, Iran Banking Institute, Central Bank of Iran, Tehran, Iran.

		Attributions						
		Conception and design	Acquisition of method	Data manipulation	Interpretation & discussion	Paper drafting	Paper revising	Final approval
Authors	Hamed Habibi	×	×	×	×	×	×	×
	Ian Howard			×	×		×	×
	Reza Habibi	×					×	×
		I acknowledge that these represent my contribution to the above research output. Signed.. Date..						

Oct. 2. 2018   Habibi

Bibliography

Abuaisha, Tareq Saber (2014). "General study of the control principles and dynamic fault behaviour of variable-speed wind turbine and wind farm generic models". In: *Renewable Energy* 68, pp. 245–254.

Agarwal, Deepshikha and Nand Kishor (2014). "A fuzzy inference-based fault detection scheme using adaptive thresholds for health monitoring of offshore windfarms". In: *IEEE Sensors Journal* 14.11, pp. 3851–3861.

Aissaoui, Abdel Ghani et al. (2013). "A Fuzzy-PI control to extract an optimal power from wind turbine". In: *Energy Conversion and Management* 65, pp. 688–696.

Amirat, Yassine et al. (2009). "A brief status on condition monitoring and fault diagnosis in wind energy conversion systems". In: *Renewable and Sustainable Energy Reviews* 13.9, pp. 2629–2636.

Badihi, Hamed, Youmin Zhang, and Henry Hong (2013). "A review on application of monitoring, diagnosis, and fault-tolerant control to wind turbines". In: *Conference on Control and Fault-Tolerant Systems (SysTol)*. IEEE, pp. 365–370.

– (2014). "Fuzzy gain-scheduled active fault-tolerant control of a wind turbine". In: *Journal of the Franklin Institute* 351.7, pp. 3677–3706.

– (2015). "Wind turbine fault diagnosis and fault-tolerant torque load control against actuator faults". In: *IEEE Transactions on Control Systems Technology* 23.4, pp. 1351–1372.

– (2017). "Fault-tolerant cooperative control in an offshore wind farm using model-free and model-based fault detection and diagnosis approaches". In: *Applied Energy* 201, pp. 284–307.

Bakka, Tore and Hamid Reza Karimi (2013). "H_∞ static output-feedback control design with constrained information for offshore wind turbine system". In: *Journal of the Franklin Institute* 350.8, pp. 2244–2260.

Bianchi, FD, RS Sánchez-Peña, and M Guadayol (2012). "Gain scheduled control based on high fidelity local wind turbine models". In: *Renewable Energy* 37.1, pp. 233–240.

Bianchi, Fernando D, Ricardo J Mantz, and Hernán De Battista (2007). *The wind and wind turbines*. Springer.

Blanke, Mogens et al. (2006). *Diagnosis and fault-tolerant control*. Vol. 2. Springer.

Blesa, Joaquim et al. (2011). "Fault diagnosis of wind turbines using a set-membership approach". In: *IFAC Proceedings Volumes* 44.1, pp. 8316–8321.

Blesa, Joaquim et al. (2014). "FDI and FTC of wind turbines using the interval observer approach and virtual actuators/sensors". In: *Control Engineering Practice* 24, pp. 138–155.

Borcehrsen, Anders Bech, Jesper Abildgaard Larsen, and Jakob Stoustrup (2014). "Fault detection and load distribution for the wind farm challenge". In: *IFAC Proceedings Volumes* 47.3, pp. 4316–4321.

Bossanyi, EA (2003). "Individual blade pitch control for load reduction". In: *Wind Energy: An International Journal for Progress and Applications in Wind Power Conversion Technology* 6.2, pp. 119–128.

Boukhezzar, Boubekeur and Houria Siguerdidjane (2011). "Nonlinear control of a variable-speed wind turbine using a two-mass model". In: *IEEE Transactions on Energy Conversion* 26.1, pp. 149–162.

Byon, Eunshin and Yu Ding (2010). "Season-dependent condition-based maintenance for a wind turbine using a partially observed Markov decision process". In: *IEEE Transactions on Power Systems* 25.4, pp. 1823–1834.

Cao, Mengnan et al. (2016). "Study of wind turbine fault diagnosis based on unscented Kalman filter and SCADA data". In: *Energies* 9.10, p. 847.

Casau, Pedro et al. (2012). "Fault detection and isolation and fault tolerant control of wind turbines using set-valued observers". In: *Proceedings of the 8th IFAC Symposium on Fault Detection, Supervision and Safety of Technical Processes.* Vol. 2931, p. 120125.

Casau, Pedro et al. (2015). "A set-valued approach to FDI and FTC of wind turbines". In: *IEEE Transactions on Control Systems Technology* 23.1, pp. 245–263.

Chen, Bindi et al. (2011a). "Wind turbine SCADA alarm pattern recognition". In: *IET Conference on Renewable Power Generation (RPG)*, pp. 1–6.

Chen, Bindi et al. (2012). "Bayesian network for wind turbine fault diagnosis". In: *European Wind Energy Association (EWEA)*. Vol. 27.

Chen, Lejun, Fengming Shi, and Ron Patton (2013). "Active FTC for hydraulic pitch system for an off-shore wind turbine". In: *Conference on Control and Fault-Tolerant Systems (SysTol)*. IEEE, pp. 510–515.

Chen, Wei et al. (2011b). "Observer-based FDI schemes for wind turbine benchmark". In: *IFAC Proceedings Volumes* 44.1, pp. 7073–7078.

Dalei, Jyotirmayee and Kanungo Barada Mohanty (2016). "Fault classification in SEIG system using Hilbert-Huang transform and least square support vector machine". In: *International Journal of Electrical Power & Energy Systems* 76, pp. 11–22.

Dey, Satadru, Pierluigi Pisu, and Beshah Ayalew (2015). "A Comparative Study of Three Fault Diagnosis Schemes for Wind Turbines." In: *IEEE Transactions on Control Systems and Technology* 23.5, pp. 1853–1868.

Ding, Steven X (2008). *Model-based fault diagnosis techniques: design schemes, algorithms, and tools*. Springer Science & Business Media.

Donders, Stijn, Vincent Verdult, and Michel Verhaegen (2002). "Fault detection and identification for wind turbine systems: a closed-loop analysis". In: *Master's thesis, University of Twente*.

Entezami, Mani et al. (2012). "Fault detection and diagnosis within a wind turbine mechanical braking system using condition monitoring". In: *Renewable Energy* 47, pp. 175–182.

Fan, L-L and Y-D Song (2012). "Neuro-adaptive model-reference fault-tolerant control with application to wind turbines". In: *IET Control Theory & Applications* 6.4, pp. 475–486.

Faulstich, Stefan, Berthold Hahn, and Peter J Tavner (2011). "Wind turbine downtime and its importance for offshore deployment". In: *Wind Energy* 14.3, pp. 327–337.

Feng, Zhipeng et al. (2012). "Fault diagnosis for wind turbine planetary gearboxes via demodulation analysis based on ensemble empirical mode decomposition and energy separation". In: *Renewable Energy* 47, pp. 112–126.

Fernández-Cantí, Rosa M et al. (2013). "Nonlinear set-membership identification and fault detection using a Bayesian framework: Application to the wind turbine benchmark". In: *52nd Annual Conference on Decision and Control (CDC)*. IEEE, pp. 496–501.

Fingersh, L and PW Carlin (1998). "Results from the NREL variable-speed test bed". In: *ASME Wind Energy Symposium*, p. 50.

Gao, Zhiwei, Carlo Cecati, and Steven X Ding (2015). "A survey of fault diagnosis and fault-tolerant techniques Part I: Fault diagnosis with model-based and signal-based approaches". In: *IEEE Transactions on Industrial Electronics* 62.6, pp. 3757–3767.

Garcia, Mari Cruz, Miguel A Sanz-Bobi, and Javier del Pico (2006). "SIMAP: Intelligent System for Predictive Maintenance: Application to the health condition monitoring of a windturbine gearbox". In: *Computers in Industry* 57.6, pp. 552–568.

Georg, Sören, Horst Schulte, and Harald Aschemann (2012). "Control-oriented modelling of wind turbines using a Takagi-Sugeno model structure". In: *International Conference on Fuzzy Systems*. IEEE, pp. 1–8.

Georg, Sören and Horst Schulte (2014). "Diagnosis of actuator parameter faults in wind turbines using a takagi-sugeno sliding mode observer". In: *Intelligent Systems in Technical and Medical Diagnostics*. Springer, pp. 29–40.

Giebhardt, Jochen (2006). "Evolutionary algorithm for optimisation of condition monitoring and fault prediction pattern classification in offshore wind turbines". In: *Proceedings of European Wind Energy Conference*. Vol. 27.

Giger, Urs, Patrick Kühne, and Horst Schulte (2017). "Fault Tolerant and Optimal Control of Wind Turbines with Distributed High-Speed Generators". In: *Energies* 10.2, p. 149.

Gordon, Neil J, David J Salmond, and Adrian FM Smith (1993). "Novel approach to nonlinear/non-Gaussian Bayesian state estimation". In: *IEE Proceedings F (Radar and Signal Processing)*. Vol. 140. 2. IET, pp. 107–113.

Habibi, Hamed, Ian Howard, and Reza Habibi (2017a). "Bayesian sensor fault detection in a Markov jump system". In: *Asian Journal of Control* 19.4, pp. 1465–1481.

Habibi, Hamed, Hamed Rahimi Nohooji, and Ian Howard (2017b). "Constrained control of wind turbines for power regulation in full load operation". In: *Control Conference (ASCC), 2017 11th Asian*. IEEE, pp. 2813–2818.

Habibi, Hamed, Hamed Rahimi Nohooji, and Ian Howard (2017c). "Optimum efficiency control of a wind turbine with unknown desired trajectory and actuator faults". In: *Journal of Renewable and Sustainable Energy* 9.6, p. 063305.

Habibi, Hamed, Aghil Yousefi Koma, and Ian Howard (2017d). "Power Improvement of Non-Linear Wind Turbines during Partial Load Operation using Fuzzy Inference Control". In: *Journal of Control Engineering and Applied Informatics* 19.2, pp. 31–42.

Hameed, Z et al. (2009). "Condition monitoring and fault detection of wind turbines and related algorithms: A review". In: *Renewable and Sustainable Energy Reviews* 13.1, pp. 1–39.

Hameed, Z, SH Ahn, and YM Cho (2010). "Practical aspects of a condition monitoring system for a wind turbine with emphasis on its design, system architecture, testing and installation". In: *Renewable Energy* 35.5, pp. 879–894.

Hand, M Maureen et al. (2004). "Advanced control design and field testing for wind turbines at the National Renewable Energy Laboratory". In: *National Renewable Energy Laboratory, Golden, CO, NREL Technical Report No. CP-500-36118*.

Hau, Erich and Horst von Renouard (2003). *Wind turbines: fundamentals, technologies, application, economics*. Springer.

Herp, Jürgen et al. (2018). "Bayesian state prediction of wind turbine bearing failure". In: *Renewable Energy* 116, pp. 164–172.

Isermann, Rolf (2006). *Fault-diagnosis systems: an introduction from fault detection to fault tolerance*. Springer Science & Business Media.

Jafarnejadsani, Hamidreza, Jeff K Pieper, and Julian Ehlers (2013). "Adaptive Control of a Variable-Speed Variable-Pitch Wind Turbine Using Radial-Basis Function Neural Network." In: *IEEE Transactions on Control Systems and Technology* 21.6, pp. 2264–2272.

Jaramillo-Lopez, Fernando, Godpromesse Kenne, and Francoise Lamnabhi-Lagarrigue (2016). "A novel online training neural network-based algorithm for wind speed estimation and adaptive control of PMSG wind turbine system for maximum power extraction". In: *Renewable Energy* 86, pp. 38–48.

Jena, Debashisha and Saravanakumar Rajendran (2015). "A review of estimation of effective wind speed based control of wind turbines". In: *Renewable and Sustainable Energy Reviews* 43, pp. 1046–1062.

Johnson, Kathryn E et al. (2006). "Control of variable-speed wind turbines: standard and adaptive techniques for maximizing energy capture". In: *IEEE Control Systems* 26.3, pp. 70–81.

Kabir, MJ, Amanullah MT Oo, and Mahbub Rabbani (2015). "A brief review on offshore wind turbine fault detection and recent development in condition monitoring based maintenance system". In: *Australasian Universities Power Engineering Conference (AUPEC)*. IEEE, pp. 1–7.

Kamal, Elkhatib et al. (2012). "Robust fuzzy fault-tolerant control of wind energy conversion systems subject to sensor faults". In: *IEEE Transactions on Sustainable Energy* 3.2, pp. 231–241.

Kamal, Elkhatib and Abdel Aitouche (2013). "Robust fault tolerant control of DFIG wind energy systems with unknown inputs". In: *Renewable Energy* 56, pp. 2–15.

Kamal, Elkhatib et al. (2014a). "Fuzzy Scheduler Fault-Tolerant Control for Wind Energy Conversion Systems." In: *IEEE Transactions on Control Systems and Technology* 22.1, pp. 119–131.

Kamal, Elkhatib, Abdel Aitouche, and Dhaker Abbes (2014b). "Robust fuzzy scheduler fault tolerant control of wind energy systems subject to sensor and actuator faults". In: *International Journal of Electrical Power & Energy Systems* 55, pp. 402–419.

Khalil, Hassan K (1996). "Noninear systems". In: *Prentice-Hall, New Jersey* 2.5, pp. 5–1.

Kim, Young-Man (2016). "Robust data driven H-infinity control for wind turbine". In: *Journal of the Franklin Institute* 353.13, pp. 3104–3117.

Lan, Jianglin, Ron J Patton, and Xiaoyuan Zhu (2018). "Fault-tolerant wind turbine pitch control using adaptive sliding mode estimation". In: *Renewable Energy* 116, pp. 219–231.

Li, Shengquan and Juan Li (2017). "Output predictor-based active disturbance rejection control for a wind energy conversion system with PMSG". In: *IEEE Access* 5, pp. 5205–5214.

Liu, Jihong, Daping Xu, and Xiyun Yang (2008). "Sensor fault detection in variable speed wind turbine system using H_-/H_∞ method". In: *7th World Congress on Intelligent Control and Automation (WCICA)*. IEEE, pp. 4265–4269.

Lu, Bin et al. (2009). "A review of recent advances in wind turbine condition monitoring and fault diagnosis". In: *Power Electronics and Machines in Wind Applications (PEMWA)*. IEEE, pp. 1–7.

Lu, Yi, Jiong Tang, and Huageng Luo (2012). "Wind turbine gearbox fault detection using multiple sensors with features level data fusion". In: *Journal of Engineering for Gas Turbines and Power* 134.4, p. 042501.

Luo, Ningsu, Yolanda Vidal, and Leonardo Acho (2014). *Wind turbine control and monitoring*. Springer.

Márquez, Fausto Pedro García et al. (2012). "Condition monitoring of wind turbines: Techniques and methods". In: *Renewable Energy* 46, pp. 169–178.

McMillan, David and Graham W Ault (2007). "Quantification of condition monitoring benefit for offshore wind turbines". In: *Wind Engineering* 31.4, pp. 267–285.

Musial, Walter, Sandy Butterfield, Bonnie Ram, et al. (2006). "Energy from offshore wind". In: *Offshore Technology Conference*. Offshore Technology Conference.

Negre, Pep Lluís, Vicenç Puig, and Isaac Pineda (2011). "Fault detection and isolation of a real wind turbine using LPV observers". In: *IFAC Proceedings Volumes* 44.1, pp. 12372–12379.

Odgaard, Peter F and Jakob Stoustrup (2010). "Unknown input observer based detection of sensor faults in a wind turbine". In: *IEEE International Conference on Control Applications (CCA)*. IEEE, pp. 310–315.

Odgaard, Peter F and Kathryn E Johnson (2013a). "Wind turbine fault detection and fault tolerant control-an enhanced benchmark challenge". In: *American Control Conference (ACC)*. IEEE, pp. 4447–4452.

Odgaard, Peter Fogh, Jakob Stoustrup, and Michel Kinnaert (2009a). "Fault tolerant control of wind turbines-a benchmark model". In: *Proceedings of the 7th IFAC Symposium on Fault Detection, Supervision and Safety of Technical Processes*. Vol. 1. 1. Barcelona, Spain, pp. 155–160.

Odgaard, Peter Fogh et al. (2009b). "Observer based detection of sensor faults in wind turbines". In: *Proceedings of European Wind Energy Conference*, pp. 4421–4430.

Odgaard, Peter Fogh and Jakob Stoustrup (2012a). "Fault tolerant control of wind turbines using unknown input observers". In: *8th IFAC Symposium on Fault Detection, Supervision and Safety of Technical Processes*. Elsevier Science, pp. 313–318.

– (2012b). "Model based fault tolerant observers for wind turbines". In: *European Wind Energy Conference and Exhibition (EWEC)*, pp. 1348–1353.

– (2012c). "Results of a wind turbine FDI competition". In: *Proceedings of the 8th IFAC Symposium on Fault Detection, Supervision and Safety of Technical Processes*, pp. 29–31.

Odgaard, Peter Fogh, Jakob Stoustrup, and Michel Kinnaert (2013b). "Fault-tolerant control of wind turbines: A benchmark model". In: *IEEE Transactions on Control Systems Technology* 21.4, pp. 1168–1182.

Odgaard, Peter Fogh and Jakob Stoustrup (2014). "Frequency based fault detection in wind turbines". In: *IFAC Proceedings Volumes* 47.3, pp. 5832–5837.

– (2015). "A benchmark evaluation of fault tolerant wind turbine control concepts". In: *IEEE Transactions on Control Systems Technology* 23.3, pp. 1221–1228.

Passino, Kevin M, Stephen Yurkovich, and Michael Reinfrank (1998). *Fuzzy control, vol. 42*.

Pisu, Pierluigi and Beshah Ayalew (2011). "Robust fault diagnosis for a horizontal axis wind turbine". In: *18th IFAC World Congress*, pp. 7055–7060.

Pöschke, Florian, Sören Georg, and Horst Schulte (2014). "Fault reconstruction using a Takagi-Sugeno sliding mode observer for the wind turbine benchmark". In: *UKACC International Conference on Control*. IEEE, pp. 456–461.

Pourmohammad, Sajjad and Afef Fekih (2011). "Fault-tolerant control of wind turbine systems-a review". In: *IEEE Green Technologies Conference (IEEE-Green)*. IEEE, pp. 1–6.

Qiao, Wei et al. (2008). "Wind speed estimation based sensorless output maximization control for a wind turbine driving a DFIG". In: *IEEE Transactions on Power Electronics* 23.3, pp. 1156–1169.

Qiu, Yingning et al. (2012). "Wind turbine SCADA alarm analysis for improving reliability". In: *Wind Energy* 15.8, pp. 951–966.

Rahimi, Hamed N, Ian Howard, and Lei Cui (2018a). "Neural adaptive tracking control for an uncertain robot manipulator with time-varying joint space constraints". In: *Mechanical Systems and Signal Processing* 112, pp. 44–60.

– (2018b). "Neural impedance adaption for assistive human–robot interaction". In: *Neurocomputing* 290, pp. 50–59.

Rothenhagen, Kai and Friedrich Wilhelm Fuchs (2009). "Doubly fed induction generator model-based sensor fault detection and control loop reconfiguration". In: *IEEE Transactions on Industrial Electronics* 56.10, pp. 4229–4238.

Rotondo, Damiano et al. (2012). "Fault tolerant control of the wind turbine benchmark using virtual sensors/actuators". In: *IFAC Proceedings Volumes* 45.20, pp. 114–119.

Ryan, EP (1991). "A universal adaptive stabilizer for a class of nonlinear systems". In: *Systems & Control Letters* 16.3, pp. 209–218.

Sami, Montadher and Ron J Patton (2012a). "An FTC approach to wind turbine power maximisation via TS fuzzy modelling and control". In: *IFAC Proceedings Volumes* 45.20, pp. 349–354.

– (2012b). "Global wind turbine FTC via TS fuzzy modelling and control". In: *IFAC Proceedings Volumes* 45.20, pp. 325–330.

Sanchez, Hector et al. (2015). "Fault diagnosis of an advanced wind turbine benchmark using interval-based ARRs and observers". In: *IEEE Transactions on Industrial Electronics* 62.6, pp. 3783–3793.

Schulte, Horst and Eckhard Gauterin (2015). "Fault-tolerant control of wind turbines with hydrostatic transmission using Takagi–Sugeno and sliding mode techniques". In: *Annual Reviews in Control* 40, pp. 82–92.

Shamshirband, Shahaboddin et al. (2014). "Adaptive neuro-fuzzy optimization of wind farm project net profit". In: *Energy Conversion and Management* 80, pp. 229–237.

Shi, Fengming and Ron Patton (2015). "An active fault tolerant control approach to an offshore wind turbine model". In: *Renewable Energy* 75, pp. 788–798.

Simani, Silvio (2015). "Overview of modelling and advanced control strategies for wind turbine systems". In: *Energies* 8.12, pp. 13395–13418.

Simani, Silvio, Paolo Castaldi, and Andrea Tilli (2011a). "Data-driven approach for wind turbine actuator and sensor fault detection and isolation". In: *Proceedings of IFAC World Congress*, pp. 8301–8306.

Simani, Silvio, Paolo Castaldi, and Marcello Bonfe (2011b). "Hybrid model-based fault detection of wind turbine sensors". In: *Proceedings of IFAC World Congress*, pp. 7061–7066.

Simani, Silvio and Paolo Castaldi (2012a). "Adaptive fault–tolerant control design approach for a wind turbine benchmark". In: *IFAC Proceedings Volumes* 45.20, pp. 319–324.

– (2012b). "Data–Drive Design of Fuzzy Logic Fault Tolerant Control for a Wind Turbine Benchmark". In: *IFAC Proceedings Volumes* 45.20, pp. 108–113.

– (2014). "Active actuator fault-tolerant control of a wind turbine benchmark model". In: *International Journal of Robust and Nonlinear Control* 24.8-9, pp. 1283–1303.

Simani, Silvio, Saverio Farsoni, and Paolo Castaldi (2015a). "Fault diagnosis of a wind turbine benchmark via identified fuzzy models". In: *IEEE Transactions on Industrial Electronics* 62.6, pp. 3775–3782.

– (2015b). "Wind turbine simulator fault diagnosis via fuzzy modelling and identification techniques". In: *Sustainable Energy, Grids and Networks* 1, pp. 45–52.

Sloth, Christoffer and Thomas Esbensen (2009). "Fault diagnosis and fault tolerant control of wind turbines". In: *Master's Thesis, Aalborg University*.

Sloth, Christoffer, Thomas Esbensen, and Jakob Stoustrup (2010). "Active and passive fault-tolerant LPV control of wind turbines". In: *American Control Conference (ACC)*. IEEE, pp. 4640–4646.

– (2011). "Robust and fault-tolerant linear parameter-varying control of wind turbines". In: *Mechatronics* 21.4, pp. 645–659.

Song, Yongduan, Xiucai Huang, and Changyun Wen (2016). "Tracking control for a class of unknown nonsquare MIMO nonaffine systems: a deep-rooted information based robust adaptive approach". In: *IEEE Transactions on Automatic Control* 61.10, pp. 3227–3233.

– (2017). "Robust adaptive fault-tolerant PID control of MIMO nonlinear systems with unknown control direction". In: *IEEE Transactions on Industrial Electronics* 64.6, pp. 4876–4884.

Spinato, F et al. (2009). "Reliability of wind turbine subassemblies". In: *IET Renewable Power Generation* 3.4, pp. 387–401.

Tabatabaeipour, Seyed Mojtaba et al. (2012). "Fault detection of wind turbines with uncertain parameters: a set-membership approach". In: *Energies* 5.7, pp. 2424–2448.

Tang, Baoping et al. (2014). "Fault diagnosis for a wind turbine transmission system based on manifold learning and Shannon wavelet support vector machine". In: *Renewable Energy* 62, pp. 1–9.

Tchakoua, Pierre et al. (2014). "Wind turbine condition monitoring: State-of-the-art review, new trends, and future challenges". In: *Energies* 7.4, pp. 2595–2630.

Tiwari, Ramji and N Ramesh Babu (2016). "Recent developments of control strategies for wind energy conversion system". In: *Renewable and Sustainable Energy Reviews* 66, pp. 268–285.

Vidal, Yolanda et al. (2015). "Fault diagnosis and fault-tolerant control of wind turbines via a discrete time controller with a disturbance compensator". In: *Energies* 8.5, pp. 4300–4316.

Wei, X and M Verhaegen (2011). "Sensor and actuator fault diagnosis for wind turbine systems by using robust observer and filter". In: *Wind Energy* 14.4, pp. 491–516.

Wei, Xiukun, Michel Verhaegen, and T Van den Engelen (2008). "Sensor fault diagnosis of wind turbines for fault tolerant". In: *IFAC Proceedings Volumes* 41.2, pp. 3222–3227.

Wei, Xiukun, Michel Verhaegen, and Tim van Engelen (2010). "Sensor fault detection and isolation for wind turbines based on subspace identification and Kalman filter techniques". In: *International Journal of Adaptive Control and Signal Processing* 24.8, pp. 687–707.

Wenyi, Liu et al. (2013). "Wind turbine fault diagnosis method based on diagonal spectrum and clustering binary tree SVM". In: *Renewable Energy* 50, pp. 1–6.

Wu, Dinghui et al. (2016). "Fault estimation and fault-tolerant control of wind turbines using the SDW-LSI algorithm". In: *IEEE Access* 4, pp. 7223–7231.

Yang, Xiaoke and JM Maciejowski (2012). "Fault-tolerant model predictive control of a wind turbine benchmark". In: *IFAC Proceedings Volumes* 45.20, pp. 337–342.

Yao, Yi-Ching (1984). "Estimation of a noisy discrete-time step function: Bayes and empirical Bayes approaches". In: *The Annals of Statistics*, pp. 1434–1447.

Zaher, ASAE et al. (2009). "Online wind turbine fault detection through automated SCADA data analysis". In: *Wind Energy: An International Journal for Progress and Applications in Wind Power Conversion Technology* 12.6, pp. 574–593.

Zhang, Xiaodong et al. (2011). "Fault detection and isolation of the wind turbine benchmark: An estimation-based approach". In: *Proceedings of IFAC World Congress*. Vol. 18, pp. 8295–8300.

Zhang, Zijun, Anoop Verma, and Andrew Kusiak (2012). "Fault analysis and condition monitoring of the wind turbine gearbox". In: *IEEE Transactions on Energy Conversion* 27.2, pp. 526–535.

Zhao, Kai, Yongduan Song, and Changyun Wen (2016). "Computationally inexpensive fault tolerant control of uncertain non-linear systems with non-smooth asymmetric input saturation and undetectable actuation failures". In: *IET Control Theory & Applications* 10.15, pp. 1866–1873.

Zhou, Enlu, Michael C Fu, and Steven I Marcus (2008). "A particle filtering framework for randomized optimization algorithms". In: *Proceedings of the 40th Conference on Winter Simulation*. Winter Simulation Conference, pp. 647–654.

been omitted or incorrectly acknowledged."